Effect of Austenite Microstructure and Composition on Transformation Behaviour in The Heat Affected Zone of Pipeline Steel

Daniel Alejandro Olguín Ramírez

Thesis submitted for the degree of Doctor of Philosophy

The University of Sheffield

Department of Materials Science and Engineering

November 2022

Acknowledgements

I want to express my acknowledgement to “Consejo Nacional de Ciencia y Tecnologia” (Conacyt) and the Roberto Rocca Education Program for the funding provided in my PhD studies. Also, I would like to acknowledge Ternium Mexico for allowing me to perform testing in their R&D laboratory at Industrial Centre in Pesquería and for the rewarding discussions about this research.

Additionally, I would like to thank my supervisor, Professor Eric James Palmiere, for allowing me to be part of his research group; all this time has been a continuous learning process. His guidance, patience, and technical support motivated and encouraged me to pursue my PhD degree.

I also want to acknowledge the Research and Development Department of Ternium Mexico, especially Omar García and Juan Pablo Pedraza, who supported me with access to the laboratories and valuable discussions about my results.

I want to thank the staff of the Department of Materials Science and Engineering, Sorby Centre and the Diamond laboratory for supporting me all this time. Special thanks to Dean Haylock for all his support in the thermomechanical laboratory. I am grateful to Le Ma, John Nutter, Elisa Alonso Lopez and Neil Hind. This work would not have been possible without their support.

I sincerely acknowledge my colleagues Luis Romano, Eduardo Pineda, Marta Muniz, Karol Rodriguez and Bhushan Rakshe. It was a fantastic research team; with them, I always found mentoring, advice, support and encouragement to pursue my PhD.

Also, I would like to thank all the valuable friends I knew in Sheffield. I had fantastic talks with them during this time, especially with Konstantina, Marissa, Kathryn, Gao Fan, Jose Luis, Ahmad, Zhiyu and Alejandro.

Finally, I would like to thank my family, who always motivated and encouraged me during all this time. Thanks to my father for guiding me, my mother and her rewarding words, my little niece, my sisters and my brother. I always had their unconditional support to follow with my PhD.

Table of contents

List of Figures

List of tables

List of Abbreviations

%EI	Percentage of elongation increase
%RA	Percentage reduction in the cross-section area
α	Ferrite
Aβ	Granular bainitic ferrite
γ	Austenite
ΔL	Difference in length
ε	Engineering strain
σ	Engineering stress
A_1	Eutectoid temperature
A_3	Ferrite transformation
Ac	Contact area
A_{c1}	The temperature at which austenite begins to form during heating
A_{c3}	The temperature at which transformation of ferrite to austenite is completed during heating
A_{cm}	Cementite transformation
A_{e1}	Eutectoid temperature
AF	Acicular ferrite
Af	Final area
API	American Petroleum Institute
ar	Area reduction
A_{r1}	The temperature which austenite to ferrite transformation is complete during cooling
A_{r3}	The temperature which austenite begins to transform to ferrite during cooling
ASTM	American Society for Testing and Materials
BC	Band contrast
BCC	Body centred cubic

Bcf	Billion cubic feet
BCT	Body centred tetragonal
BF	Bainite ferrite
BS	Band slope
CBMM	Companhia Brasileira de Metalurgia e Mineração
CCD	Charge coupled device
CCR	Conventional controlled rolling
CCT	Continuous cooling transformation
CE	Equivalent carbon content
CO2	Carbon dioxide
C_R	Cooling rate
DBTT	Ductile-brittle transition temperature
D_γ	Grain diameter of austenite
E	Elastic modulus
EBSD	Electron backscatter diffraction
EDM	Electric discharge machining
EDS	Energy dispersive spectroscopy
e_t	Total elongation
e_u	Uniform elongation
FCC	Face centred cubic
Fe_3C	Cementite
FEI	Field Electron and Ion Company
FTTU	Fast thermal treatment unit
FZ	Fusion zone
G	Temperature gradient
GF	Granular ferrite
GMAW	Gas metal arc steel weld
GOS	Grain orientation spread
HAGB	High angle grain boundary
HAZ	Heat affected zone
HI	Heat input
HRC	Hardness Rockwell C

HSLA	High strength low alloy steels
HTP	High temperature processing
HV	Hardness Vickers
IAF	Intergranular acicular ferrite
IPF	Inverse pole figure
IQ	Image quality
ISIJ	The Iron and Steel Institute of Japan
JEOL	Japan Electron Optics Laboratory Company
L0	Initial length
LAGB	Low angle grain boundary
LB	Lower bainite
L_f	Final length
M	Martensite
MA	Martensite-Austenite
NbC	Niobium carbide
NbCN	Niobium carbonitrides
OPEC	Organization of the Petroleum Exporting Countries
P	Load
PAGS	Prior austenite grain size
Pcm	Weld cracking parameter
PF	Polygonal ferrite
PHMSA	The Pipeline and Hazardous Materials Safety Administration
PSC	Plain strain compression sample
PWC	Preferential weld corrosion
QF	Quasi polygonal ferrite
R	Growth rate of the solid-liquid interface
S	Velocity
SAW	Submerged arc welding
SDAS	Secondary dendrite arm spacing
SEM	Scanning electron microscopy
SMAW	Shielded metal arc welding
$T_{5\%}$	Recrystallisation stop temperature

TEM	Transmission electron microscopy
TiN	Nitride of Titanium
TMC	Thermomechanical compression machine
TMCP	Thermomechanical controlled processing
TS	Tensile strength
TTT	Time temperature transformation
UB	Upper bainite
WF	Widmanstätten ferrite
YS	Yield stress
USGC	United States Geological Survey

Chapter 1

Introduction

1.1 Perspective of energy

Hydrocarbons transformed promptly into the primary energy source of modern civilisation used to generate electricity, fuel for transportation, fertilisers in agriculture and even to produce clothes[1]. However, hydrocarbons are a source of energy that is finite. After Marion King Hubbert modelled the peak oil in 1956, the world concern has been to stretch the bell-shaped curve (Hubbert curve)[2-5]. Delaying the peak of production allows the provision of energy in a world that continues to grow in population.

Increasing oil and gas extraction has evolved from conventional to offshore and shale techniques. Even exploration has reached remote regions such as The Artic[6-10]. The US Geological Survey (USGS) estimates that around 22% of the world's undiscovered energy is in that region[6]. Furthermore, that region represents technical challenges due to extreme weather conditions and infrastructure investment. Also, the possibility of a spill has stopped hydrocarbon exploration in the Arctic due to the Deepwater Horizon Oil spill in the Gulf of Mexico in 2010[6,11].

During the last decade, shale extraction has mainly increased oil and gas production in The United States. Consequently, shale technology enabled the United States to become the largest producer of oil and gas in the world[12]. The U.S. Energy Information Administration published in 2020 the future of US energy production in the next 30 years[13]. Figure 1 shows the growing tendency of natural gas, while renewables are increasing in production. Furthermore, renewables need backup energy to cover the variability of electricity generation because of weather conditions, the primary source of which is natural gas[14].

1.2 Natural gas

In the last decade, the significant increment in natural gas extraction changed the US's position as a net natural gas exporter. That lends an essential competitive advantage to the industry through a drastic decrease in market price[12]. Figure 2 illustrates the natural gas trade; exportations to Mexico are the result of pipeline infrastructure developing mainly in the Gulf of Mexico; after 2030, exportations will stabilise due to an increment in domestic production[13].

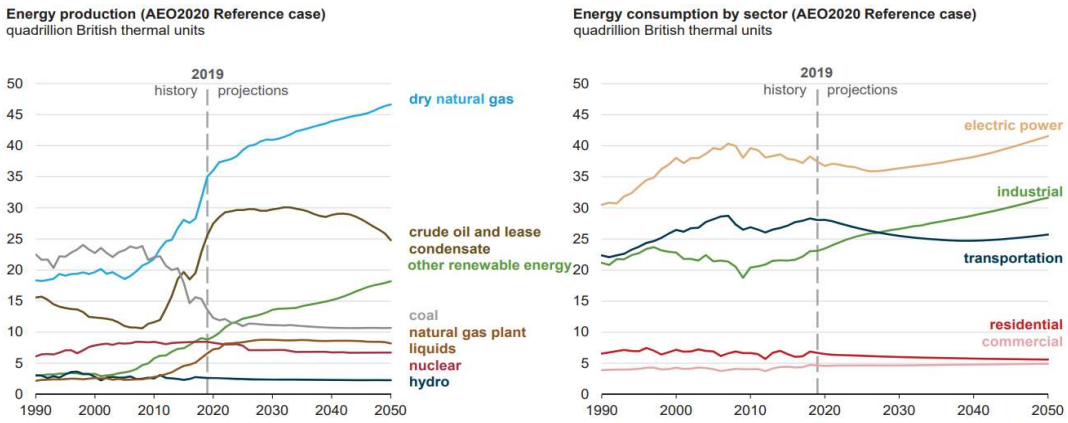

Figure 1 Expectative of energy production in the US [13].

In contrast, China's dependence on hydrocarbons is significant, importing 70% Oil and 43% natural gas. Those energy sources are crucial in managing strategies and national security. The growth of the average annual consumption of natural gas is estimated at 5.7% (2020-2030), 2.7% (2030-2040) and 0.7% (2040-2050). The Silk Road Economic Belt initiative will access energy in the Middle East, Eastern Europe and Africa, increasing trade in those countries[15-17].

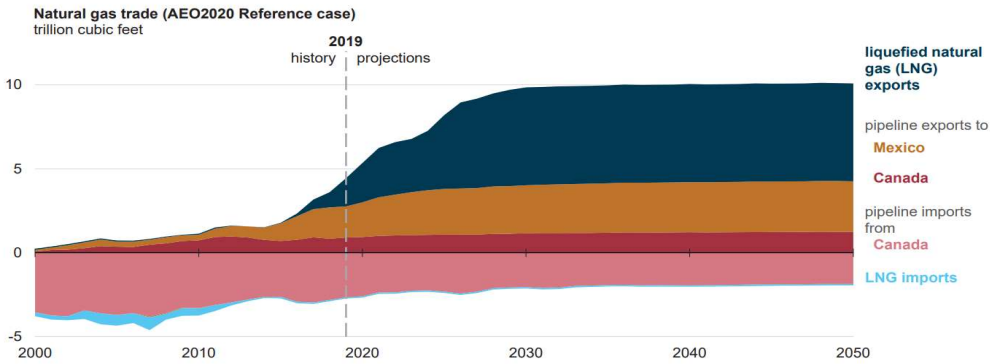

Figure 2 US natural gas trade [13].

1.3 Pipelines

Pipelines are the most efficient form to transport an array of substances such as oil, natural gas, water and chemicals. In the beginning, it needs a high investment due to steel price and installation, which also, could increase the project cost depending on the geographical area[18]. However, the life period is more than 40 years with no critical maintenance issues. Typically, natural gas and oil tubes are among the longest pipelines installed, spanning entire countries and, in some cases, even continents. For example, the infrastructure project which connects Russia and China with 5 111 Km of pipeline from Siberia to Shanghai[19]. Thus, some of the challenges associated with these great lengths in pipelines, particularly in earthquake-prone areas and arctic regions[20].

In North America more than 5.5 million kilometres of pipelines in service are distributed as follows: The United States (4,827,000)[21], Canada (830,000)[22] and Mexico (68,843)[23]. Infrastructure projects continue to increase on an annual basis. In 2019, The United States grew between 16 to 17 BCF per day in natural gas capacity with 134 projects, of which 40% of the new projects were located in the South-central region (Figure 3)[24].

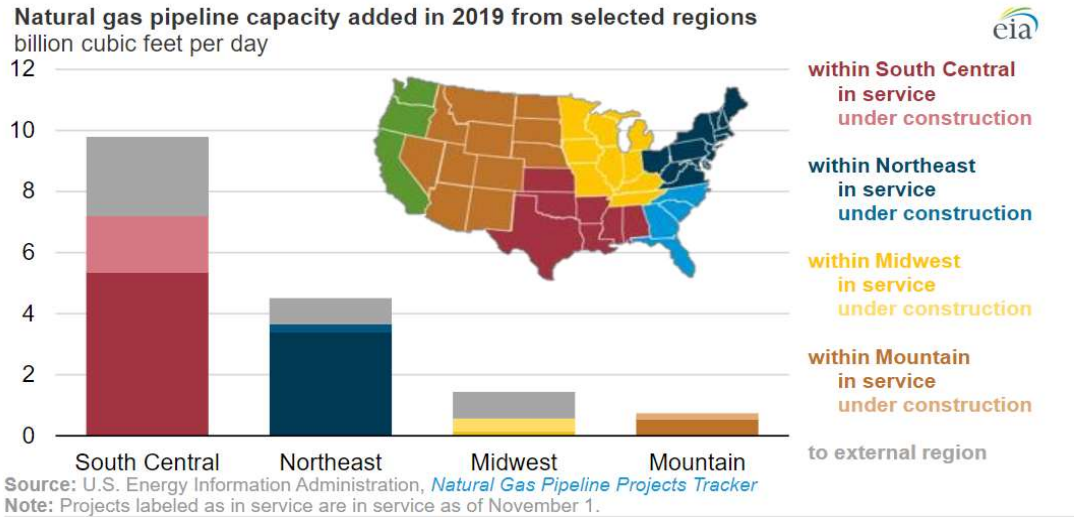

Figure 3 Natural Gas Capacity added in 2019 in pipelines[24].

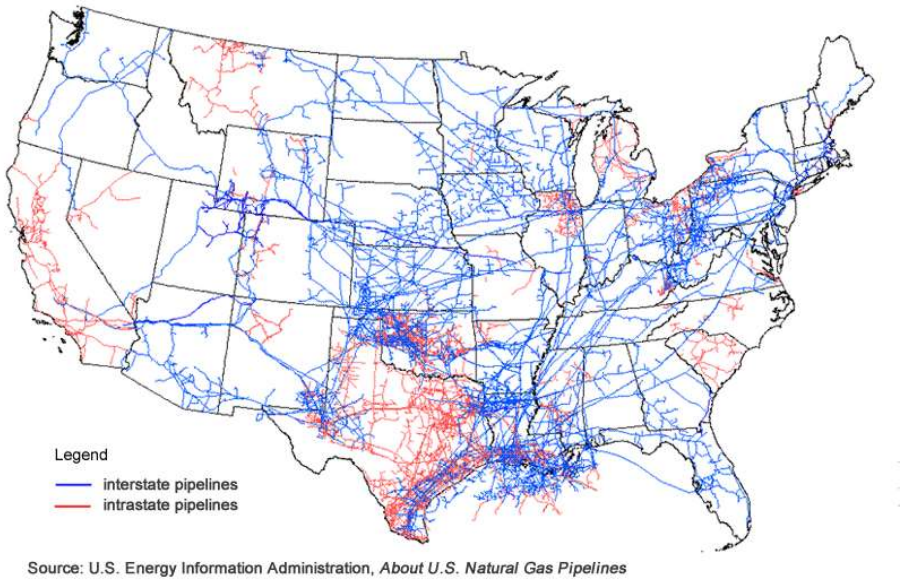

Figure 4 U.S. Map intrastate and interstate natural gas pipelines [21].

The consequences of pipeline failures are usually severe, and the impact of these failures can be economical, environmental, and even human loss. The Pipeline and Hazardous Materials Safety Administration (PHMSA) identifies the causes of these failures associated with material welding and corrosion, with 43% and 17% as the leading causes of pipeline incidents between 2009 and 2018 [25]. Causes of material-welding issues can be attributed to various factors, such as defects and impurities present in the metal, the chemical composition of the materials, and the welding techniques utilized. Corrosion issues are related to thinning on walls due to chemical reactions with environments. Preferential Weld Corrosion (PWC) is one of the most critical issues which affect pipelines [26]. Preferential corrosive attack in welding appears where there are differences between the base and weld material, such as composition and microstructure (including differences in Heat Affected Zone (HAZ) microstructure)[26,27]. An example of such a catastrophe appeared on May 19, 2015, in Refugio, California. A failure in the pipeline resulted in 100,000 gallons of crude oil to spill, killing hundreds of animals in the affected zone. The company was fined 100 Million USD; in this failure, PHMSA reported advanced corrosion in the pipelines, with a 74% reduction of original thickness in some areas [28,29]. In this event, the criticality of the pipes is demonstrated both safety and environmental issues.

1.4 Microalloyed steels

The expansion in microalloyed steels started in 1973 with the OPEC oil embargo. Scarcity and increases in oil prices result in the exploration of hydrocarbons outside the Arabian Peninsula. In this situation, pipelines were critical to transport oil and gas from stable regions to the market. In those circumstances, oil companies demand the highest yield strength to explore and produce in the most elevated corrosive environments and extract hydrocarbons to greater depths under the sea. In 1970, heat treated steel was the majority of high strength material; however, it was insufficient to meet the new demand. Existing hot rolled steels had low yield strength, API X50-X60 (σ_{yp} 350 – 420 MPa). Two characteristics must be necessary to improve steel strength. First, high levels of refinement, beginning with austenite at the temperature of transformation[30]. Second, low temperature products are required in the cooling process to achieve high strength levels, such as non-polygonal ferrite, acicular ferrite, bainite and martensite [30]. To control the cooling temperature in hot lamination, the runout table water spray is decisive in obtaining high strength steels [30]. Besides grain refinement and transformation products, precipitation hardening is fundamental in microalloyed steels [30].

Microalloyed steels use a reduced amount of microalloying elements from 0.10 up to 0.15 wt %, which are titanium, vanadium and niobium [30]. Adding microalloying elements is necessary to ease the dispersion of precipitates and refine grain microstructure [31]. Suppressing recrystallisation and elevating dislocation density are advantages of precipitation of Nb, V, and Ti carbonitrides [31]. Table 1 shows the effect of mean microalloyed elements and %wt.

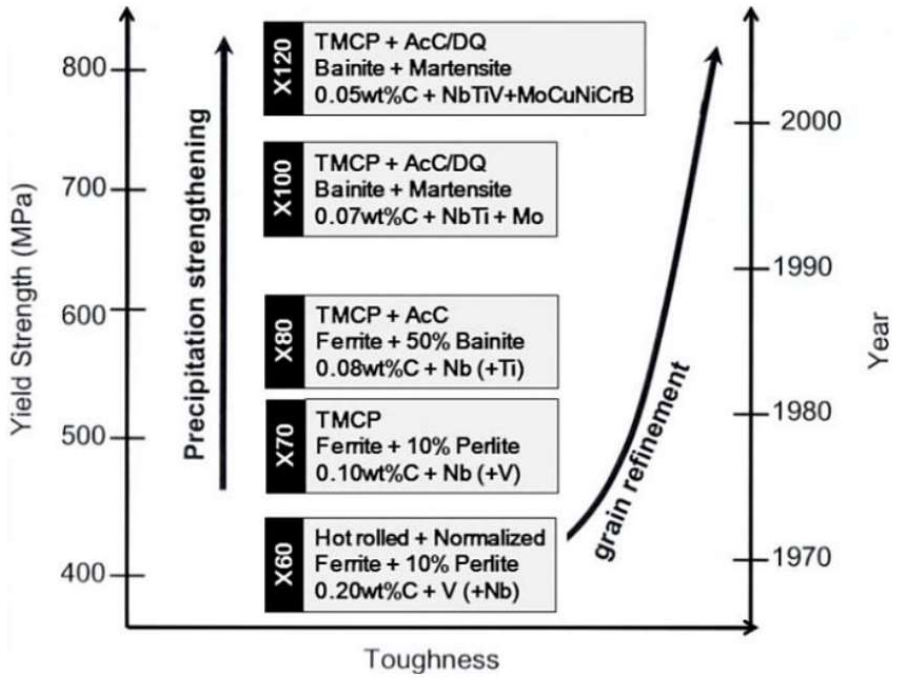

Figure 5 Progression in pipelines steel grades since 1970 [32].

Table 1 Effect of principal microalloyed elements [31].

Element	wt %	Effect
C	<0.25	Strengthener
Mn	0.5–2.0	Retards the austenite decomposition during accelerated cooling Decreases ductile to brittle transitions temperature Strong sulfide former
Si	0.1–0.5	Deoxidizer in molten steel Solid solution strengthener
Al	<0.02	Deoxidizer Limits grain growths as aluminum nitride
Nb	0.02–0.06	Very strong ferrite strengthener as niobium carbides/nitrides Delays austenite-ferrite transformation
Ti	0–0.06	Austenite grain control by titanium nitrides Strong ferrite strengthener
V	0–0.10	Strong ferrite strengthener by vanadium carbonitrides
Zr	0.002–0.05	Austenite grain size control Strong sulfide former
N	<0.012	Strong former of nitrides and carbonitrides with microalloyed elements
Mo	0–0.3	Promotes bainite formations Ferrite strengthener
Ni	0–0.5	Increase fracture toughness
Cu	0–0.55	Improves corrosion resistance Ferrite strengthener
Cr	0–1.25	In the presence of copper, increase atmospheric corrosion resistance
B	0.0005	Promotes bainite formation

1.5 Scope of this thesis

The most susceptible locations for failure in large diameter transportation pipes are the weld metal and Heat Affected Zone (HAZ)[33]. This project will analyse the Heat Affected Zone. The HAZ mechanical properties have a substantial role in the functioning of the welding joint [33]. While the weld metal exhibits a strength mismatch, the HAZ and base metal originate strain concentration focused in the zone with the lowest strength [33]. The lowest strength zone is related to softening phenomena and brittle fracture. HAZ softening is influenced by martensite tempering. A lower quantity of heat input in welding promotes stabilisation of coarse austenite-martensite regions and restricts the embrittle grain boundary precipitates forming[33].

The present work consists of the study of Heat Affected Zone in X80 pipeline steel which was processed through Submerged Arc Welding. This steel contains a significant amount of niobium, approximately 0.094%, and has a carbon content of 0.06%. The pipeline is installed in the states of Wyoming, Colorado and Kansas with 410 miles [34,35]. The microstructure evolution and mechanical properties' impact can be evaluated by utilising a thermomechanical simulator to reproduce various austenitisation temperatures and cooling rates. By examining these parameters, it becomes possible to observe the heat-affected zone's effect under similar conditions.

1.6 Aims and Objectives

The aim of this project is to assess how the resulting microstructure and mechanical properties in an X80 pipeline steel are affected by cooling rates and prior austenite grain size. The austenitisation time will exceed previous research in order to ensure a homogeneous temperature distribution throughout the sample. The use of these parameters will enable us to observe any potential behaviour in the Heat Affected Zone. The aim is subdivided into the following objectives:

1. Investigate the influence of cooling rate, the solubility of niobium and prior austenite grain size on the decomposition kinetics and the following microstructures and subsequent mechanical properties. This will be compared when all the niobium are in solution.

2. The transformation kinetics and austenite of a material will be studied using a Gleeble simulator and thermomechanical machine to perform the heat treatments. The cooling rates will be adjusted between 0.5 and 50 °C/s during the heat treatments to investigate how the material behaves and to gain insight into its properties under different conditions. Precise control and measurement of temperature and mechanical properties will be ensured with the help of the experimental setup.

3. The microstructures resulting from the experimental procedure will be analysed using several methods, including optical microscopy, scanning electron microscopy (SEM), and electron backscatter diffraction (EBSD). To evaluate the nano precipitates, transmission electron microscopy (TEM) will be utilised.

4. To determine how microstructure impacts the mechanical properties of the material, it will conduct Vickers microhardness, tensile, and Charpy testing. These tests will allow to assess how the microstructure affects the properties of the material and provide valuable insights into the relationship between microstructure and mechanical properties

Chapter 2

Background

2.1 Phases and structures

Different microstructures and mechanical properties appear during the steel manufacturing. By adjusting the heating, holding time, and cooling rates during processing, it is possible to produce different types of microstructures. All heat treatments of steel are based on the iron-carbon equilibrium phase diagram. The iron carbon equilibrium diagram shows the ranges of temperature and composition where different phases in steel are in equilibrium, and it also shows the limits that define the transitions between those phase fields (Figure 6)[36].

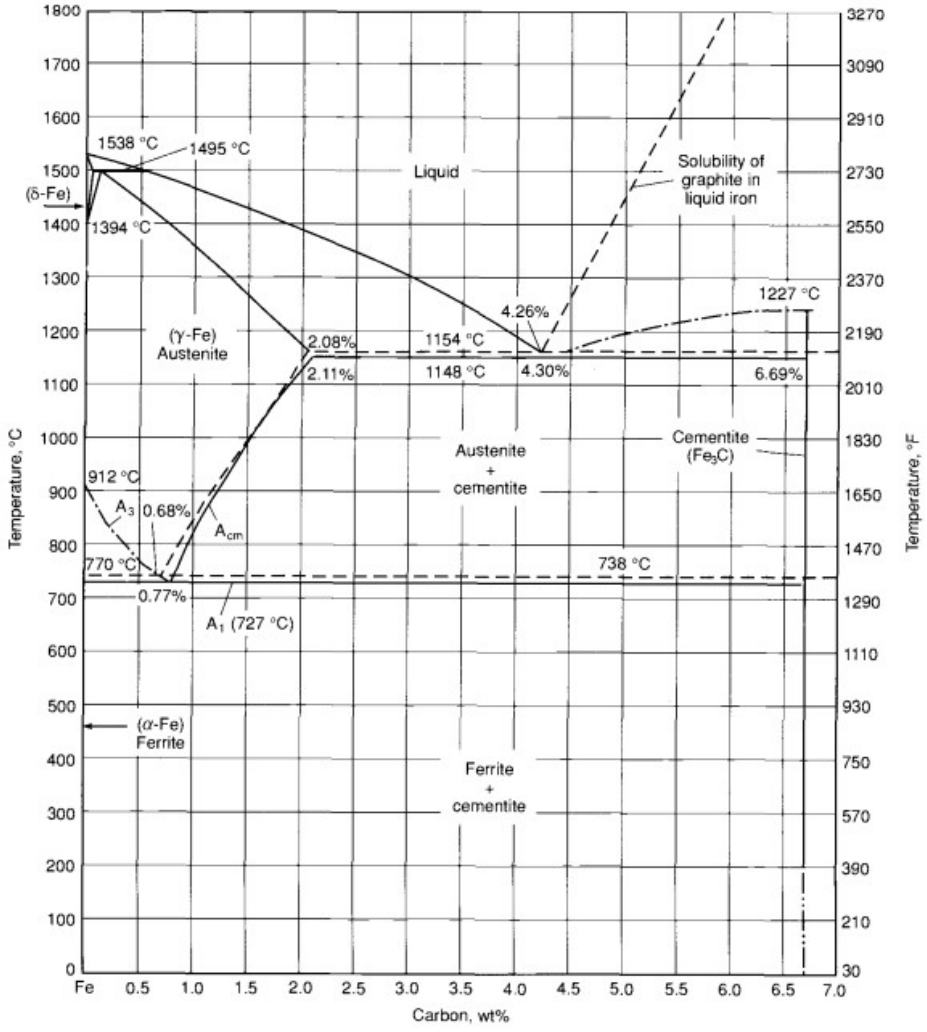

Figure 6 Iron carbon equilibrium diagram up to %C 6.67 wt. Fe-Fe3C diagram is indicated by solid lines and iron graphite diagram appears in dashed lines [37].

While the iron carbon equilibrium diagrams are used in stable conditions, the Continuous Cooling Transformation diagram (CCT) is utilised at different temperatures of cooling. CCT diagram is a graph that represents the relation between temperature, cooling rates, and the austenite transformation into variety of microstructures (such as ferrite, pearlite, bainite and martensite) in a steel alloy. CCT diagrams are used to define the appropriate cooling rate to obtain the desired microstructure and mechanical properties. The diagram illustrates the temperature at which the transformation begins and finishes (Figure 7) [38].

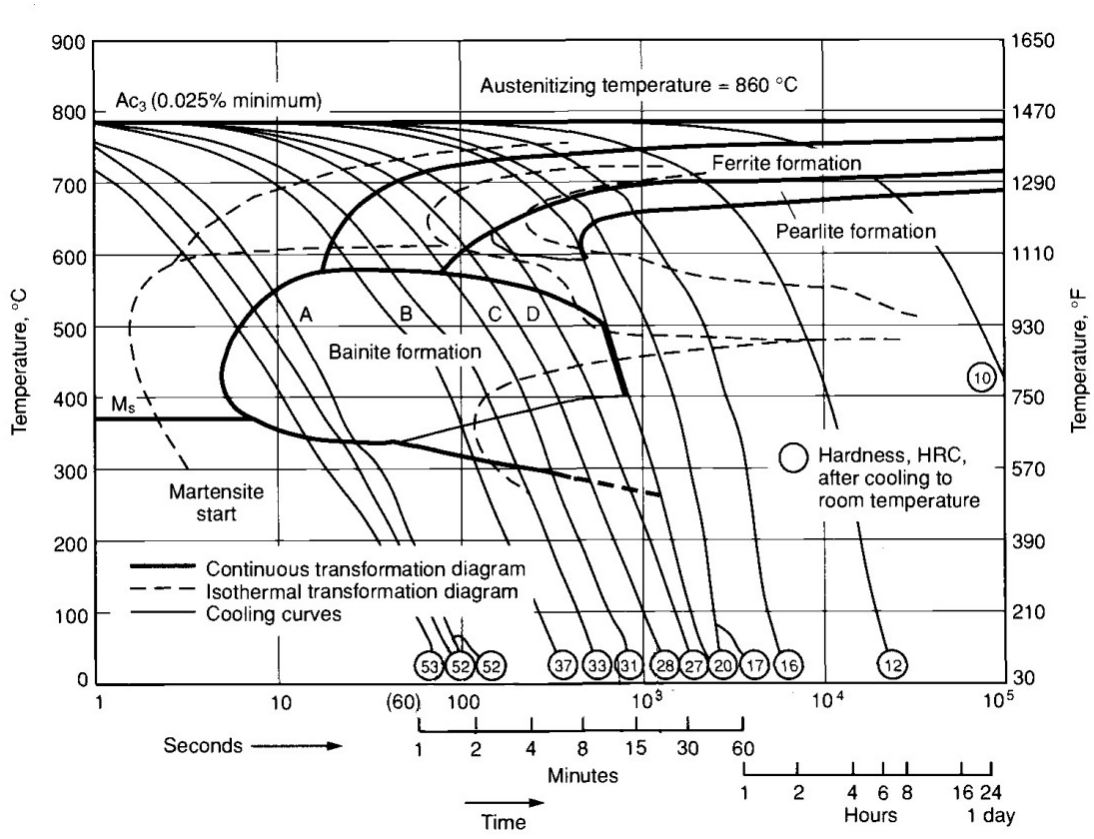

Figure 7 CCT diagram and isothermal transformation of steel containing 0.4%C, 0.2% Mo and 1.0% Cr [37].

2.2 Phase Transformation

2.2.1 Transformation Mechanism

An array of mechanical properties in iron alloys are influenced by atomic distribution in different phases. The atomic crystal partition can be changed by displacive transformation and reconstructive transformation. In the displacive mechanism, the alteration of crystal structure affects the macroscopic form in the specimen when the latter is unconstrained. The shape deformation through the transformation in a constrained way is organised by a plastic and elastic combination of strains. Resultant phase growth occurs in the shape of thin plates to achieve strain decrease. As a result, the atoms change their position in a coordinated movement occupying a new place in the surrounding matrix (Figure 8)[39].

Atom diffusion leads to reconstructive transformation, which produces a new structure of crystals. During alloy transformation, diffusion guides the solute redistribution (among phases). The matter flow could prevent any shear constituent of the shape deformation, making only the volume modification as an effect. The diffusion process consistently leads to solute redistribution among phases with a whole free energy decrease (Figure 9)[39].

The retardation of displacive transformation occurs as a consequence of dislocation debris or also called mechanical stabilisation. There are two characteristics which explain the reason that mechanical stabilisation is the only feature of displacive transformation:

- Plastic deformation cannot generate a delay in reconstructive transformation by any mechanism. While reconstructive transformations accelerate austenite defects.

- Mechanical stabilisation only occurs in displacive transformations. Because this mechanism is connected with a glissile interface, which restricts movement in a matrix which includes an array of dislocations or other defects.

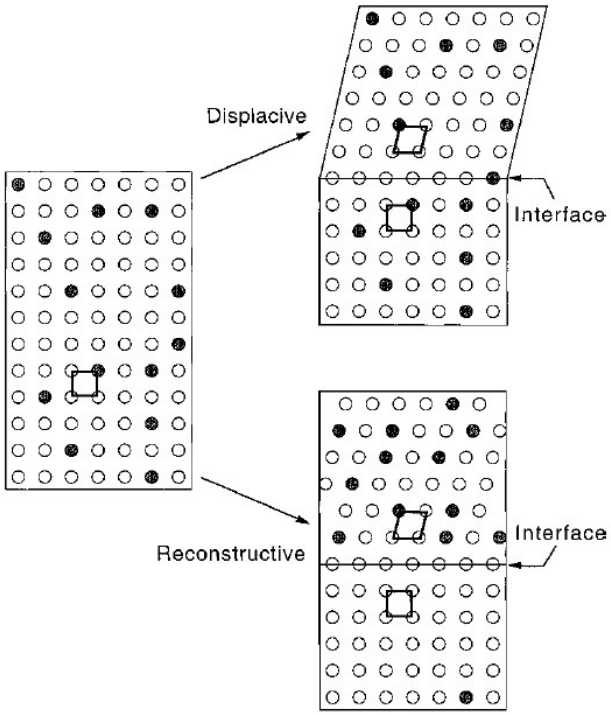

Figure 8 The principal mechanisms of phase transformations: reconstructive and displacive[39].

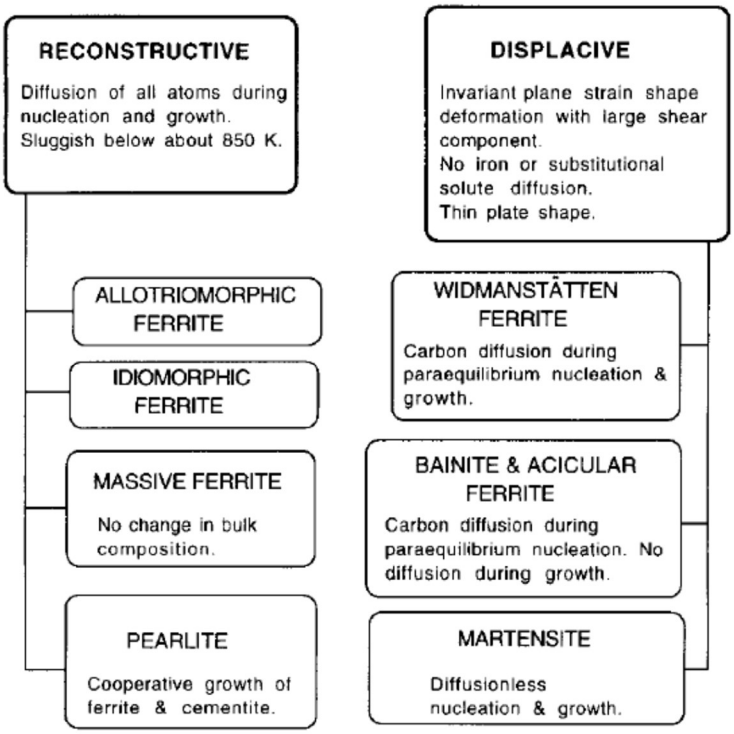

Figure 9 Fundamental features in steels transformations mechanisms[39].

2.2.2 Ferrite

The carbon iron alloys will form proeutectoid ferrite below equilibrium conditions, up to 0.8% C contents. At 910°C, the reaction occurs in pure iron, while in iron-carbon alloys occurs between 910°C and 723°C. However, the ferrite could form at low temperatures till 600°C when the material is quenched from austenite to temperatures down the Ae_1 (eutectoid temperature). Lower transformation temperature produces high morphological changes[40].

Due to different changes in the transformation behaviour of carbon steels, Dubé[36] suggested a morphologies classification of ferrite, which occurs when the temperature transformation of γ/α is lowered. Dubé[36] classified the next four morphologies (Figure 11):

- Grain boundary allotriomorphs, the nucleation of these crystals occurs in the grain boundaries of austenite. This morphology is characterised by lenticular or equiaxed shape (Figure 11-a)[36].

- Widmanstätten side plates. The nucleation takes place in the austenite grain boundaries in a primary way (Figure 11-b_1). However, secondary side plates can also initiate growth through the allotriomorphic grain boundary (Figure 11-b_2). Figure 11-c shows another variation of Widmanstätten, saw teeth which are characterised by more triangle semblance. These morphologies can nucleate on grain boundaries or also into allotriomorphic grain boundaries[36].

- Intragranular idiomorphs: the nucleation of these microstructures is formed within austenite grains or in the grain boundaries characterised by equiaxed crystals (Figure 11-d)[36].

- Intragranular plates. The growth of these plates is similar to those which nucleate in the grain boundaries, however, nucleation occurs completely into the γ grains. (Figure 11-e)[36].

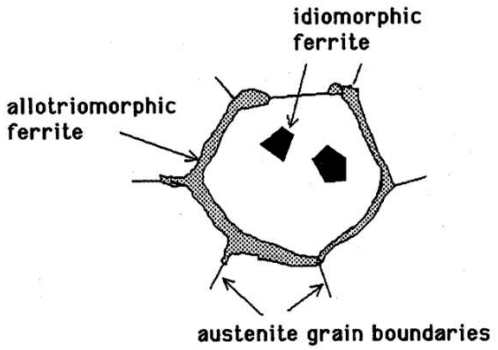

Figure 10 Representation of allotriomorph and intragranular idiomorphs ferrite [41].

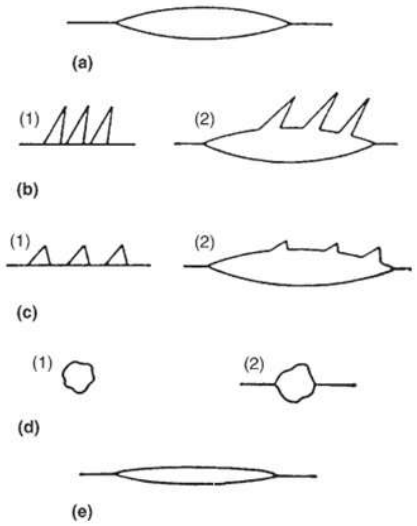

Figure 11 Classification system of Dubé used to describe ferrite morphologies[36].

2.2.2.1 Effect of cooling rate on ferrite morphology

Austenite decomposition affects the restriction of atom movement with the reduction of transformation temperature. This results in the formation of different ferrite morphologies besides an array of microstructures. To obtain the rearrangement of iron atoms from the austenite phase to equiaxed ferrite is necessary to increase the temperature. At the same time, when the temperature is increased is produced a movement of carbon atoms by diffusion. At medium temperatures of cooling, interstitial carbon atoms keep good mobility, but the iron atoms start in a sharply slow motion. At these cooling temperatures, to form no equiaxed crystals of ferrite requires a small reorder in ledges of ferrite/austenite or mechanism of shear. At low temperatures, iron and carbon atoms cannot diffuse; consequently, the martensite forms directly through austenite transformation by shear. Figure 12 represents changing of microstructures depending on cooling rate and temperature decrease[36].

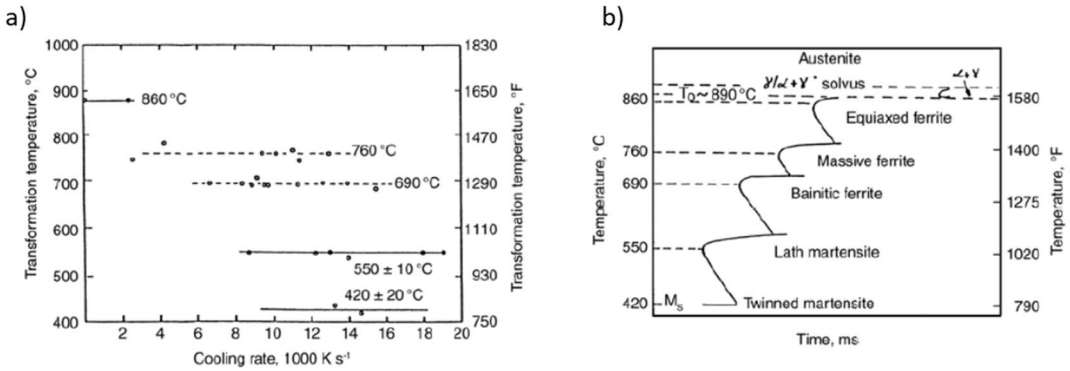

Figure 12 Initiate transformation temperatures depending on a) cooling rate, b) curves of austenite decomposition products in Fe – 0.01% alloy[36].

2.2.2.2 Classification systems for ferritic microstructures.

Low carbon steels have obtained significant attention in recent years because during the austenite decomposition is formed different ferritic microstructures. These morphologies are obtained with the modification of cooling rates and isothermal holding time at intermediate transformation temperatures. Table 2 illustrates the classification of The Iron and Steel Institute of Japan (ISIJ) Bainite Committee[36].

Table 2 ISISJ Bainite Committee classification for different ferritic microstructures[36].

Symbol	Nomenclature
I_O Major matrix phases	
α_P	Polygonal ferrite
α_q	Quasi-polygonal α
α_W	Widmanstätten α
α_B	(Granular bainitic) α
α_B^O	Bainitic ferrite
α′m	Dislocated cubic martensite

Symbol	Nomenclature
II_O Minor secondary phases	
γ_r	Retained austenite
MA	Martensite-austenite constituent
α′M	Martensite
ATM	Autotempered martensite
B	BII, B2: upper bainite Bu: upper bainite B_L: lower bainite
P′	Degenerated pearlite
P	Pearlite
Θ	Cementite particle

2.2.2.3 Polygonal or Equiaxed Ferrite

This microstructure is a proeutectoid ferrite. In low carbon steels, polygonal ferrite appears at elevated austenite transformation temperatures and slow cooling rates. The nucleation of ferrite grains grows through boundaries of austenite grains until equiaxed grains are shaped. The prompt substitutional atom must control polygonal ferrite growth because the substitutional atoms are transferred through the austenite-ferrite interface. And, the carbon atoms diffusion is rejected by the growing ferrite. Figure 13-a represents polygonal ferrite in HSLA steel; the ferrite grains are equiaxed and divided by uninterrupted linear boundaries. Martensite appears in dark zones shaped by the untransformed austenite (during quench) occurring after 500s of holding[36].

2.2.2.4 Quasi-Polygonal or Massive Ferrite

To have a microstructure change from temperatures where the austenite phase is stable to stable ferrite without composition alteration, it is necessary for high cooling rates in low carbon steels. High cooling rates impede carbon portioning through the austenite to ferrite transformation. Also, rapid cooling rates produce coarse ferrite grains; hence, this ferrite is known as massive ferrite. Furthermore, the transformation which originates the coarse ferrite is known as massive transformation. Massive ferrite implicates a crystal structure change (from fcc to bcc); in the transformation, atoms move from austenite to ferrite interfaces[36].

Figure 13-b illustrates ultra-low carbon steel with massive ferrite. This structure shares some similarities with polygonal ferrite, such as harshly equiaxed, coarse grains, and their grain limits intersect the limits of austenite prior grain boundaries. Moreover, massive ferrite grain boundaries are irregular, and a substructure in the etching is observed in the grains. Quasi polygonal ferrite, α_q, was defined by ISIJ to distinguish between massive and polygonal ferrite[36].

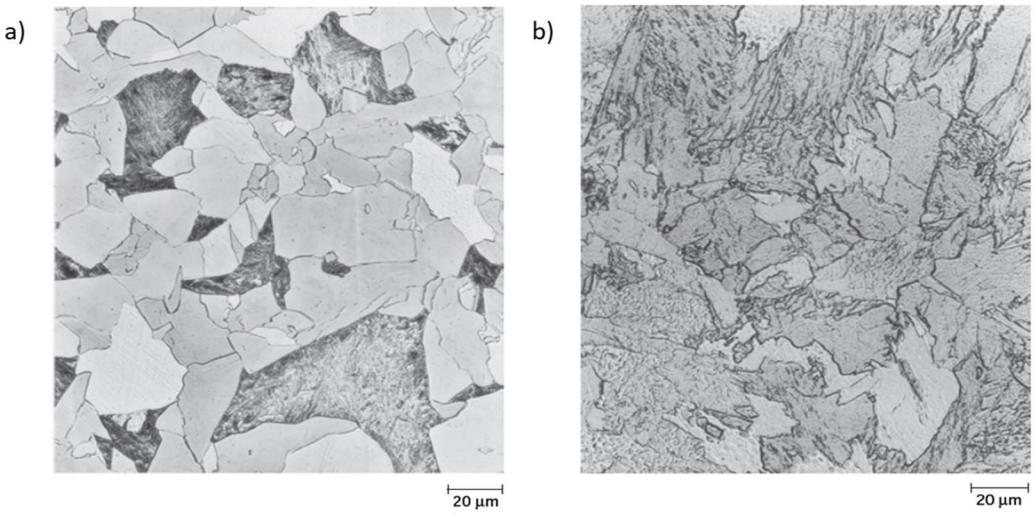

Figure 13 a) Polygonal ferrite transformed isothermally during 500s at 675 °C in an HSLA steel. b) Quasi polygonal ferrite shaped in ultra-low carbon steel with a cooling rate of 50°C/s with a chemical composition of 0.003% C and 3% Mn[36].

2.2.2.5 Bainitic or Acicular Ferrite

Austenite converts into a thin ferrite crystal at rapid cooling rates (in ultra and low carbon steels). The acicular or elongated form is a characteristic of these crystals. In the ISIJ system, the acicular ferrite is referred to as α_B. Figure 14-a illustrates the CCT diagram of HSLA -80 steel. In high cooling rates, granular ferrite and acicular ferrite are transformed during intermediate temperatures. The upper and lower bainite is shaped at low cooling rates. Figure 14-b represents an acicular ferrite microstructure shaped at 500°C. In this microstructure appears elongated, parallel and aligned forms. The structure is constituted of many thin ferrite crystals; however, the crystals share the same orientation divided only by the low angle boundaries. High dislocation density between crystals is a characteristic of the acicular ferrite; this could be observed in TEM[36].

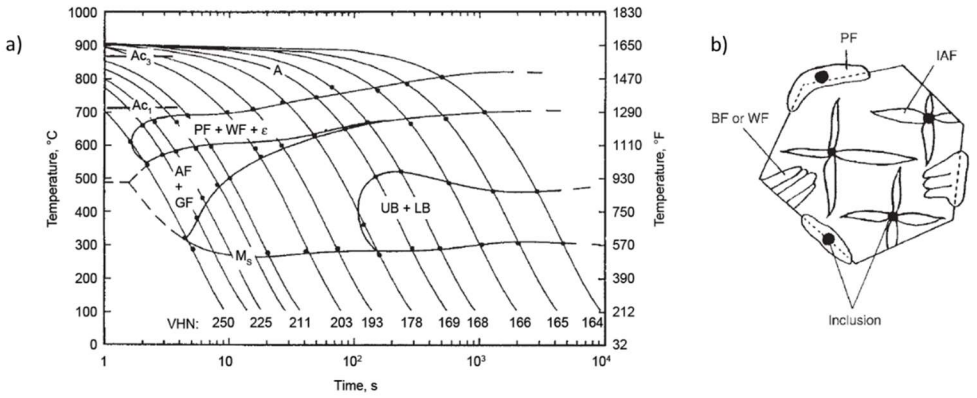

Figure 14 a) CCT diagram of HSLA-80 steel (0.05% C, 0.88% Ni, 0.20% Cr, 0.50% Mn and 0.20% Mo). b) Schematic of intergranular acicular ferrite, IAF, with other morphologies of ferrite[36].

2.2.2.6 Granular Ferrite or Granular Bainitic Ferrite

In low carbon steels, granular bainitic ferrite (α_B) shapes in the intermediate temperatures of transformation. Figure 15-b illustrates A710 steel with granular ferrite microstructure. The microstructure of granular ferrite is formed by retained austenite (M/A) islands scattered in a matrix; the M/A constituents reveal the grain boundaries of austenite during etching. The dispersion of particles maintains an equiaxed or granular morphology. The ferrite crystals in the matrix are fine, equiaxed, and also appear with high dislocation density and low angle boundary division[36].

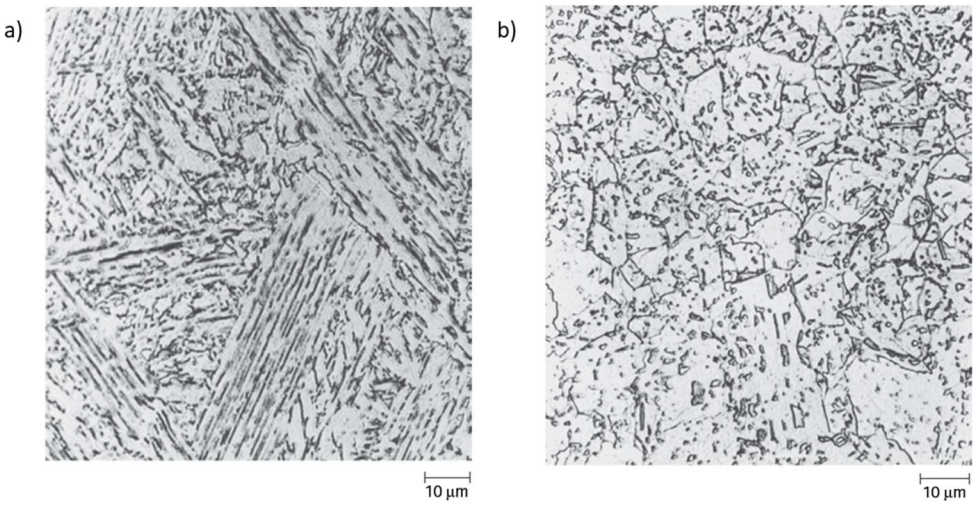

Figure 15 a) Acicular ferrite in HSLA-80 steel with isothermal transformation (5 000s at 500°C). b) Microstructure of granular ferrite in A710 steel (0.33%C, 1.44% Mn, 2.19% Ni, 0.67% Cr, 1.20% Cu and 0.46% Mo)[36].

2.2.3 Pearlite

Pearlite is a eutectoid reaction formed by austenite decomposition in ferrite (α) and cementite (Fe_3C). The nucleation of this lamellar structure is located on grain boundaries of austenite (γ), growing gradually into the grains. When A_{R3} temperature is achieved, it initiates the proeutectoid ferrite formation. During austenite decomposition (fcc to bcc), carbon atoms are refused into untransformed austenite grains; because the carbon atoms maintain a low solubility in ferritic structures. When A_{R1} temperature is attained, the majority of proeutectoid ferrite transforms. Then, the carbon content is enriched at 0.77wt% in the remaining austenite (γ), initiating the pearlite reaction[37].

Figure 16 illustrates ferrite and cementite nucleation at the grain boundaries of austenite; then the nuclei grow inside the austenite grain as a colony. In this process, the orientation layers maintain the same direction as the colony. The formation of nodules with larger shapes is the result of a simultaneous colony growth drive. During pearlite growth, the carbon is rejected to the plates from ferrite and joins into the cementite. This mechanism is through carbon diffusion in different forms: across the austenite, the ferrite, or the interface[42].

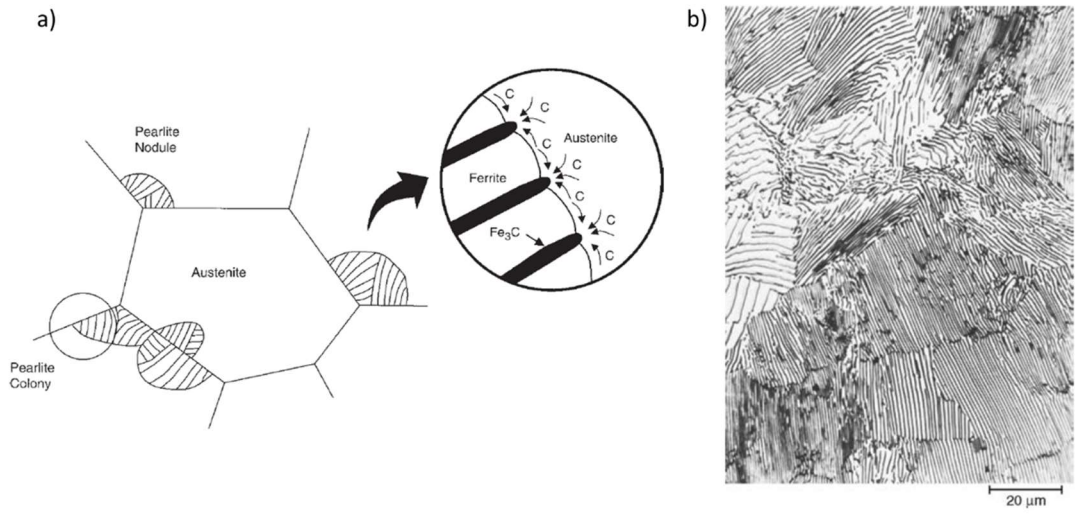

Figure 16 a) Mechanism of pearlite initiation through colonies in the austenite grain boundary b) Pearlite microstructure in eutectoid steel[42].

2.2.4 Bainite

Bainite is the microstructure resulting from the austenite decomposition in ferrite and cementite. To obtain this microstructure, the temperatures must be below pearlite and above martensite transformation. A significant overlap range is visualised between the pearlite and the bainite transformation temperature in plain carbon steels. Furthermore, the division between pearlite and bainite temperature in alloy steels is different, generating a bay among pearlite and bainite transformation curves (Figure 17-a, 17-b). When the isothermal transformation starts, the amount of bainite elevates as a sigmoidal function of time until the limit point. These phenomena occur even in prolonged heat treatment, although an essential quantity of austenite still exists. This unfinished transformation ends when the austenite obtains the equilibrium composition [43].

Depending on the initiation of transformation temperature, the bainite is divided into lower and upper bainite. At high temperatures, diffusion occurs in supersaturated carbon plates rejecting carbon in the surrounding austenite. This results in internal free carbides in the upper bainite.

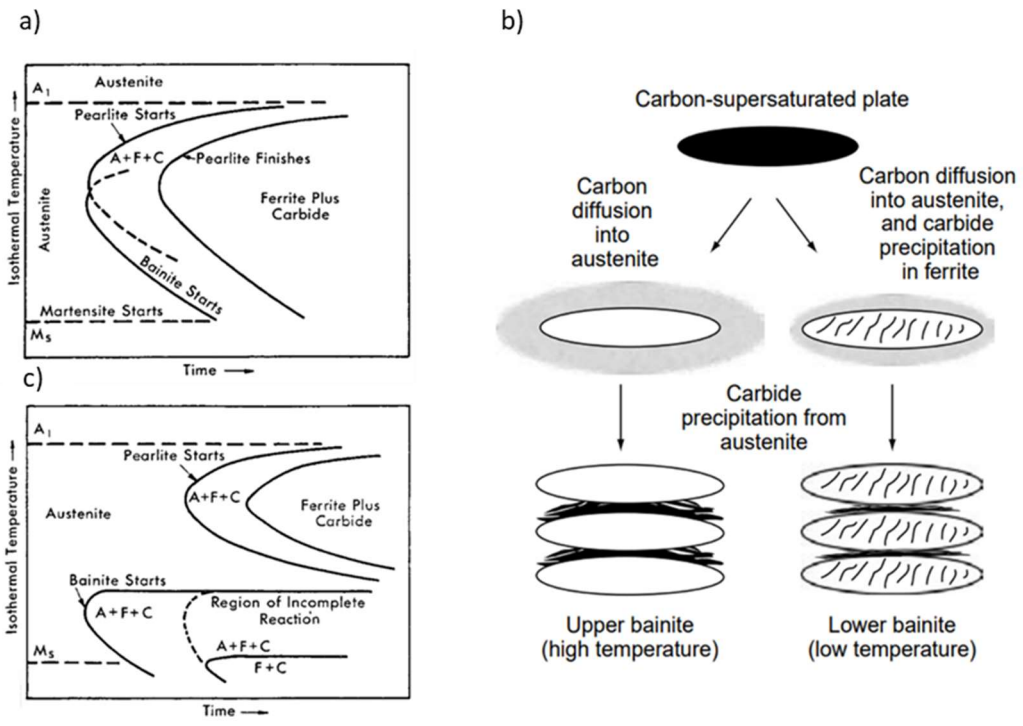

Figure 17 (a)(b) Transformation diagrams of time-temperature, a) diagram of pearlite and bainite phase overlap, b) the pearlite and bainite are differenced in separate temperature zones, c) representation of the bainite growth and decomposition of upper or lower bainite[43].

2.2.4.1 Upper bainite

Upper bainite (UB) forms below the temperature range of pearlite (550 °C - 400°C). The morphology of this structure has a close similarity to Widmanstätten ferrite. The UB morphology consists of fine ferrite laths without inner precipitation (Figure 18-a). In the upper bainite, the laths expand in clusters (sheaves); in these sheaves, each plate is divided with low angle boundaries (or cementite particles). These structures of ferrite are parallel between them, containing similar crystallographic orientations. The crystal orientation in parent austenite and ferrite is near Nishiyama-Wassermann and Kurdjumov-Sachs orientation relationships[40,43].

The nucleation of bainite occurs on grain boundaries of parent austenite, and the bainite growth is contained on the parent austenite grain. The orientation relationship between austenite and bainite in the advanced interface avoids growth beyond the grain boundaries of austenite[43].

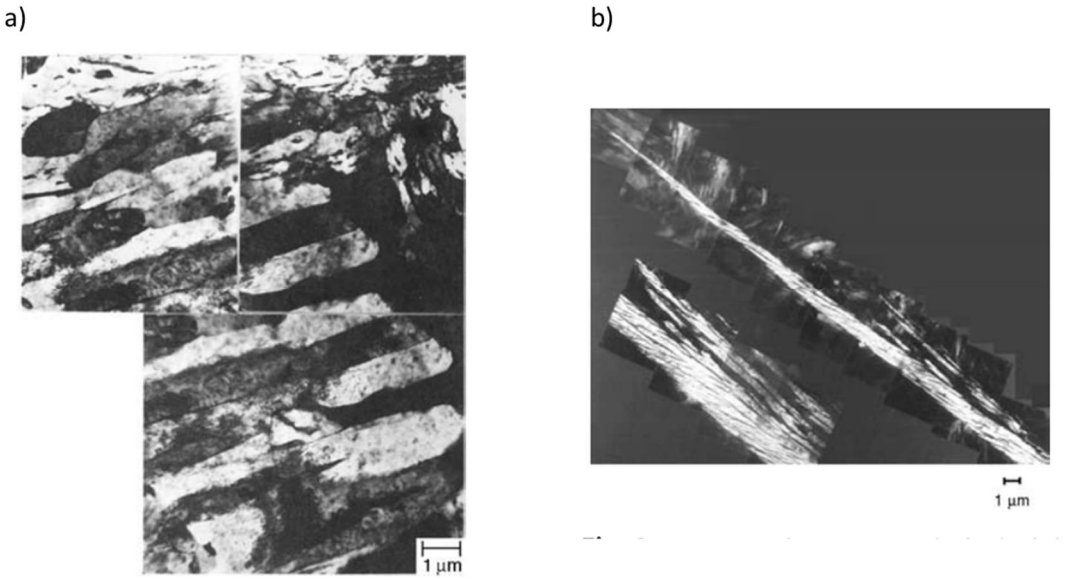

Figure 18 a) Thin foil image of upper bainite substructure plates in 2340 steel austenitised at 1,095°C and transformed isothermally at 540°C during 15 hrs. b) Upper bainite sheaf in transmission electron micrograph (TEM) obtained in a partially transformed alloy (0.43C-2Si-3Mn wt%)[43].

Bainite transformation is followed by a crystal structure shift from austenite/γ to ferrite/α. The bainite has a more extensive molar volume than austenite and needs a simultaneous shape transformation (Figure 19)[43]. To visualise the laths of upper bainite, it is necessary to use electron microscopy because the laths are 0.5µm wide.

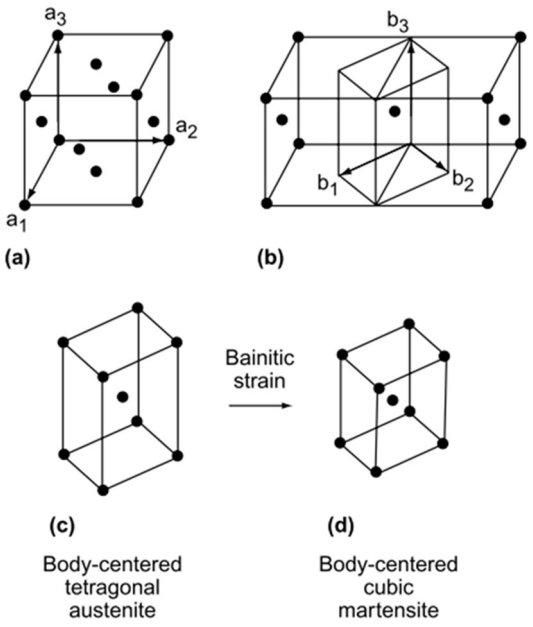

Figure 19 Shift crystal structure due to transformations of bainite. a) Austenite FCC unit cell with a1, a2 and a3 vectors; b) FCC and body centre tetragonal cell (b1, b2, b3) relation; c) Strain of bainite deforming austenite lattice in a BCC lattice of martensite (d)[43].

2.2.4.2 Lower bainite

The cementite precipitation in lower bainite occurs in the interlath regions of the carbon-rich austenite as in the upper bainite. The precipitation also occurs in the ferrite plates. In the lower bainite, the cementite which precipitates in the interiors of ferrite grains shows the same orientation relationship that appeared in tempered martensite (Bagaryatski and Isaichev orientation relationships). Lower bainite plates have similarities with upper bainite substructure, with 0.5 μm wide and light disorientation between them. Plates in lower bainite contain a higher dislocation density than upper bainite but less than martensite. The fine carbides of ferrite usually form an angle of 60° referencing the long axis of ferrite crystals[36,43].

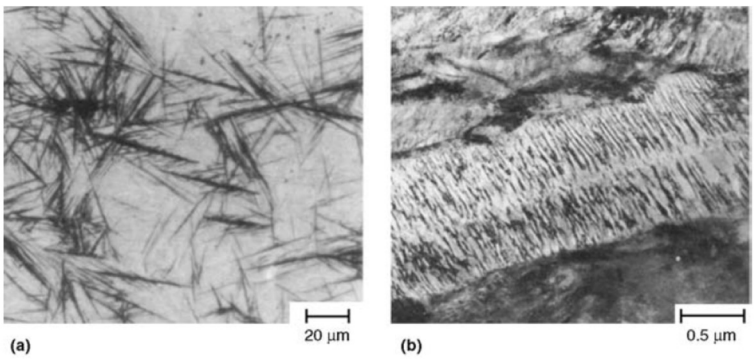

Figure 20 Lower bainite transformed at 190°C for 5 hrs in carbon steel with 1.10%. a) Optical microscope, b) Micrograph of TEM[36].

2.2.5 Martensite

Martensite transformation needs faster cooling rates or quenches to develop a fine structure during non-isothermal conditions. During this transformation, diffusion is repressed by rapid cooling, and carbon atoms do not divide themselves among ferrite (α) and cementite (FeC_3). Nevertheless, carbon atoms are snared in the octahedral sites of the bcc structure forming another phase, martensite (Figure 21-a)[36]. A mechanism of shear shapes martensite. A massive quantity of atoms moves almost coordinately to produce the transformation. This mechanism differs in atom per atom motion through interfaces in diffusion transformations. Figure 21-b illustrates the displacive or shear transformation of austenite (γ) to martensite. The arrows indicate the shear direction on the plane on the contrary side, which started the transformation. The shaped crystal of martensite is displaced above and below the austenite surface by the mechanism of shear[36,44].

Two morphologies are observed in microstructures of ferrous martensite: lath martensite (Figure 21-c) and plate martensite (Figure 21-d). Plate martensite forms lenticular crystals (lens-shaped), also known as acicular martensite. The zigzag pattern in small plates and microcracks are characteristics of this morphology. Lath martensite is known as packet martensite; lath presents a fine structure in the crystal of martensite. Laths align themselves in groups of a similar orientation, known as packets[44].

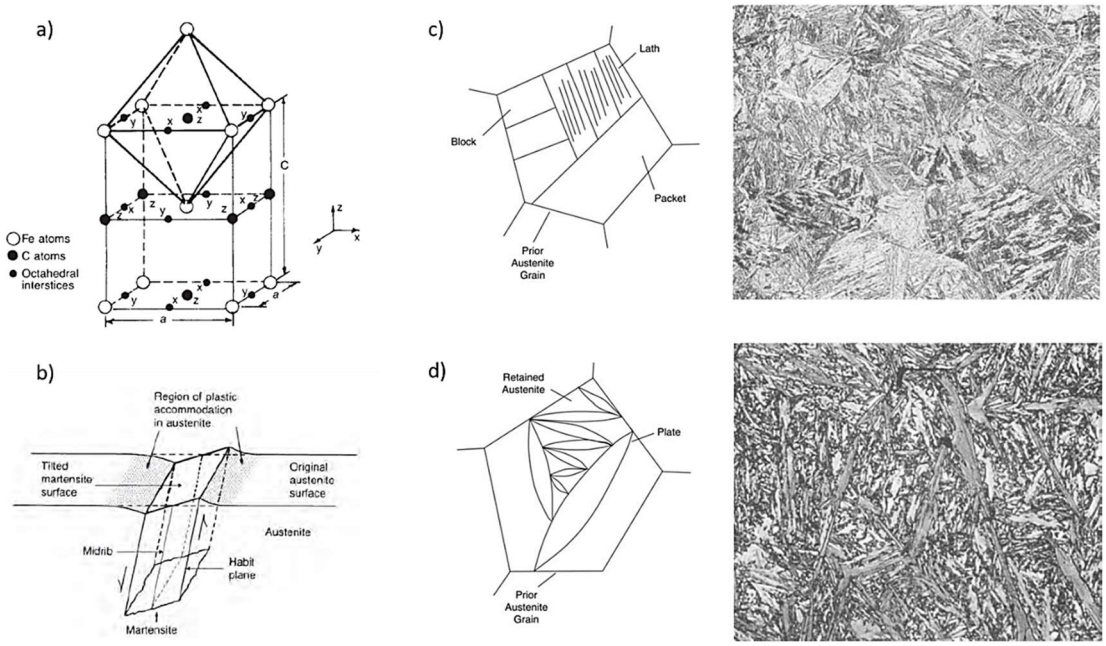

Figure 21 a) BCT Martensite crystal structure in Fe-C alloy. Atoms of carbon are trapped in one set (z) of interstitial octahedral sites. b) Schematic of martensite crystal displaying shear inclination and surface. c) Lath martensite. d) Plate martensite [36,42,44].

2.2.6 Austenite

At elevated temperatures in steel and iron, the austenite crystal structure shows stability. The FCC austenite structure possesses high carbon solubility in the octahedral-interstitial site with an array of iron close-packed atoms. An array of ferrite and cementite microstructures which are steady at room temperatures will change to a single phase of austenite during heating. Dissolution of cementite and concentration of carbon in the cementite transform into austenite solution because the carbon has a high solubility in the austenite phase. Austenite has elevated hot ductility, allowing easy working in the rolling and forging process. Because of this, single austenite structure is an ideal phase; however, steels heated in the austenite phase contains also carbides (depending on time and alloying availability in solution), inclusions and precipitates[36].

Figure 22-a shows the terms used for the critical temperatures of transformation are: A_1, which indicates the eutectoid temperature, A_3 that refers to the primary ferrite transformation, and A_{cm} that refers to the primary cementite transformation. Additionally, "c" (heating) and "r" (cooling) subscripts define the critical temperatures during cooling or heating conditions. The initial step in the heat treatment is full austenitisation, the temperature of Ac_3 must be passed to achieve the austenitisation condition [45]. Figure 22-b shows the kinetics of austenite transformation during isothermal conditions.

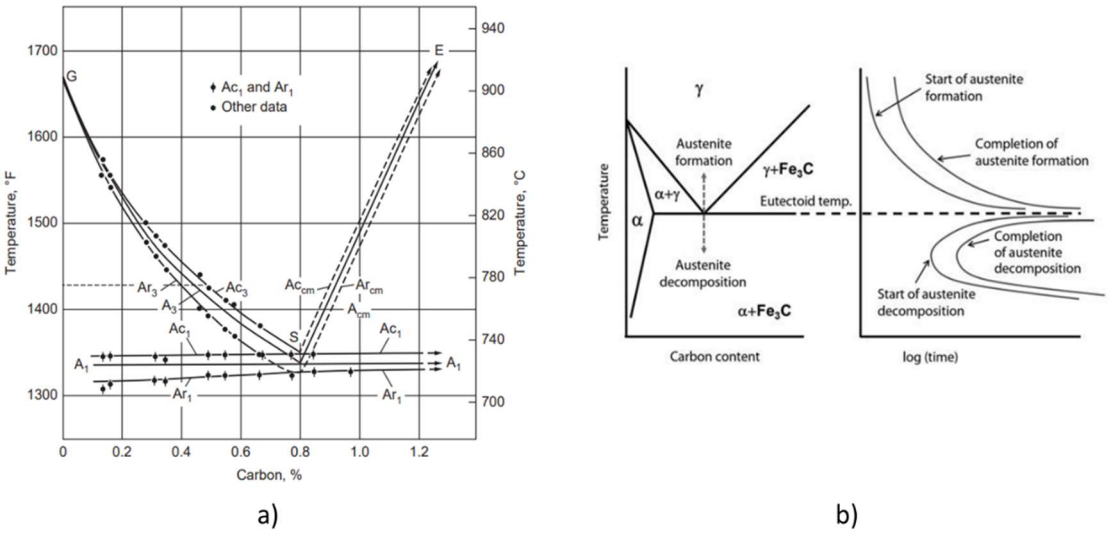

Figure 22 a) Iron carbon transformation temperatures from the binary phase diagram, the heating and the cooling were at 0.125 °C/min (critical temperatures depend on processing and alloy composition) b) Phase diagram of iron-carbon (left). The austenitisation diagram shows kinetics formation upon heating of isothermal austenite (upper right) and decomposition of isothermal austenite during cooling[45].

The austenite formation implicates a change in composition and crystal structure. An atom rearrangement in the interface occurs during the transformation of BCC ferrite or orthorhombic cementite to FCC austenite. These structural reorder does not control the reaction kinetics, because obtaining the equilibrium composition of austenite requires the diffusion of substitutional solute and a long range of carbon. In this transformation process, the coarse alloy of enriched carbides mixed with coarse ferrite appears as the slowest kinetics in austenitisation because the homogenous in the formation of austenite is necessary to dissolve coarse carbides, redistributing substitutional solutes[45].

Figure 22-b (left) shows the kinetics of isothermal austenite transformation from eutectoid composition (pearlite) in a phase diagram, while the right indicates the TTT diagram (time–temperature–transformation). Up eutectoid temperature, austenite constitution starts from pearlite, while austenite decomposition appears down the eutectoid temperature. The formation of austenite needs less time when the temperature is elevated[45].

2.2.6.1 Austenite Grain Growth

During austenitisation, the desired austenite grain size depends on the application. Coarse grains of austenite elevate hardenability; however, in practice, alloy elements are added to control hardenability. In the case of finer austenite, it increases toughness and strength with a refined microstructure. The austenite grain size growth is a function of temperature and time (Figure 23-a). In HSLA steels, alloy elements and precipitates delay the grain growth due to precipitate pinning on grain boundaries[45]. Thus, the grain size of austenite is relevant in the final properties and last microstructure; the prior austenite grain size measure is desirable.

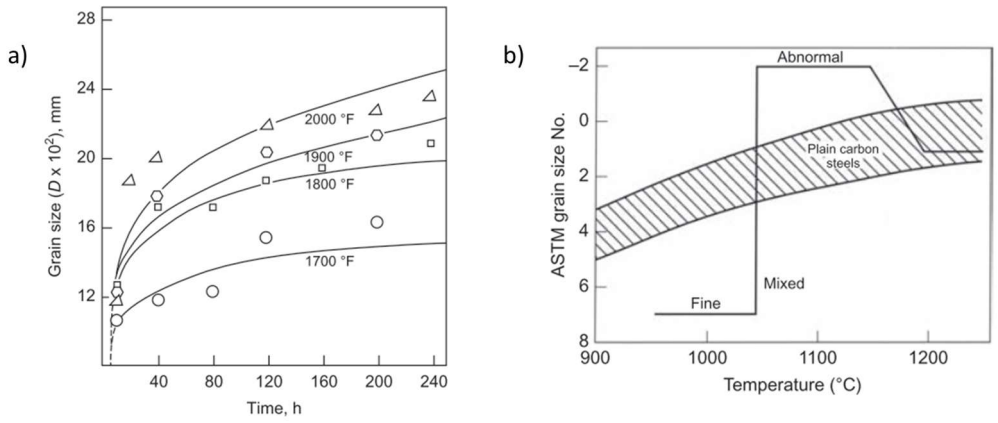

Figure 23 a) Austenite grain size behaviour in function of time and temperature, b) Austenitisation temperature effect on the austenite grain size in plain carbon steel, the grain size is measured according to the ASTM standard. The solid line represents the fine grain, and the shaded area represents the coarse grain[45].

2.3 Grain Growth

Recrystallisation is finished when the polygonised matrix is changed by the new grain with strain-free (though the structure of the grain is not steady), and then the annealing boosts an increase in average grain size. This process is known as grain growth, and a grain boundary migration follows it. Equation 1[36] represents the grain growth kinetics:

$$D^2 - {D_0}^2 = K_t \qquad 1$$

Where the grain size in determining time (t) is D after the growth of grain has initiated at a specific temperature, D_0 is the size of the grain at the initiation of growth, and K is a dependent temperature constant related to the diffusion and linked with the growth of grain. The Equation 2 represents the initiating behaviour of the grain size, which is fast in the beginning stages of grain growth and rises with time and temperature[36].

$$\mathrm{D} = \mathrm{Kt}^{1/2} \qquad 2$$

Figure 24-a illustrates the grain growth in carbon steel with the following chemical composition: 0.22% C, 1.04% Mn, 0.33% Si and 0.16% Al. The atom mobility increases with the increase of austenite temperatures. At low temperatures, small growth appears because the material aluminium killed steel. In this process, the nitride particles of aluminium suppress the grain growth because the aluminum oxide particles can serve as sites for the initiation of new crystals in the solution. When the temperature has elevated, the nitride particles dissolve. Figure 24-b shows the grain boundary pinning. In this diagram, it is possible to observe the effect of the energy increase and the rise in the grain boundary area. This area and energy increment are a consequence of the pinning force acting in the boundary motion in each particle[36].

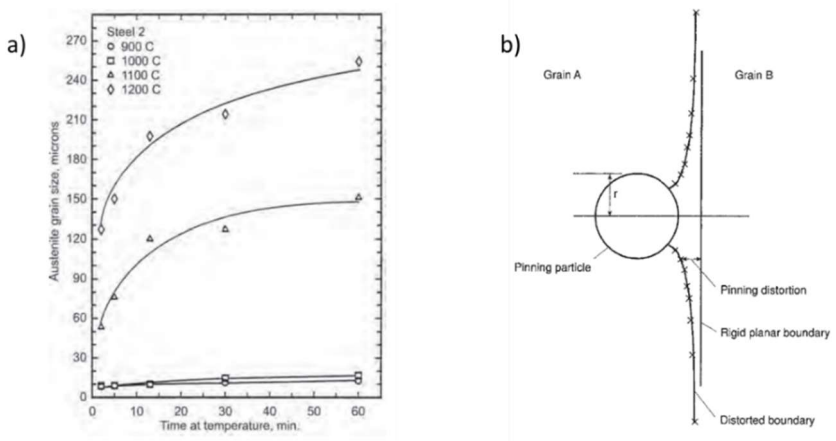

Figure 24 a) Diagram of austenite grain size as a function of time b) Schema of grain boundary pinning[36].

2.3.1 Precipitation

The addition of microalloyed elements influences the strengthening. These improvements in properties are produced by different factors such as grain refining, particle precipitation in significant precipitates dispersion, grain growth inhibition in particles of the second phase, and grain refining. To understand these phenomena, it is essential to know the dissolution factors of the carbides and nitrides in the alloy[46].

In the austenite zone, the microalloyed carbide and nitride dissolution at elevated temperatures offers different possibilities in the successive process of "re-precipitation" at below temperatures; these possibilities are:

- Precipitation in the austenite after a decrease in temperature, this could appear in the slow cooling or during holding treatment (isothermally) in the range of austenite temperature[46].
- Precipitation in the decomposition process of austenite-ferrite, in this form, the solubility declines in no continuous way at the boundary of austenite-ferrite[46].
- Precipitation after the ferrite transformation, as a consequence of fast cooling across the austenite (γ) and temperature transformation intervals[46].

2.3.2 Precipitation in austenite

The temperature of soaking combined with the steel composition are significant parameters in the dissolution control of the carbide/nitride microalloy. The precipitation behaviour depends on dissolution extension in two ways:

- Solute content increases through heating at elevated temperatures, thus dissolving the carbides and nitrides. Consequently, it will raise the supersaturation in the cooling and grow the precipitation rate at lower temperatures[46].
- The partial dissolution of carbide/nitride will quit particles free as nuclei for the following process of reprecipitation during cooling. To accelerate the solute precipitation on the pre-existing speck is necessary lower temperatures of dissolution[46].

In the lack of hot deformation, nitride/carbide microalloyed precipitation in austenite is highly slow. However, when hot deformation is applied, the insertion of dislocations, low angle sub grain boundaries and dislocation cells provisioned large precipitation sites for the carbides and nitrides. In this condition, the austenite precipitation is significantly increased[46].

2.3.3 Niobium

The niobium is a stabiliser of ferrite (α). Also, niobium has a high tendency to constitute carbonitrides. However, niobium has a low disposition to form sulphides, oxides or solid solutions of those compounds. Therefore, the niobium has similar behaviour to vanadium in the solution. In another way, the titanium does not react as a former of carbides till nitrogen, oxygen and sulphur are consumed by the first titanium additions[47]. Figure 25 shows the solubility of NbC_xN_y composition depending on carbon content (C), niobium content (Nb) and the temperature of precipitation in the austenite.

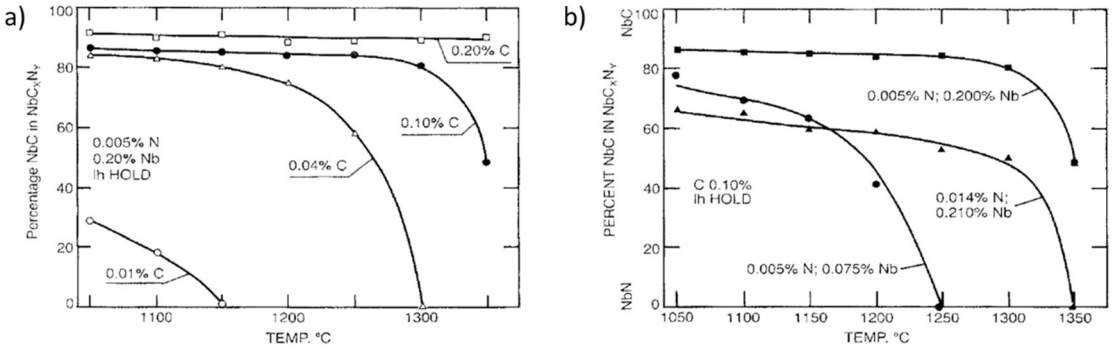

Figure 25 a) NbC_xN_y-solubility as a function of carbon content and precipitation temperature. b) Variation in NbC_xN_y solubility as a function of niobium content and temperature[47].

The solubility products have a fundamental role in understanding microalloyed steels, particularly the precipitation phenomena. Table 3 illustrates an array of solubility products divided into five different techniques. It is classified into the next methods[47]:

A – Thermodynamic calculations

B – Precipitate isolation and chemical separation

C – Equilibrating a steel series with array contents of niobium at different temperatures, after which contents of carbon are verified (during H_2-CH_4 atmosphere)

D – Measures of hardness

E – The statistical process of prior solubility products

Figure 26-a shows a relationship between solubility products in austenite versus an increase in temperature using the studies of Nordberg and Aaronson. The graph indicates two essential issues regarding solubility. First, when the product is enriched with nitrogen, the solubility decreases. Second, the precipitate compound solubility diminishes in austenite, and at the same time, the vacancy content is smaller[47].

Table 3 Solubility products in austenite systems for NbC, NbN and NbCN[47,48].

Product	Method	Reference
Nb-C system		
log[Nb][C]=2.9-7500/T	D	Nordberg and Aaronson,1968
log[Nb][C]=3.04-7290/T	B	Nordberg and Aaronson,1968
log[Nb][C]=3.7-9100/T	C	Smith,1966
log[Nb][C]=3.42-7900/T	B	Narita,1975
log[Nb][C]=4.37-9290/T	C	Johansen, Christenen and Augland, 1967
$\log[Nb][C]^{0.87}$=3.18-7700/T	B	Mori, Tokizane, Yamaguchi et al., 1968
$\log[Nb][C]^{0.87}$=3.11-7520/T	E	Nordberg and Aaronson,1968
log[Nb][C]=2.96-7510/T	E	Nordberg and Aaronson,1968
$\log[Nb][C]^{0.87}$=3.4-7200/T	A	Nordberg and Aaronson,1968
log[Nb][C]=3.31-7970/T + φ†	B	Andrade, Akben and Jonas, 1987
$\log[Nb][C]^{0.87}$=2.81-7019.5/T	A	Sharma, Lakshmanan and Kirkaldy, 1984
log[Nb][C]=1.18-4880/T	-	Balasubramanian and Kirkaldy, 1988
log[Nb][C]=3.89-8030/T	-	Balasubramanian and Kirkaldy, 1988
log[Nb][C]=4.04-10230/T	C	Smith, 1962
log[Nb][C]=3.79-10150/T	B	Mori, Tokizane, Yamaguchi et al., 1968
Nb-C system		
log[Nb][N]=2.8-8500/T	B	Narita,1975
log[Nb][N]=3.7-10800/T	B	Hoogendorn abd Spanraft, 1977
$\log[Nb][N]^{0.87}$=2.86-7927/T	A	Sharma, Lakshmanan and Kirkaldy, 1984
log[Nb][N]=4.2-10000/T	-	Balasubramanian and Kirkaldy, 1988
Nb-C -N system		
$\log[Nb][C]^{0.87}[N]^{0.65}$=4.09-10500/T	B	Nordberg and Aaronson,1968
log[Nb][C+12/14N]=3.97-8800/T	C	Santella,1981
log[Nb][C+N]=1.54-5860/T	B	Nordberg and Aaronson,1968
$\log[Nb][C]^{0.83}[N]^{0.14}$=4.46-9800/T	B	Nordberg and Aaronson,1968
log[Nb][C+12/14N]=2.26-6770/T	C	Irvine, Pickering and Gladman, 1967

**φ†=[Mn](1371/T-0.9)-$[Mn]^2$(75-T0.0504)

It is known that the solubility of precipitates increases in austenite compared with ferrite. Figure 26-b illustrates the solubility product of different precipitates in the austenite and ferrite in ultra-low carbon steel. Palmiere et al. published in 1994 the solubility product of niobium in steel with the composition 0.08C-1.5Mn-0.008N-0.02Nb (Equation 3).

$$\log[Nb][C] = 2.06 - 6700/\mathrm{T} \qquad 3$$

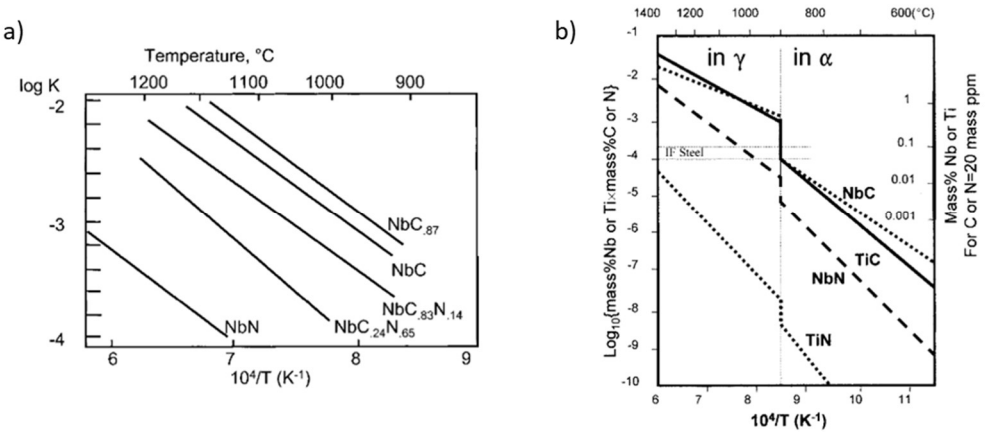

Figure 26 a) Solubility products in different precipitates of Nb in γ. b) Solubility products in precipitates of NbC, TiN, TiC in γ and α (published by Taylor, 1994)[47].

Crystallography of precipitation has two main issues, first is the orientation relationship between the precipitation crystal structure and the matrix. Second, the lattice degree registry among the matrix and the precipitation. For example, Carbonitrides of Nb, V and Ti have the characteristic that can precipitate in austenite but also in ferrite. When the precipitates of NbC_xN_y in martensite or ferrite use the orientation relationship of Baker Nutting (O_{R1})[47]. Figure 27 shows the austenite structures and the NbC_xN_y are located to illustrate the parallel orientation relationships, while the ferrite structures and NbC_xN_y are located to show the orientation relationship of Baker Nutting.

$$[100]_{NbC} \parallel [100]_{\alpha} \qquad O_{R1}$$
$$[011]_{NbC} \parallel [010]_{\alpha}$$

The orientation relationship which is observed between the ferrite and NbC is useful to detach the NbC nucleated in ferrite from the NbC nucleated in austenite. When the austenite has a transformation to ferrite or martensite uses the orientation relationship of Kurdjumov Sachs (O_{R2})[47]

$$(111)_{\gamma} \parallel (100)_{\alpha} \qquad O_{R2}$$
$$[110]_{\gamma} \parallel [111]_{\alpha}$$

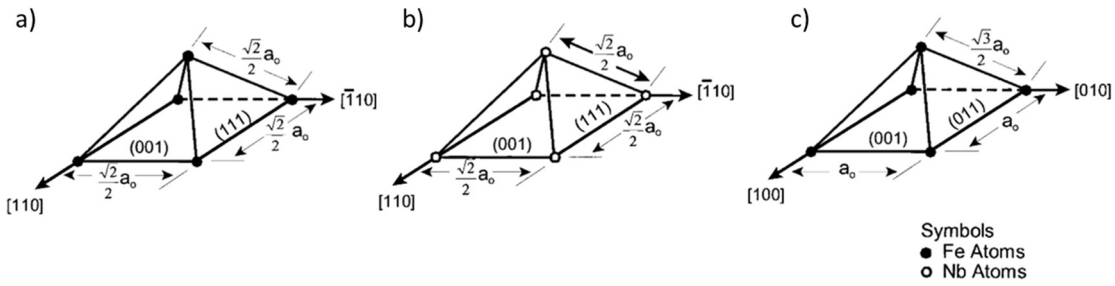

Figure 27 Metal atom octahedra for a) austenite, b) NbCN, and c) ferrite[47].

2.4 Thermomechanical controlled processing of pipeline steel

Conventional hot rolling uses high finishing temperatures (above 1050°C) without cooling control resulting in ferrite and pearlite microstructures. While thermomechanical controlled processing (TMCP) uses lower finishing temperatures avoiding the coarse prior austenite grain size and controlling the cooling after finishing [31,49]. The addition of microalloying elements in TMCP results in diverse microstructures such as ferrite-pearlite, varieties of ferrite and bainite, and bainite with martensite islands and retained austenite (MA constituents). TMCP controls different strengthening mechanisms in these phases, such as grain refinement, solid solution strengthening and dislocation strengthening. In addition, strength and toughness are controlled through microstructure formation in pipeline steels[22]. The developments which enabled to achieve these properties are outlined as follows:

- Reduce the carbon concentration from 0.2 to 0.05% and increase the number of microalloying elements.

- Reduce the pearlite percentage and shift from “ferrite-pearlite” to “ferrite-bainite” or “bainite-martensite” microstructures.

- Shift the processing route from hot rolling/normalisation to TMCP mixing with quick cooling.

Low carbon with manganese and other microalloying elements are used in pipeline steels. These elements are used to equilibrate contradictory properties: high weldability and mechanical properties (ductility, toughness and strain hardening). Strength is achieved with quenching and tempering in medium carbon steel with a high hardenability. However, medium and high carbon steels are often associated with poor toughness, ductility and weldability due to their carbon concentrations [22].

To furnish good weldability, TMCP uses a low carbon percentage in conjunction with manganese to reduce the transformation temperature of austenite to ferrite. Also, TMCP utilises a cooling rate and the addition of microalloyed elements (V, Ti, Nb and Mo) and different strengthening mechanisms such as dislocation density, grain refinement, precipitation hardening and preamble of second phases. In addition, cleanliness is mandatory in these steels, decreasing phosphorus and sulphur to the part per million. Table 4 represents the typical composition of the most used grades of pipeline steel [22].

Table 4 Typical grade of pipeline steel composition [31]

Grade	X-65		X-70		X-80		X-100		X-120	
	Min	Max	Min	Max	Min	Max	Min	Max	Min	Max
C	0.041	0.170	0.037	0.125	0.028	0.142	0.025	0.100	0.027	0.050
Mn	0.300	1.680	1.440	1.760	1.520	1.900	1.560	2.000	0.540	2.140
S	0.0002	0.030	0.001	0.015	0.001	0.009	0.001	0.0024	0.001	0.004
Si	0.020	1.390	0.140	0.440	0.170	0.310	0.100	0.250	0.080	0.310
Cu	0.020	0.310	0.006	0.270	0.015	0.200	0.250	0.460	0.010	0.015
Mo	0.005	0.140	0.010	0.300	0.050	0.300	0.190	0.430	0.001	0.400
Nb	0.018	0.060	0.051	0.092	0.038	0.090	0.043	0.089	0.048	0.100
V	0.042	0.210	0.001	0.095	0.002	0.100	0.003	0.070	<0.025	
Ti	0.002	0.010	0.009	0.030	0.007	0.024	0.011	0.020	<0.015	
Al	-	-	-	-	-	-	0.006	0.030	0.045	0.040
Cr	0.020	0.157	0.007	2.266	0.015	0.120	0.016	0.420	0.220	0.420
Ni	0.005	0.800	0.020	0.230	0.020	0.750	0.130	0.540	0.017	1.350
B	-	-	-	-	-	-	-	-	0.0013	0.0017

To produce a fine-grained microstructure, it is important to carefully control the distribution of rolling reduction in the regions where austenite undergoes transformation, both above and below the non-recrystallization temperature, $T_{5\%}$[50]. At these deformation conditions, $T_{5\%}$ represents the maximum temperature at which no more than 5% of the austenite grains undergo recrystallization[51]. During the deformation process, recrystallization below $T_{5\%}$ is suppressed or retarded due to the cessation of strain-induced precipitation [52]. As a result, controlling the rolling reduction distribution in the regions surrounding T5% is crucial for achieving a fine-grained microstructure in the final product.

To obtain strongly deformed austenite (no recrystallised), the last hot rolling passes should be taken below the $T_{5\%}$. Before the austenite transformation to ferrite, the austenite microstructure has been processed to a high strain. This austenite results in many internal defects, such as slip/shear bands, dislocation tangles, and high/low angle grain boundaries (HAGB / LAGB). HAGB and LAGB furnish various nucleation sites for the BCC and BCT constituents (ferrite, martensite and bainite)[53]. As a result of the temperature control and deformation, a fine-grained microstructure is obtained. This fine microstructure increases the toughness and strength of TMCP steels. Figure 28 illustrates the final microstructures obtained in TMCP processing.

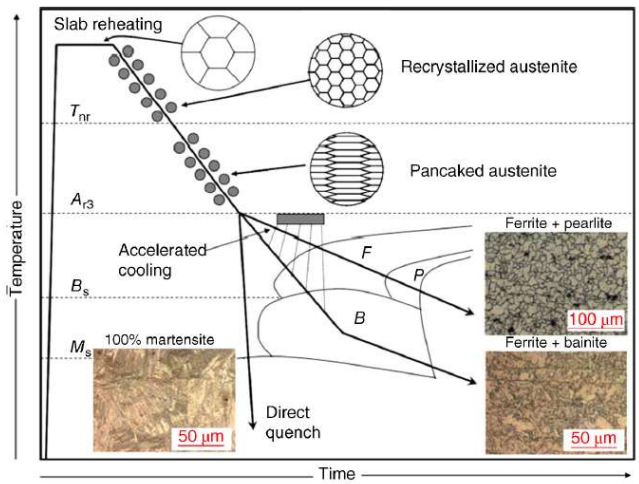

Figure 28 Microstructures resulting from thermomechanical controlled processing (TMPC) [53].

The microstructure formation in the hot strip mill must be controlled in different parts: reheating the slab, rough rolling, finish rolling, and cooling control[53]. Figure 29 shows a classic arrangement for the hot strip mill (sheet final product).

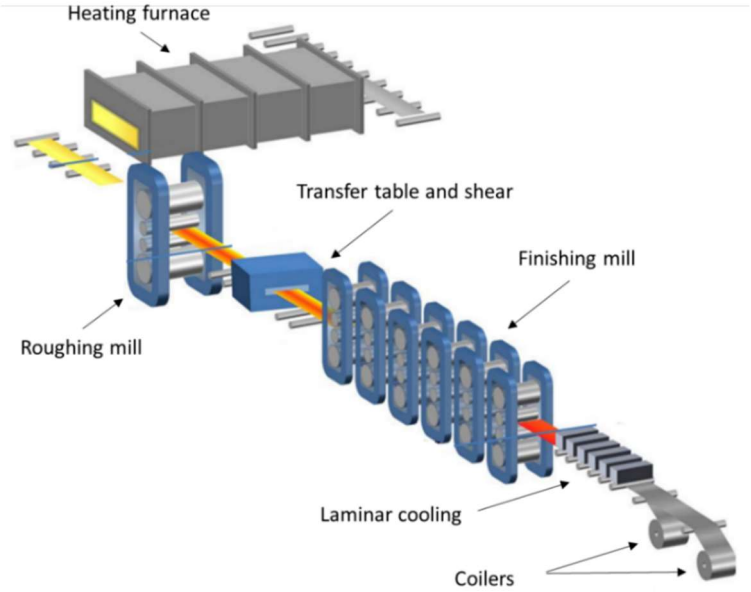

Figure 29 Hot strip mill classic arrangement[54]

2.4.1 Slab Reheating.

Reheating is the first stage of conventional controlled rolling (CCR) production and TMCP. The slab is soaked at a high temperature (above 1150° C) during reheating. Those temperatures allow the dissolution of the particles, and as a consequence, the dissolution of the particles results in more microalloyed elements in all the solutions [55,56].

Slabs feed the reheating furnace. It is known that the large dendritic and alloy elements segregate interdendritically, characteristic of the microsegregation that occurs in a slab casting microstructure. These phenomena act in conjunction with distinctive centreline segregation (macrosegregation). Macrosegregation is a fundamental microstructure pattern due to the difference in the plate thickness composition, creating an array of microstructures through the thickness (Figure 30-31) [53].

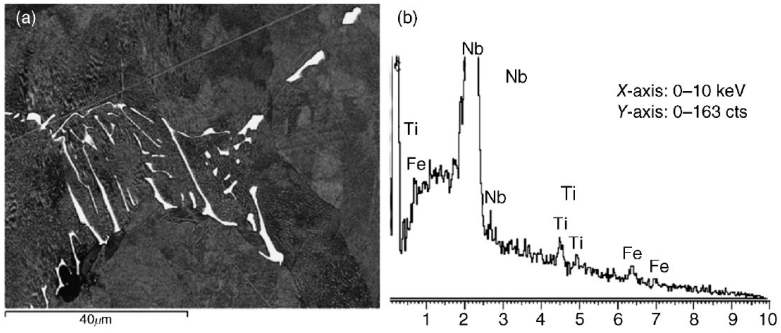

Figure 30 a) Nb (C, N) particles visualised in the slab centreline area; b) The spectrum of energy dispersive spectroscopy (EDS) in one particle [53]

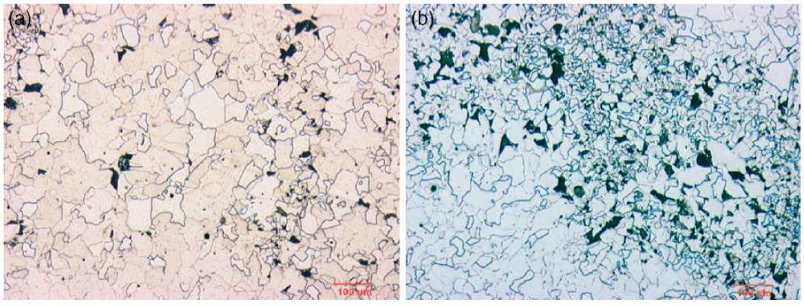

Figure 31 Microstructure segregation in slab pipeline composition: 0.03% C, 1.7% Mn, 0.25% Si, 0.005% S, 0.008% P, 0.082% V, 0.052% Al, and 0.063% Nb. a) near the surface and b) centreline [53].

Pipeline steel production uses continuous casting, and the solidification rate in this process reduces the secondary dendrite arm spacing (SDAS). If the secondary dendrite arm spacing (SDAS) is reduced, it can result in more dendrites and decreased interdendritic spacings, which can help prevent the formation of defects like porosity, shrinkage cavities, and hot tearing[57,58].

After the solidification, slab macrosegregation appears across the thickness and along the width. During slab reheating, it is only possible to remove macrosegregation partially [53]. Because in large distances, the solutes in the solid state are characterised by low diffusivity, then macrosegregation cannot be prevented when the solidification has finished in the casting[59].

The reheating temperature and the soaking time have a relevant influence on the slab microstructures. Those conditions affect not only the grain growth and homogeneity of austenite but the dissolution of precipitates[60]. Then, the suppression of austenite grain growth is a consequence of the unfinished dissolution of alloy elements[53]. The most important limitations in the selection of slab reheating temperatures are the next:

- The microalloying additions will be dissolved at high temperatures. It is crucial to understand the role of elements additions in the precipitates forming and the effect at high reheating temperatures.

- At temperatures above 1000°C, austenite grains begin to grow rapidly, and if left unchecked, this can result in excessively large grains, which can negatively affect the properties of the material. However, the presence of precipitates can limit the growth of austenite grains, thereby promoting the formation of a desirable microstructure during rolling. Therefore, it is important to control the grain growth during reheating to obtain the desired microstructure in the final product.

- The oxide layer formation on the surface grows excessively at high temperatures of austenitisation (above 1200°C). This effect limits the high austenitisation temperatures in the slab.

As mentioned before, the precipitates have an essential role in the processing of microalloyed steels because of their influence in retarding the recrystallisation of austenite. Because of this, several authors such as Zajac and Jansson[61], Palmiere[48], Balasubramanian[47] and Irvine[47] have studied the carbonitrides niobium solubility in austenite. Those studies determine the dissolution temperatures of microalloyed additions; based on thermodynamic calculations. Figure 32 shows the calculated curves of Zajac and Jansson[61]. In this graph, it is possible to compare the volume fraction of niobium carbonitrides with theoretical calculations and experimental results. It is observed that at high temperatures, most of the precipitates are TiN, while at lower temperatures, the majority of precipitates are prevailingly Nb (C, N)[61].

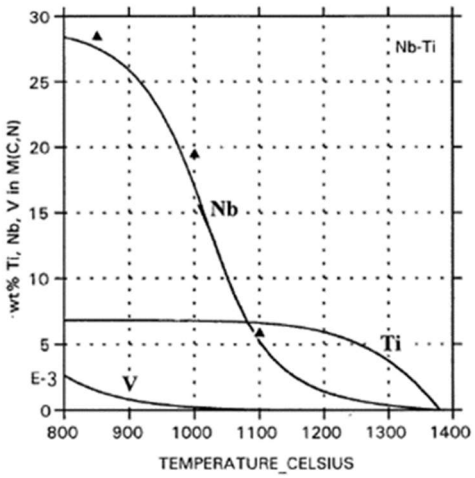

Figure 32 Calculated curves of Nb (C, N), TiN and V (C, N) precipitation and experimental data points of Nb (C, N) precipitates from a microalloyed steel containing 0.013% Nb and 0.007%[61].

Figure 33 shows the change in size and composition of precipitates for a microalloyed steel containing 0.050% Nb and 0.019% Ti. It is observed as a change in the shape and size of precipitates when the temperature increases. At 1075°C, the precipitates are coarse compared with the precipitates at 1200°C. Also, in the EDS analysis, the precipitates are mainly Nb-rich at lower temperatures, and when the temperature increases, it becomes Ti-rich. Even at high temperatures (until 1250°C), the small amounts of Ti (CN) and Nb (CN) precipitates stay undissolved. Those small quantities prevent an excessive grain growth of austenite which is fundamental in the reheating stage[62].

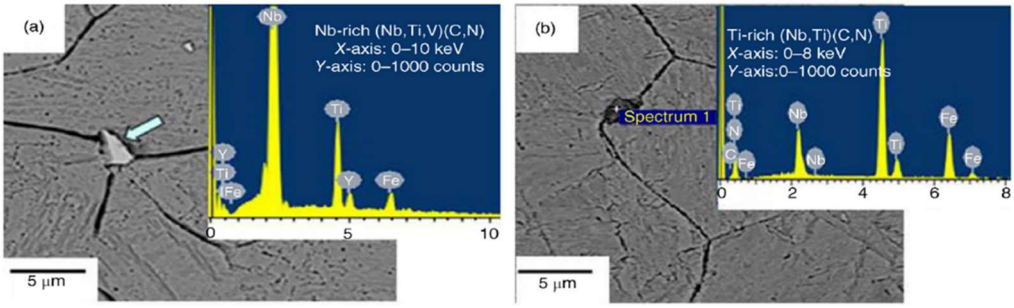

Figure 33 Difference in microalloying precipitates composition depending on reheat temperature. a) 1075°C - Nb rich (Nb, Ti, V) (C, N) to b) 1200°C – Ti-rich (Nb, Ti) (C, N) indicates in EDS analysis[62].

2.4.2 Rough rolling microstructure formation

During descaling, powerful water jets use to remove the thick oxide layer originating in the reheat furnace. Rough rolling starts when the slab is shifted to the roughing mill after descaling. Then, 5 to 7 passes are conducted through the reversing roughing mill; at the end of the reversing mill, the reduction achieves 85%. The inter-pass times are long in this process because the slab is rolling forward and backwards. After the roughing, the slab is generally transferred to the coil box before starts the finishing rolling. The slab shows a better temperature distribution when it is coiled in coilbox[55].

The slab continues the processing until the finishing rolling starts. During the reversing roughing mill to the coil box, the temperature decreases around 1000°C before the finishing mill initiates[55]. At this temperature, the transfer bar is processed at $T_{5\%}$, achieving the non-recrystallisation temperature of austenite. The non-recrystallisation temperature depends on the chemical composition, especially in the amount of Ti, Al, V and Nb. It is known that the most substantial effect in the increase of recrystallisation temperature is obtained with the niobium. Figure 34 shows the microalloyed elements' effect on the recrystallisation stop temperature of the austenite for a steel chemical composition of 0.07%C, 1.4% Mn and 0.25% Si[53].

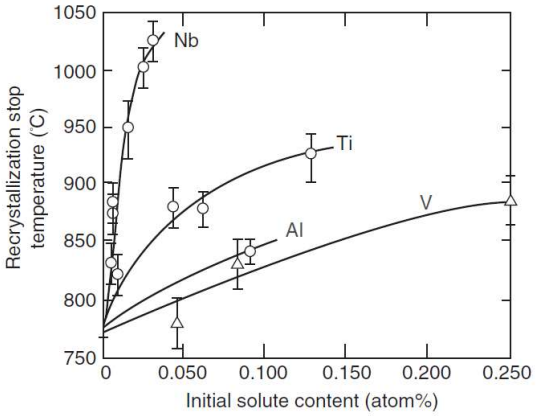

Figure 34 Microalloying elements effect of recrystallisation stop temperature on austenite for steel (0.07C -1.4 Mn – 0.25 Si)[53].

The effect of rough rolling on the austenite grain size appears in Figure 35. It is observed in the evolution of austenite grain size after the slab leaves the reheating furnace and before the material starts the finishing rolling for a steel chemical composition of 0.06%, 1.6% Mn, 0.055% Nb, and 0.01%>(Mo+Ni+Cu+Cr). Figure 35-a shows the initial γ grain size of 58.1 μm after the slab was reheated at 1250°C for 1 hr. Then, the slab passed three times at 1250°C, 1220°C and 1180°C, and the γ grain size is reduced to 26.1 μm. Finally, after 1 min of cooling between the exit roughing and finishing mill, the temperature decreases from 1180°C to 1060°C, producing an increase in γ grain size to 34.5 μm[53].

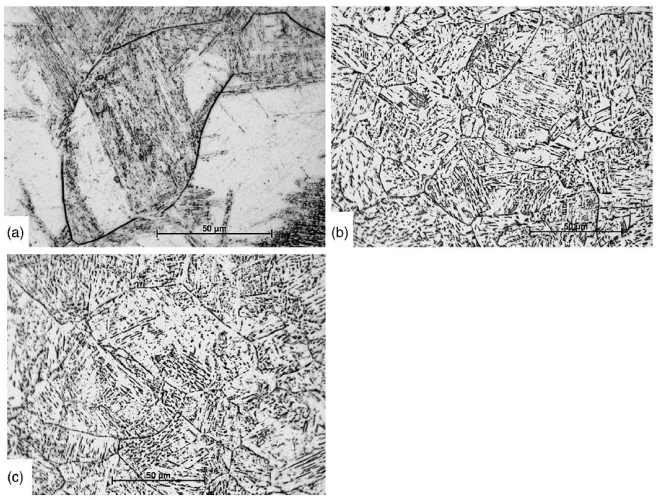

Figure 35 Austenite grain size microstructure of a microalloyed steel a) 1250°C reheating for 1hr and an austenite grain size of 58.6 µm, b) after 3 rough rolling passes at 1250, 1220, and 1180 °C with an austenite grain size of 26.1 µm and c) 1060 °C after the slab was cooled by 1 min (austenite grain size of 34.5 µm), the material was previously at 1180°C in the last roughing pass [53].

2.4.3 Finish rolling and cooling microstructure formation

Slabs continue in the finish rolling mill after rough rolling; in this stage, the length and thickness obtain the final measures. The final microstructure is affected by different parameters such as temperature distribution during passes, reduction percentage per pass, finish rolling temperature and the cooling rate. Figure 36-a illustrates the evolution from conventional rolling at high temperatures to thermomechanical rolling (TMCP). TMCP has two principal stages: the control of rolling and a successive accelerate cooling. During rolling in the finishing, the grains of austenite are elongated as pancake shape having high density of crystal discontinuities such as deformation bands and ledges.

Figure 36-b shows the TMCP rolling and the resulting microstructures after the cooling. The final microstructure depends on the cooling velocity after finishing. The Niobium additions promote the carbonitride precipitates through fine strain, which can delay the recrystallization process. The zone where the T-t-curve intersects between the onset of Nb(C,N) precipitation and the initiation of recrystallization is referred to as the non-recrystallization temperature (T_{nr}). T_{nr} is essential parameter in the rolling processing [53,63].

During finish rolling, the microstructure is affected by the austenite evolution. The mean properties of the austenite during this process are morphology, grain size and ingrain defects allocation. The deformed austenite can serve as sites of heterogeneous nucleation during the transformation of ferrite or bainite into an extremely fine structure [53,63].

The pipeline's microalloyed steels are processed under continuous cooling conditions. After the cooling, the final microstructure is a mixture of different phases such as ferrite, degenerated pearlite, upper bainite, lower bainite, martensite, and islands of martensite – austenite even carbides. Electron backscatter diffraction (EBSD) is used in the differentiation of morphology. To obtain the morphology separation utilises the lattice misorientation and crystallography basics [53].

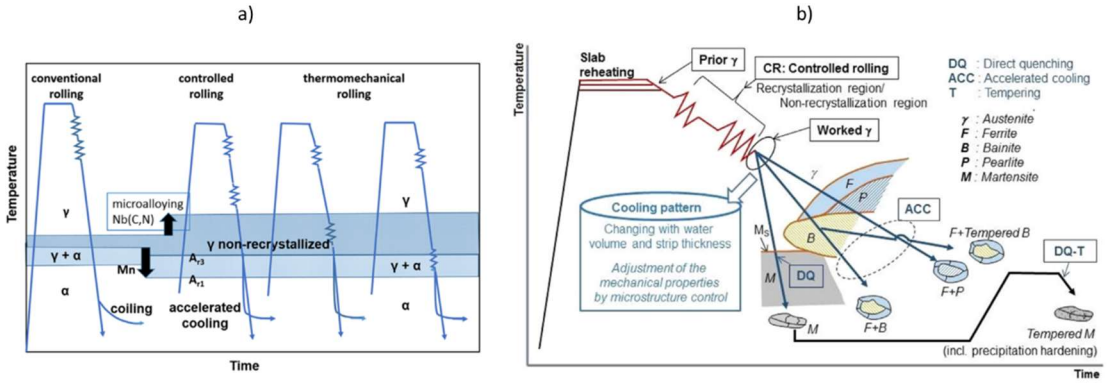

Figure 36 a) Rolling schemes from conventional rolling to TMCP rolling. b) TMCP rolling and cooling strategy in strips or high strength steels[63].

2.5 Welding Process

2.5.1 Submerged Arc Welding

Submerged Arc Welding (SAW) is a welding process in which granular fusible material (flux) covers the arc. Flux material is positioned over the base material and ahead of the arc. Then, the electrode feeds the filler material; this way of providing the material allows the process to be continuous. The granular flux is a characteristic of SAW; this increases quality and weld rates deposits during the process. The slag is another advantage of shielded metal arc welding. Slag has a critical characteristic that enables it to isolate the weld, resulting in a reduction of cooling velocity and refinement of the weld material with deoxidizers. Figure 37 illustrates the submerged arc welding process[64].

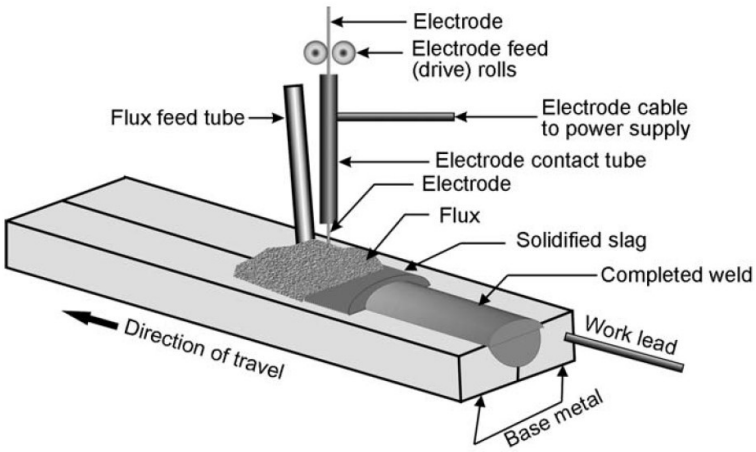

Figure 37 Schematic of Submerged Arc Welding Process [64].

The arc is automatically positioned at a short distance from the workpiece during the welding application. As a result, some of the flux melts during the heat application in the continuous process. Then, lighter molten flux arises overhead the melt material forming slag when the electrode advances along the joint. Finally, the slag solidifies over the weld material, protecting against nitrogen and hydrogen contamination that could appear at high temperatures. Figure 38 shows a schematic of a submerged arc weld pool[64].

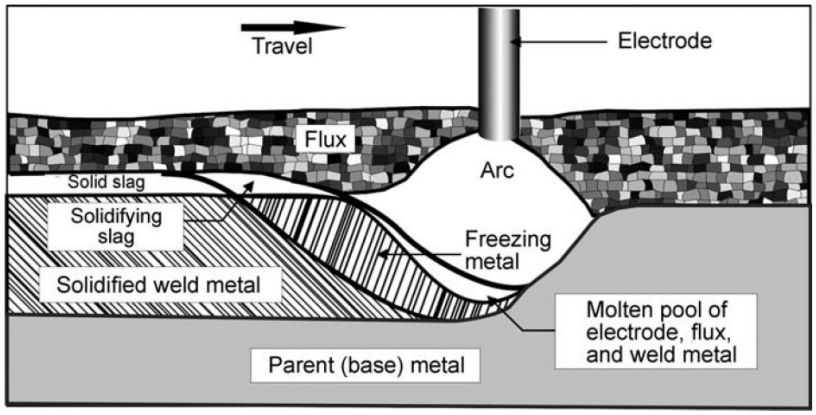

Figure 38 Schematic of submerged arc weld pool [64].

Some advantages of SAW

- The increase of welding velocity and deposition rates. To have higher velocity and deposition rates, it is possible to feed with more than one wire at the same time[65].

- High-quality welding improves mechanical properties. In addition, the flux feed tube protects the formation of polluted elements such as oxygen, nitrogen and sulphur from the liquid weld pool (Figure 37)[65].

- Low cost per length of joint welding[65].

Limitations of SAW

- The time to remove slag in multiple weld passes. Before the deposit of subsequent passes, the slag must be removed[65].

- Base material thickness. SAW is used in joints above 6.4 mm (0.25 inches) because it needs high heat input during welding[65].

SAW is used in any application that requires continuous and long joints. Shipbuilding, pipe manufacturing, structural components (bridges and buildings) and pressure vessels are examples of industrial applications for SAW[65]. Figure 39 represents an improved design of the pipeline SAW with a double "V" groove; the diagram shows the SAW' s versatility. In the original design, the possible distortion in the pipe during high heat input was reduced by the weld backing strip in the internal diameter. In contrast, in the double "V" improved design, it is not necessary to weld a backing strip. With this weld joint improvement, the electrode flux and work hours were decreased by 46%, and the total welding cost diminished by 62%[66].

To joint plain carbon steels, the usual process is submerged arc welding. Also, low alloy and alloy steels can be easily welded with SAW. However, it is essential to control the heat input and interpass temperature during the welding. The control of those parameters avoids the undesirable hardness and grain coarsening, besides cracking in the Heat Affected Zone. Therefore, heat input control and interpass temperature are mandatory to obtain determined mechanical properties in welding[64].

Usual defects in SAW

- *Insufficient fusion and slag entrapment.* An inadequate welding procedure and weld bead cause slag entrapment and incomplete fusion. Also, the inappropriate placement will cause the weld metal to overturn and snare the slag below. Finally, slag entrapment is promoted by high and low voltage[64].

- *Solidification cracking.* The fracture on the centre of the weld bead is typically a consequence of the join design; also, applying the weld procedure and weld bead shape has a negative effect. For example, if the weld bead is overly deep, the deformation stresses during solidification will cause cracking in the centreline[64].

- *Hydrogen-induced cracking.* Hydrogen cracking takes hours to days after the welding procedure has been finished. All sources of Hydrogen (such as grease, water, dirt, primer paint, and oil) must be removed from the joint. To reduce cracking in high-strength steels, weld deposit consumables should be used with low diffusible hydrogen[64].

- *Porosity.* The trapped gas typically produces porosity. In SAW, the porosity is not a usual defect because the flux protects the arc welding. However, when it appears, it does in two different patterns: internal porosity and seeable holes on the surface. When the gas bubbles originate from the porosity, it is because of the lack of atmosphere protection or the presence of contaminant sources such as water, dirt or grease[64].

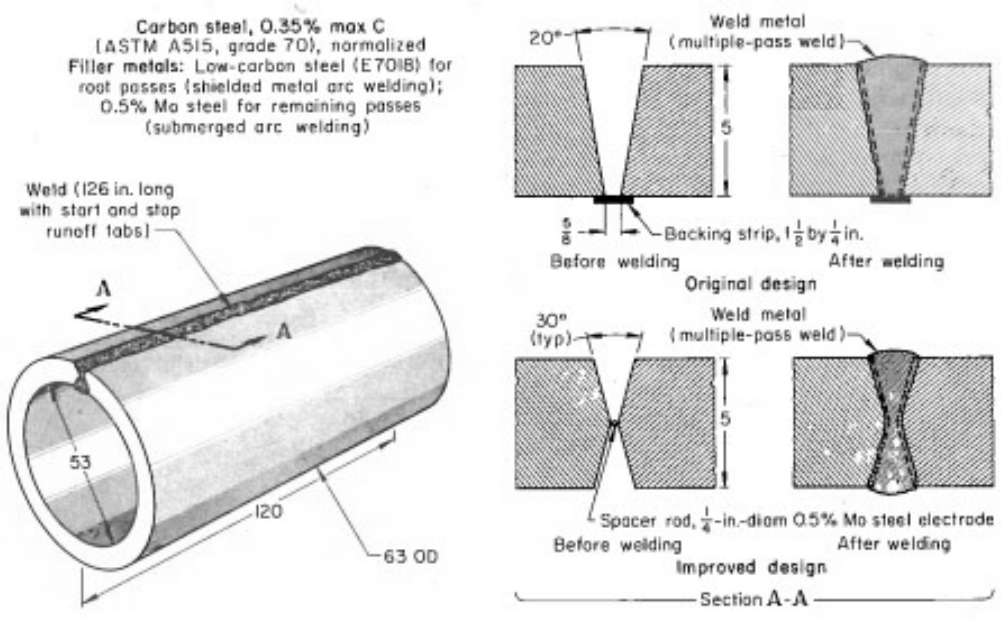

Figure 39 Submerged arc welding schematic for pipeline[66].

2.5.2 Heat flow in the fusion welding

The movement of the heat source in fusion welding produces different effects on the material, such as phase transformations, temporal thermal stress, physical state shift and metal motion (Figure 40-a). When the process is finished, the weld bed might include physical disruption because of distortion (inappropriate plastic strains), unsuitable cooling rates and residual stress. The high heat is an important parameter because the heat intensity of welding melts the filler metal, transforming it into a melting pool[67].

Figure 40-b illustrates the calculation of peak temperature at a different distance of the fusion zone in the gas metal arc steel weld (GMAW); the image shows a transverse section of a single pass welding[68]. Figure 41 represents the influence of welding velocity on the isotemperature contour in low carbon steel. When the speed is elevated, weld size reduces, and the isotemperature shape extends behind the arc. If the heat input is increased, it will be necessary to increase the travel velocity to achieve a similar weld size[67].

Rosenthal's thick plate solution calculates temperature distribution considering the differential heat flow source in a semi-stable state. Rosenthal Equation is a three-dimensional model which uses proportionate thermal conditions at a specific point (Equation 1). The model uses an isotropic semi-infinite body which it is limited to one direction plane. At time t=0, q_0 is a point source of constant power refers to a single location emitting a steady amount of energy. q_0 starts at a particular location on the surface and travels at a constant velocity in the x-direction. The increase of temperature $T\text{-}T_0$, in a point P at specific time (t) is shown in Equation 4. Where R is the distance from the heat source, X is the distance from the heat source determine along x-axis, λ is the thermal diffusivity, and "a" is the volumetric heat capacity. Figure 42-a shows Rosenthal's thick plate solution in a three-dimensional diagram[68].

$$T - T_0 = \frac{q_0}{2\pi\lambda}\left(\frac{1}{R}\right) exp\left(-\frac{\nu}{2a}(R + x)\right) \qquad 4$$

Another necessary calculation is the fast-moving high-power source. Following Equation 4, the isotherms behind the heat source continue to elongate as the power, q_0, and welding velocity, ν, rise. In limiting conditions, when $\nu \to \infty$, $q_0 \to \infty$ and $^{q_0}/_{\nu}$ remains finite, isotherms will be degraded in an area corresponding to the x-direction welding (Figure 42-b). As a result, heat conduction will be in the same direction as the x-axis, holding heat flow in two dimensions.

Equation 5 shows a simple solution on a semi-infinite slab for a fast-moving high-power source[68].

$$T - T_0 = \frac{q_0/\nu}{2\pi\lambda}\left(\frac{1}{t}\right) exp\left(-\frac{(r*)^2}{4at}\right) \qquad 5$$

Where r^* is the radius vector in two dimensions in the plane of y-z

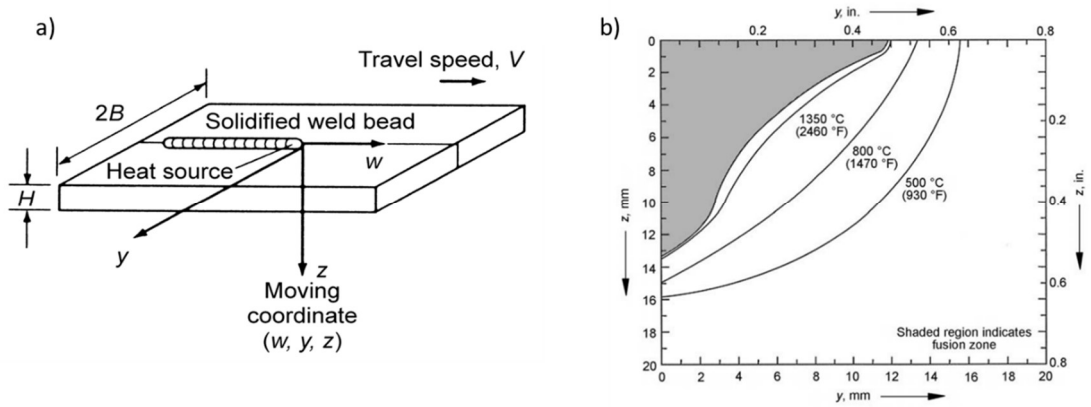

Figure 40 a) Welding thermal schematic; b) distribution of temperatures shape model in the transverse section of GMAW. Settings: I=450 A, v=2.6 mm/s, U= 30V and d=50 mm [67,68]

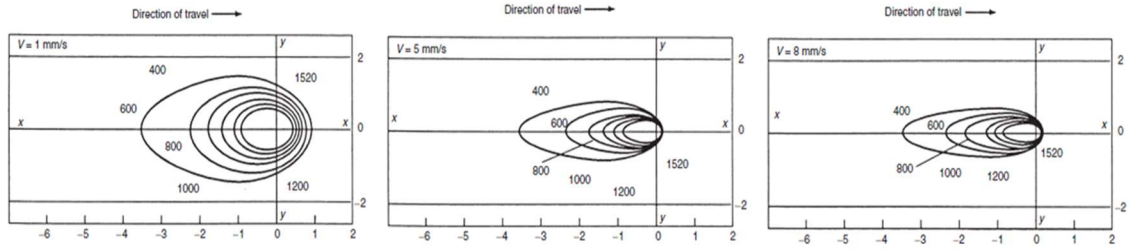

Figure 41 Welding velocity effect (V) on isotemperature contour of low carbon steel (4200 J/s heat input)[67]

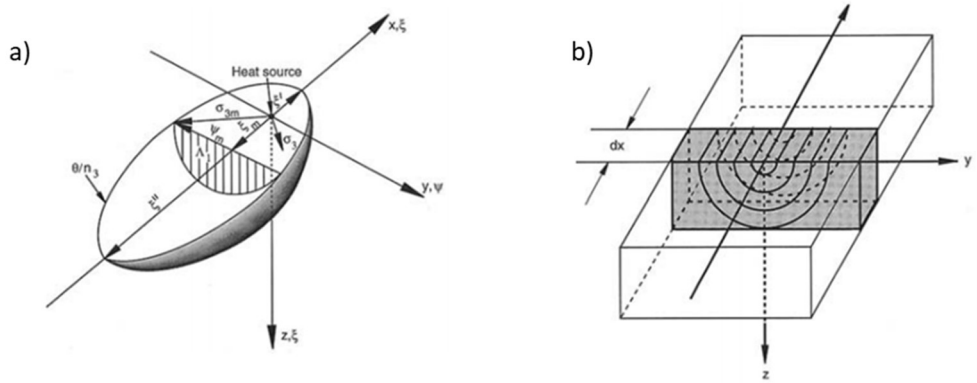

Figure 42 a) Thick plate Rosenthal representation; b) quick movement semi-infinite slab with high power source [68].

2.5.3 Weld solidification

The microstructural evolution that occurs during solidification in the fusion zone is a critical factor in determining the final properties of a welded joint. The three primary parameters that are typically controlled during solidification to achieve the desired microstructure and properties are the temperature gradient (G), cooling rate (ε), and growth rate of the solid-liquid interface (R). By controlling these parameters during welding, it is possible to achieve the desired microstructure and properties in the welded joint.

Figure 43 illustrates a fixed-rate temperature gradient (*R*) that travels from right to left, which implies $t_1 > t_2$. The temperature decreases from T1 to T2 over the time period of t1-t2, at a fixed position (x*). The cooling rate, which is determined by the speed (R) of the temperature gradient across space, controls the time required for the temperature to decrease [69].

$$\varepsilon = GR \tag{6}$$

In addition to the cooling rate, the solidification of the weld is also determined by other welding parameters. Moreover, the rate of growth in welding is influenced by the speed of the heat source and the shape of the weld pool, as explained in Equation 7. In this formula, the heat input controls temperature gradient and cooling rate, where the transfer efficiency of the heat source is η, the power of the heat source is *P* and the heat source travel velocity is *S*. The energy amount liberated per unit weld length is represented by heat input. The ε, *G and R* values depend on the time and position; when the heat input increase, the cooling rate and temperature gradient is reduced[69].

$$HI = \frac{\eta P}{S} \tag{7}$$

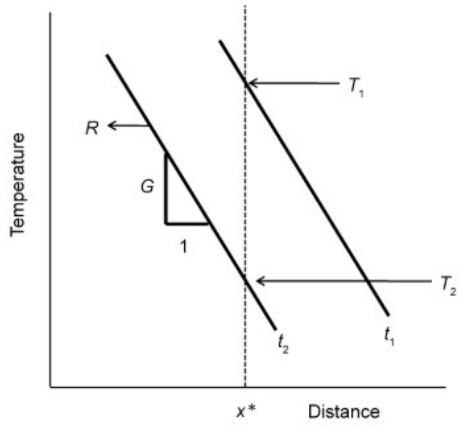

Figure 43 Graph illustrates the temperature gradient (G), cooling rate (ε) and growth rate (R) relation. The rate of temperature gradient movement controls the cooling rate. [69].

The fusion weld has another essential factor which is competitive grain growth. The grains of weld metal will occur since their previous forming grains of base metal are in an epitaxial manner. Furthermore, not all grains will be oriented in the same direction for continued growth. The main factors to control the increase in weld metal grains in a continued and competitive form are the next:

- The grain growth trend is transversal to the highest heat extraction way. In this process, the latent heat solidification requires transfer from the temperature gradient to the base metal. Because of that, the highest heat flow rate is perpendicular to the solid-liquid interface. Consequently, the tendency of grains growth is in the direction of the perpendicular way of the solid-liquid interface[69].

- Solidified grains will grow in the crystallographic direction of "easy growth". Cubic metals have [100] direction as preferential crystallographic growth[69].

Furthermore, fusion welding has additional challenges because, during the application, the weld pool (melted material) constantly moves in the solid-liquid interface, which affects the fusion line. Figure 44 shows the grain orientation in the fusion line; in those grains, the growth direction is favourable to the fusion line. Nevertheless, when the weld pool starts to shift position, the grain growth changes in an unfavourable direction. Eventually, other grains with favourable orientation to the weld line will overgrow the first ones[69,70].

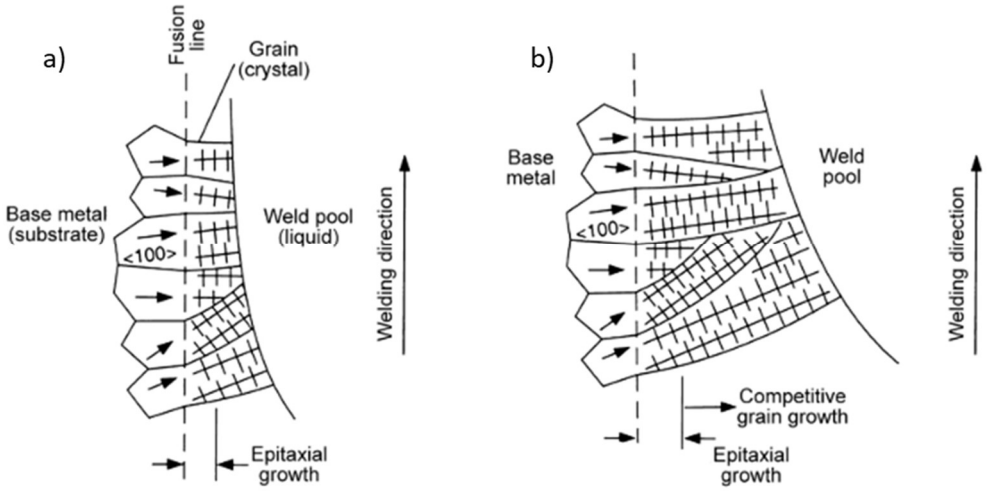

Figure 44 Illustration of grain growth competition in welds. a) Early grain growth near the line of fusion. b) Favourably grains growth-oriented continuously after application welding with different cordons [59].

2.5.4 Heat Affected Zone

The Heat Affected Zone (HAZ) refers to the area near the welded joint where the material has undergone repeated cycles of high temperatures. As a result, the material properties can be significantly altered, which may result in formation of defects and potential structural failures. Because of this the Heat Affected Zone (HAZ) is the most critical issue in welding [71]. Usually, the weld metal problems are solved with the change of electrodes. However, the only way to solve HAZ problems occasionally involves changing the base material, drastically increasing the product cost. Therefore, weldability is one of the most critical issues in the HAZ.

To evaluate weldability is used the empirical carbon equivalent formula. European countries, the United States and the International Institute of Welding (IIW) use equation 8, while Japan, to evaluate the low carbon steel is utilised the parameter of composition-characterise P_{cm} (Equation 9)[72]. If a steel alloy has a high carbon equivalent (CE) value, it means that it contains more carbon and other alloying elements, which can increase the risk of cracking during welding due to hardening and cooling stresses. Contrary, a steel alloy with a low CE value is less likely to crack during welding and is considered to have good weldability, indicating a lower concentration of carbon and other alloying elements [72].

$$CE(IIW) = C + \frac{Mn}{6} + \frac{Cu + Ni}{15} + \frac{Cr + Mo + V}{5} \quad 8$$

$$P_{cm} = C + \frac{Si}{30} + \frac{Mn + Cu + Cr}{20} + \frac{Ni}{60} + \frac{Mo}{15} + \frac{V}{10} + 5B \qquad 9$$

These equations have been used to evaluate steel's hardenability with the chemical composition of the material. To predict the steels susceptibility of cracking during welding is used the CE, while the susceptibility of cold cracking during welding is determined by P_{cm} in high-strength low-alloy (HSLA) [73]. Figure 45 illustrates the carbon equivalent relation, P_{cm}, with the martensite volume in the coarse-grained and grain-refined region. When P_{cm} elevates, hardness and martensite in the two areas increase at the same time[72].

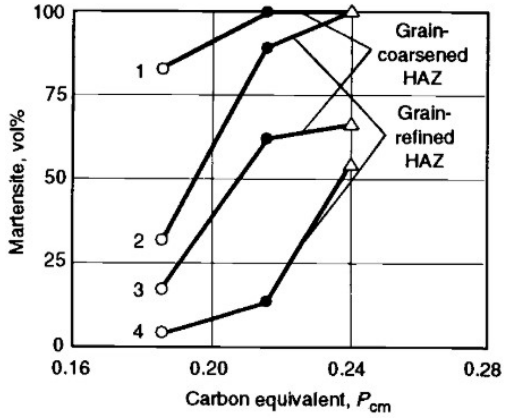

Figure 45 Relation between the martensite in the HAZ volume fraction and the Pcm in the thermally cycled samples. The parameters are: (1) peak temperature, T_p=1350°C, time of cooling 800 to 500 °C ($\Delta t_{8/5}$) =3s; (2) T_p=1000°C, $\Delta t_{8/5}$=3s; (3) T_p=1350°C, $\Delta t_{8/5}$=13s; (4) T_p=1000°C, $\Delta t_{8/5}$=13s[72].

The alloying elements in the Heat Affected Zone play a crucial role in modifying the microstructure and mechanical properties of a material, which can be influenced by the cooling rate and transformation behavior. These effects can be analyzed and predicted through the use of the CCT diagram (Figure 46) [72], which provides a graphical representation of the material's transformation characteristics during cooling under a steady cooling rate from a high temperature to room temperature. The CCT diagram provides information on the start and end temperatures of the transformation process, the transformation rate, and the resulting microstructure that forms during the cooling process. The impact of alloying elements on the microstructure of Heat Affected Zone (HAZ) and toughness in low alloy and carbon steels can vary. Some of the effects are as follows:

Carbon has a meaningful role in hardness and the carbon equivalent equations P_{cm}. When carbon increases, it promotes the constitution of transformation products at a lower temperature, such as bainite and martensite. However, the increment of carbon reduces the cleavage strength in the HAZ[72].

Manganese. Additionally to the hardening of solid solution, it can lower the transformation temperature in austenite to ferrite. Also, it provides grain refinement resulting in a strengthening effect. Moreover, the restriction of manganese quantity reduces microstructural banding and solidification segregation[72].

Chromium is a carbide former and solid solution strengthener. In addition, It elevates steel hardenability, increases corrosion and oxidation resistance[72].

Nickel is similar to manganese; the addition of nickel decreases the austenite transformation temperature. Also, this element increases toughness and hardening[72].

Niobium and Vanadium. In low alloy steels, these elements are added in small quantities. V and Nb precipitate in V(C,N) and Nb(C,N); these elements delay austenite grain growth and recrystallisation during rolling and normalisation. In fusion welding, temperatures achieve more than 1100°C; at those temperatures, V(C,N) and Nb(C,N) are dissolved. Also, the dissolution of the precipitate allows an effect of reprecipitation when the cooling occurs at slow temperatures. The V(C,N) and Nb(C,N) reprecipitation impair the HAZ toughness[72].

Titanium. The titanium nitride inhibits the prior austenite grain coarsening in the adjacent zones of weld fusion boundaries[72].

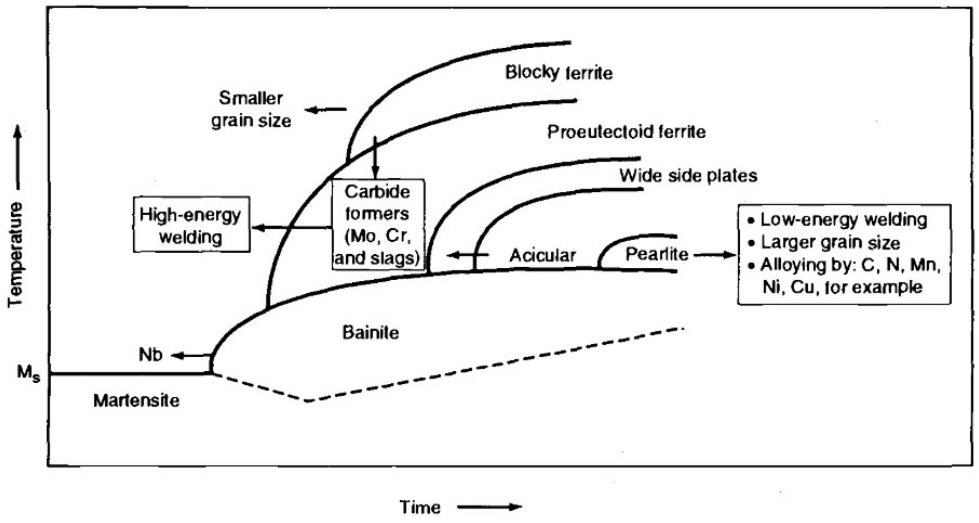

Figure 46 Continuous cooling transformation (CCT) diagram in weld metal sums up the microstructure effect and transformation products depending on alloying elements and cooling time in weld[72].

During welding of high-strength low alloy steels (HSLA), coarse grained embrittlement is one of the most critical issues in the HAZ. The slow cooling rate increase the embrittlement forming undesirable microstructures such as grain boundary ferrite and side plates of coarse ferrite (Upper bainite and Widmanstätten ferrite) and grain boundary ferrite[72].

In HSLA steels which contain vanadium and niobium, the HAZ and the weld metal show low toughness in submerged arc welding applications. Because the high heat inputs increase the HAZ's coarse grain. Furthermore, a low cooling rate in the HAZ is associated with a reduction in grain refinement and the probability of precipitation increase in the Nb and V carbides. The carbides dilution and the high inputs heat conduct the niobium and vanadium precipitation hardening problem in the coarse-grained weld metal. Other critical factor in the microalloyed elements is titanium and nitrogen. The slight Ti (up to 0.04 %) and N additions reduce the grain growth in the coarse-grained region of HAZ. This is owed to the higher stability of titanium nitride in the peak temperature achieved in coarse-grained regions (up to 1100 °C), where Nb and V carbides have been dissolved at high temperature[72].

In annealed low carbon steels, the primary microstructure is soft ferrite in a dispersed manner with tiny particles of carbides. In contrast, the hot rolled or normalised low carbon steel contains pearlite islands meanly. To avoid some failures in the welding, such as stress corrosion cracking, steels used in hydrogen sulfide environments must achieve a hardness of less than 22 HRC (248 HV). This hardness limit is recommended for pipeline steel in sour gas application[72].

Thermomechanically controlled processing steels (TMCP) improve the accelerating cooling technology by the obtention of a similar strength level to the conventional controlled rolled steels with lower carbon content (<0.06%). TMCP steels acquire their toughness and strength from the second phase's greatly fine ferrite and microstructure (finely distributed pearlite or bainite, which occur during cooling acceleration). Furthermore, HAZ softening is an issue because the TMCP steel could return the microstructure during a slow cooling rate in the HAZ with high heat input levels. Figure 47 illustrates hardness variance in the HAZ using different heat inputs[72].

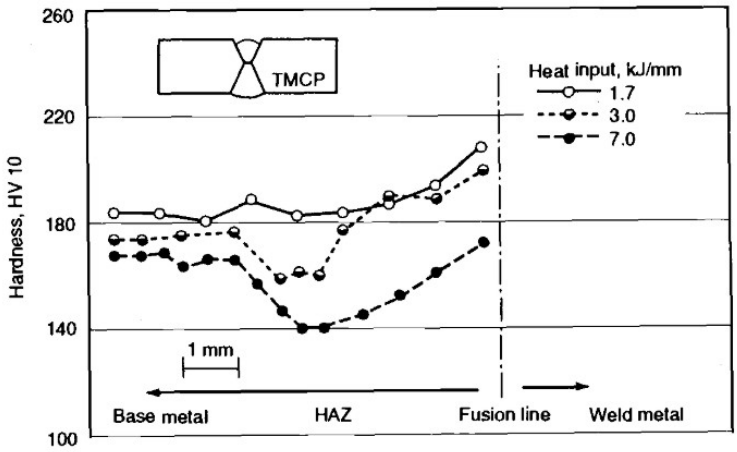

Figure 47 Difference of HAZ hardness profile in a TMCP steel welded. Heat input parameters are 1.7, 3.0, and 7.0 kJ/mm. Chemical composition: C, 0.06%; Si, 0.14%; Mn, 1.33%; P, 0.010%; S, 0.001%; Cu 0.31%; Cr, 0.05%; Nb, 0.15%; and Al, 0.034%[72].

2.5.5 Solid-State Transformations

Solid-state transformations appear during welding, and they typically take place in a non-equilibrium condition due to the high heating and cooling rates involved. The two main regions in welding metallurgy are the Heat Affected Zone (HAZ) and the fusion zone (FZ). The welding metallurgy divides into two main regions: the heat affected zone (HAZ) and the fusion zone (FZ), and phase transformations occur primarily during heating and cooling.

Figure 48 shows a typical microstructure transformation during heating and cooling in the Heat Affected Zone. When the heating increases, the austenite starts to form at Ac1 temperature and it finishes at Ac3 temperature when austenite is fully transformed. Until the temperature is above Ac3 the grain size starts to grow. On the other hand, during cooling, as the temperature decreases below Ar3, the austenite begins decomposition into various microconstituents. The transformation temperatures Ac3 and Ar3 are not fixed values, but depend on the heating or cooling rate. At higher cooling rates the difference between Ac3 and Ar3 increases [74].

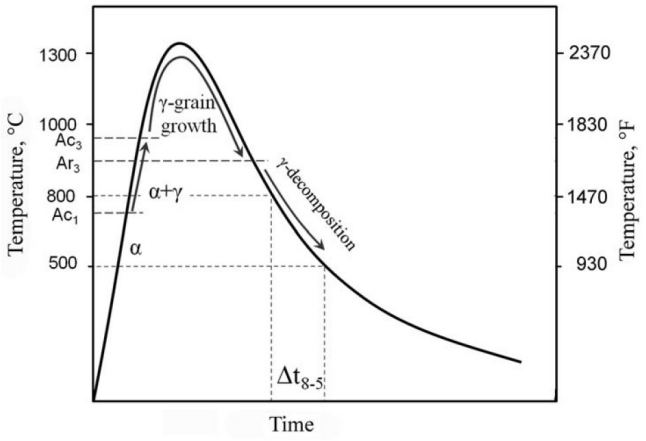

Figure 48 Illustration of microstructure behaviour during heating and cooling in the HAZ [74].

The HAZ could be separated into different zones depending on the distance respecting the fusion line (Figure 49). In the adjacent zone to the fusion line, the temperature is the highest, which can cause the austenite grains (γ) to coarsen. This can result in an increase in hardenability in this zone. Austenite Grain Size reduces faster when the distance of the fusion line increases. Some regions away from the fusion line experiment a partial austenitisation in the heating process. Figure 50 illustrates the microstructure of HAZ in single pass and multiple pas welds [75]. Table 5 illustrates the temperature interval in the Heat Affected Zone regions as a function of the fusion line distance.

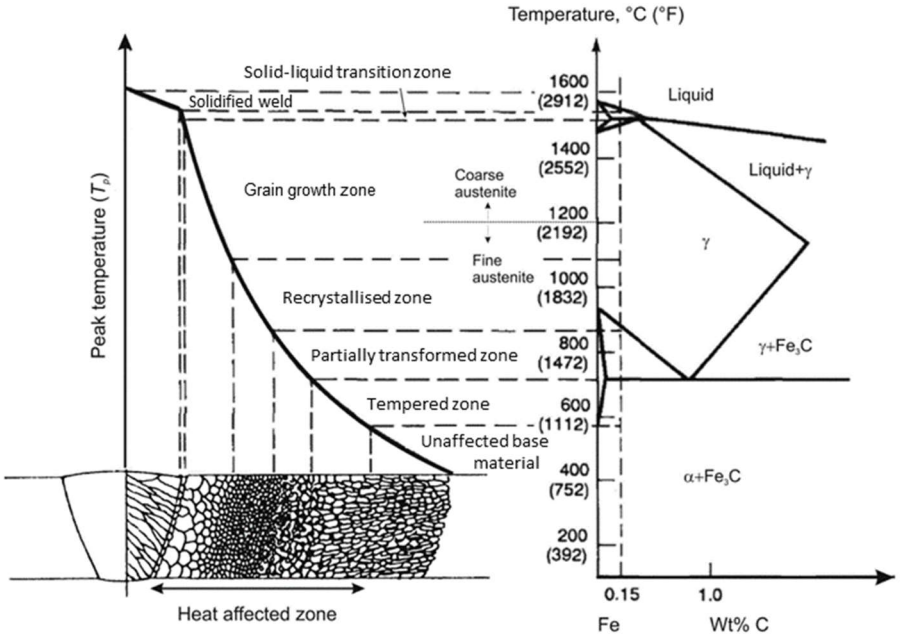

Figure 49 Iron Carbon diagram represents microstructural variation in the HAZ [74].

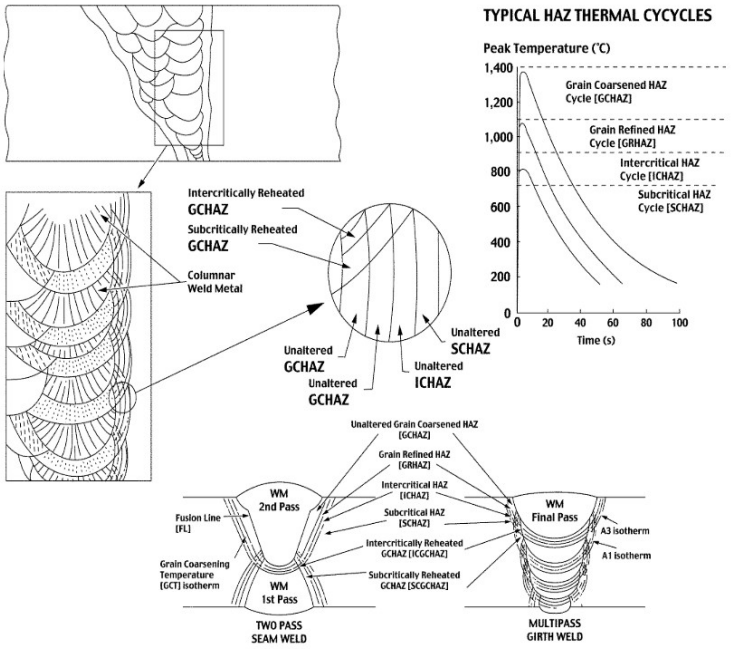

Figure 50 The microstructure of HAZ in single and multiple pass welds [75].

Table 5 Interval of temperatures in the different HAZ regions [74]

HAZ Microstructures	Temperatures range
Coarse grained austenite	1500 °C > T_p > 1200 °C
Fine grained austenite	1200°C > T_p > Ac_3
Partially austenitised zone	Ac_3 > T_p > Ac_1
Tempered regions	Ac_1 > T_p

2.5.6 Austenite Grain Growth and Grain Boundary Pinning

The growth of Austenite Grains promotes phase transformation kinetics and contributes to the formation of bainite and martensite. Additionally, it significantly affects the grain size of the weld, with the grains growing in the same epitaxial orientation as the Heat Affected Zone. The grain growth affects strength and toughness, besides the weld grain size[74]. Figure 51 illustrates the change in grain growth when it moves away from the fusion line.

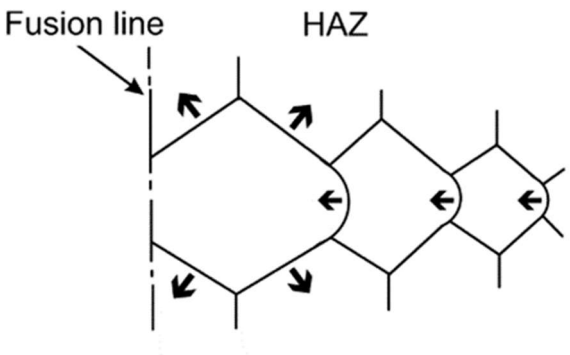

Figure 51 Grain growth changes in the HAZ[74].

In the past, increasing carbon and manganese quantities was the usual practice to increment the strength. However, the addition of those elements detriment toughness and promotes weld cracking[74]. Because of this, grain size reduction is the best method to increment the two properties: strength and toughness[74]. In microalloyed steels, to achieve an accurate grain size (before the austenite–ferrite transformation) is necessary to add some microalloyed elements such as niobium, vanadium, titanium, and aluminium. Nb, V and Ti are extraordinary formers of carbides and nitrides, while Al only forms nitrides. The addition of these refining microalloyed elements modifies the austenitic matrix with fine precipitates. The particles are auspicious to locate in the grain boundaries. The fine precipitates are pinned in the austenite grain boundaries stopping the grain coarsening[74].

In the Heat Affected Zone is not possible to obtain the optimum microstructure and desirable precipitation as in thermomechanical processing. The principal issue in the HAZ is the peak of elevated temperatures, that energy produces dissolution and coarsening of precipitate particles. As a consequence, high temperatures increase the austenitic grain size. Figure 29 represents the effect of microalloyed steel and the second-phase particles on the austenitic grain size depending on the fusion line[74].

The effect of solubility products could be minimised using undissolved precipitate particles at high temperatures. Figure 52-a shows the stability of the nitrides compared with the carbides. The nitride of Titanium (TiN) has the most increased stability; this relevant advantage allows it to use in different steels. Figure 52-b illustrates the effect of varying microalloying additions in the austenite grain coarsening at different temperatures. Titanium is the most influential element in grain refining of microalloyed steels because TiN has the lowest solubility in γ[74].

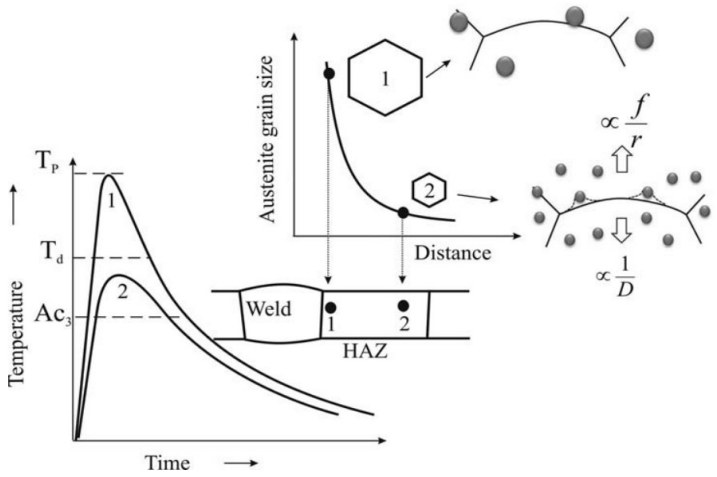

Figure 52 Diagram of the austenite grain size in the HAZ and the effect of the second-phase particles in the weld. The second phase particles are distributed depending on the distance of the fusion line and thermal cycle[74].

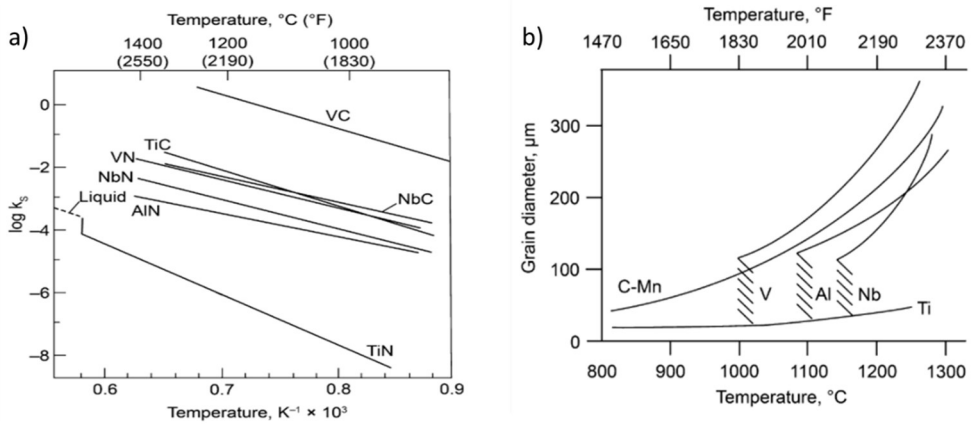

Figure 53 a) Carbides and nitrides solubility products in austenite. b) Result of the microalloyed additions on the temperature of austenite grain coarsening[74].

2.5.7 Fusion Zone of a Single Pass Weld

The filler metal is an essential issue in the design of welding. Typically, the chemical composition of filler metal is equal to the base metal; however, it is not mandatory. Weld metal must have the same properties referring to strength, toughness and corrosion-resistant[74]. In the transformation behaviour of weld metals, ferrite nucleation is more favourable at grain boundaries than in the inclusions because of the energy levels. However, grain boundaries are a good area for ferrite nucleation because it needs less energy. Figure 54-a illustrates the particle radius effect on the energy barrier allowing ferrite nucleation at inclusions. Inclusions must be more significant than 0.2 to 0.5 µm to get the maximum nucleation potency. Figure 54-b shown the shape of acicular ferrite and inclusions particles[71].

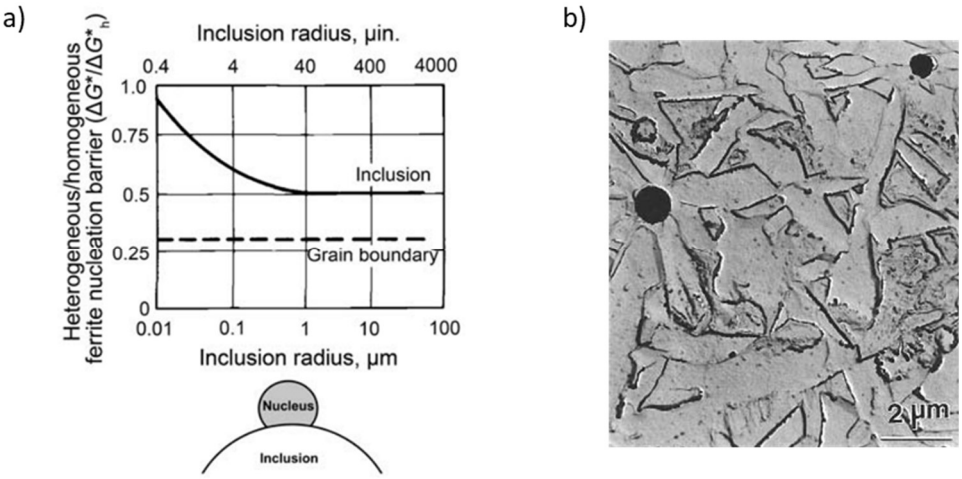

Figure 54-a Result of the energy barrier at inclusions nucleation in ferrite. The discontinued line shows the energy barrier to ferrite nucleation at the austenite grain size. [74]. Figure 31-b Acicular ferrite and inclusions particles in a microalloyed steel[71].

2.5.8 CCT weld diagram

The CCT welding diagram is illustrated in Figure 55. The first phase that appears during cooling is allotriomorphic ferrite (this phase doesn't have a standard external form). In lower temperatures, the curve of γ/α allotriomorphic boundaries reduces, and the side plates of Widmanstätten start to shape. The Widmanstätten plates grow faster because the carbon is redistributed to the sides of the growing tip; this prevents the solutes heap up. Subsequently, when grain boundary sites saturate with allotriomorphic or Widmanstäten ferrite and cannot continue growing in the interior of the grains, ferrite nucleation and inclusions starts to compete. While acicular ferrite forms in the inclusions and nucleation of laths. At a higher cooling rate or when the content of inclusions is extremely low, nucleation of bainite could form in austenite grain boundaries. Figure 56 shows the microstructural constituents in typical welding of low alloy steel[74].

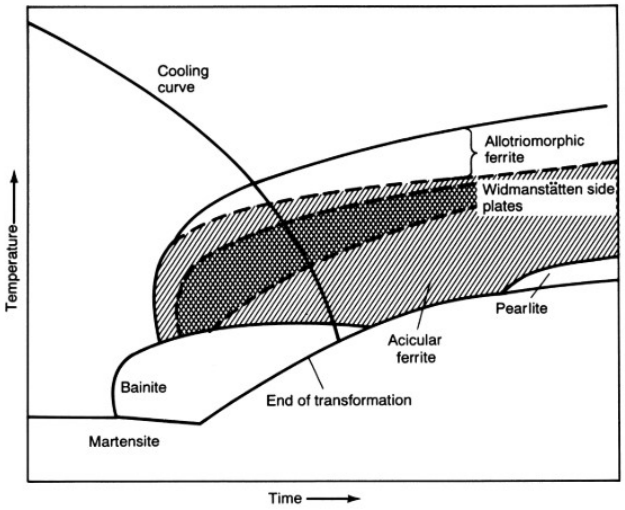

Figure 55 CCT diagram of continuous welding showing the resulting microstructures[74].

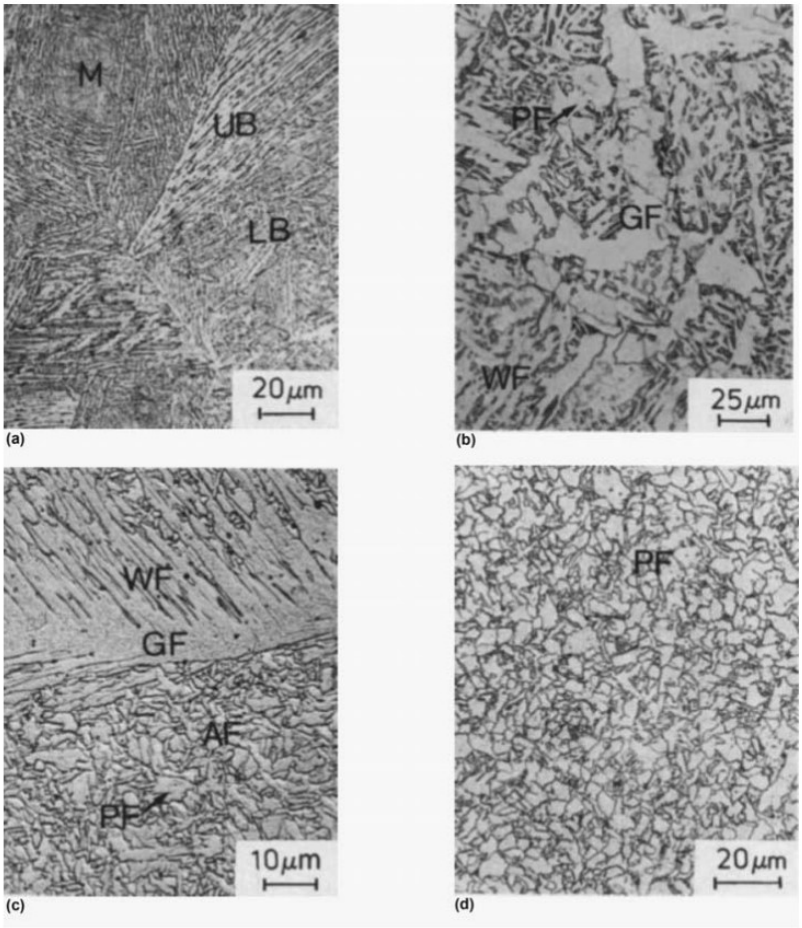

Figure 56 Low alloy steel weld metal representative microstructures. (a) and (b) Coarse grain HAZ (low heat input), c) Deposited weld metal (low heat input), and d) Reheated weld zone (low heat input). M - martensite; UB - Upper Bainite; LB - Lower Bainite, PF – Polygonal ferrite, AF – Acicular ferrite, GF – Granular Ferrite, WF – Widmanstätten Ferrite[74].

Summary

The present chapter covers the literature review in different stages. Firstly, it explains the evolution of austenite in different microstructures when it is cooling at various velocities. Next, it appears the effect of temperature in the prior austenite grain size and solubility of various precipitates such as niobium carbides and titanium nitrides. Afterwards, it describes the thermomechanical controlled processing; the welding process is focused in the heat affected zone and the temperature distribution during the application.

Niobium is crucial in the control of prior austenite grain size. Previous publications did not report in the experimental work high niobium concentrations and long holding times. Present work will experiment with long austenitisation times (>30 min) and niobium concentration of 0.094% at different cooling rates and austenitisation temperatures. This will allow to understand the behaviour of the prior austenite grain size and the effect on the microstructure evolution.

Experimental Procedure

3.1 Experimental design

The experimental process is essential to plan the following steps in the research work. The experimentation was divided in characterisation and evaluation of mechanical properties. Figure 57 shows the experimental process used during the research.

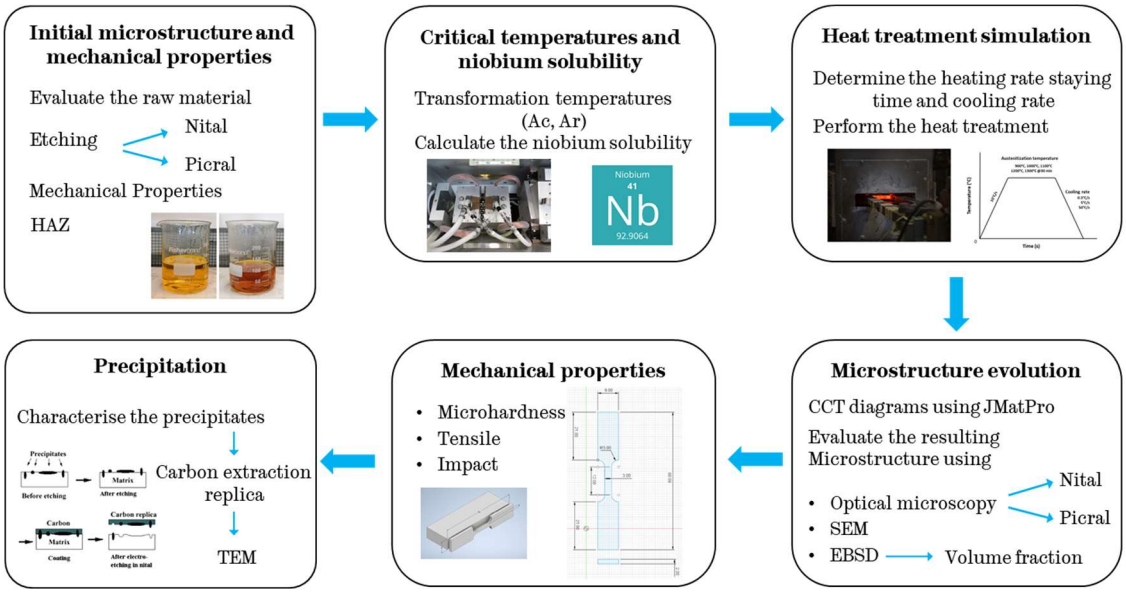

Figure 57 Experimental process chart during the research.

3.2 Material

A section of pipeline was supplied by Companhia Brasileira de Metalurgia e Mineração (CBMM). The material is an API X80 steel, which works in the Cheyenne Plains Project to transport natural gas in Colorado State in The United States. It was manufactured in California by Napa Pipe Corporation. The pipe has the next dimensions, 14.38mm (0.566") thickness wall x 762mm (30") outside diameter. The pipeline was welded using a double submerged arc (SMAW). The chemical composition of the steel is shown in Table 6. The material corresponds with a chemical composition between API X80 and X100 steel.

Table 6 Chemical Composition (wt %)

C	Mn	P	S	Si	Cu	Ni	V	Nb	Al	Cr	Mo	Ti	N2	Ca
0.060	1.560	0.014	0.002	0.130	0.240	0.130	0.002	0.094	0.037	0.230	0.010	0.014	0.005	0.003

3.3 Metallography

Optical microscopy was performed on a Nikon Eclipse. The objective lenses in the microscope has magnifications from 50X to 1000X. To use the samples in this technique, it is necessary to keep a flat surface. Therefore, as a previous preparation, it is required to follow the next steps:

1. To standardise the samples, the material is mounted in a conductive resin (Bakelite). The conductive resin allows using in the Scanning Electron Microscopy after the optical microscopy. All the samples were mounted in 32 mm diameter for use in the automatic polisher.

2. Then, diamond abrasives and grinder polisher were utilised in the automatic polisher EcoMet 250 Pro by Buehler. Table 7 shows parameters utilised in the specimen's preparation using the automatic polisher[76]. This method makes it possible to obtain a mirror-like surface without scratches in the sample. At the end of the process, it was used diamond solution, in this step is important to have adequate polishing cloths. It utilised WhiteFelt™ in 3 μm and Micro Cloth in 1 μm supplied by Buehler.

Table 7 Semiautomatic procedure in sample preparation [76].

	Abrasive Parameters			Mechanical Properties				
Stage	Type	Grade	Fluid	Speed an (rpm) *	Speed b (rpm) *	Direction	Force (N)	Time (min)
1	SiC	240-2500	Water	60	240	Comp	22	2
2	Diamond	3 μm	-	60	150	Comp	18	3
3	Diamond	1 μm	-	60	150	Contra	18	5

(*) Speed (a) refers to the head speed and speed (b) refers to plate speed

3.3.1 Etching

Depending on the microstructure to be revealed, two different etching solutions were used to characterise the steel. In the revealing microstructure, the sample's surface is submerged in the reagent during a determined time. This procedure is after polishing the surface until a mirror-like surface as it was described in the last section.

Nital

The first etching to characterise the material was nital. In the revealing of the microstructure was used a concentration of 2% nital. The solution consists of a combination of 98ml of ethanol and 2ml of nitric acid at room temperature. The samples immersed until the mirror-like surface starts to lose brightness, and a contrast change in the sample is observed. This process occurs between 5 to 25 seconds of etching. The nital is the most common etching to reveal the final microstructure in steels[77].

Picral

The prior austenite grain size (PAGS) was revealed using picric acid in a saturated aqueous solution. The picric acid was dissolved in distilled water, additionally, hydrochloric acid (HCl) and a wetting agent was added to the solution. The chemical composition of the steel will determine the quantity of each component. F. Vander Voort, Brewer, F.G. Caballero, et al. have pointed out the challenge of revealing austenitic grain, this is because it depends on some variables such as chemical composition and heat treatment of the material[77-85]. The difficulty of revealing the austenitic grain size increases when C < 0.3% and P < 0.010% in the alloy composition. Brewer recommends increasing HCl addition in etching when the carbon content is small[81].

To start with the picric acid concentration was used in the previous works reported by Romano-Acosta[86] and Rakshe[87] as a base recipe. In those works, the steel has a chemical composition of 0.07% C and 0.012% P in the Romano-Acosta material and 0.20%C and 0.015% P in the Rakshe material. The etching used in the X80 steel was found after different variations in the quantity of picric acid, HCL and wetting agent. The description of the procedure appears in the next paragraph.

The temperature is a fundamental parameter during the etching. The picric acid is saturated at 1.3% of the weight at room temperature, however, when the temperature is heated to 100 °C, it is possible to saturate until 6.6% of picric acid[88,89]. The solution was made at room temperature with 120 ml of distilled water, and 4.2 g of picric acid crystals. Then it was stirred for 4-5 min, and at the same time, the solution began to heat up to 70°C, until the crystals of picric acid were dissolved. Afterwards, 1.2 g of Sodium dodecyl (wetting agent) was added. After the addition of the wetting agent, a foam appears on the top of the solution. It is necessary to stir for 2-3 min until the foam starts to settle down because the foam could affect the etching causing pitting.

Finally, the solution is heated to 80 - 90 °C. Then, the HCL is slowly added to the solution starting in 15 drops. Because the fresh solution is overly aggressive with the steel, it has to mature using 6 dummy samples for 5 min each. The solution is ready to use when the colour has been swapped from bright yellow to dark pale orange. Figure 58 shows the solution before the dummy samples were added and when the solution has matured. The prior austenite grain size was determined in quenched samples at the austenitising temperatures of the different heat treatments.

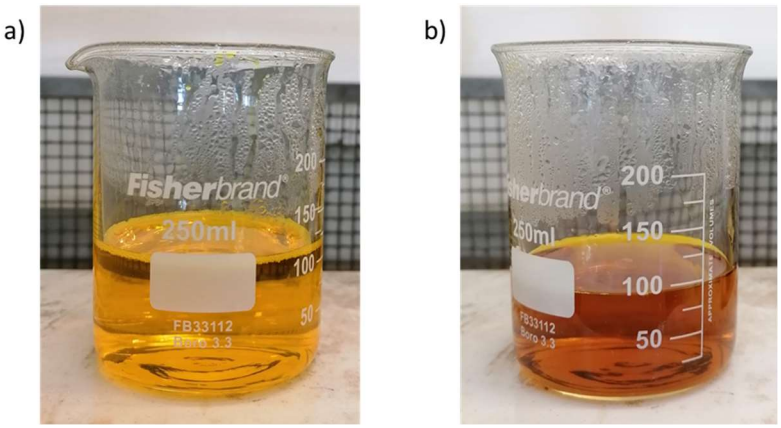

Figure 58 Picric acid solution at 80°C a) before the dummy samples were added and b) matured solution after dummy samples.

3.4 Prior Austenite Grain Size measurement

To calculate the average grain size is selected the standard ASTM E112-13 11. In this standard, it was utilised the lineal Intercept Procedure for this measurement[90]. The procedure specifies that the interceptions of grains should be more than 50. All the samples had at least 70 measurements, and it used at least 6 lines in every condition. Equation 12 is used to determine the standard deviation (s) and the 95% of confidence in the calculus (95% CI)[90].

$$s = \left[\frac{\sum(\chi_i - \overline{\chi})^2}{\eta - 1}\right]^{\frac{1}{2}} \qquad 95\%\ CI = \frac{t * s}{\sqrt{\eta}} \quad t = 2.571 \qquad 12$$

3.5 Scanning Electron Microscope (SEM)

The Scanning Electron Microscope is used to observe the microstructure that could not be observed in the Optical Microscope. To start the characterisation, the sample was etched with nital 2%. The equipment FEI Inspect F50 was used in this technique. The parameters used in the SEM were 20kV voltage, a spot size of 4.0, sample distance between 9.5 and 11 mm and 1,000X – 10,000X magnifications. Table 8 illustrates the capabilities of FEI Inspect F50.

Table 8 FEI Inspect F50 specifications and capabilities[86].

Source	Field Emission gun
Acceleration voltage	5kV to 30kV
Point resolution	1.4 nm
Tilt	+90°, -10° (holder specific)
Magnification	50 to 150,000 X
Elemental Analysis	Aztec EDS

3.6 Electron backscattering diffraction (EBSD)

Electron backscattering diffraction (EBSD) is a useful technique to evaluate microstructural characterisation and crystal structure behaviour. Using EBSD, it is possible to obtain different properties such as grain size, misorientation, constituents of phases and crystallographic texture. Similar to that of optical microscopy, the preparation of the EBSD samples used the same parameters that are shown in Table 7. Additionally, to that process, after the 1 μm cloth polishing, further polishing was performed using colloidal silica (0.5 μm) for 20 minutes. The colloidal silica must always be used with water to avoid drying in the cloth polishing because that contaminates it. After the colloidal silica, the cloth polishing is cleaned and then the sample is polished again for 10 min using only water. Finally, ultrasonic cleaning is used for 20 min to remove the colloidal silica remainder in the sample.

In the testing was used a FEI Inspect F50 microscope with a 20-kV voltage and spot 5.0, focusing at 10,000 magnifications in the evaluation. Then, the sample is tilted 70° with the reference to the horizontal plane. After that, the holder is adjusted the “y” and “z” axis reference until the working distance respecting the beam is 19.8 mm.

Then, the charge-coupled device (CCD) detector is positioned at a distance of 152.4 mm from the sample. To analyse the misorientation and microtexture the step size accepted is at least $\frac{1}{10}$ of the grain size measurement[91]. The samples were analysed with a step size of 0.2 μm. The index rate in the analysis had variations from 78% for martensite to 94% for pearlite and ferrite structures. The data were processed and evaluated in HKL Chanel 5 software.

3.6.1 Determination of volume fraction using EBSD software

To determine the phases and the volume fraction, the samples were analysed using the EBSD. In all the EBSD analyses, the collected data obtained at least 86% of the indexing rate. The only samples that obtained less indexing rate were the samples at 50°C/s of cooling and austenitisation temperature of 1200°C and 1300°C, which in these conditions obtained 78%. The data was processed in the HKL Channel 5 software by Oxford instruments.

The software analysis started with the subsets; this allowed focusing on a specific zone. Also, the selection of subsets avoids scratches zones or obvious miss-indexed points. As a previous step in constructing the map, each subset noise reduction function was utilised. The noise reduction consisted of two types: the first is the wild spikes, and the second is the zero solutions. The first step in the subsets noise reduction was the processing with the wild spikes function.

The wild spikes function identified isolated points which could not index correctly. When a pixel does not match with a similar orientation with its surroundings, the wild spike function extrapolates the pixel for one which fits with the near pixels. This function is utilised to identify the non-indexed pixels and change them into indexed pixels. Then, it is used the noise reduction function; this function removes the “zero solutions”.

The zero solutions isolate the incorrect index points because of the polishing issues or surface pollution. The indexed levels of noise reduction are between 8 (minimum) to 1 (maximum). This function takes in a non-indexed pixel the reference of the neighbours, and it will be substituted with the most common orientation of their neighbours. The function starts with pixels with indexed levels of 8 and continues until it reaches 1. In the present work, the filter was used until the non-indexed pixels achieved levels of 0.5% maximum; this value was commonly in level 5 of noise reduction.

Different maps in the EBSD were constructed to separate the present phases in each sample. The maps used in this work were band contrast (BC) or image quality (IQ), band slope (BS), and inverse pole figure (IPF). The higher values in BC and BS mean a high-quality diffraction pattern; contrary, deformed regions show a low BC value. Different filters such as grain orientation spread (GOS), aspect ratio, grain size, and grain boundaries were used to identify and separate the phases. The maps constructed to analyse the sample with a 50°C/s of cooling rate and 1100°C of austenitisation temperature are shown below. The rest of the EBSD maps related to the other conditions are shown in Appendix II. All the conditions were analysed with the same identification parameters for phase separation.

Band contrast and band slope are related to the Kikuchi pattern[92] . BC is associated with image quality; BC measures the average Kikuchi band intensity concerning the pattern intensity[92,93]. At the same time, BS measures the gradient of maximum intensity compared to the background and the Kikuchi band. The Tango section in HKL Channel 5 software constructs BC and BS maps in scales of black and white; the scale starts from 0 (white) to 255 (black), and the colour is assigned to each pixel according to BS or BC value.

Figure 59 shows a BC and BS map of the sample with 1100°C and 50°C/s of cooling rate. Lower numbers (close to white) of BC and BS indicate that the pixel pattern is near the solution determined by Channel 5 software. The HKL Channel 5 software evaluates BCC and FCC crystal structures; therefore, when BC or BS values are higher (dark pixels), the crystal structure is not similar to the software solution. Because most of the indexed pixels are matched with BCC structure, darker pixels of BS or BC maps relate to an imperfect BCC crystal structure or defects.

The analysis of EBSD is based on grain detection and pixels. The misorientation angle delimitation was the first step in detecting the grains in a selected area. After this, the detected grains were ordered according to phase criteria. The misorientation angle and a minimum grain area were used to define the grain criteria. The misorientation angle criteria were equal to or greater than 5°, and the minimum grain area criteria were higher than 0.4 μm^2 or 10 pixels.

The separation of phases carries through the following steps. Firstly, retained austenite was identified with the FCC crystal structure; the EBSD detected this structure automatically. Figure 59 shows the retained austenite in green colour using the FCC filter. Then, the process continues with the martensite; this phase has a body-centred tetragonal (BCT) crystal structure. The carbon content determines the lattice parameter of martensite. Nevertheless, the BCT structures cannot be detected in the EBSD. Thus, the BCT structure is indexed as a BCC structure with distortions. As a result of this distortion, the BCC structure shows a poor-quality pattern.

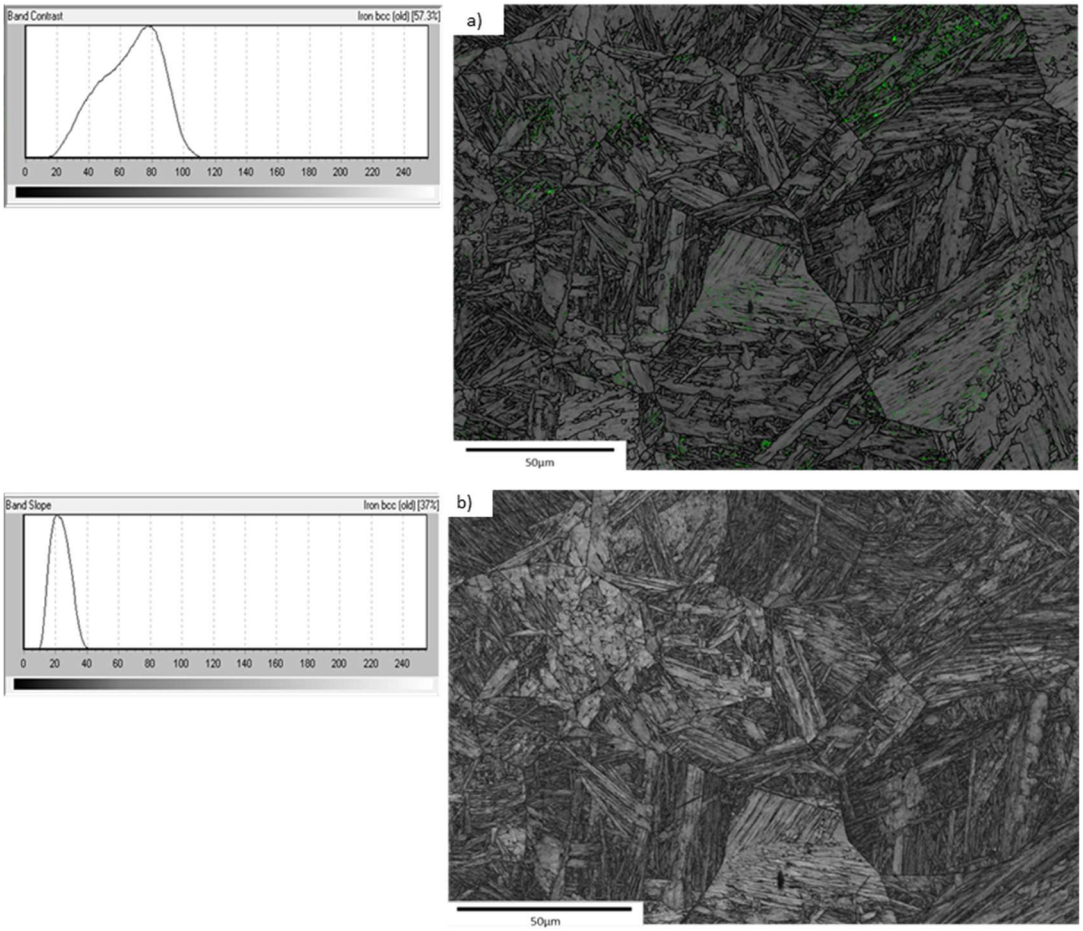

Figure 59 a) Band contrast map and b) Band slope map, Grain boundaries > 5° of X80 steel using a holding temperature of 1100°C and cooling rate of 50°C/s and their pixel distribution.

To continue with the phase discrimination, it was used a threshold value. This value was applied in the BC and BS maps to separate the martensite of the other BCC structures. BC and BS maps are constructed per pixel, meaning that an interval of BC and BS values does not have any grains. Therefore, all the pixels inside the grains are averaged to determine the BC or BS grain value. Following the previous criteria of BC and BS maps, dark grains are classified as martensite, while shiny grains are associated with ferrite[94]. The division of martensite from ferrite was done with the BC average distribution in each subset [95,96]. Figure 60 illustrates the grain averaged BC map with its distribution in the sample at 1100°C and 50°C/s of cooling rate, and the grain boundaries equal to or greater than 5° appear in green.

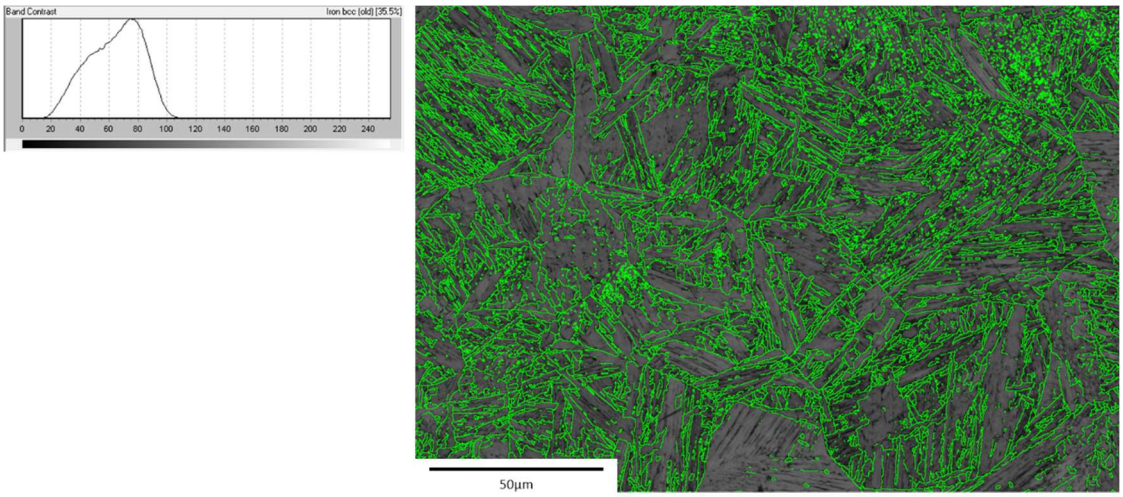

Figure 60 Grain averaged BC map of 1100°C and cooling rate of 50°C/s, green lines indicate the grain boundaries greater than 5° and its distribution.

After separating martensite from ferrite, the process continues with bainite from ferrite separation. One of the criteria to separate the bainite ferrite from the polygonal ferrite is the dislocation density associated with defects inside the grains. Another way to distinguish bainite ferrite from polygonal ferrite in EBSD maps is by using a grain orientation spread (GOS) filter. GOS is associated with the change of orientation degree between each pixel inside the grain and the average misorientation inside the grains[97]. Figure 61 illustrates the grain orientation spread map and distribution in the sample at 1100°C of austenitisation temperature and 50°C/s of cooling rate. Thereby, when the grain shows a high value of GOS, there is a high misorientation level inside that grain. The high level of misorientation indicates that the phase keeps numerous defects, but it could be a result of the displacive transformation associated with the bainite.

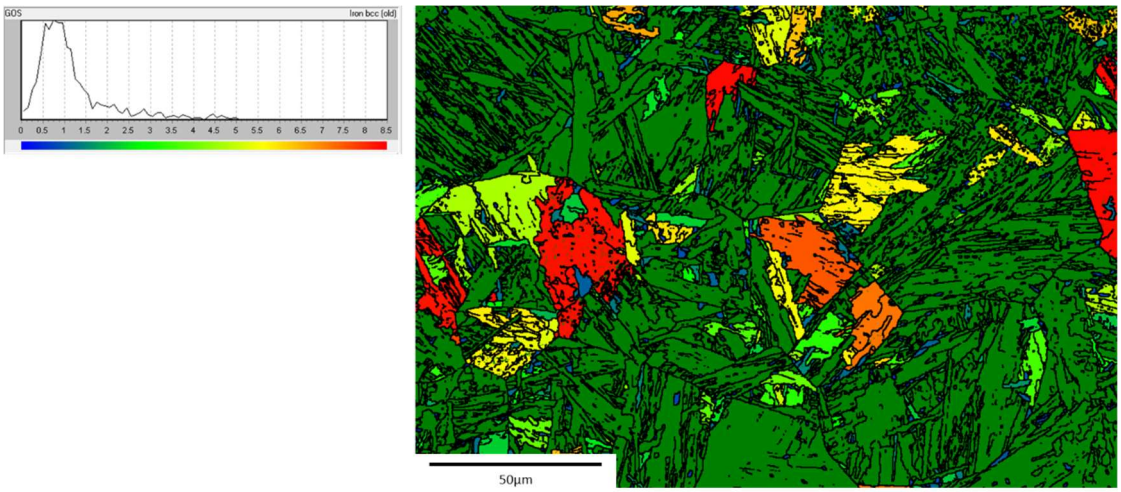

Figure 61 Grain orientation spread map of 1100°C and cooling rate of 50°C/s sample and the distribution histogram

The low grain orientation spread map shows an absence of internal misorientation inside the grain; this is a common feature of polygonal ferrite because it maintains a clear and well-organised phase. Figure 62 shows a minimum misorientation of 2° in low-angle grain boundaries; the grain boundaries appear in blue. The bainite ferrite substructures are related to a misorientation of 2° in grain boundaries; at the same time, this matches with the high values of grain orientation spread[98,99]. Depending on the GOS distribution, it is possible to separate the bainite ferrite from the polygonal ferrite. The GOS value in deformed samples has an interval between 1 and 1.25, while in non-deformed samples depends on GOS distribution[100,101]. Moreover, another difference between polygonal ferrite compared with bainite and martensite is the low aspect ratio[102]. Additionally, the GOS map was added to the grains with an aspect ratio restriction; thus, the polygonal ferrite grains are restricted to a maximum of 1.7 aspect ratio. The low GOS value in the grains (blue) is related to a higher low aspect ratio or equiaxed shape and maintains a small grain size.

Figure 63 shows the inverse pole figure map (IPF) at 1100°C and a cooling rate of 50°C/s sample. The maps did not show a defined texture orientation in one direction of the BCC structure. This non-defined texture did not exist because the material was not deformed; if the material were laminated, the texture direction must be [111] in the BCC structure.

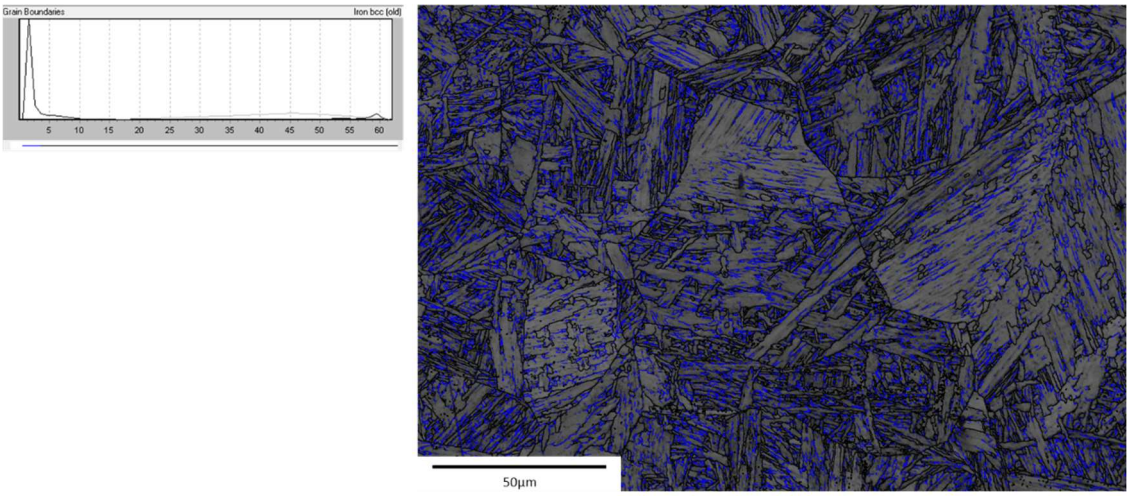

Figure 62 Grain boundaries misorientation map of 1100°C and cooling rate of 50°C/s with their distribution. Blue lines represent 2° to 5° of misorientation, and black lines represent misorientation higher than 5°.

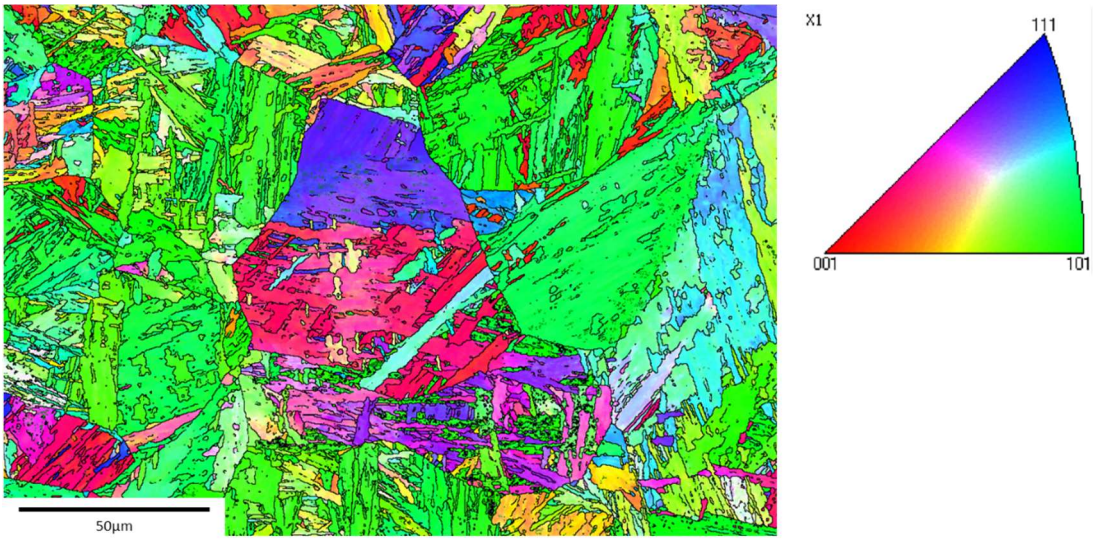

Figure 63 Inverse pole figure map of 1100°C and cooling rate of 50°C/s sample and their orientation legend.

3.7 Transmission Electron Microscopy (TEM)

A transmission electron microscope was used to observe the distribution and size of precipitates. A JEM-F200 microscope by the JEOL manufacturer was used in the analysis. Table 9 illustrates the equipment capabilities. In order to observe the precipitates in the TEM, a carbon extraction replica technique was used, which will be explained in the next point.

Table 9 JEM-F200 specifications and capabilities[103].

Resolution	Point to point	0.19nm
	TEM lattice image	0.10 nm
	STEM HAADF image	0.14 nm
Magnification	TEM	20X to 2,000,000X
	STEM	200X to 150,000,000 X
Electron gun	Schottky field emission gun	
Acceleration voltage	20 to 200 kV	
Tilt angle	± 80°	

Carbon extraction replica

Carbon extraction replicas were used to reveal the precipitates in different microstructures. In the extraction replicas, the changes in size and distribution of precipitates can be observed. Using this technique, the precipitates hosted on the surface are extracted from the sample by the addition of a carbon layer on the surface. Then, the carbon replica is dissolved with nital 10%. Finally, the sample is submerged in isopropanol until the carbon layer floats in the solution. Then, the film is taken with a 3.05 mm diameter mesh support grid. Figure 64 shows the representation of the process. The carbon replicas films allow us to observe the extracted particles in the matrix.

The carbon extraction replica starts with polishing, this process is done using the parameters described in Table 7. After that, the samples are etched with Nital 2% in a slightly way avoiding an overetching. The etching reveals the microstructure and the precipitates. Following this, carbon is obtained with a carbon coater; this equipment operates at a high vacuum. The carbon film must be from 6.5 to 7.0 nm, that layer allows to distinguish the precipitates in the TEM. Afterwards, the sample is covered with varnish in the zones that will not analyse.

Also, to extract the replica is necessary to do a grid using a precision cutter ticking squares around 1 mm x 1 mm. Then, the samples were etched with Nital 10% until the carbon replica was released from the steel surface, after which the sample was submerged in isopropanol enabling the replica to float to the surface. Finally, the carbon replicas were picked up using the Copper/Palladium mesh support grid.

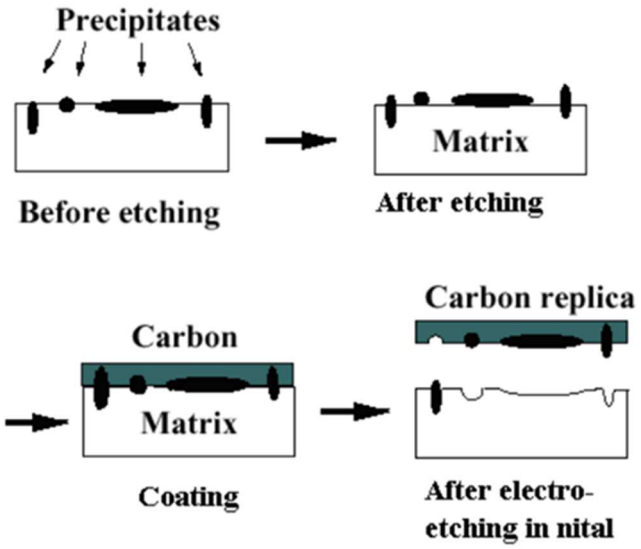

Figure 64 Representation of carbon extraction replica technique[104].

The carbon replicas were observed at different magnifications in the JEM-F200. After that, the images were analysed at different austenitisation temperatures and cooling rates to visualise the effect of those parameters in the precipitates.

3.8 Critical temperatures of transformation

Transformation temperatures are an important part of steel characterisation. Critical temperatures are necessary to understand the phase transformation of austenite grains and the subsequent effect on the mechanical properties. Also, the transformation temperatures are affected by heating/cooling rate. When the heating rate is increased, the A_c temperature elevates as well. While the cooling rate has the contrary effect, high cooling rates decrease the Ar temperature[105]. A_c and Ar temperatures are not only influenced by heating and cooling rates. Also, the transformation temperatures are affected by chemical composition and prior austenite grain size of the material [37].

3.9 Simulation Software

To obtain the CCT Diagrams was used the JMatPro Software (Java-based materials properties acronym). JMatPro is utilised in the calculation of phase transformation temperatures and the CCT diagram. Additionally, the software calculates different properties such as Young´s modulus, thermal conductivity, volume fraction and the Poisson's ratio in each phase[106]. In the evaluation of the CCT diagram, it is necessary to introduce the chemical composition, austenite grain size and temperature of austenitisation.

To determine the CCT diagrams, the software is based on the model of Kirkaldy et al [107]. JMatPro uses the the Kirkaldy model in the transformation calculus of ferrite, pearlite and bainite in HSLA steels [106,108]. The general formula to determine the time (τ) to transform an austenite fraction (x) at Temperature (T) is shown in Equation 13 [109].

$$\tau(x,T) = \frac{1}{\alpha(N) D_{eff} \Delta T^{q}} \int_{0}^{X} \frac{dx}{x^{2(1-x)/3} \, (1-x)^{2x/3}} \qquad 13$$

Where:

$\alpha = 2\beta^{(N-1)/2}$,

β = empirical coefficient

N = ASTM Grain Size

D = effective diffusion coefficient

ΔT = difference in temperature

q = exponent depending on effectiveness in the diffusion mechanism

3.10 Temperatures of phase transformation

Dilatometry is used to measure the volume changes which takes place as a function of the temperature. Usually, it is used on small samples to determine phase transformation and thermal expansion coefficients. Dilatometry measures the change of length in the material as a consequence of volume change in the transition zone. During the test, it is used a specific heating and cooling rate. Dilatometry is also used in the analyse of structural defects such as dislocations, vacancies and grain boundaries. This technique has the clear advantage of simplicity during testing and the consequent interpretation of results [110,111].

Figure 65 illustrates a dilatometry curve in a carbon steel with a chemical composition of 0.58% C, 0.024% P, 0.92% Mn, 0.033% S, 0.25% Si [110,111]. The curve illustrates the contraction in volume during heating and expansion upon cooling. During heating, the contraction in the expansion rate indicates the change from the more openly packed bcc phase (ferrite) to the more closely packed fcc phase (austenite). The opposite effect appears during cooling where the expansion in volume indicates the change from the fcc to the bcc phase.

The dilatometers have different devices to support the testing which are divided into control and mechanism. The thermal cycles are controlled by a computer which it is used to store and export the data. The dilatometry uses a cooling and heating mechanism to keep the thermal cycle programme, also it makes use of transducers to measure temperature, time and change of length during testing (Figure 66)[111]. During the cooling cycles, helium is normally used to enable high change rates because the helium thermal conductivity is six times that the nitrogen. The testing with steel normally uses an inert atmosphere chamber to decrease the decarburisation and oxidation degree [112].

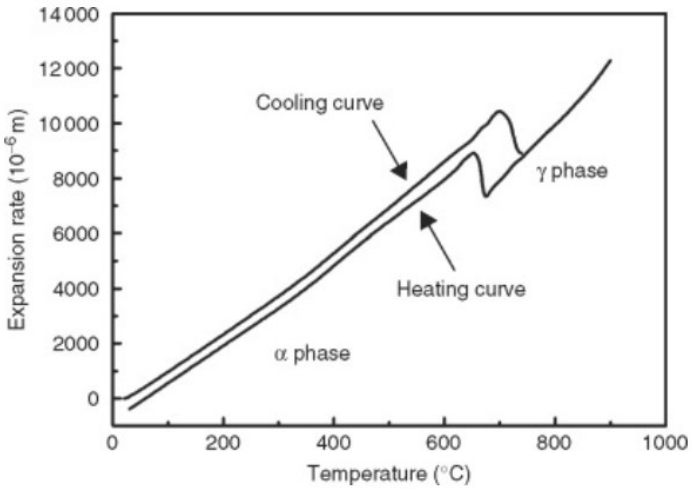

Figure 65 Expansion rate variation in a carbon steel[110].

Dilatometry testing was performed using a Gleeble 3800. The test was done in the Research and Development Laboratories of Ternium Mexico. The equipment works with a system of direct resistance with an inert gas chamber during the test. The cooling system is through the clamps which are manufactured with copper. Prior to testing, thermocouple was welded in the middle of the sample using a K-type thermocouple. The equipment measures the temperature setpoint every 0.005 seconds allowing high accuracy during the test. To measure the length change uses a sensor of displacement. Figure 67 shows the dilatometer mechanism utilised in the measurement of length change.

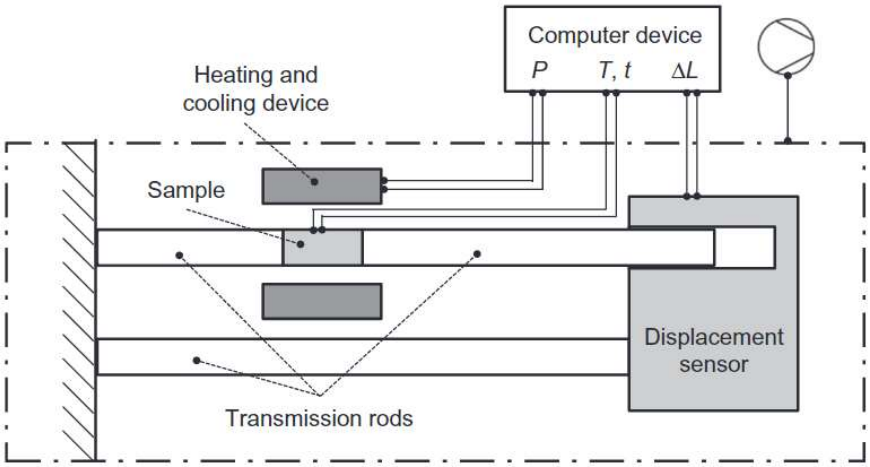

Figure 66 Diagram of rod system dilatometer for measurement of length [111].

Figure 68 illustrates the sample drawing of dilatometry. The sample consists of a cylindrical bar with holes in the extremes to communicate the cooling through the copper clamps. The length of the sample is in the same orientation as rolling direction. The measured area of the thermal expansion is located in 5 mm in diameter and 5 mm in length. The small dimension allows us to measure quick temperature changes [112].

The experiment was conducted to assess how the cooling rate and prior austenite grain size influence the transformation behaviour of the material. Dilatometry testing was used to determine the transformation temperatures during both heating and cooling phases at various cooling rates. The transformation temperatures are directly affected by the cooling rates and prior austenite grain size. In all samples, the heating rate was maintained at 10°C/s. The test started at room temperature, it was selected at three cooling rates and two austenitisation temperatures. The cooling rates were 0.5, 5 and 50°C/s. The austenitisation temperatures were 900°C and 1200°C, those temperatures allow us to analyse the effect of those temperatures on fine and coarse prior austenite grain size. It is expecting a linear behaviour in transformation temperatures during cooling according to Yuan and Mintz calculations[113,114]¹¹⁴¹¹⁴. To obtain a homogenised temperature and microstructure was selected for 12 min of holding [115]. Figure 69 illustrates the heat treatment performed in the dilatometry test.

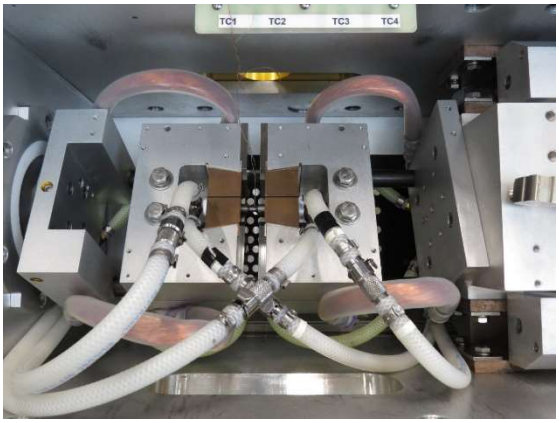

Figure 67 Gleeble 3800 dilatometer utilised in the measurement of phase transformation.

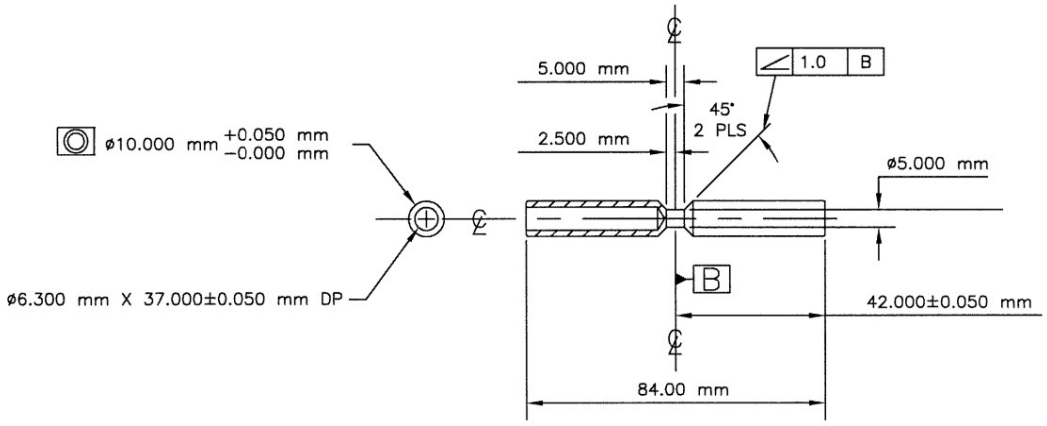

Figure 68 Drawing of dilatometry sample used in the testing.

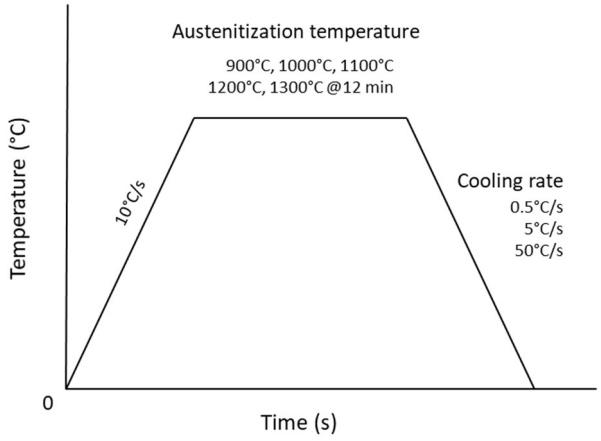

Figure 69 Heat treatment schematic used in the dilatometry test.

3.11 Prediction of transformation temperatures

Empirical formulas are used to approximate transformation temperatures quickly. Chemical composition, cooling rate and austenite grain size are parameters used in the formulas by several authors. Table 10 shows equations to calculate Ac_1, Ac_3, Ar_1 and Ar_3 utilised during the experiments. Section 4.2 will report the variation between the experimental transformation temperatures and the prediction equations of transformation temperatures.

Table 10 Equations of austenite transition temperature by various authors (weight in %).

Author	Equation	Notes
Andrews[116]	Ac_1=723-20.7Mn- 6.9Ni+16.9Cr+290As+6.38W Ac_3=910-203$\sqrt{C}$-15.2Ni+44.7Si+104V+31.5Mo+13.1W	
Trzaska[117]	Ac_1=742-29C-14Mn+13Si+16Cr-17Ni-16Mo+45V+36Cu Ac_3=925-219$\sqrt{C}$-7Mn+39Si-16Ni+13Mo+97V	
Eldis [118]	Ac_1=712-17.8Mn-19.1Ni+20.1Si+11.9Cr+9.8Mo Ac_3=871-254.4$\sqrt{C}$-14.2Ni+51.7Si	
Choquet [119]	Ar_3=902-527C-62Mn+60Si	
Ouchi [120,121]	Ar_3=910-310C-80Mn-20Cu-15Cr-55Ni-80Mo+0.35(h-8)	h=thickness plate (mm)
Shiga [122]	Ar_3=910-273C-74Mn-56Ni-16Cr-9Mo-5Cu	
Yuan [113]	Without hot deformation Ar_3=370exp$\left[-\frac{\sqrt{D_\gamma}}{6.7}\right]$-$325C_R^{0.1} - 5649Nb + 78194Nb^2 + 1019$	D_γ=grain diameter of austenite (μm) C_R=Cooling rate (°C/s)
Mintz [114]	Ar_3=833.6-190.6C+67.4Mn+1522S-2296N_{Ti}-1532Nb+7.91$d^{-1/2}$- 0.117C_R	D_γ=grain diameter of austenite (μm) C_R=Cooling rate (°C/s) $N_{Ti}=N_t$ - $\frac{Ti}{3.5}$ where N_t= total content of nitrogen

3.12 Austenite heat treatment

The austenite grain size required a heat treatment to reveal the grain borders. To reveal the grain borders was used quenching. In this treatment, the samples were heated up at 900°C, 1000 °C, 1100°C, 1200°C, 1280°C and 1300°C for 30 min in a furnace [115], and then it was immediately thrown in the water to obtain martensite. At 1280°C, it is expected that all the niobium precipitates are dissolved. The samples were cut into 12mm x 12 mm x 30 mm. The holding time was selected to homogenise the transversal area and have a uniform grain size. A thermocouple was located inside the furnace chamber to control the temperature.

3.13 Thermomechanical testing

The heat treatment simulation was done in the thermomechanical compression (TMC) machine at The University of Sheffield. The TMC was utilised only to perform the heat treatment without any compression. The machine works with a servo-hydraulic system. The equipment controls different parameters such as: displacement, velocity, temperature, holding times and heating/cooling rates. TMC works with a Fast-Thermal Treatment Unit (FTTU), this system is used to control the temperatures during the heat treatment. FTTU consists of two devices, the first is an induction coil heater and the other is a cooling control. The cooling control uses air, water or mist to force the temperature reduction. Figure 70-a illustrates the TMC machine and Figure 70-b the sample during the heating in the FTTU. The TMC specifications are shown in Table 11.

a) b)

Figure 70 a) Thermomechanical controlled processing machine. b) Sample in the FTTU chamber.

Table 11 TMC specifications of temperature, FTTU and hydraulic system[123].

	Machine characteristics
Actuators	Servo-hydraulic
Maximum strain	-2
Maximum strain rate	150 - 200 1/s
Maximum deformation temperature	1200°C
Maximum load	500 kN
Machine stiffness	410 kN/mm
Maximum FTTU reheating temperature	1300°C
Full quench start time	< 0.5 seconds from the end of deformation
Controllable cooling variables	Forced air, mist and water quench
Reheating rate	Rapid and controlled heating (up to 1300°C)
Atmosphere control	None (natural air)
Temperature measurement	Up to 3 thermocouples inside in the PSC sample

Figure 71 illustrates the plain strain compression sample (PSC) used in the TMC machine. The sample was machined with the 60 mm length parallel to the direction of plate rolling. The sample has a drilled hole in the middle of the sample. The thermocouple was positioned in the hole, located 10 mm from the surface. The equipment registers the temperature every 0.20 seconds. It was used a thermocouple type K in all the testing.

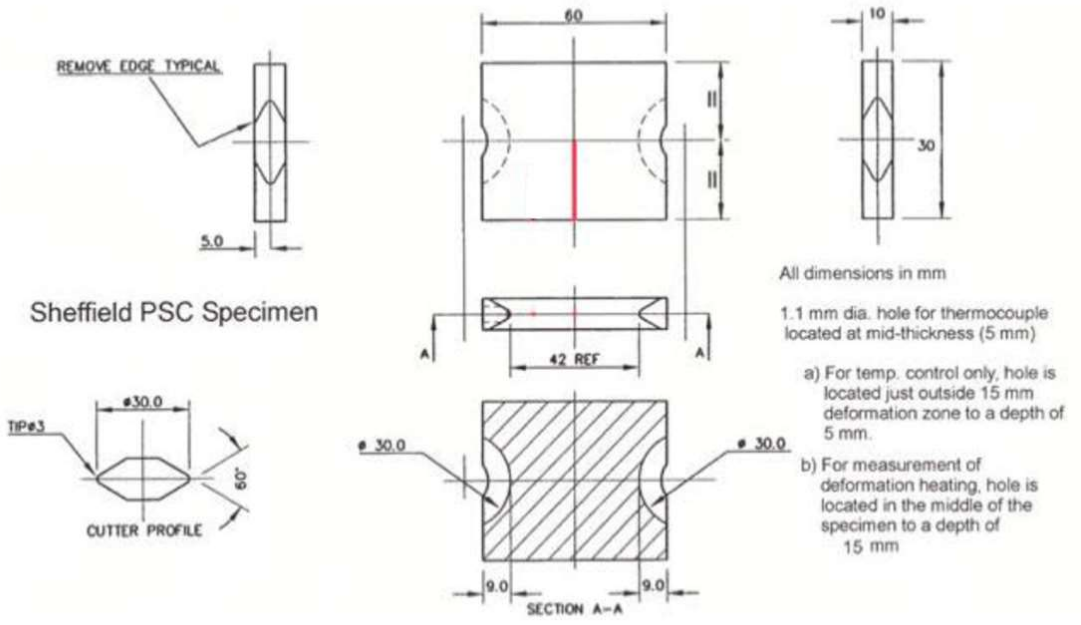

Figure 71 Drawing of PSC sample used in the TMC machine.

3.14 Heat treatment simulation

To simulate heat treatment conditions in the thermomechanical controlled processing machine was used plane strain compression testing (PSC). This testing is normally used to simulate deformation on a flat surface in hot conditions. However, it was used during the experiments to simulate the heat treatment because the control of temperature is extremely accurate in the test. Figure 72 represents the PSC diagram and how the sample is located inside the FTTU chamber.

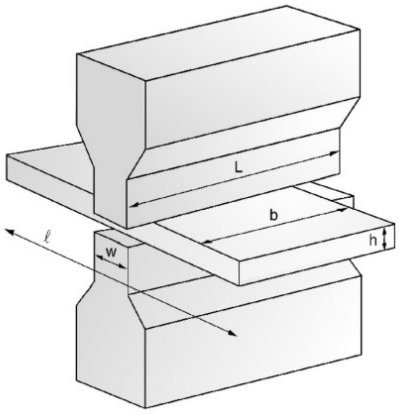

Figure 72 Diagram of plane strain compression used in the testing [124].

Figure 73 shows the heat treatment diagram used in the PSC testing. The heating rate was 10°C/s, to homogenise the microstructure was selected a holding time of 30 min. With that holding time, it is possible to complete the phase transformation from bcc to fcc [115]. In the design of the thermomechanical route was considered the interval of heat affected zone (HAZ) temperatures. In the HAZ, the recrystallised zone has a range of temperatures from 900 to 1100°C, while the grain growth zone includes temperatures from 1100 to 1500°C. As the TMC has a temperature limit of 1300°C, austenitisation temperatures between 900°C and 1300°C were used.

In the cooling process, three different temperatures were selected. The cooling temperatures were 0.5, 5 and 50°C/s. To obtain 0.5 and 5°C/s was used air cooling while to achieve the cooling rate of 50°C/s was used air-water mist. Those cooling rate temperatures are used to analyse the microstructure behaviour in the two ways of crystal atomic partition. Those mechanism transformations are reconstructive and displacive. In the process design, it was obtained 15 different heat treatments allowed us to observe the microstructure evolution and the effect on mechanical properties.

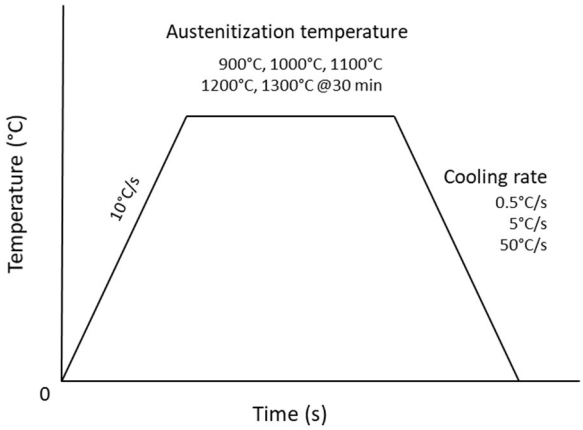

Figure 73 Heat treatment schematic in the thermomechanical processing test.

3.15 Characterisation after heat treatment simulation

In the characterisation of PSC samples, it was necessary to remove 0.045 mm from the surface of the sample because of decarburisation. In high temperatures above 1200°C, samples were more affected by the decarburisation[125]. The removal of material was used to avoid misleading measurements in the mechanical properties testing. To characterise the material was used an area near the thermocouple hole. The thermocouple hole is located at 10 mm of the surface. Figure 74 shows a PSC sample after the heat treatment.

Figure 74 PSC sample after the heat treatment, the sample was processed at 1300°C and 5°C/s of cooling rate.

3.16 Evolution of microstructure

During this analysis, the evolution of microstructure was quantified through different austenite grain sizes and cooling rates. PSC samples were heat treated according to the profile illustrated in Figure 73. After the testing, the samples were cut according as described in Section 3.15. The first analysis was done in optical microscopy. Then, the samples were reviewed in SEM described in Section 3.5. After that, it was done the EBSD analysis, in this test was used 5 x 5 x 11 mm area, and the samples were polished according to Section 3.6. The volume fraction was performed in EBSD software according to the Section 3.6.1. Then, the precipitates were analysed in the TEM with the carbon replica extraction technique. This sample preparation was utilised in the procedure of Section 3.7.

To measure the austenitic grain size was used the procedure of Section 3.12. Etching using the aqueous solution of saturated picric acid was used to reveal the grain boundaries. Then, the dilatometer was used to evaluate the transformation temperatures, this technique was utilised according to Section 3.10. In the end, it was tested different mechanical properties such as hardness, tensile test and impact test. The impact test includes different test temperatures to evaluate the behaviour in freezing conditions. The mechanical properties will be described in the next section of this Chapter.

3.17 Mechanical Properties

Hardness testing

Hardness is a useful method to quickly determine material strength. The pyramid indentation shape was used in this test. To measure the Vickers microhardness was utilised the Durascan 70 equipment. The load was 1 kg_f, this force is equivalent to HV1. The samples were polished according to Section 3.3, and it was performed by making 12 indentations in each sample. The ASTM E384-17 [126] standard was used to determine the indentation distribution. Figure 75 illustrates the pyramid indentation shape and the recommendation of space distribution.

The Vickers microhardness value (V) is obtained with the load (P) in kilograms divided by the contact area (Ac) printed in mm^2. To calculate the area is used the mean diagonal d_1 (Equation 14). To measure the indentation was used a light microscope image. The Durascan 70 is equipped with a filar micrometre that allows measuring the diagonal.

$$V = \frac{P}{A_c} = \frac{1.854P}{{d_1}^2} \qquad 14$$

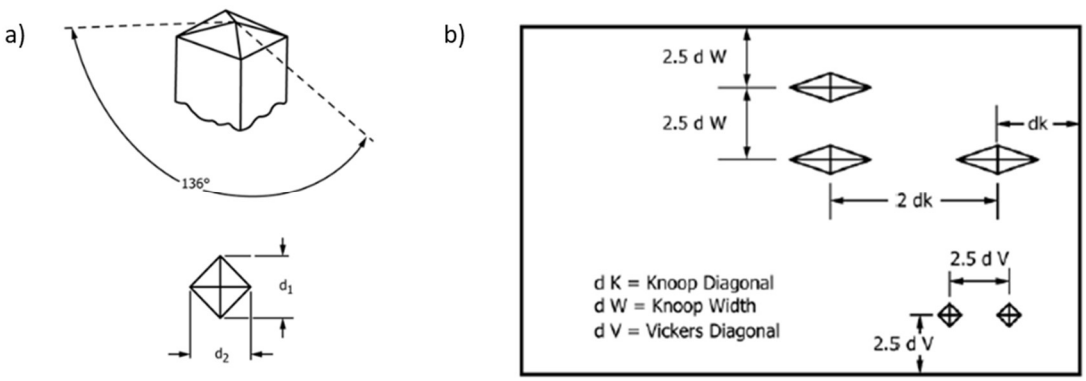

Figure 75 a) Shape of Vickers pyramid indentation, b) Minimum space between indentations according to the standard ASTM E384 - 17 [126].

Tensile testing

The tensile test is one of the most important destructive tests used for evaluation of mechanical properties. The test uses a specific velocity of deformation until the specimen fails. The sample is fixed through clamps in the extremes where the tension force is applied. During the test, the deformation is measured in the centre (gauge length) of the sample using a video extensometer, and the force is measured through the cell. Following thermal processing, tensile bars were machined from the PSC samples, where the tensile axis was parallel to rolling direction. The samples were machined according to Figure 76-a. Electric discharge machining (EDM) was used to avoid the machining heat affecting the microstructure of the samples. Also, the EDM affords strain free cutting during the process.

Tensile testing was performed using a Zwick Roell machine model Z050 kN, using the 50kN load cell. Samples were fixed to the crosshead and test frame using a modified Zwick Roell grip. The grips have a modification which consists of clamps type "U" with 4 bolts in the extremes. The clamps put pressure on the sample and do not allow slip during the testing. The possibility of slip during testing is more likely as these test samples are sub-sized according to the ASTM standard. With the addition of clamps type "U", any slip that may have occurred is avoided (Figure 76-b). Figure 76-c illustrates the machining orientation to obtain the tensile samples through the PSC sample. The thickness of the PSC sample was 10mm; however, before the tensile sample machining, the oxidation was removed (~1mm).

An optical extensometer was used to measure the elongation along the gauge length. To have a reference was used 2 wires glued in the middle of the tensile sample. This gauge length was measured as 11±1 mm (Figure 77). During the tests, a video extensometer was used to measure the gauge length. The tensile samples are shorter than the sub-sized standard ASTM E8. Because of this, the crosshead velocity was changed according to the standard. To determine the yield strength in a closed loop control system, it was utilised the video extensometer signal. The ASTM E8 specifies a straining rate set velocity, which should held at $0.015\ ^{+.006}_{-.006}$ mm/mm/min[127]. In the testing, the crosshead speed was 0.18mm/min in all the samples. At the initiation of the test, the cross-section was measured with a digital caliper.

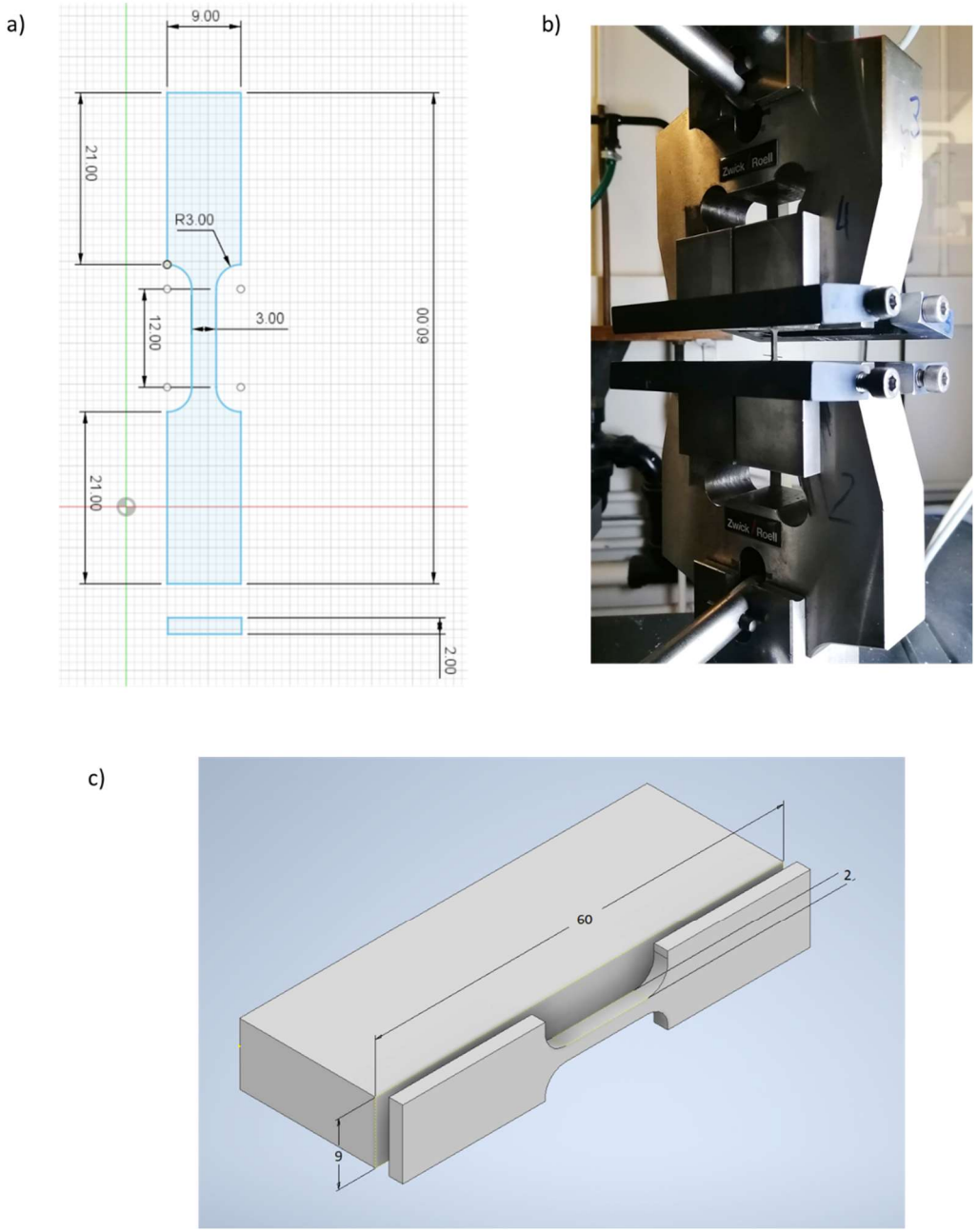

Figure 76 a) Drawing of tensile samples used in the testing b) Grips with clamps type "U" to avoid slipping during the test, c) PSC sample machining orientation to obtain the tensile specimen.

The machine registers the load and gauge extension during the test. With this output data, it is possible to obtain the engineering stress (σ) and engineering strain (ε) (Equation 15 and 16). Where the tensile load is P, the initial area is A_0 (Eq 15), and L_0 and L_f are the initial and final gauge lengths (Eq 16).

$$\sigma = \frac{P}{A_0} \quad (15)$$

$$\varepsilon = \frac{L_f - L_0}{L_0} = \frac{\Delta L}{L_0} \quad (16)$$

The flow stress engineering curve was calculated with the output data. This curve permits obtaining a variety of mechanical properties such as yield stress (YS), elastic modulus (E), tensile strength (TS), total elongation (e_t), area reduction (a_r) and uniform elongation (e_u). To calculate the yield strength, a line is drawn originated at 0.2% strain that is parallel with the elastic modulus. The point where this parallel line intersects with the engineering stress-engineering strain curve represents the yield stress. For the tensile stress, it will be indicated by the maximum stress, prior to the drop-in stress due to the development of a triaxial state of stress in the form of a reduced cross section. Equation 17 represents the percentage of elongation increase (%El) and Equation 18 illustrates the percentage reduction in the cross-section area ($\%R_A$).

$$\%El = \frac{\Delta L}{L_0}\ x\ 100 \quad (17)$$

$$\%R_A = \frac{A_0 - A_f}{A_0}\ x\ 100 = \frac{\Delta A}{A_0}\ x\ 100 \quad (18)$$

Where A_f represents the cross-section area at the fracture zone.

Figure 77 Tensile sample before and after the test, the scale is represented in centimetres.

Impact testing

The impact test is used to determine the capability of a material to absorb energy during fracture. The Charpy test is the standardised method to measure the absorption of energy. The test utilises a pendulum with a standard weight and length which drops from a distance to impact the sample. The sample is machined with a "V" notch in the middle. The transferred energy to the sample is measured by comparing the height change in the hammer after the fracture.

Charpy impact testing was performed using a Zwick Roell model HIT50P, using a 50J pendulum. The standard ASTM E23-18 was used to machine the samples[128]. The samples were machined according to a quarter sub-size Charpy with a thickness of 2.5 ± 0.025mm. The width was modified to 9.1 mm because the PSC sample does not have enough area, and the length was machined 57.5 $^{+2.5}_{-0.0}$ mm (Figure 78). Electric discharge machining (EDM) was employed to cut the samples, mitigating the effects of heat during machining. The reduction in width will result in decreased energy absorption, although all the samples will be machined to the same dimensions, enabling a comparison of energy absorption across all possible heat treatments.

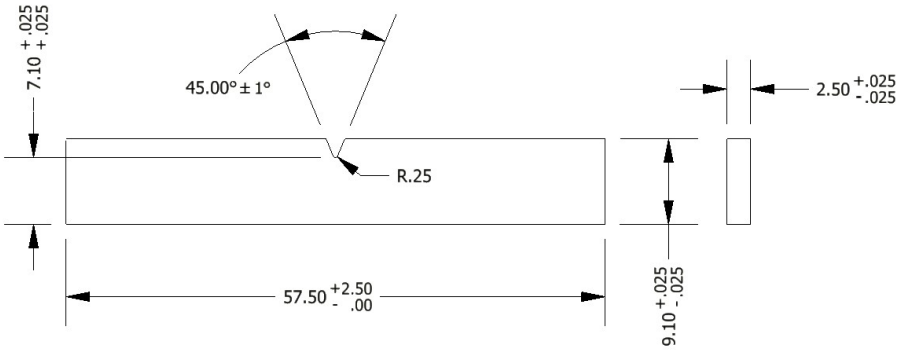

Figure 78 Drawing of sub sized Charpy sample used in the impact test [128].

At lower temperatures, the steel is characterised by embrittlement. In the test, it was used 3 temperatures to analyse: 20°C, 0°C and -50°C. The temperature tolerance during the test was ± 1°C. To achieve the 0°C was used only ice, while it was utilised a cooling bath to obtain -50°C [129]. The cooling baths consist of a mixture of solvent with a cryogenic agent such as ice, dry ice (CO_2) or liquid nitrogen. To obtain -50°C, it was blended dry ice with m-Xylene (thinner) and the temperature mixture was monitored with a thermocouple type "K". To obtain the testing temperature, it was used a recipient with the thermocouple at the bottom. After that, the dry ice was added (-78°C), and then m-Xylene was slowly aggregated until -50°C was reached (Figure 79).

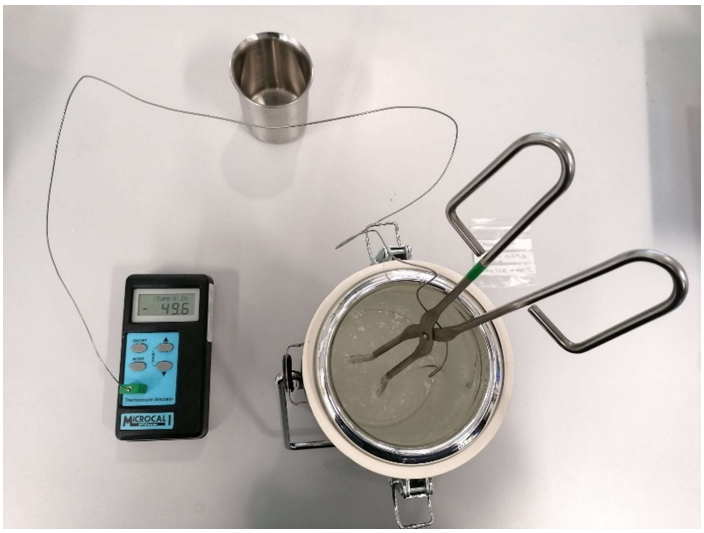

Figure 79 Cooling bath using a mixture of dry ice and m-xylene at -49.6°C.

Summary

Chapter 3 explains the experimental procedure utilised in the present work. This chapter starts with the chemical composition of the material and dimensions. It continues with the different metallurgical techniques, starting with nital and saturated picric etching, measurement of prior austenite grain size and the characterisation in different microscopes such as optical, SEM, EBSD and TEM. Then, it describes the critical temperatures using dilatometry and empirical formulas. Afterwards, it explains the heat treatment simulation using the PSC samples. Finally, it describes the mechanical testing utilised for the measurement of mechanical properties, including microhardness, tensile and impact.

Chapter 4

Results

4.1 Initial Characterization

The X80 steel was characterised by optical microscopy and SEM on sections that were transverse to the rolling direction. The general microstructure was characterised using 2% nital (Figure 80–81). The microhardness value of the material was 231±4.1HV. The microstructure showed an acicular ferrite (AF) as the dominant microstructure. Figure 80 shows the microstructure in the optical microscope, and Figure 81 illustrates the microstructure in the SEM. Figure 82 illustrates the distribution of precipitates in the carbon extraction replica. Non-equiaxed ferrite laths were observed in a disorganised arrangement; this microstructure is characteristic of acicular ferrite (AF). High cooling rates are necessary to obtain an AF microstructure. PAGS was measured using the ASTM E112-13 standard[90] utilising the linear intercept method. PAGS of the raw material were 3 ± 0.17µm (Figure 83).

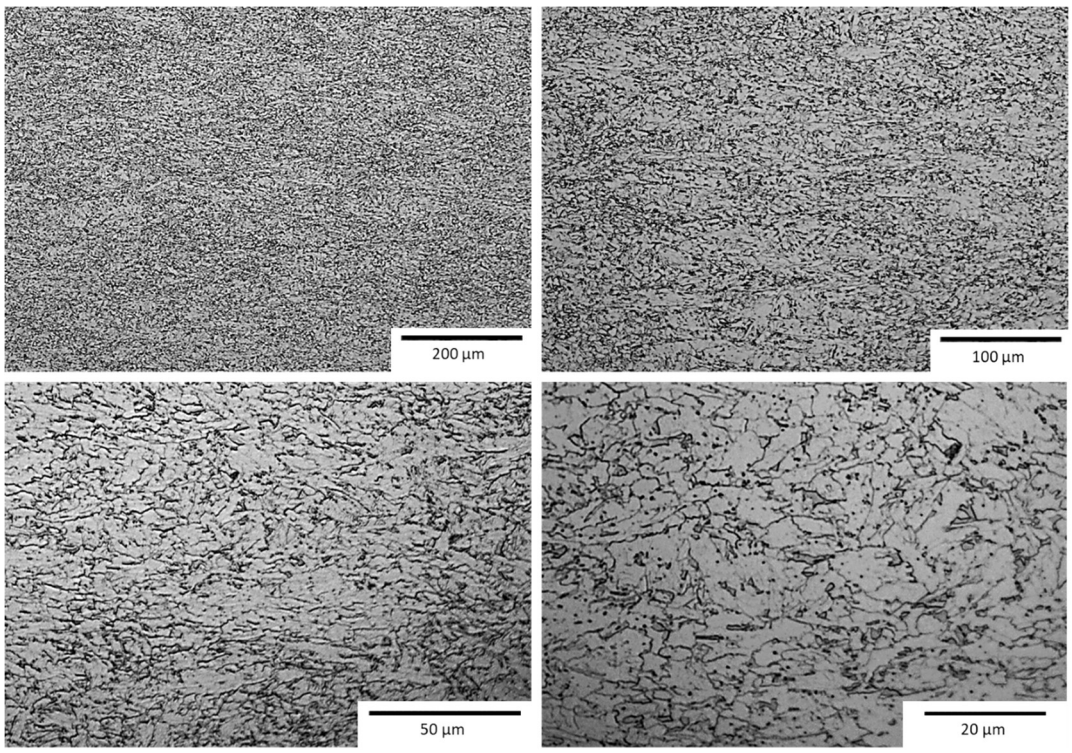

Figure 80 Initial X80 steel microstructure, etching with 2% nital.

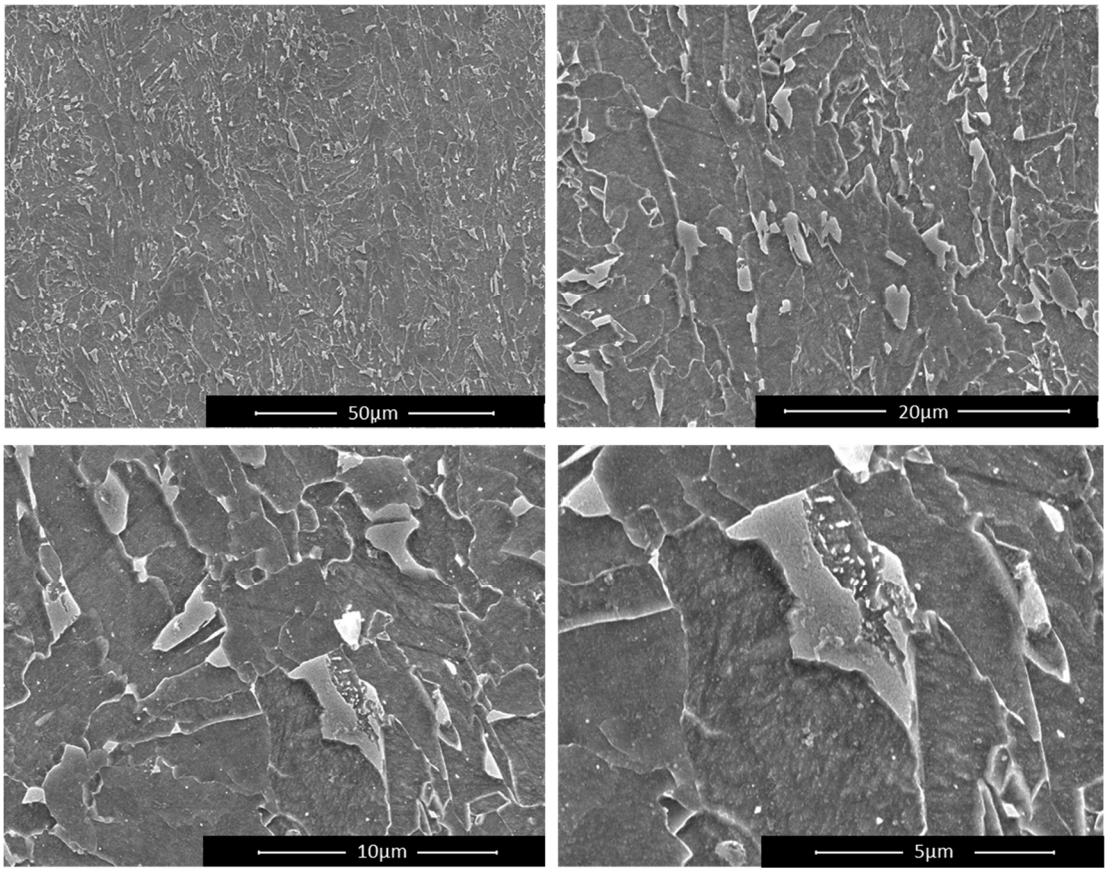

Figure 81 X80 microstructure in SEM.

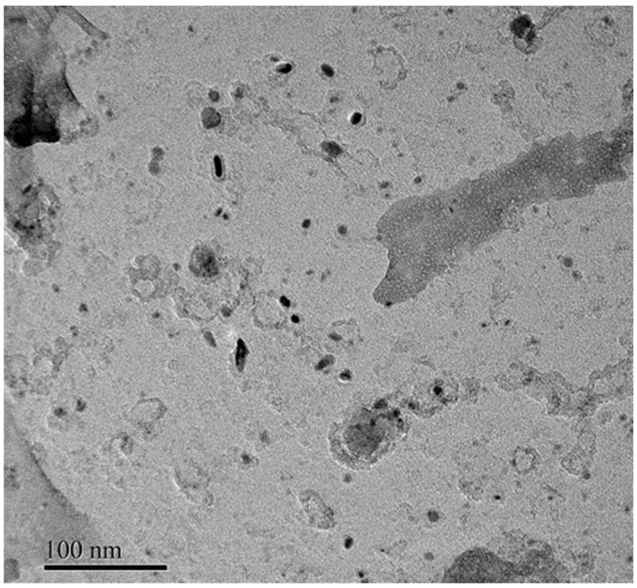

Figure 82 Carbon extraction replica acquired in the X80 steel.

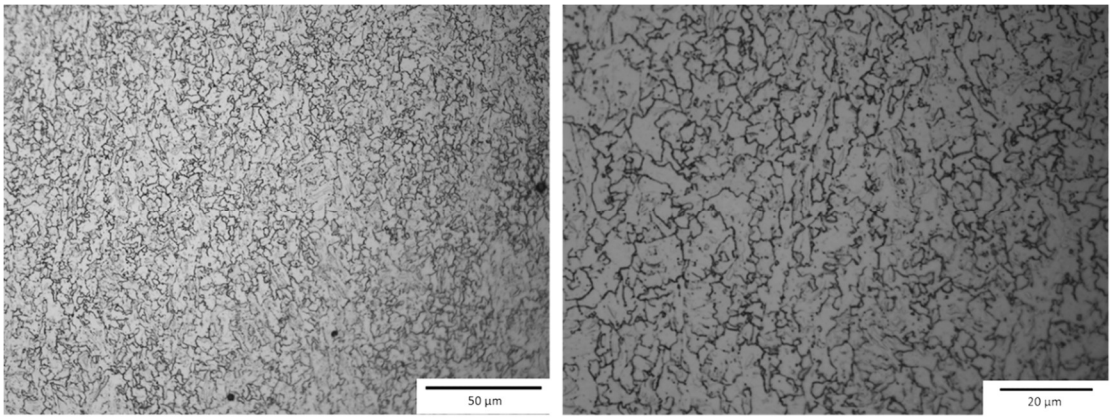

Figure 83 Prior austenite grain size of the X80 steel.

Figure 84 shows the macrostructure of the welding; the sample was polished until 1µm and then etched with nital at 2% [130]. Different zones in the welding were observed. First, the filler material obtained at fusion temperatures appears in the middle of the welding. Then, two zones were observed next to the fusion zone, this is associated with the coarse austenite and fine austenite growth zone. Finally, after the end of those shadows, a partially recrystallised zone appeared.

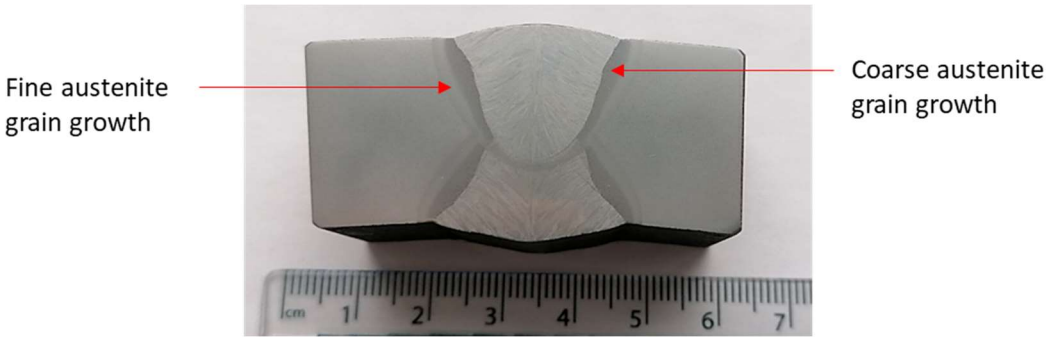

Figure 84 HAZ macrostructure etched with nital 2%

After the microhardness measurements were performed, the material was etched with Nital 2%. Following this, the microstructure evolution in the HAZ was observed using the optical microscope. Figure 85 illustrates the microhardness pattern in the welding showing three clear zones: base material, heat affected and welding zone. The analysed zone was 10mm long, and representative microstructures were obtained in each area.

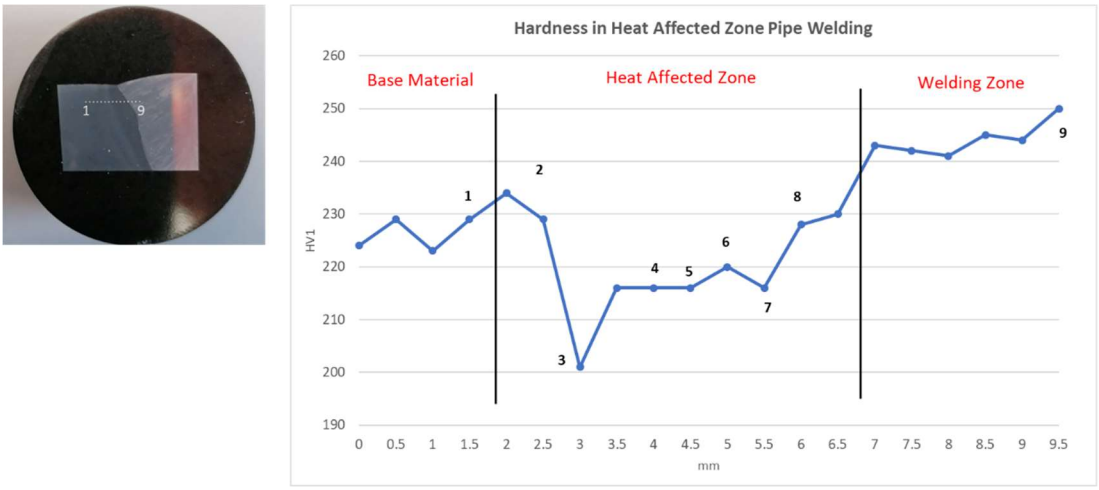

Figure 85 HAZ microhardness pattern in the X80 steel through the heat affected zone in the welding. Microhardness measurements were taken from the base material to the welding zone using a Bakelite sample.

Figure 86 represents the evolution of microstructures in the heat affected zone, each number in the metallography represents the location in the graph of Figure 85. Figure 86 (1-4) shows an acicular ferrite structure while starting to evolve in bigger packets and bainitic structures (Figure 86 (6-8)). A parallel morphology characterises the bainitic structure. Figure 86-9 illustrates the fusion zone where dendrite's solidification can be observed. The difference in hardness is associated with the microstructure evolution. Appendix I contains more images at lower magnifications.

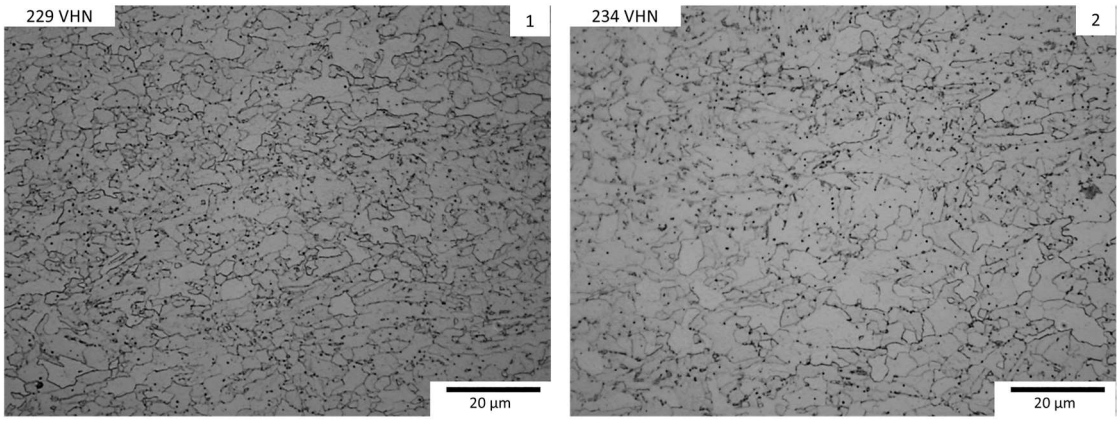

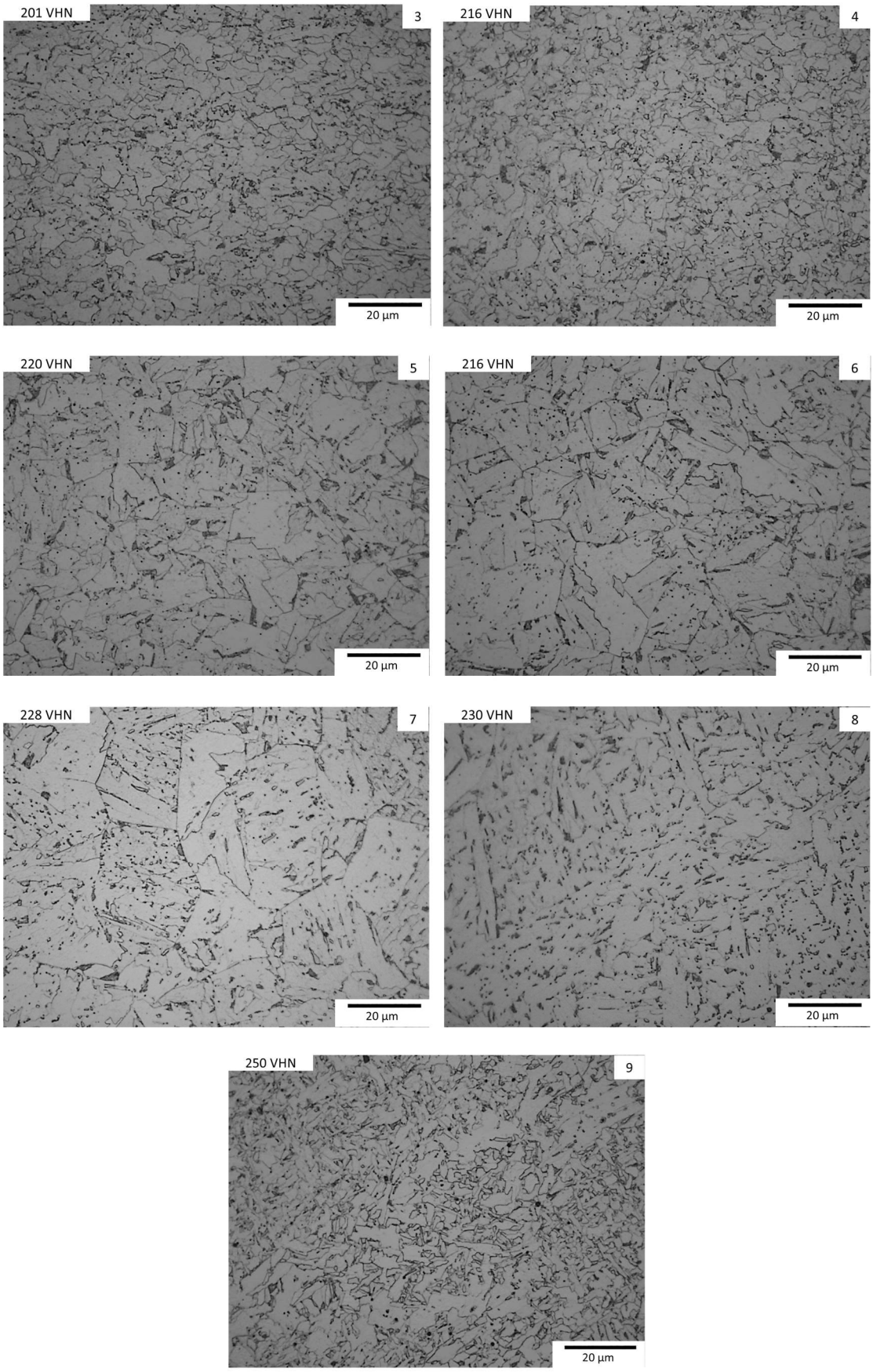

Figure 86 Evolution of the welding microstructure.

4.2 Transformation temperatures

Transformation temperatures were measured at three cooling rates of 0.5, 5 and 50°C/s, and the austenitising temperatures were 1200°C and 900°C. The temperature of 1200°C was selected according to the maximum testing temperature of Gleeble 3800 equipment. The heating rate in all the conditions was 10°C/s. During testing, A_{C1} and A_{C3} did not significantly change the transformation temperatures. A_{C1} and A_{C3} were not reported at 900°C at 5°C/s and 50°C/s because the samples were reused after the thermocouple misreading at 750°C and the test was stopped. Austenite transformation was not finished at 750°C. Thus, it did not affect the prior austenite grain size (Figure 87).

Table 12 shows the phase transformation temperatures during the testing. The slow cooling rate increased the transformation temperatures, while fast cooling rates reduced them. In addition, the prior austenite grain size affected the A_{R1} and A_{R3} temperatures. At 900°C, the fine austenite grain size increased the A_{R1} and A_{R3} transformation temperatures. At the same time, coarse austenite grain size decreased the transformation temperatures. Some authors, such as Matsuzaki and Bhadeshia, have reported that a finer grain size accelerates kinetics by increasing the number density of nucleation sites [131].

Table 12 Transformation temperatures for the X80 steel with different austenitisation and cooling rates conditions.

	Sample	A_{c1} (°C)	A_{c3} (°C)	A_{R1} (°C)	A_{R3} (°C)
900°C	0.5°C/s	735	810	690	790
	5°C/s	N/A	N/A	680	780
	50°C/s	N/A	N/A	620	735
1200°C	0.5°C/s	732	811	528	615
	5°C/s	727	805	495	596
	50°C/s	728	813	430	590

This phenomenon occurred because the steel achieves a thermodynamical equilibrium at a slow cooling rate. Meanwhile, high cooling rates diminish the velocity of atomic diffusion[132].

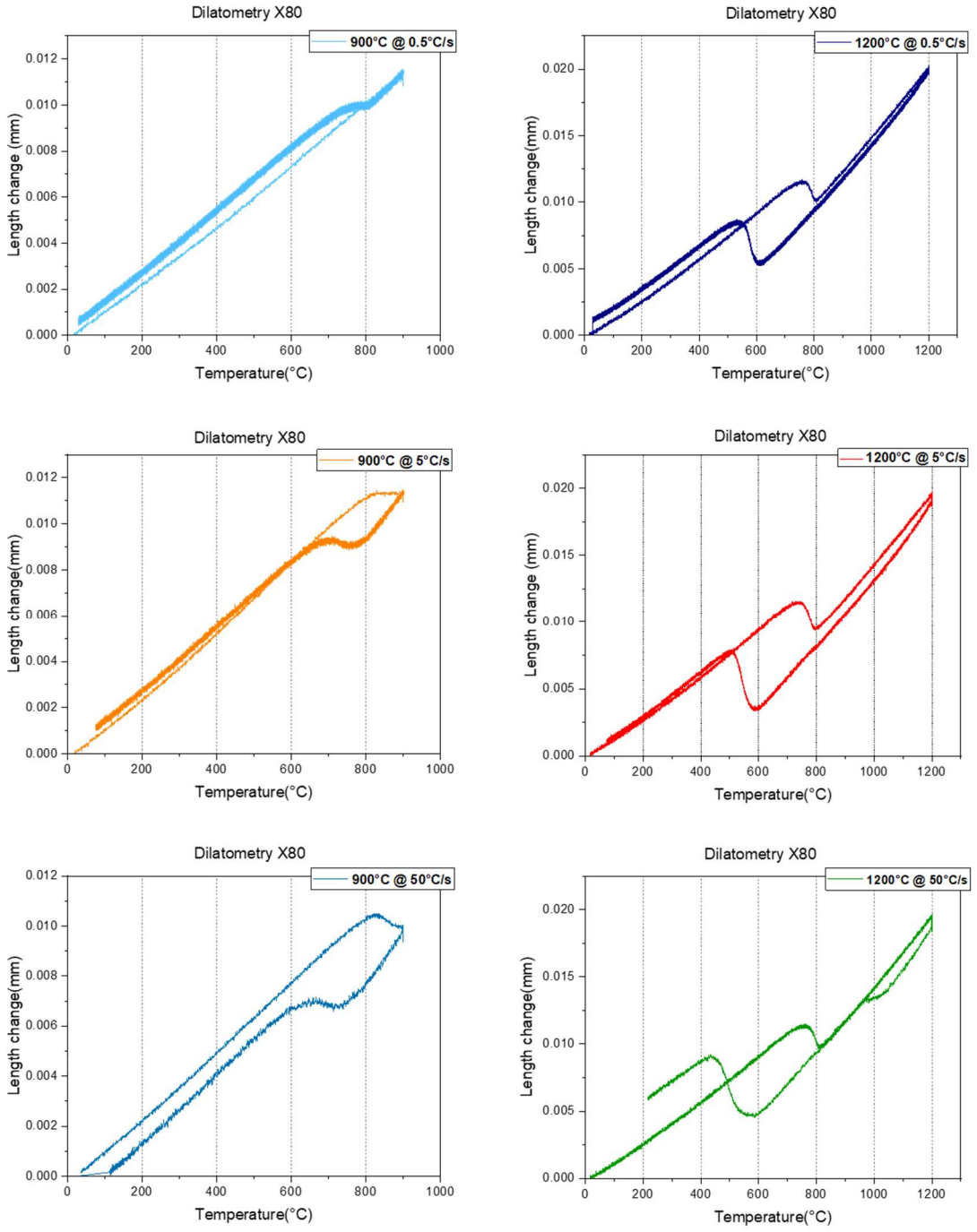

Figure 87 Phase transformation dilatometry of X80 steel cooled at 0.5, 5 and 50°C/s at 900°C and 1200°C.

Table 13 represents the calculations of transition temperatures A_{C1} and A_{C3}. The most accurate result compared with the dilatometry was the Trzaska calculation in A_{C1}, while the Eldis formula was in A_{C3}. The chemical composition was used in these calculations.

Table 13 Temperatures estimation of A_{C1} and A_{C3} using different author formulas.

Author	A_{C1}	A_{C3}
Andrews [116]	692°C	864°C
Kasatkin [133]	718°C	873°C
Trzaska [117]	730°C	863°C
Eldis [118]	687°C	813°C

Table 14 illustrates the estimation of transformation temperature A_{R3} using the chemical composition. Choquet calculation was the nearest to the transformation temperature according to the dilatometry at 0.5°C/s (790°C) and 5°C/s (780°C). Prior austenite grain size and cooling rate were not considered in the Choquet, Ouchi and Shiga estimations.

Table 14 Calculation of A_{R3} using the chemical composition of X80 steel.

Author	A_{R3}	Notes
Choquet [119]	781°C	Estimations do not use a cooling rate
Ouchi [120,121]	744°C	
Shiga[122]	766°C	

Finally, the Mintz calculation[114] was used to determine A_{R3} utilising cooling rate and austenite grain size parameters (Table 15). The estimation was accurate in low cooling rates of 0.5°C/s and 5°C/s using a prior austenite grain size of 3.15 µm. However, in PAGs of 44.8 µm, a difference of more than 150°C between the experimental data and the formula appeared. Mintz equation[114] was used in low cooling rates of 0.1 to 3 °C/s and with PAGs from 70 to 950µm. Another equation to calculate the temperatures is the Yuan formula[113]. However, it was dismissed because the equation uses niobium concentration between 0 to 0.038%; the quantity was inferior to the niobium of the X80 steel (0.094% Nb). The niobium is a crucial element in elevating the austenite transformation temperatures, explained in Chapter 2 of this work.

Table 15 Mintz[114] calculation using prior austenite grain size and cooling rate.

Author	PAG's	Cooling rate	A_{R3}	Useful parameters
Mintz[114]	3.15 µm	0.5°C/s	788°C	(0.04-0.75) %C (0.30-1.6) %Mn (0.00-0.31) %Nb (70.0-950.0) µm PAGS (0.1 to 3) °C/s cooling rate
		5°C/s	787°C	
		50°C/s	782°C	
	44.8 µm	0.5°C/s	785°C	
		5°C/s	784°C	
		50°C/s	779°C	

Phase transformation temperatures were performed using JMatPro version 13 software. The calculations were done at thermodynamic conditions obtaining A_{C3} at 836°C and A_{C1} at 680.3°C. Figure 88 illustrates the CCT diagram at 900°C and PAGs of 3.15 µm, and Figure 89 shows the CCT diagram at 1000°C and PAGs of 11.2 µm; in those diagrams are observed ferrite and pearlite phases during the transformation of γ to α. Figure 90 shows the CCT diagram at 1100°C and PAGs of 33.9 µm, Figure 91 illustrates the CCT diagram at 1200°C and PAGs of 44.8 µm and Figure 92 represents the CCT diagram at 1300°C and PAGs of 97.9 µm; in those temperatures coarse grain size appeared, achieving martensite and bainite phases. At 1300°C, the quantity of martensite and bainite increased drastically when the temperature was raised above 10°C/s of the cooling rate. The following section of the chapter will explain the results of prior austenite grain size.

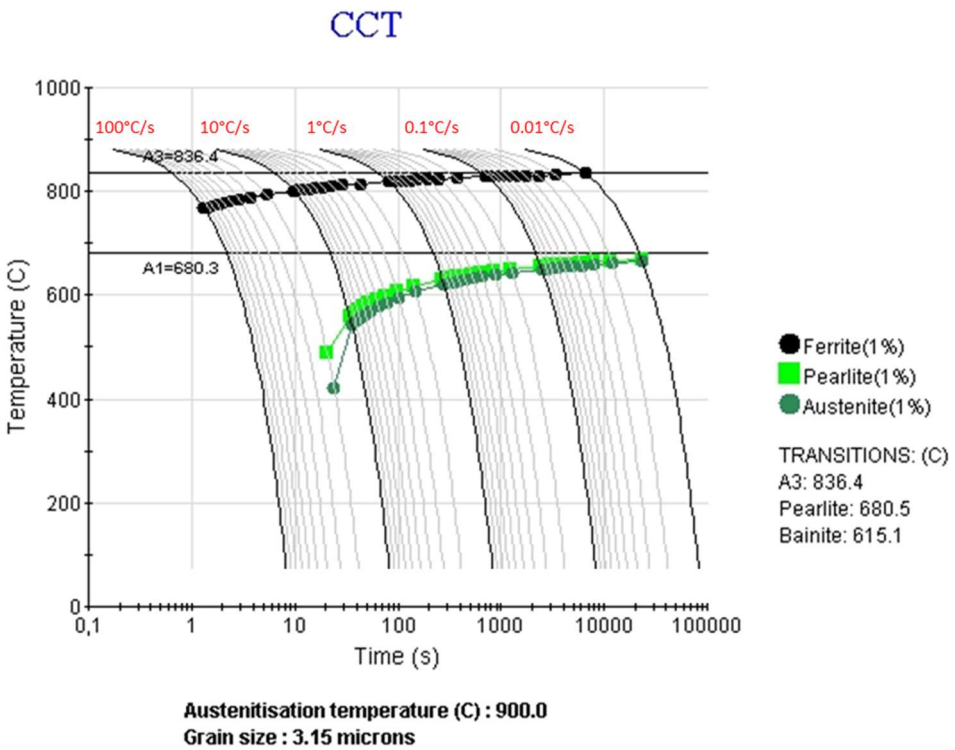

Figure 88 CCT diagram of X80 steel from JMatPro. The temperature of austenitisation was 900°C, and the prior austenite grain size was 3.15µm.

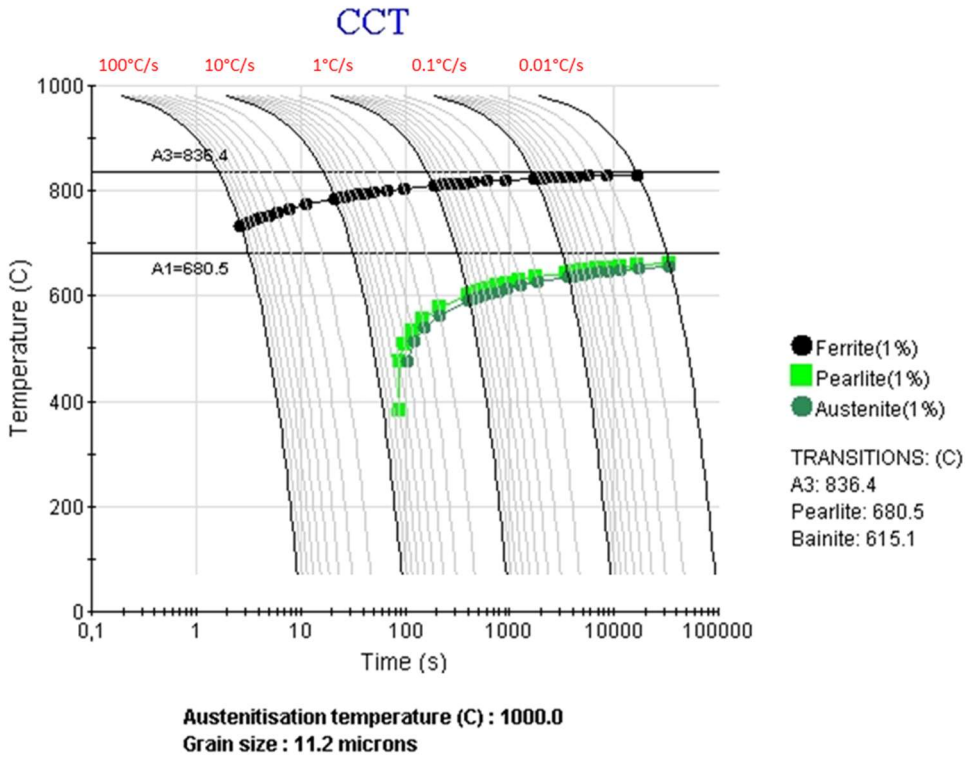

Figure 89 CCT diagram of X80 steel from JMatPro. The temperature of austenitisation was 1000°C, and the prior austenite grain size was 11.2 µm.

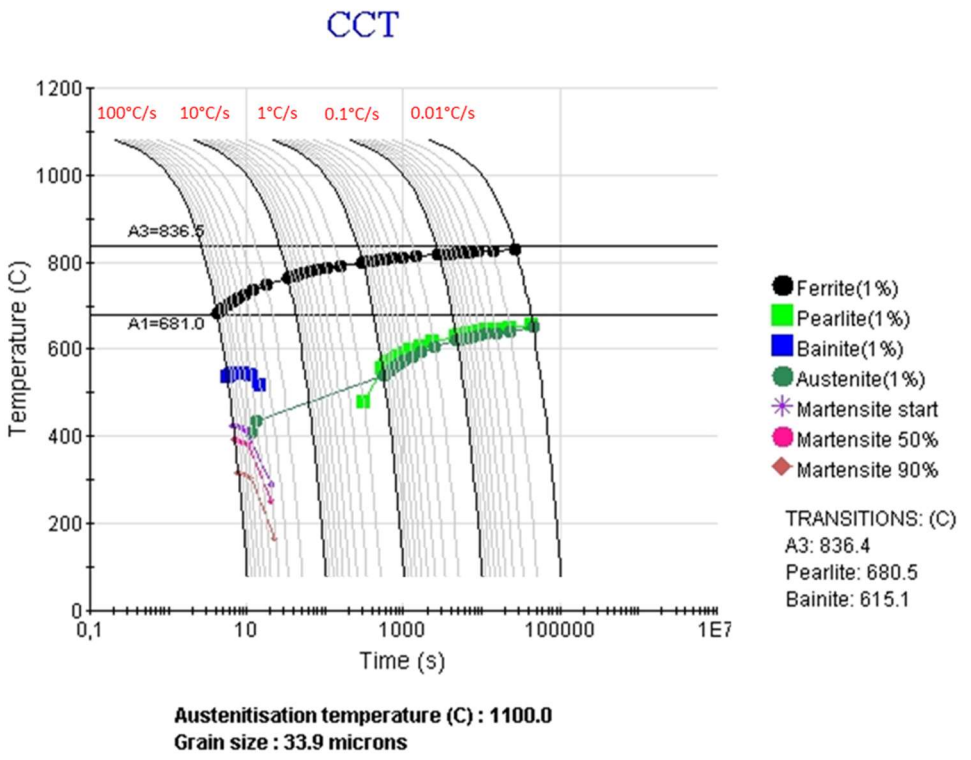

Figure 90 CCT diagram of X80 steel from JMatPro. The austenitisation temperature was 1100°C, and the prior austenite grain size was 33.9 µm.

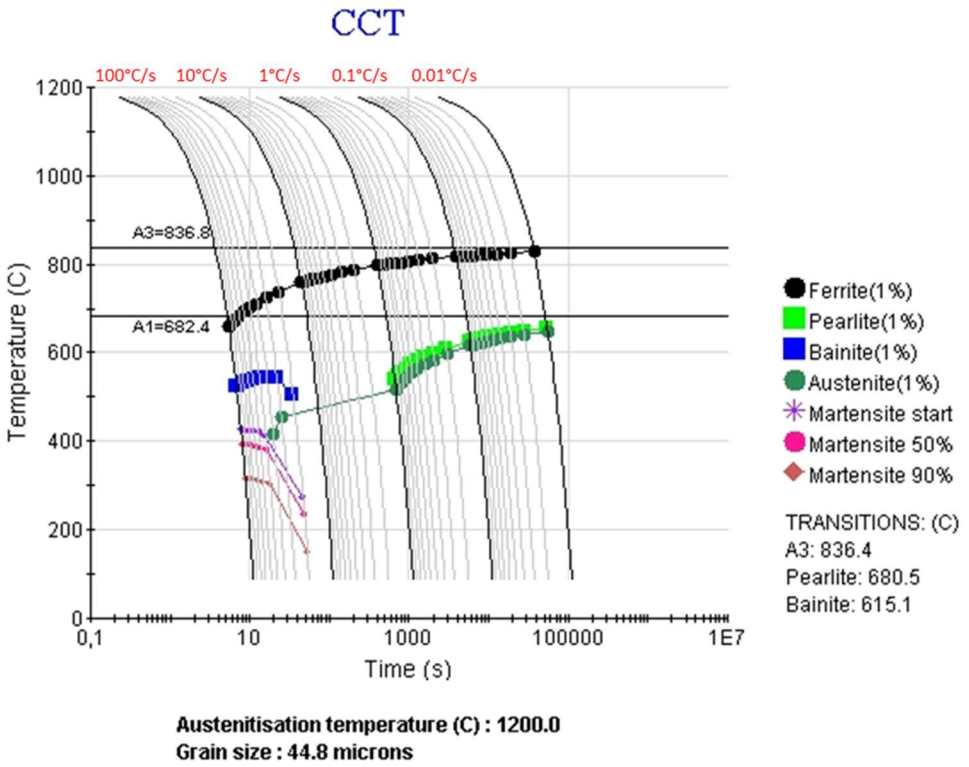

Figure 91 CCT diagram of X80 steel from JMatPro. The temperature of austenitisation was 1200°C, and the prior austenite grain size was 44.8 µm.

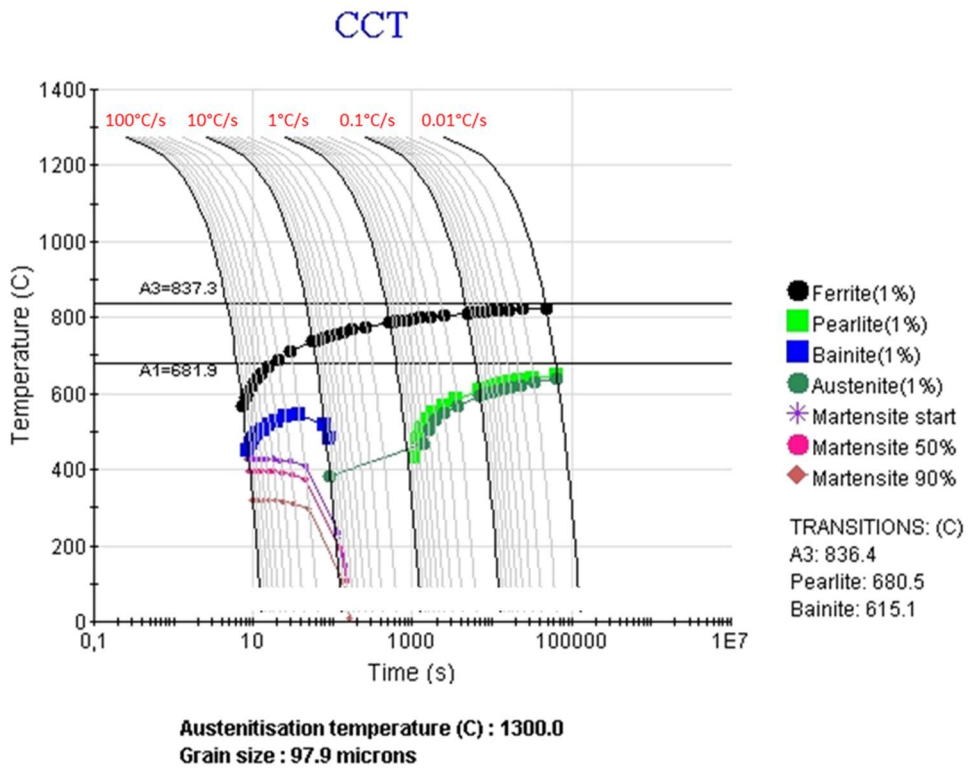

Figure 92 CCT diagram of X80 steel from JMatPro. The temperature of austenitisation was 1300°C, and the prior austenite grain size was 97.9 µm.

4.3 Solubility of Niobium

Niobium in solution is an essential factor in grain growth and the transformation behaviour and subsequent microstructural evolution during cooling. Therefore, different equations were utilised in niobium solubility product calculation. The estimation was based mainly on thermodynamic calculations, chemical division with precipitate isolation and carbon analysis in different niobium contents (Figure 93) (Table 16). The solubility products analysed were [Nb][C][48], [Nb][C][N][47] and [Ti][N] [134]. At lower temperatures, the solubility of niobium was low; however, above 1100°C, the solubility increased drastically. The material of this study contains 0.094% Nb and 0.014% Ti, the complete solubility of these product was obtained at 1282°C in [Nb][C][48] carbide, while in the [Nb][C][N][47] was 1292 °C and finally [Ti][N][134] nitride was 1653°C. Therefore, at 1300°C, the niobium in the material completely dissolves in the solution, but the titanium dissolves above 1600°C.

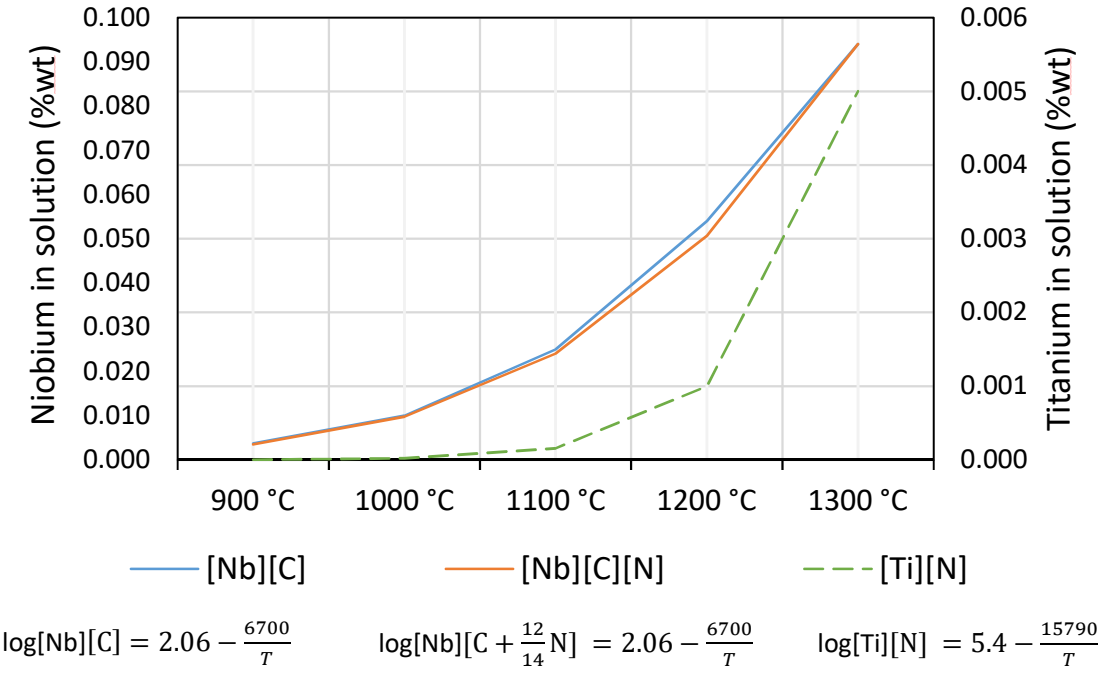

Figure 93 Calculated niobium and titanium in solution using solubility product formulas of NbC [48], NbCN [47] and TiN [134].

Table 16 Niobium solution predicted by solubility products at temperatures between 900°C and 1300°C.

Temperature (°C)	[Nb][C][48]	[Nb][C][N][47]	[Ti][N][134]
900	0.004	0.004	0.000
1000	0.010	0.010	0.000
1100	0.025	0.024	0.000
1200	0.054	0.051	0.001
1300	0.105	0.099	0.005

4.4 Prior austenite grain size

The prior austenite grain size characterisation was performed using saturated solution of aqueous picric acid. To determine the PAGs, the samples were heated at 900°C, 1000°C, 1100°C, 1200°C, 1280°C and 1300°C. The samples were heated for 30 min, and after that treatment, the samples were quenched. Table 17 shows the measurements at the austenitising temperatures. To measure the PAGs was selected the standard ASTM E112-13 1 used the linear intercept method.

Figure 94-95 shows the change in prior austenite grain size when the temperature was increased. At 900°C, PAGs did not show a significant difference compared with the PAGs of the raw material. At 1000°C, the PAGs did increment more than three times the starting PAGs. At 1100°C, the rise was more than three times the PAGs at 1000°C, while at 1100°C and 1200°C the growth continued above 25%. Above 1200°C, the grain size increased at a high growth rate; this phenomenon is related to the solubility of niobium carbides at high temperatures.

Table 17 Measurements of prior austenite grain size at temperatures between 900°C and 1300°C.

Temperature (°C)	Grain Size (µm)	ASTM
900	3.15 ± 0.29	13.35 ± 0.29
1000	11.2 ± 0.88	9.7 ± 0.22
1100	33.9 ± 1.87	6.5 ± 0.14
1200	44.8 ± 1.93	5.7 ± 0.13
1280	77.8 ± 8.38	4.1 ± 0.29
1300	97.9 ± 18.2	3.4 ± 0.47

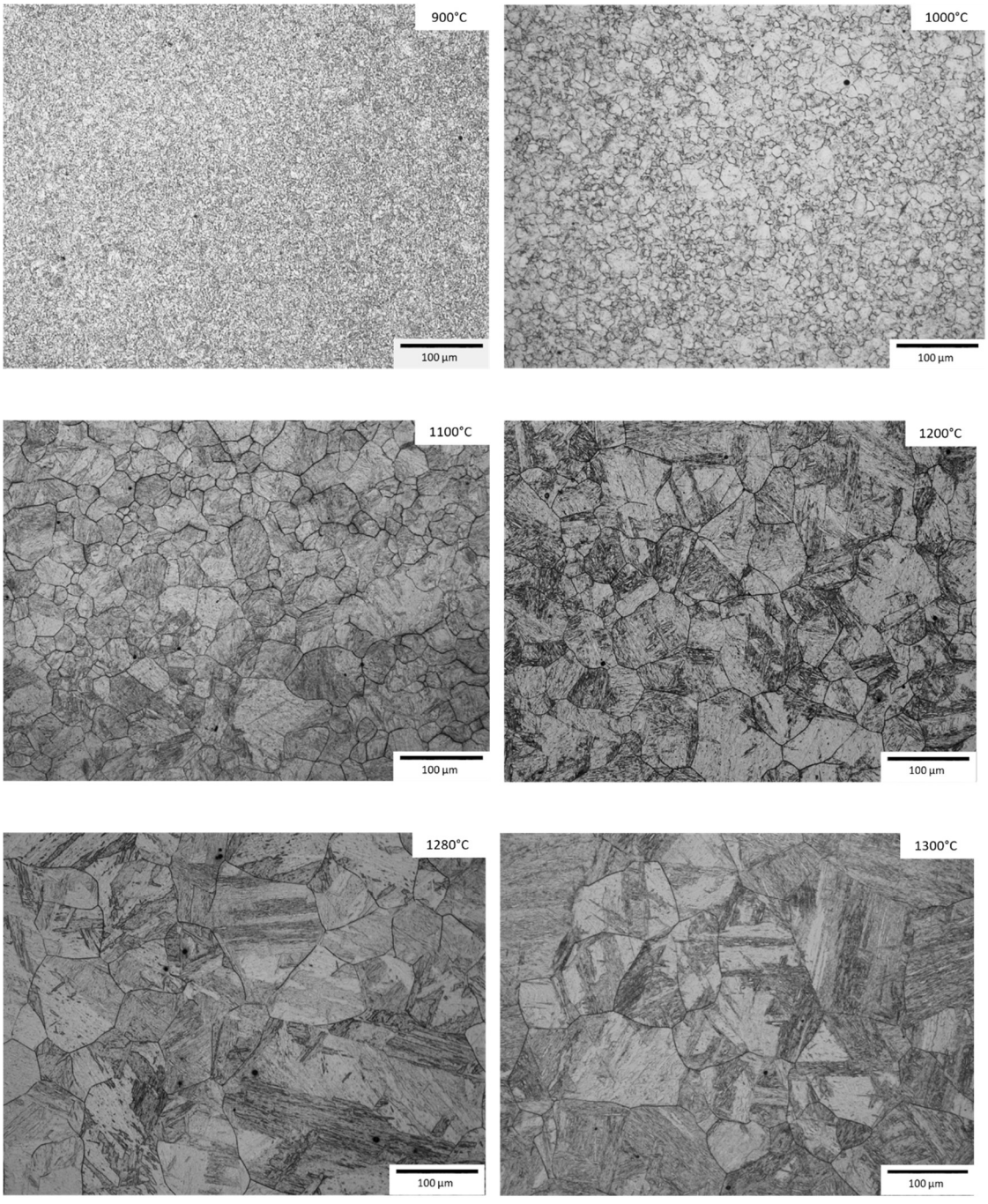

Figure 94 Prior austenite grain boundaries at 900°C, 1000°C, 1100°C, 1200°C, 1280°C and 1300°C.

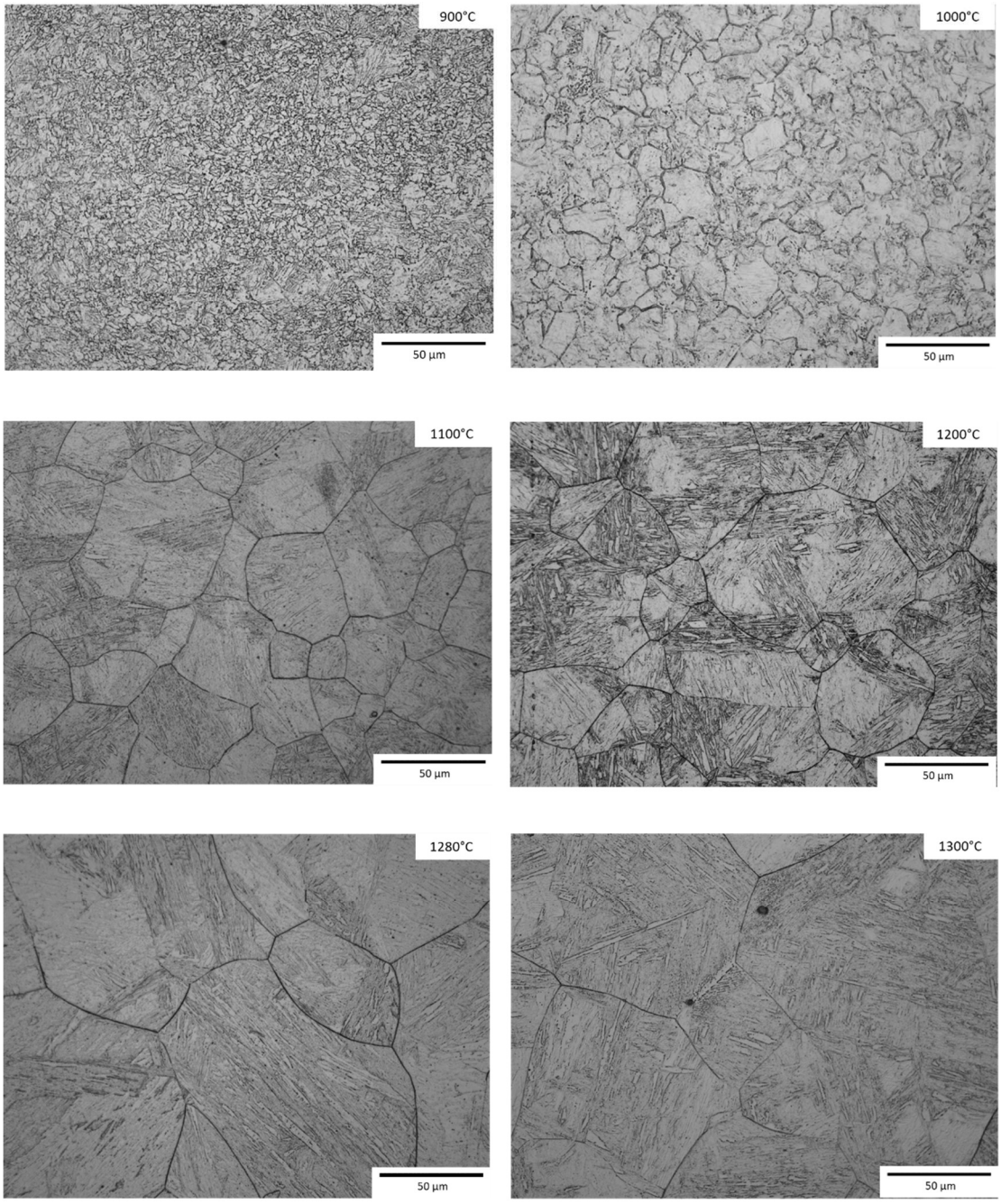

Figure 95 Prior austenite grain boundaries at 900°C, 1000°C, 1100°C, 1200°C, 1280°C and 1300°C.

4.5 Heat treatment simulation

The TMC was used to perform the heat treatment simulation described in Section 3.14 of Chapter 3. The samples were heated between 900° and 1300°C for 30 min. Then, each condition was processed at 0.5°C/s, 5°C/s and 50°C/s of cooling rates. After the simulation, the samples were observed in optical microscopy and SEM, evaluating the microstructure evolution at different austenitising temperatures and cooling rates.

4.6 Microstructure evolution at a slow cooling rate (0.5°C/s)

The evolution of microstructure at 0.5°C/s of cooling rate is shown in Figure 96, and SEM images appear in Figure 102. The samples were heated between 900°C and 1300°C for 30 min. The austenitising temperature affected the PAGs. At higher temperatures, the niobium carbides were dissolved, allowing the grain coarsening of the austenite. Appendix I contains images at higher magnifications in the optical microscope and SEM.

At 900°C and 1000°C, ferrite + pearlite microstructure was observed (Figures 97-98). At 900°C, PAGs was 3.15 ± 0.29μm while at 1000°C was 11.2 ± 0.88μm. Equiaxed grains were observed at those temperatures. At 900°C, the polygonal shapes were well-defined (Figure 97), while at 1000°C, the polygonal shapes started to be non-uniform (Figure 98). Figure 102 shows the microstructure in SEM; pearlite (P) colonies in a ferrite matrix appeared in those microstructures. At 1100°C, PAGs grew to 33.9 ± 1.87μm; a polygonal ferrite (PF) mixture with quasi-polygonal ferrite (QF) structure was observed. Also, it was observed areas related to bainite (BF) (Figure 99). When the temperature increased, the PF+QF started to vanish and the bainite transformed into the primary structure.

Finally, a bainite microstructure was observed at 1200°C and 1300°C (Figures 100-101). At those temperatures, PAGs was 44.8 ± 1.93 at 1200°C and 97.9 ± 18.2 at 1300°C. The bainite transformed in the predominant structure at high austenitisation temperatures. The displacive transformation occurred at coarse austenite, and the supersaturated carbon plates diffused into the austenite grains. At 1300°C, the thin plate shapes increased, regarding the austenitisation temperature of 1200°C.

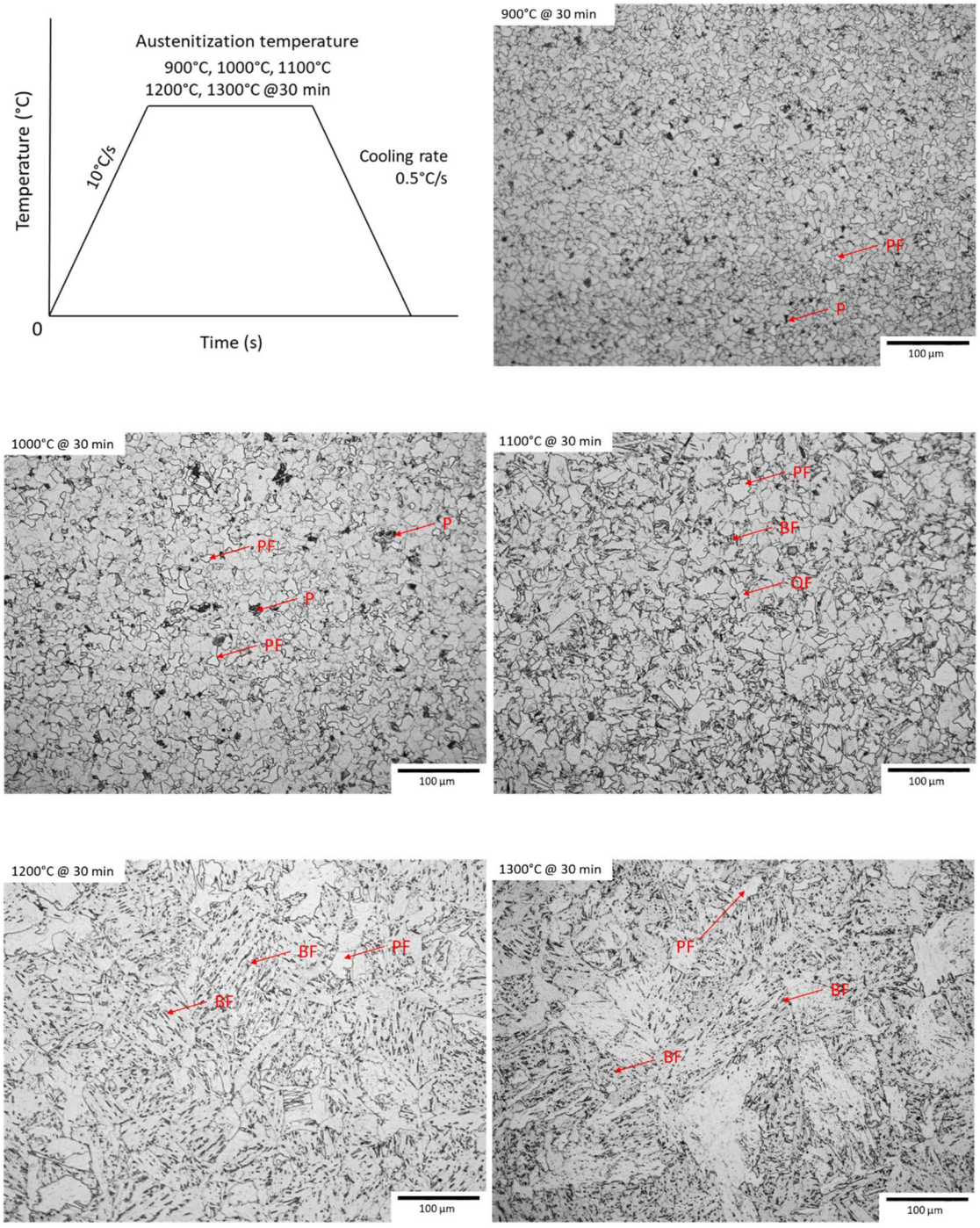

Figure 96 Microstructure evolution between 900°C and 1300°C at 0.5°C/s of cooling rate.

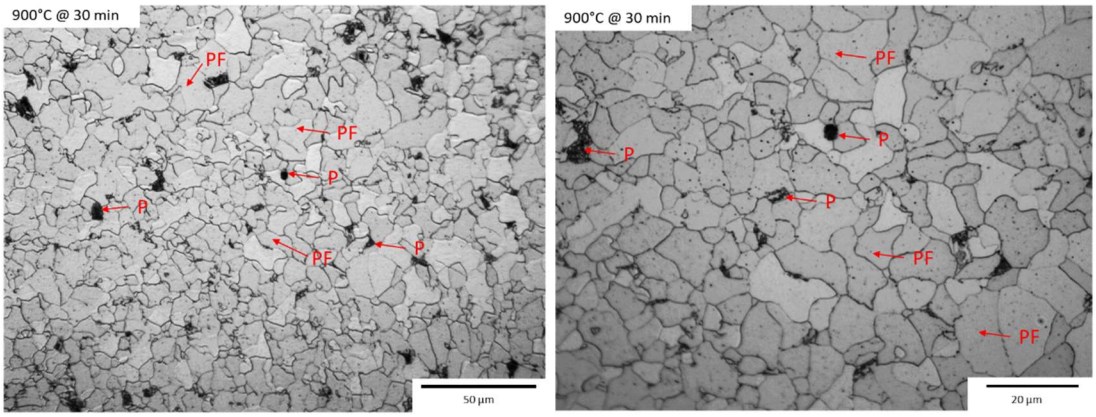

Figure 97 Microstructure evolution at 900°C and 0.5°C/s of cooling rate.

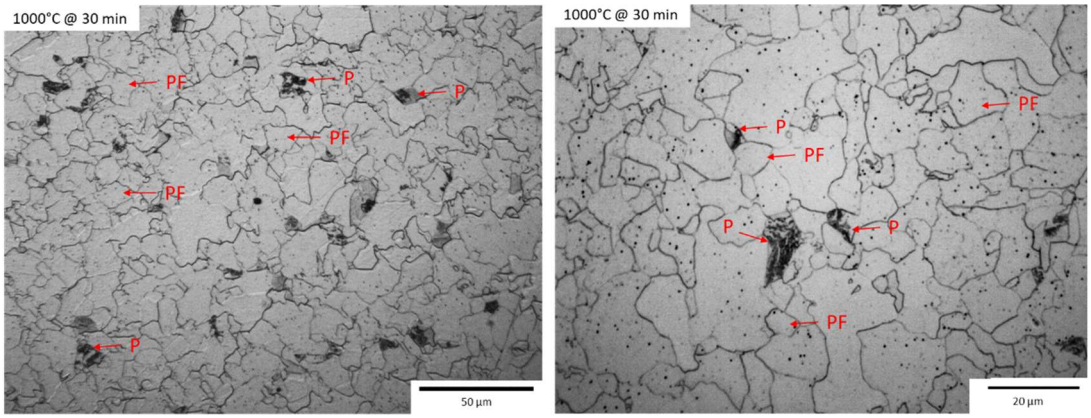

Figure 98 Microstructure evolution at 1000°C and 0.5°C/s of cooling rate.

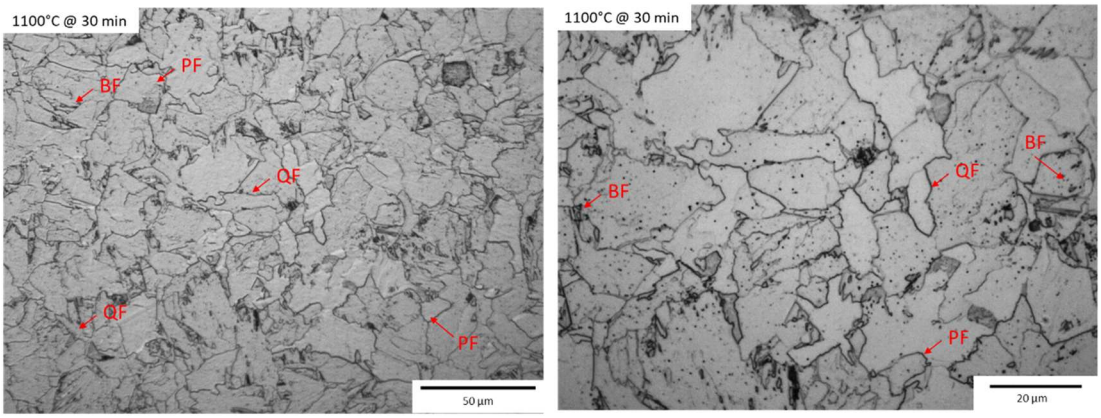

Figure 99 Microstructure evolution at 1100°C and 0.5°C/s of cooling rate.

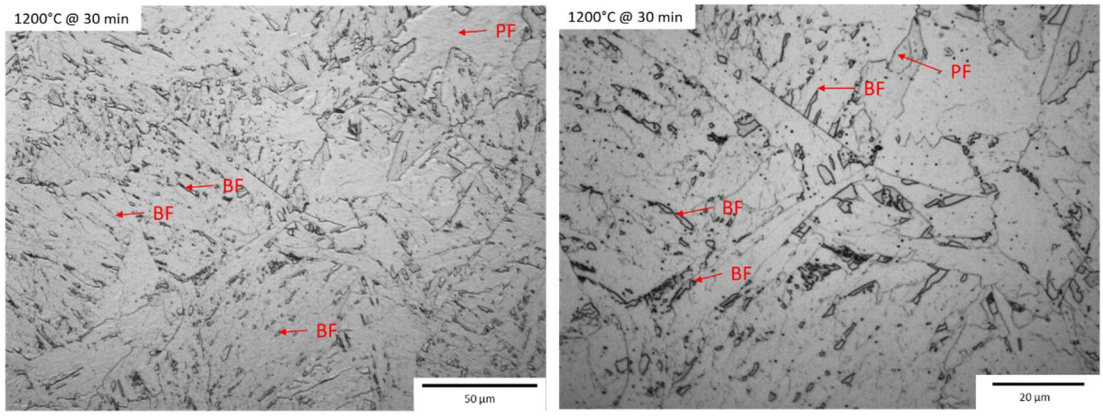

Figure 100 Microstructure evolution at 1200°C and 0.5°C/s of cooling rate.

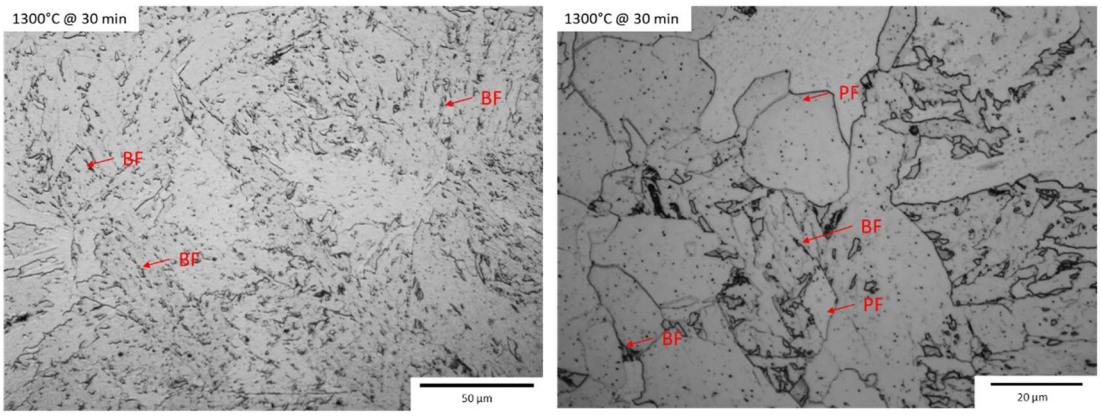

Figure 101 Microstructure evolution at 1300°C and 0.5°C/s of cooling rate.

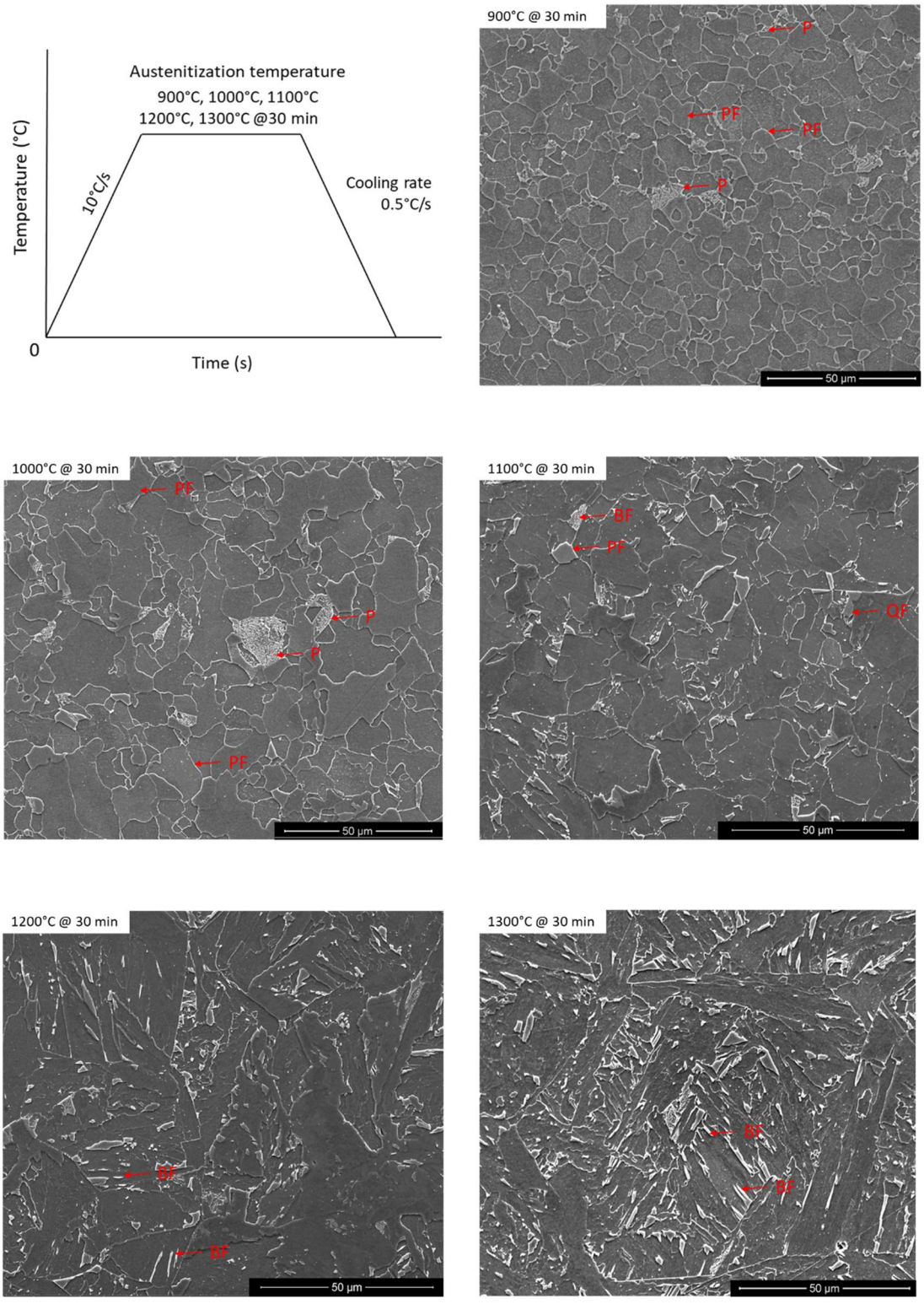

Figure 102 SEM microstructure evolution between 900° and 1300°C at 0.5°C/s of cooling rate.

4.7 Microstructure evolution at a medium cooling rate (5°C/s)

The evolution of microstructure at a medium cooling rate is shown in Figure 103. The samples were heated between 900° and 1300°C for 30 min; after that, the cooling was performed at 5°C/s. This cooling was a medium temperature between forced cooling with mist and cooling at the environment temperature. Appendix I contains images at higher magnifications in the optical microscope and SEM (Figure 109).

A polygonal ferrite with pearlite microstructure was observed in the lowest austenitisation temperature of 900°C (Figure 104). Equiaxed shape microstructure was observed at this temperature, with a less smooth shape than the same austenitising temperature at 0.5°C/s of cooling rate. At 1000°C, quasi-polygonal ferrite with some areas of bainite microstructure appeared (Figure 105).

Bainite formation was massive when the temperature was elevated to 1100°C (Figure 106). PAGs showed high growth, reaching a size of 33.9 ± 1.87μm. At this temperature, the volume fraction of ferrite diminished quickly compared with the same austenitising temperature at a slower cooling rate of 0.5°C/s. Bainite and ferrite microstructure increased the tensile strength, which will observe in Section 4.12 about mechanical properties.

The microstructure evolves to predominantly bainite at higher austenitisation temperatures (Figures 107 and 108). Furthermore, austenite grain boundaries are apparent in the microstructure. The visualisation of austenite grain boundaries areas is related to the formation of martensite-austenite constituents (M/A)(Figure 110 and 111). The M/A constituents were distributed in the matrix. These M/A constituents appeared equiaxed in the micrograph. The mechanical properties were affected by the M/A constituents. This microstructure increased the strength and reduced the ductility compared with the lower austenitising temperatures at the same cooling rate (Section 4.12).

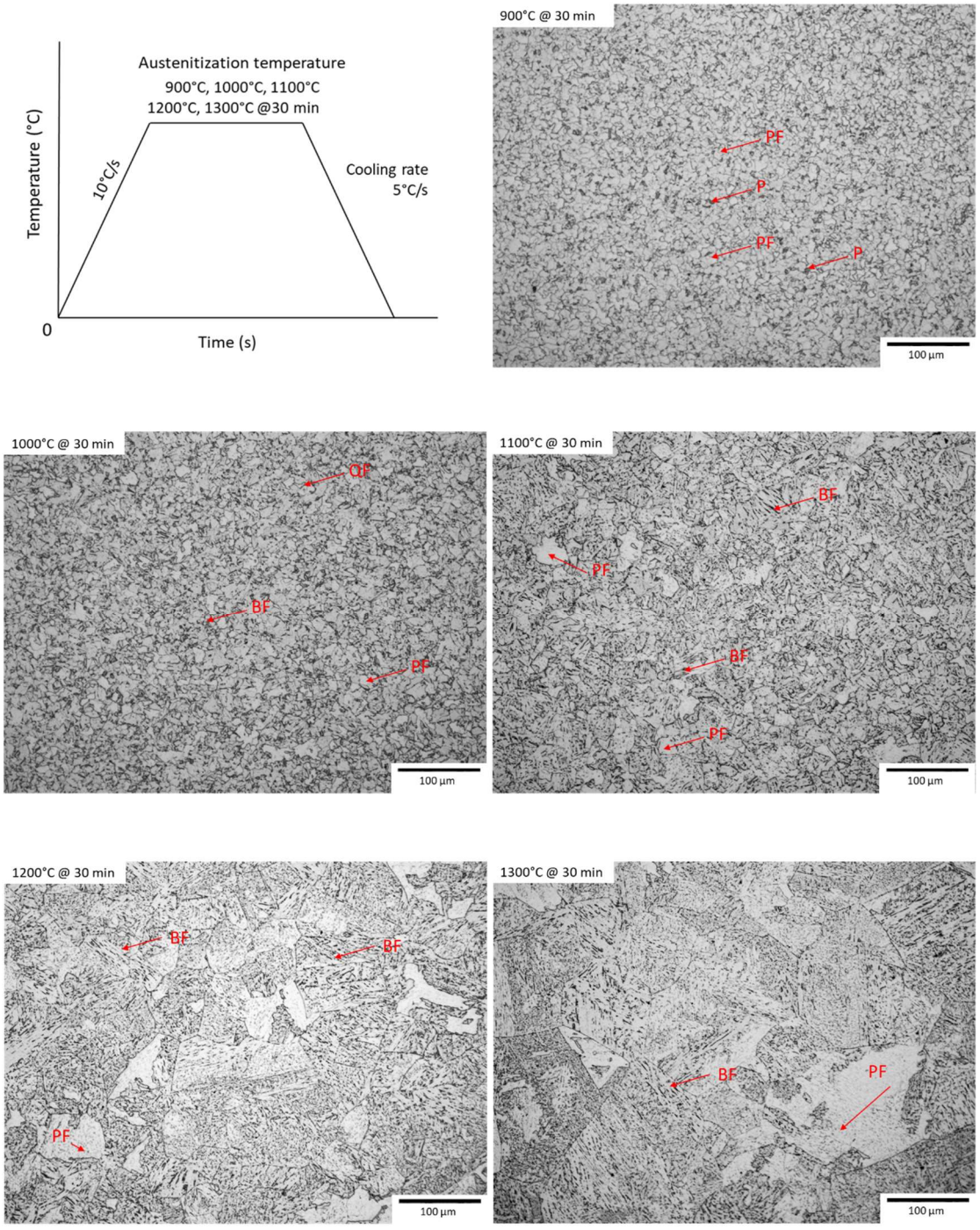

Figure 103 Microstructure evolution between 900°C and 1300°C at 5°C/s of cooling rate.

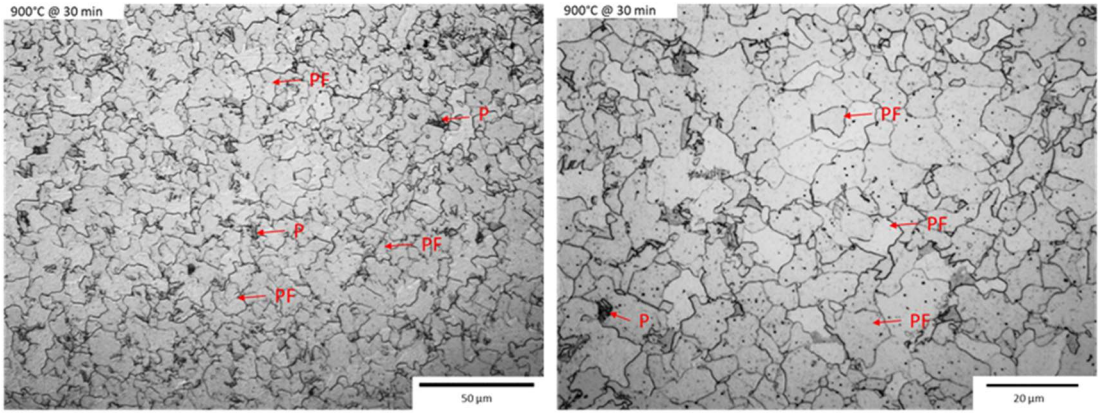

Figure 104 Microstructure evolution at 900°C and 5°C/s of cooling rate.

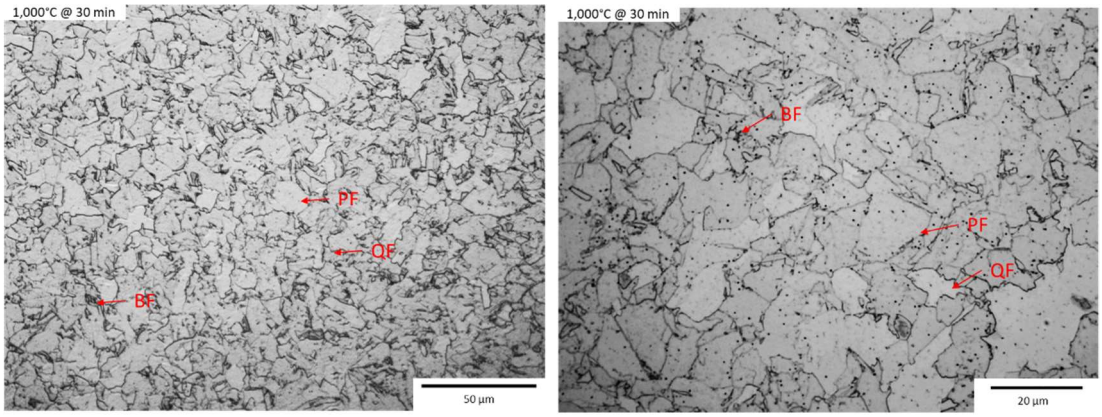

Figure 105 Microstructure evolution at 1000°C and 5°C/s of cooling rate.

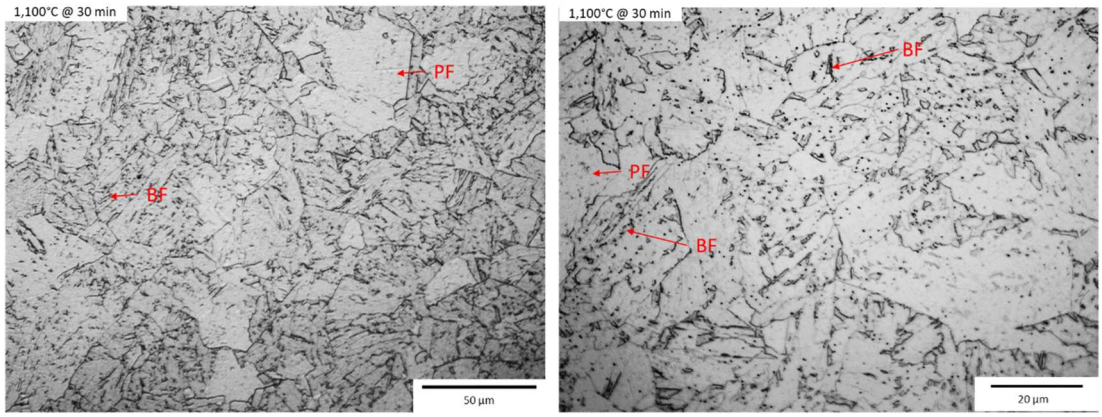

Figure 106 Microstructure evolution at 1100°C and 5°C/s of cooling rate.

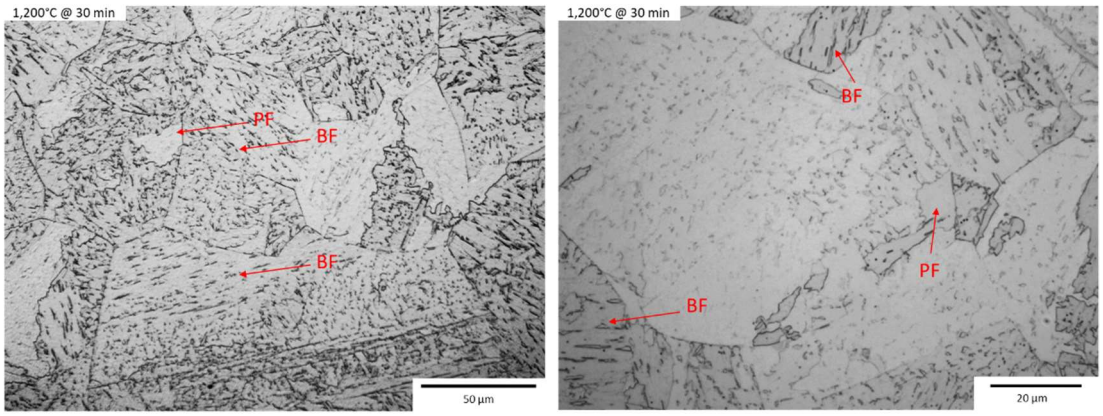

Figure 107 Microstructure evolution at 1200°C and 5°C/s of cooling rate.

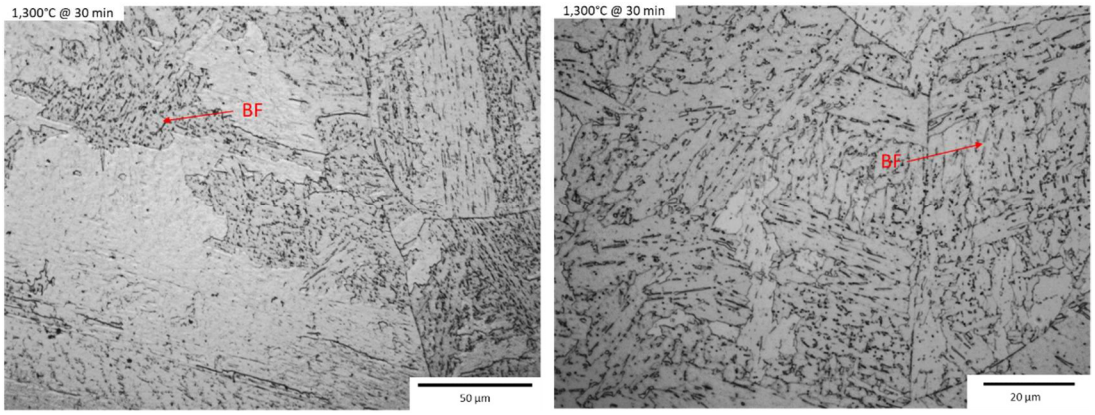

Figure 108 Microstructure evolution at 1300°C and 5°C/s of cooling rate.

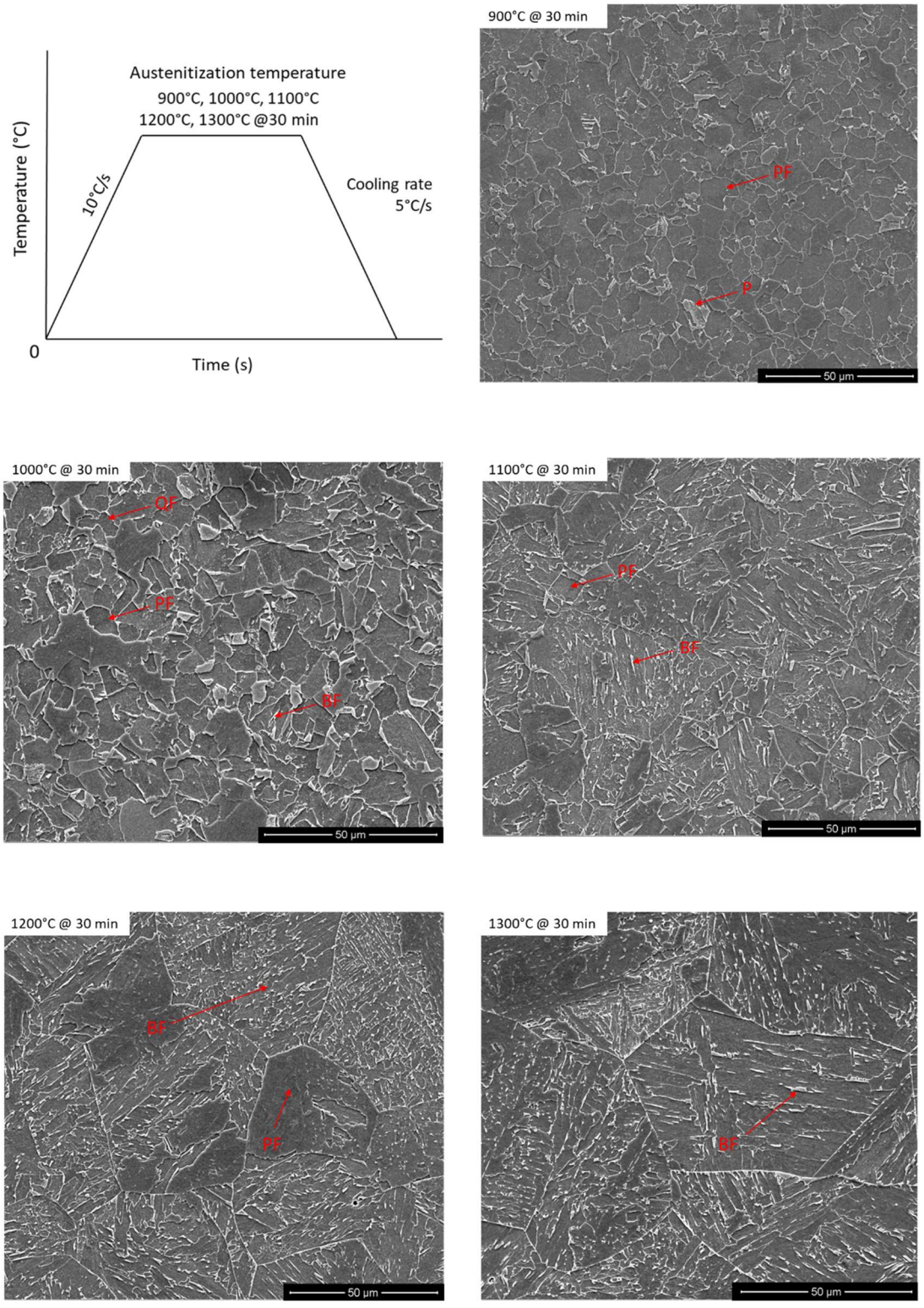

Figure 109 SEM microstructure evolution between 900°C and 1300°C at 5°C/s of cooling rate.

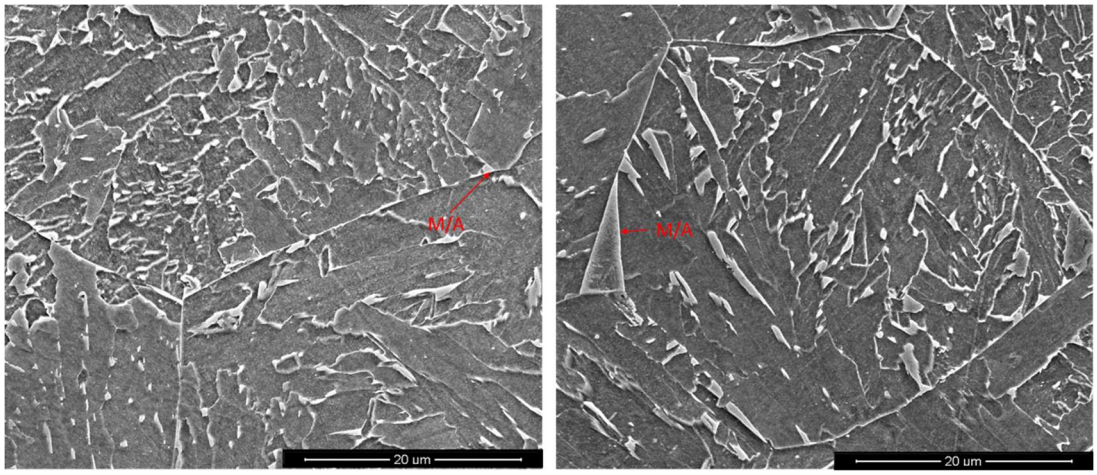

Figure 110 SEM microstructure at 1200°C and 5°C/s of cooling rate.

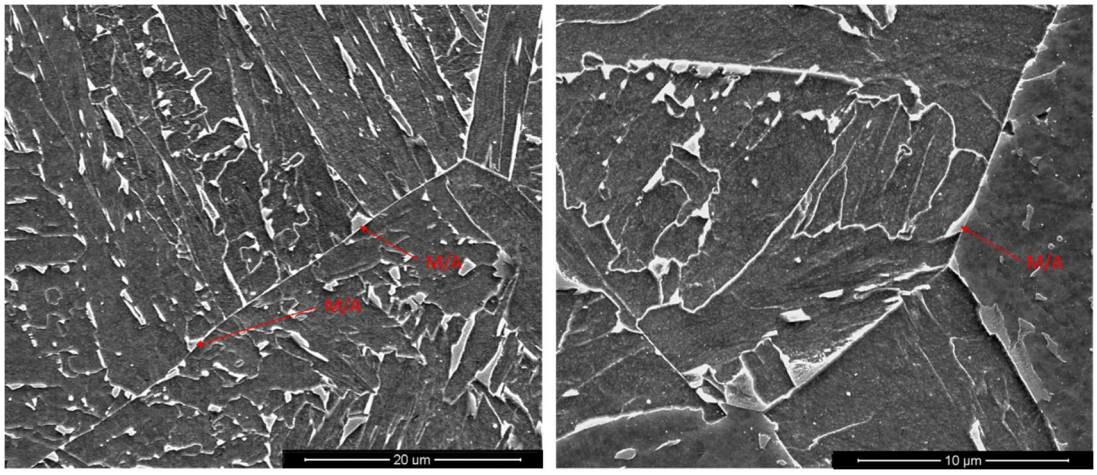

Figure 111 SEM microstructure at 1300°C and 5°C/s of cooling rate.

4.8 Microstructure evolution at a high cooling rate (50°C/s).

The evolution of microstructure during the heat treatment is shown in Figure 112. The samples were heated between 900°C and 1300°C for 30 min; after that, the cooling was performed at 50°C/s. This cooling was achieved using forced air and water mist. Appendix I contains images at higher magnifications in the optical microscope and SEM (Figure 118).

At 900°C, quasi-polygonal ferrite with bainite and martensite zones was observed (Figure 113). The equiaxed shapes disappeared from the microstructure at this temperature compared with the previous cooling rate at 5°C/s and 0.5°C/s. At this austenitisation temperature, it was observed that ferrite grains disorder increased, generating more dislocations. As a consequence of this, the material strength increased compared with lower cooling rates. At 1000°C, the microstructure evolved to a mixture of bainite + quasi-polygonal ferrite with martensite zones (Figure 114).

When the austenitising temperature reached 1100°C, the quantity of bainite with martensite increased (Figure 115). At this temperature, the bainite and martensite created more dislocations than the smooth bainite at 5°C/s and 0.5°C/s cooling rates. To observe the dislocations, it is necessary to use thin foils in TEM; however, this technique was not employed in this work. Besides, the prior austenite grain boundaries appear clearly in the SEM micrographs (Figure 118). With this microstructure, the strength increment was significant compared with the same cooling rate at 1000°C. The tensile results will be verified in the mechanical properties section.

Finally, at 1200°C (Figure 116) and 1300°C (Figure 117), a microstructure of martensite with small areas of bainite and ferrite was observed. At 1300°C, the martensite has a volume fraction increment related to the growth of prior austenite grain size. The ductility above the austenitisation temperature of 1100°C will be considerably reduced because the martensite volume fraction increases in the microstructure. This can be verified in Section 4.12 and compared with the same austenitising temperatures at 0.5 and 5 °C/s of cooling rate.

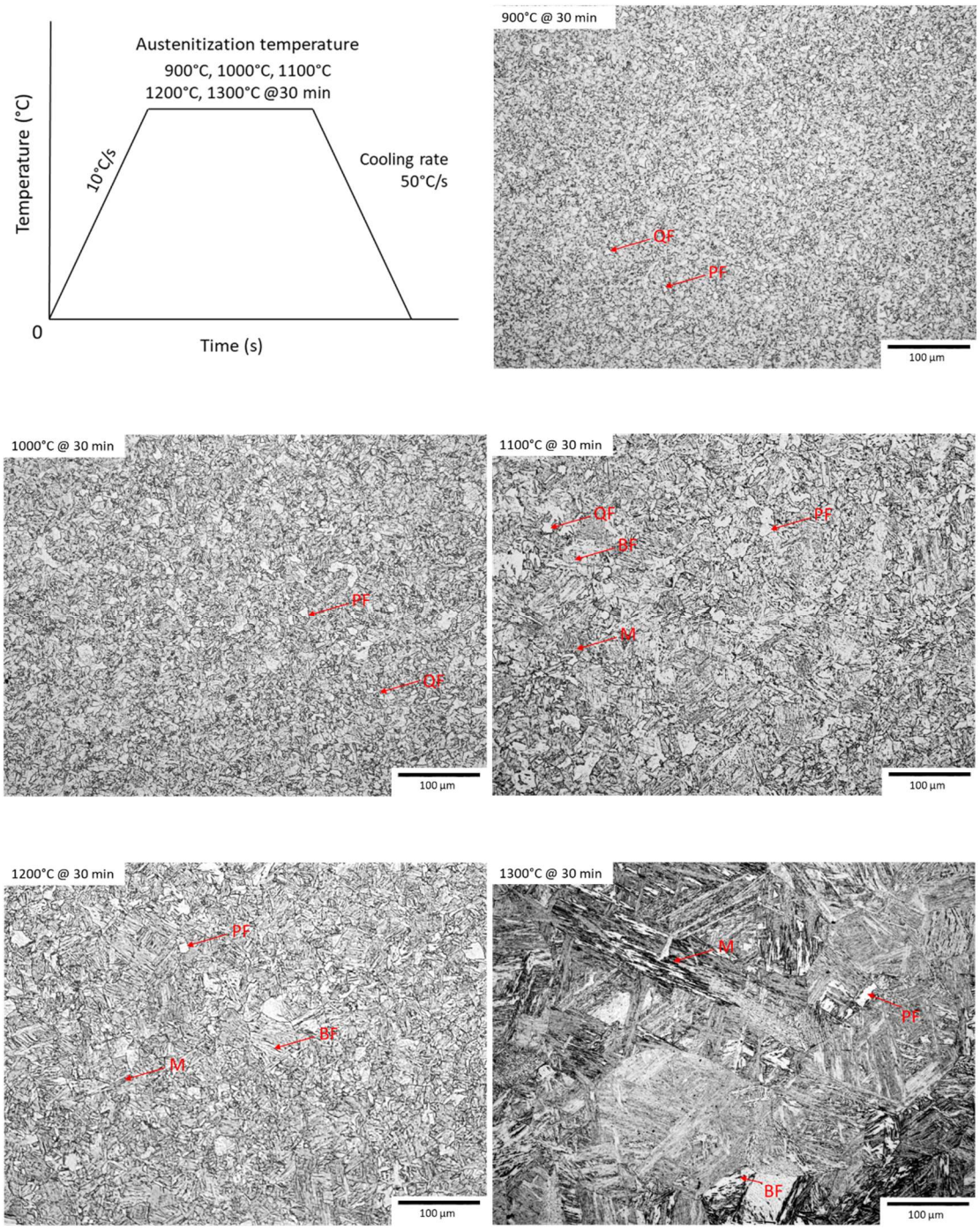

Figure 112 Microstructure evolution between 900°C and 1300°C at 50°C/s of cooling rate.

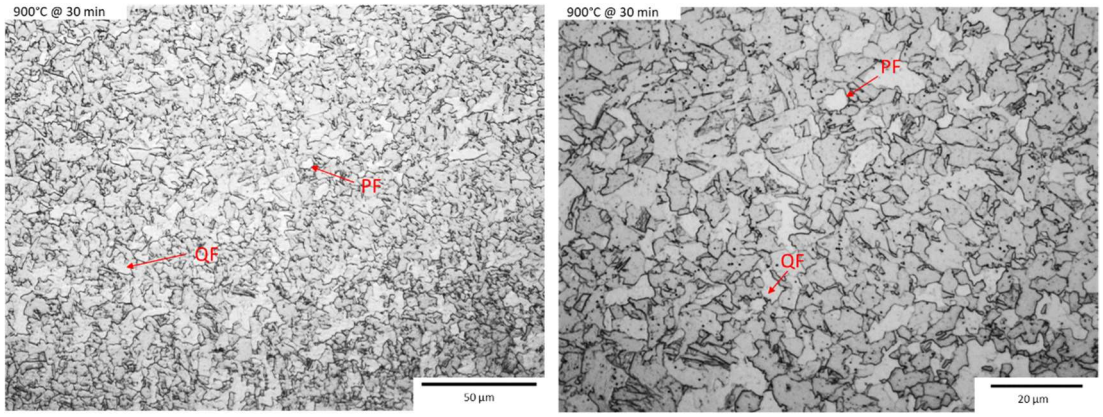

Figure 113 Microstructure evolution at 900°C and 50°C/s of cooling rate.

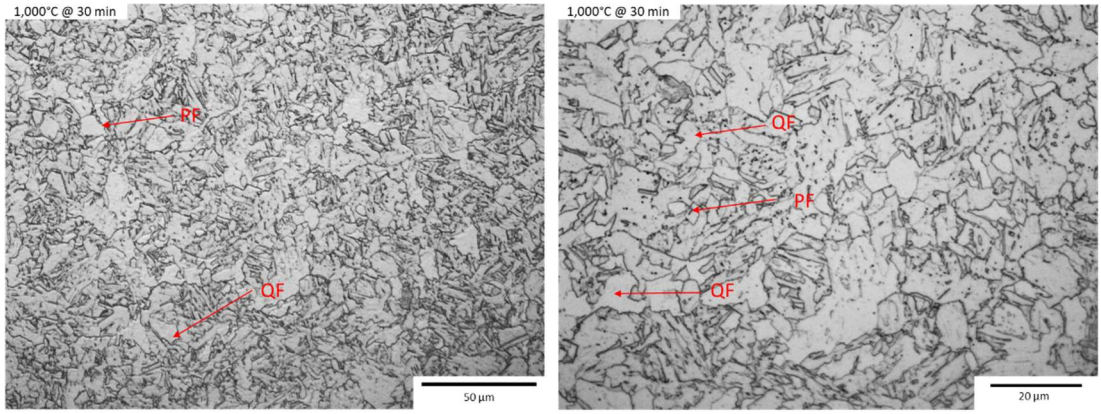

Figure 114 Microstructure evolution at 1000°C and 50°C/s of cooling rate.

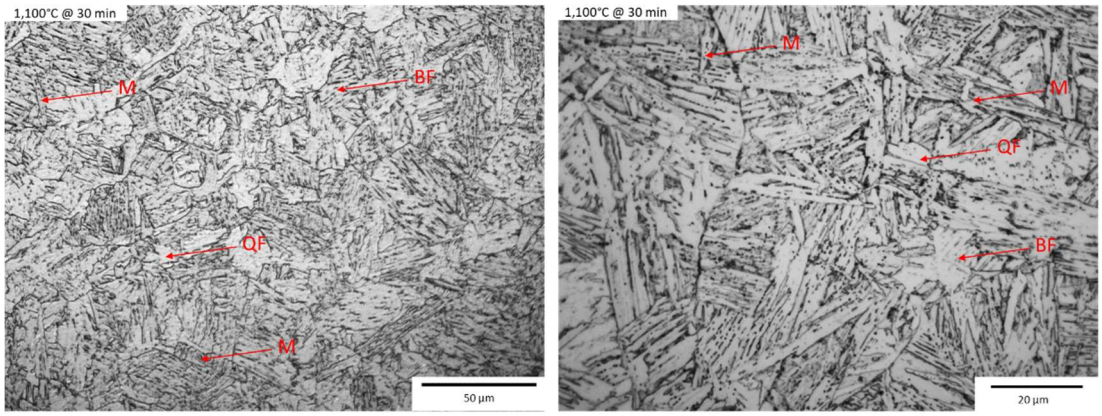

Figure 115 Microstructure evolution at 1100°C and 50°C/s of cooling rate.

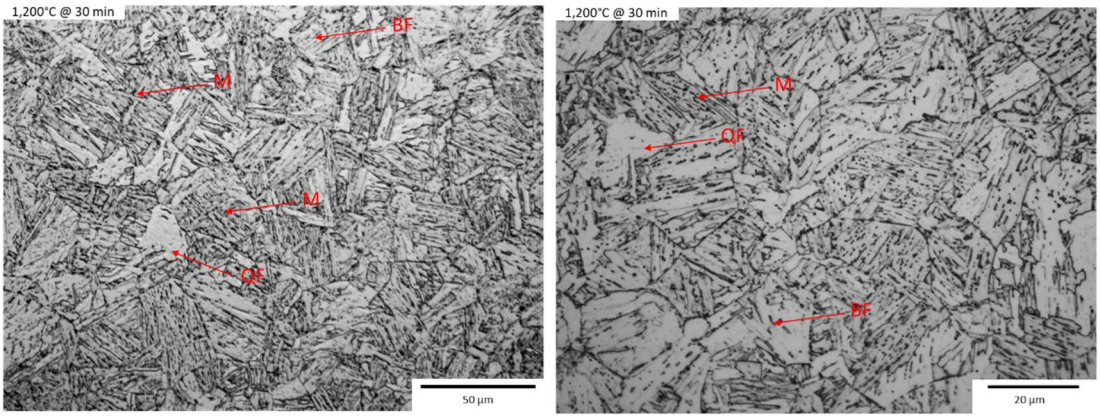

Figure 116 Microstructure evolution at 1200°C and 50°C/s of cooling rate.

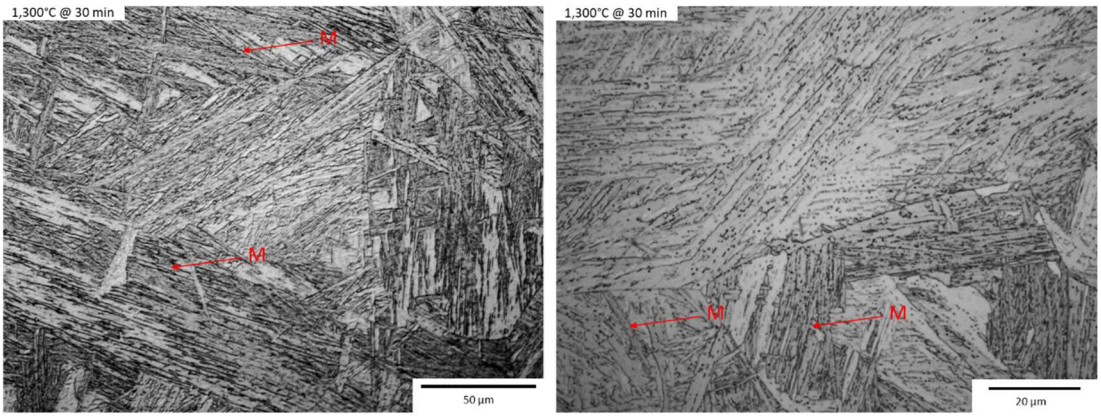

Figure 117 Microstructure evolution at 1300°C and 50°C/s of cooling rate.

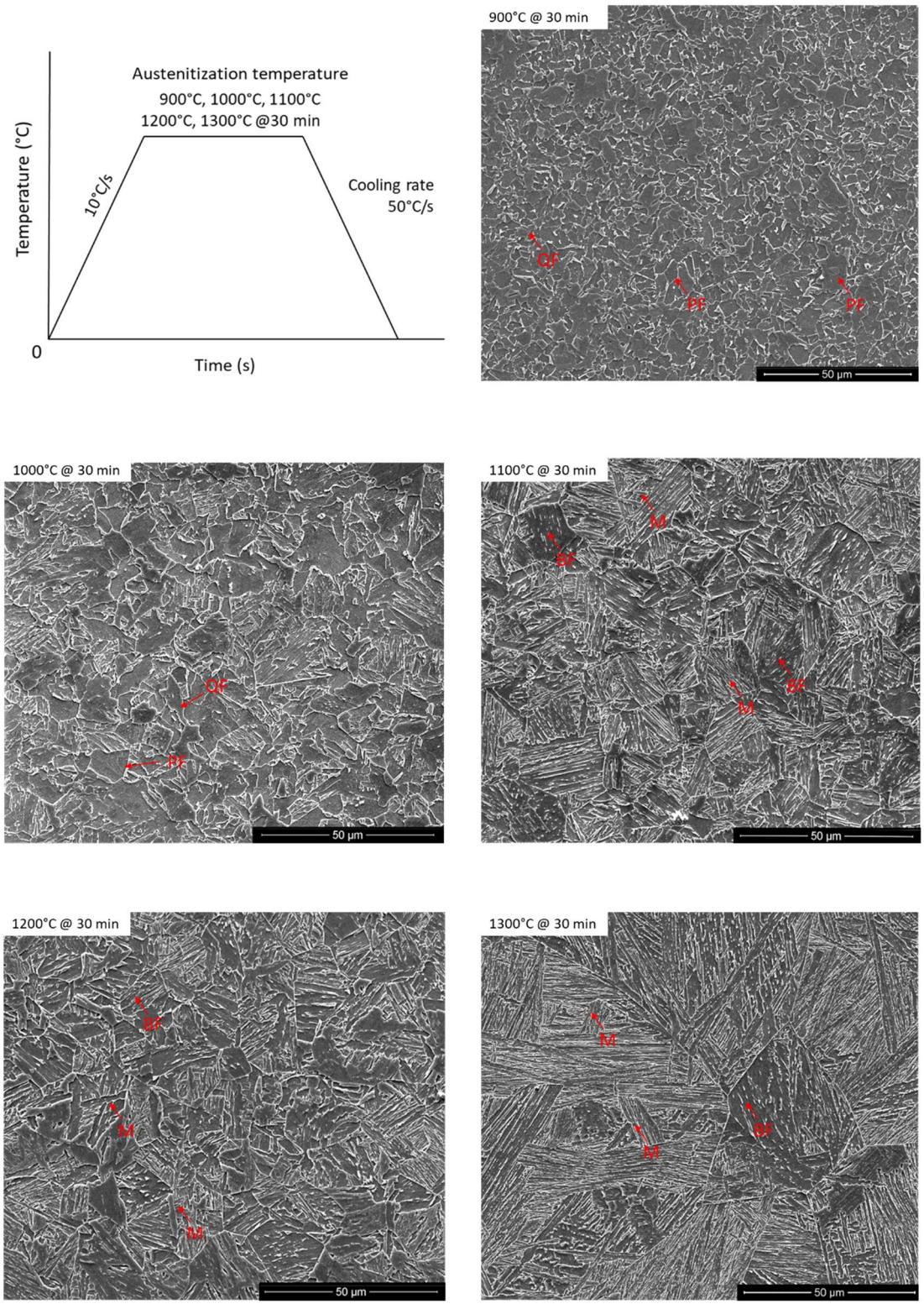

Figure 118 SEM microstructure evolution between 900°C and 1300°C at 50°C/s of cooling rate.

4.9 Carbon extraction replicas

The carbon extraction replica technique was used to characterise the precipitates. The precipitates were analysed in function of austenitising temperature for X80 steel. The analysis of the present work is limited to visualising the morphology and size distribution for each condition; it was not considered to measure the volume fraction of the precipitates. The precipitation behaviour was evaluated to comprehend the solubility product of niobium and the effect on the prior austenite grain size.

The distribution of precipitates at 900°C and 1100°C is shown in Figure 119; in these conditions, the particles were finely-distributed in the replica. However, at 1100°C coarse particles increased compared with 900°C. The solubility of niobium precipitates at 900°C was 0.004%, while at 1100°C, the niobium solubility was 0.024%. The effect of solubility was observed in the distribution and size of the precipitates.

Figure 120 illustrates the carbon replica at 1200°C and 1300°C with a cooling rate of 0.5°C/s and 5°C/s. The solubility of niobium at 1200°C was 0.054%, while at 1300°C, the solubility elevated to 0.099%. This effect was observed in the carbon replica because the distribution and quantity of precipitates decreased at high austenitisation temperatures. In addition, at 1200°C was observed particles of large size around 100nm; the primary particles consisted of large cuboids related to TiN precipitates (Figure 121). The TiN particles were distributed in the carbon replica with a random pattern.

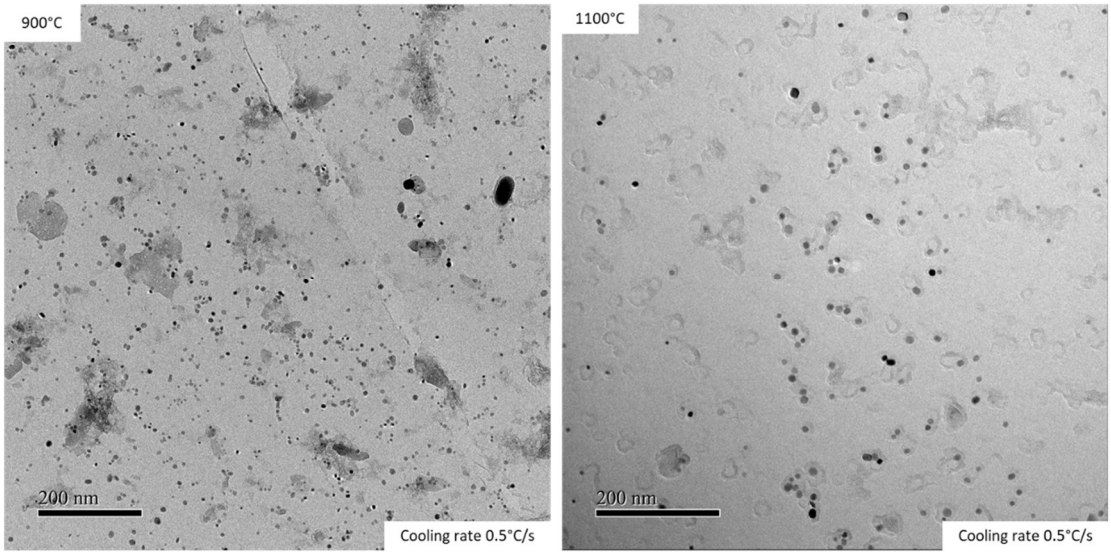

Figure 119 Carbon replica extraction at 900°C and 1100°C at 0.5°C/s of cooling rate.

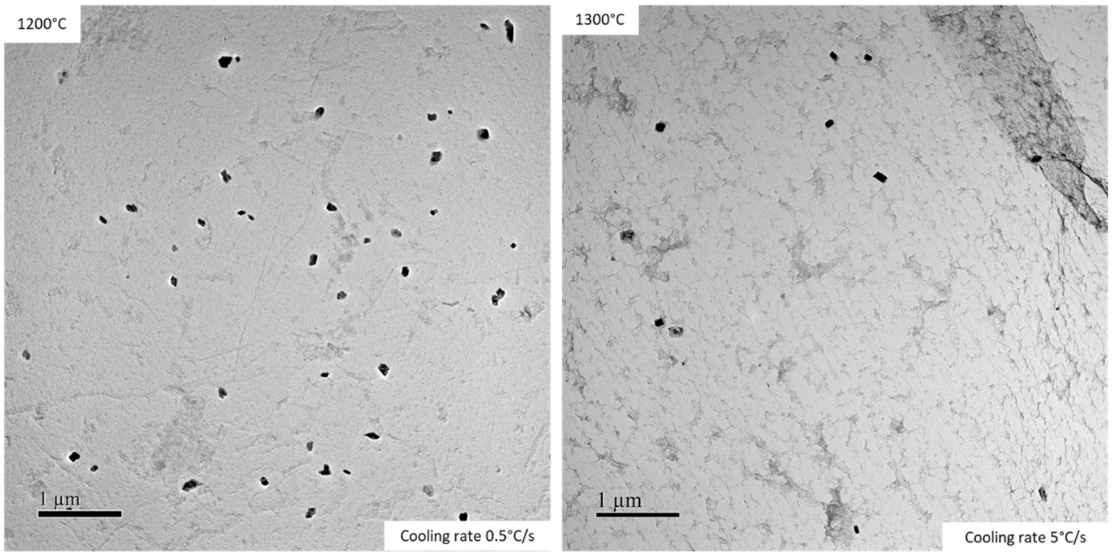

Figure 120 Carbon replica extraction at 1200°C and 1300°C with cooling rates of 0.5°C/s and 5°C/s.

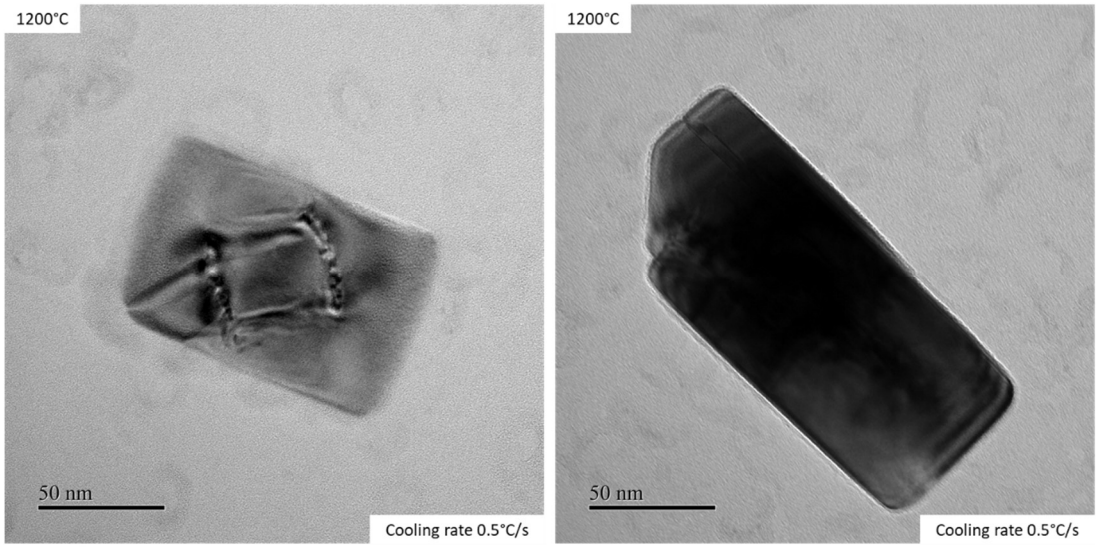

Figure 121 TEM images of TiN precipitate at 1200°C and 0.5°C/s of cooling rate.

4.10 Determination of transformation product volume fraction from optical microscopy

The volume fraction determination was used to obtain the percentage of the second phase through the microstructure. ASTM standard E 562-0115 was used to measure the second phase [135]. In the optical microscopy, ferrite and pearlite were observed at a cooling rate of 0.5°C/s with austenitisation temperatures of 900°C and 1000°. Additionally, ferrite and pearlite microstructure were observed in the medium cooling rate of 5°C/s at 900°C of austenitisation temperature. All the samples were analysed at the same magnifications. The measurement used a square grid with nine fields. Table 18 shows the volume percentage of those phases in each condition. Figure 122 illustrates the square grid in each microstructure.

Table 18 Volume fraction of the second phase in cooling rate of 0.5°C/s and 5°C/s with the austenitising temperature of 900°C and 1000°C.

Cooling rate (°C/s)	Temperature (°C)	Ferrite	Pearlite	95% CI
0.5	900	90.40	9.60	0.58
	1000	93.50	6.50	0.51
5	900	91.40	8.58	0.30

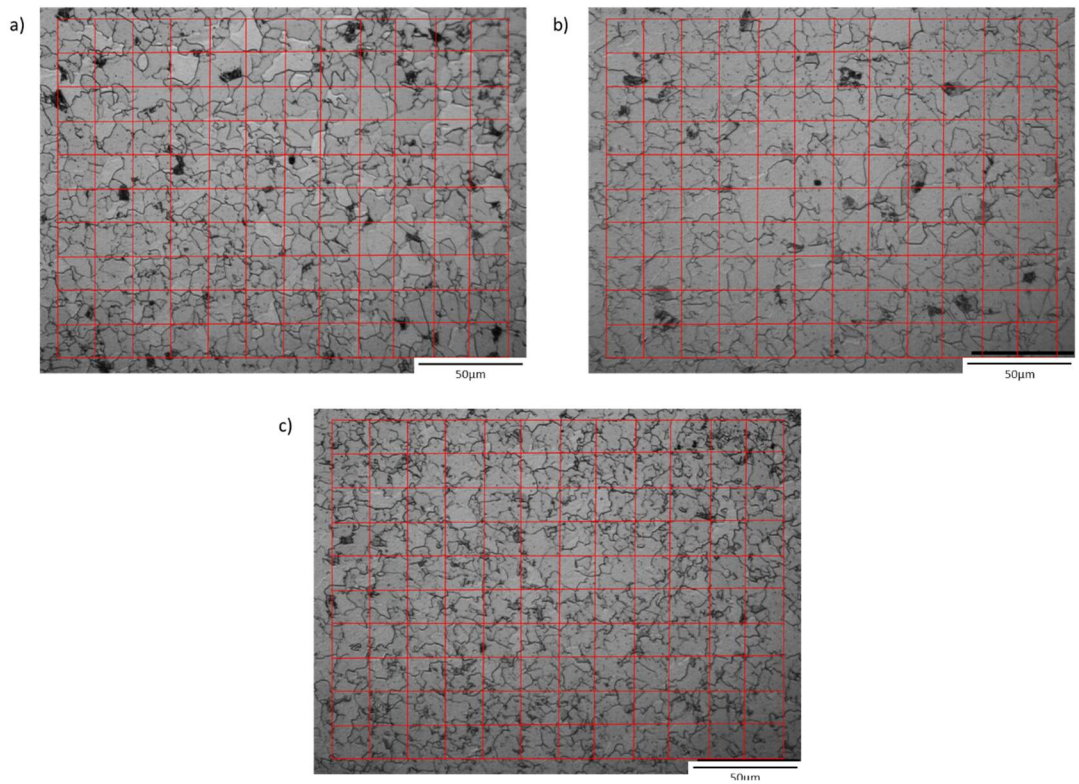

Figure 122 Square grid used in a) 900°C at 0.5°C/s, b) 1000°C at 0.5°C/s and c) 900°C at 5°C/s.

4.11 Determination of transformation product volume fraction using EBSD

Figure 123-125 illustrates the segmentation of phase maps utilising the criteria of Section 3.6.1 in all the samples. This research did not consider the segmentation between polygonal ferrite and quasi-polygonal ferrite. In all these phases, the ferrite segmentation appears with a yellow colour. The M/A constituents are part of the bainite ferrite segmentation, which appears in blue. Finally, the green grains represent martensite and the pink phase represents retained austenite[86]. Table 19 shows the results of phase quantification. To quantify the phases was used the area of the grains.

In the map appears black spots; these spots were not identified as a part of the phases. Generally, nonidentified spots do not match the selected criteria in the grain definition; the most relevant criterion of grains is to have a greater misorientation than or equal to 5° and have a minimum area of 10 pixels. These non-identified spots are filed as pseudosymmetries related to indexing errors in the data points. In all the samples were obtained the pseudosymmetry quantification using the misorientation profile. The pseudosymmetries have a misorientation of 30° or 60°. This could be linked to the Kikuchi bands quantity used in the indexing procedure, but also, the specimen preparation affects the pseudosymmetries.[136].

Table 19 Percentage of phases in the different heat treatments evaluated in EBSD.

Cooling rate (°C/s)	Temperature (°C)	Ferrite	Bainite	Martensite	Retained austenite	Pseudosymmetry
0.5	1100	64.9	31.1	-	1.8	2.2
	1200	23.7	75.6	-	0.3	0.3
	1300	14.5	83.9	-	0.7	0.9
5	1000	72.7	26.1	-	0.5	0.7
	1100	28.4	69.8	-	0.7	1.1
	1200	21.6	76.5	-	0.2	1.6
	1300	17.3	81.8	-	0.1	0.6
50	1100	8.9	6.5	75.3	0.4	1.2
	1200	2.1	7.9	89.3	0.2	0.4
	1300	1.7	2.6	95.4	0.1	0.2

At a cooling rate of 50°C/s, the volume fraction using EBSD was not considered for 900°C and 1000°C due to the microstructure consisting in ferrite. Additionally, the JMatPro simulation showed that only ferrite was present in these conditions.

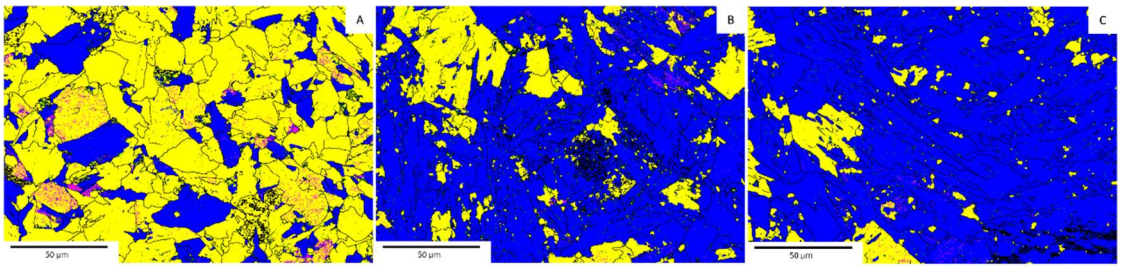

Figure 123 Phase segmentation maps at a cooling rate of 0.5°C/s, austenitisation temperature a)1100°C, b) 1200°C and c) 1300°C. Colour representation: yellow= ferrite, blue=bainite ferrite and pink = retained austenite.

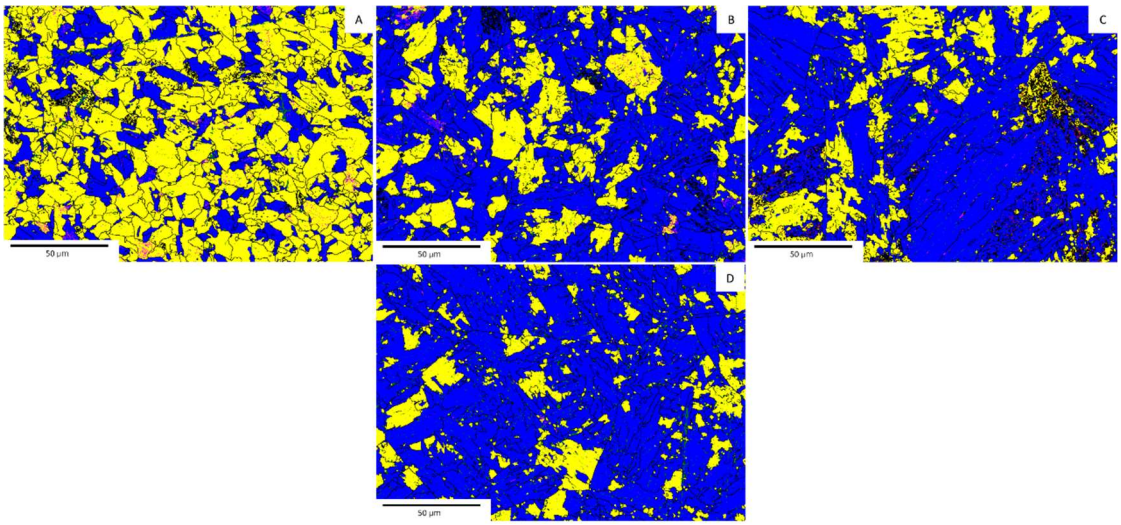

Figure 124 Phase segmentation maps at a cooling rate of 5°C/s, austenitisation temperature a)1000°C, b) 1100°C, c) 1200°C and d) 1300°C. Colour representation: yellow= ferrite, blue=bainite ferrite and pink = retained austenite.

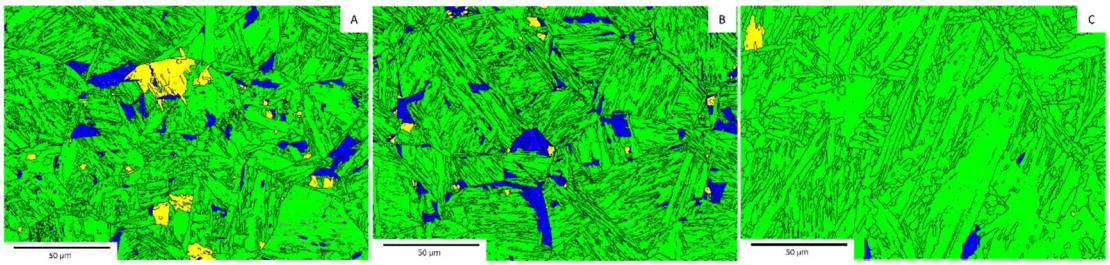

Figure 125 Phase segmentation maps at a cooling rate of 50°C/s, austenitisation temperature a) 1100°C, b) 1200°C and c) 1300°C. Colour representation: yellow= ferrite, blue=bainite ferrite, green=martensite and pink = retained austenite.

4.12 Mechanical properties

Microhardness testing

The tensile strength and hardness are indicators of a metal's resistance to plastic deformation[137]. Microhardness was the first test to determine the mechanical properties in this investigation. During the test, 12 indentations to determine the hardness was performed in each sample. The cooling rate and austenitising temperatures affected the hardness as these parameters determine each phase's volume fraction and prior austenite grain size. The microhardness values are shown in Table 20. The quenching hardness was measured to compare the effect of this treatment with that of a cooling rate of 50°C/s. At 1300°C and a cooling rate of 50°C/s, the volume fraction of martensite is around 95%, which is near the quenching hardness value at 1300°C.

The increment of hardness was observed in all the austenitising temperatures; the higher temperature of austenitisation elevates the hardness in every cooling rate. However, quenching was an exception at 1200°C and 1300°C when the hardness decreases 6 HV1 at 1300°C; this could be associated with the high standard deviation presented at 1100°C, 1200°C and 1300°C. At the highest austenitic temperatures and elevated cooling rate are obtained the highest hardness; these values are related to a significant percentage of martensitic structures in the material. Furthermore, it was observed that the hardness decreases drastically at the lowest cooling rates and austenitising temperatures. Finally, the hardness of the raw material was 231 ± 4.1 HV. The raw material was observed as acicular ferrite in the microstructure. The values of 5°C/s of the cooling rate at 1200°C and 1300°C and 50°C/s of the cooling rate at 1100°C present a similar hardness to the raw material.

Table 20 Microhardness values at different austenitising temperatures and cooling rates.

Austenitising temperature	Vickers microhardness (HV1)			
	Cooling rates			
	0.5°C/s	5°C/s	50°C/s	Quenching
900°C	155 ± 1.7	165 ± 3.0	200 ± 1.8	245 ± 10.0
1000°C	159 ± 3.9	187 ± 2.4	211 ± 3.4	249 ± 4.30
1100°C	187 ± 3.5	207 ± 2.2	227 ± 4.5	324 ± 8.90
1200°C	204 ± 7.9	221 ± 2.8	255 ± 7.4	328 ± 10.3
1300°C	211 ± 5.0	225 ± 6.0	300 ± 6.8	322 ± 4.90

The X80 steel microhardness testing continued with the welding. The heat affected zone was defined using microhardness. Following microhardness indentations, nital etching was done to reveal the microstructure. It was done over 1600 indentations to have a proper hardness behaviour. The indentations were separated by 0.5 mm on the x-axis and 1 mm on the y-axis. To visualise the welding hardness was utilised a hardness mapping code in MATLAB[138] (Figure 126). This map shows the hardness variations of the HAZ between 200 and 240 HV. However, in the centre of the weld, the highest hardness appears at 280HV. The highest hardness zone appears because the welding centre is the most affected zone by heat flow. After all, it receives high temperatures twice during the welding application. The first is in the inside welding beads application, and the second is the outside diameter welding.

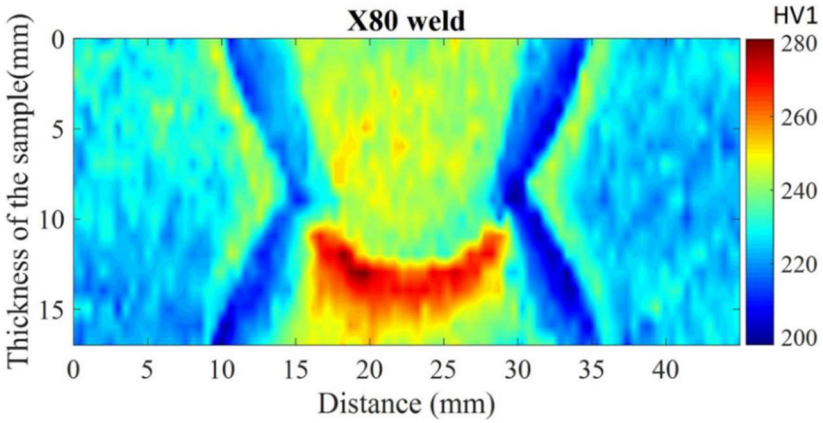

Figure 126 Hardness Mapping of Welding

Tensile testing

The mechanical properties were evaluated with the tensile test to calculate the tensile strength (TS), yield strength (YS) and elongation (%EL) of each condition. The TS in the as-received material was 670 ± 9.1 MPa, the YS was 612 ± 7.5 MPa, and the elongation was 24.8 ± 0.3%. Table 21 shows the evolution of mechanical properties at 0.5°C/s of cooling rate depending on the austenitising temperature. The most significant change in the TS was between 1000°C and 1100°C; this change is related to the difference in the microstructure when the polygonal ferrite + pearlite microstructure evolves to quasi-polygonal ferrite with bainite. Figure 127 illustrates the engineering stress-strain curve with a cooling rate of 0.5°C/s. At 900°C and less at 1000°C discontinuous yielding was observed; these conditions are related to ferrite+pearlite microstructure.

Table 21 Mechanical properties at 0.5°C/s of cooling rate calculated in the tensile test.

Austenitising temperature	Tensile testing		
	The cooling rate of 0.5°C/s		
	TS (MPa)	$YS_{(0.2\%)}$ (MPa)	% EL
900°C	490 ± 1.6	403 ± 7.5	37.7 ± 0.5
1000°C	498 ± 2.7	332 ± 2.0	39.8 ± 0.1
1100°C	598 ± 4.9	447 ± 1.5	31.5 ± 0.5
1200°C	629 ± 5.6	480 ± 4.0	26.8 ± 0.3
1300°C	639 ± 0.4	495 ± 8.5	24.0 ± 0.2

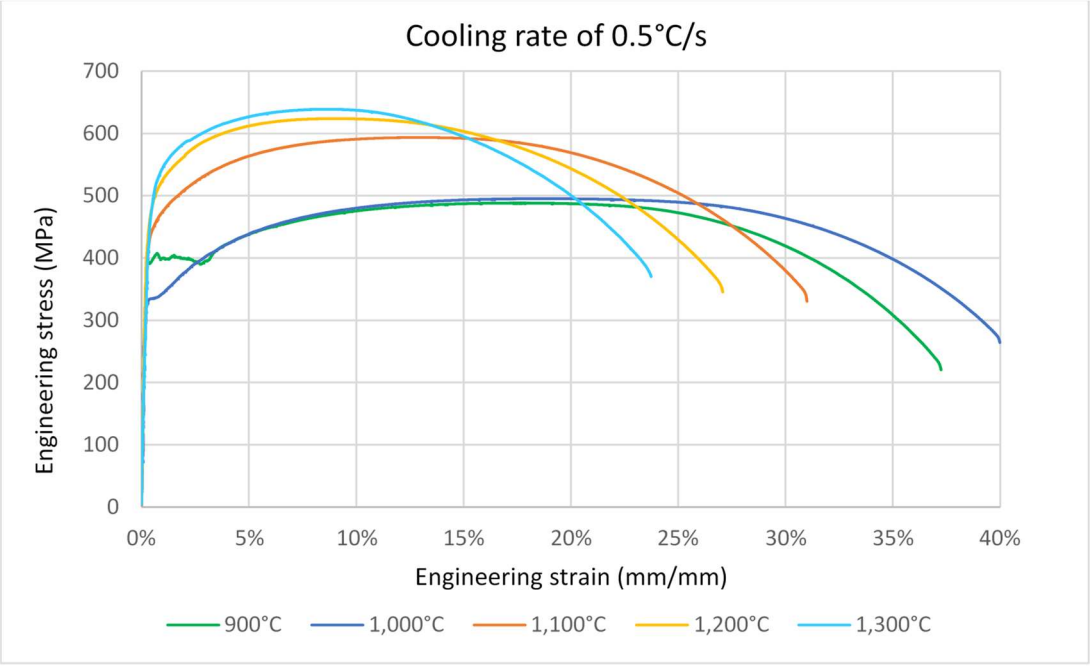

Figure 127 Engineering strain stress curve at a cooling rate of 0.5°C/s

When the cooling rate increases, the tensile and yield strength also elevate (Table 22). The initial values at a lower austenitising temperature of TS had better behaviour than the cooling rate of 0.5°C/s, and the elongation did not reduce significantly (Figure 128). At 900°C, a mixture of ferrite with pearlite was observed, and the ferrite was less smooth than the ferrite at 0.5°C/s of cooling rate. At 1000°C, the quasi-polygonal ferrite with bainite areas appeared; this irregular shape in the ferrite produces more dislocations, increasing the strength. Above 1100°C of austenitising temperature, the strength started to be close to the values of 0.5°C/s of cooling rate. The slow and medium cooling rates at these temperatures initiated the bainite transformation in the steel.

Table 22 Mechanical properties at 5°C/s of cooling rate calculated in the tensile test.

Austenitising temperature	Tensile testing		
	The cooling rate of 5°C/s		
	TS (MPa)	YS (0.2%) (MPa)	% EL
900°C	570 ± 0.3	352 ± 4.5	35.2 ± 0.1
1000°C	599 ± 1.9	425 ± 1.0	31.4 ± 0.4
1100°C	624 ± 6.2	490 ± 2.5	28.5 ± 0.2
1200°C	646 ± 6.7	530 ± 2.0	24.4 ± 0.5
1300°C	651 ± 2.7	530 ± 4.0	24.3 ± 0.7

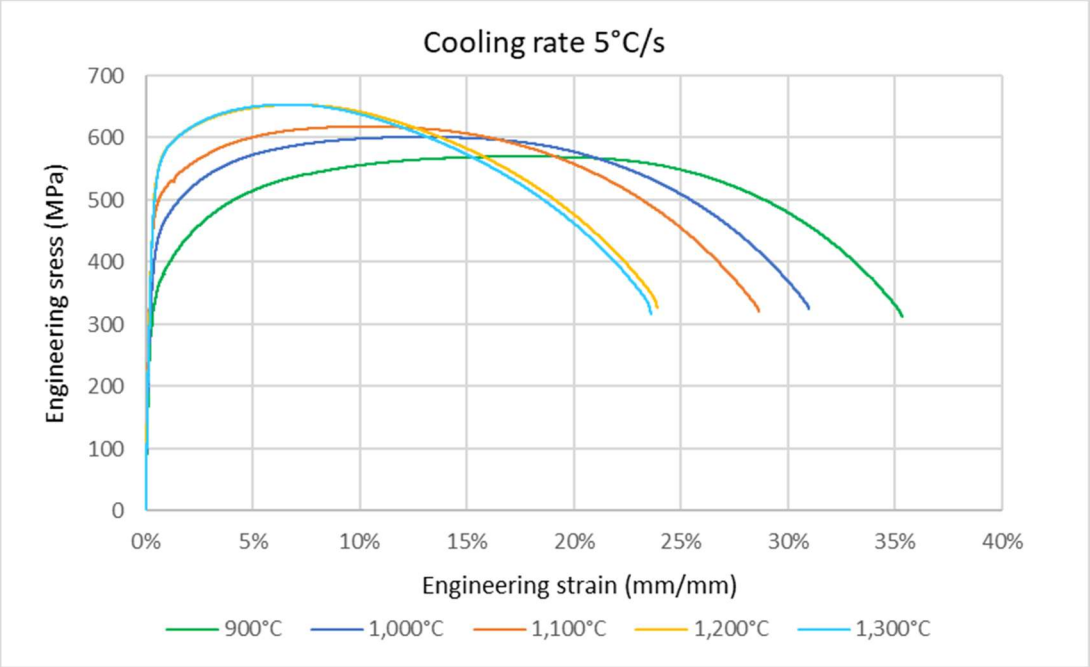

Figure 128 Engineering strain stress curve at a cooling rate of 5°C/s

Finally, the fastest cooling rate is reviewed (Figure 129). At 50°C/s was obtained the highest tensile and yield strength; at the same time, the elongation decreased (Table 23). Starting at 900°C, the TS and YS showed a substantial increase in mechanical properties. The TS at 900°C had a variation of 25% compared with 0.5°C/s and 13% with a 5°C/s of cooling rate. At this temperature was possible to observe the effect of ferrite in the strength increment compared with 0.5°C/s and 5°C/s. Between 1000°C and 1100°C appeared a significant reduction in terms of elongation in the material. At 1100°C, the martensite volume fraction increased; this diminished the elongation. Above 1200°C, the TS, YS and elongation did not have a significant variation; in these austenitising temperatures appear, principally, the martensite phase appears.

Table 23 Mechanical properties at 50°C/s of cooling rate calculated in the tensile test.

Austenitising temperature	Tensile testing		
	The cooling rate of 50°C/s		
	TS (MPa)	YS (0.2%) (MPa)	% EL
900°C	658 ± 2.7	495 ± 1.0	29.2 ± 0.8
1000°C	716 ± 6.3	570 ± 7.5	25.3 ± 0.5
1100°C	762 ± 2.1	600 ± 2.0	20.0 ± 0.5
1200°C	814 ± 2.6	648 ± 6.0	18.2 ± 0.3
1300°C	830 ± 1.8	650 ± 2.0	18.4 ± 0.3

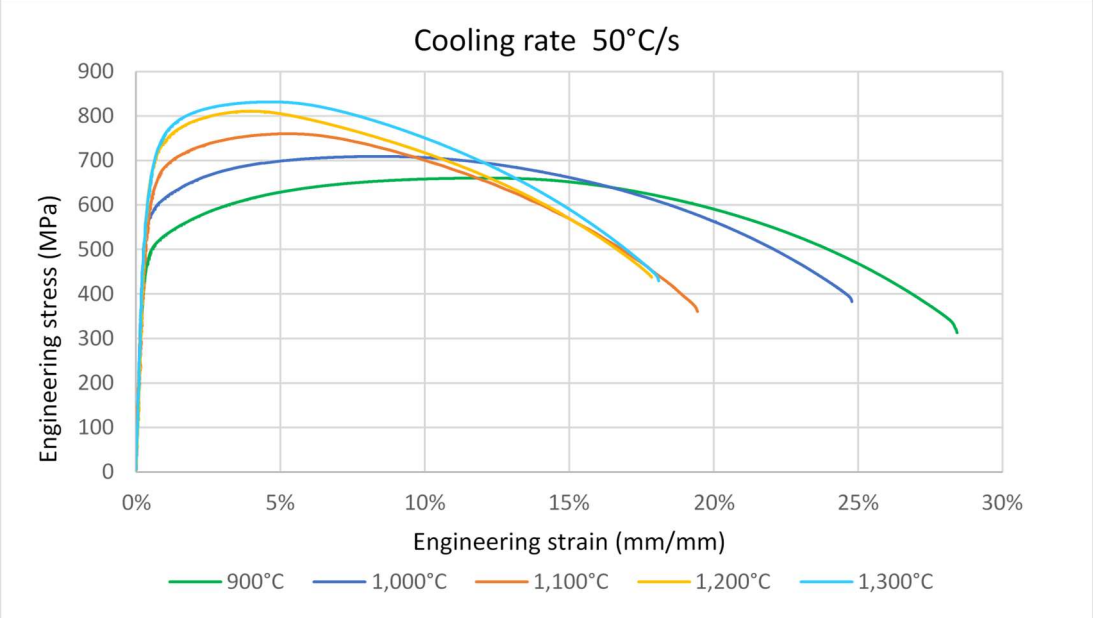

Figure 129 Engineering strain stress curve at a cooling rate of 50°C/s

Impact testing

To determine one measure of the steel's toughness, Charpy impact testing was performed on sub-size specimens for each condition at test temperatures of 20°C, 0°C and -50°C. The lowest temperature was selected to verify if it does not exist an embrittlement phenomenon at freezing temperatures. The samples in this thesis were machined with a 9.1mm width according to the drawing in Section 3.17. The raw material of X80 steel had the impact fracture energy values of 31.30±0.63 J at 20°C, 32.26±0.16 J at 0°C and 31.01±1.01 J at -50°C. Table 24 shows the impact results with a cooling rate of 0.5°C/s. The values at 900°C of austenitising temperature are the only ones which appeared with a slight increase in toughness compared with the raw material. Figure 130 illustrates the impact energy's tendency at a low cooling rate velocity.

Table 24 Charpy testing at a cooling rate of 0.5°C/s with three temperatures of the test 20°C, 0°C and -50°C.

Austenitising temperature	Impact fracture energy at a cooling rate of 0.5°C/s		
	The temperature of the testing		
	20°C	0°C	-50°C
	Joules	Joules	Joules
900°C	31.36 ± 0.78	32.60 ± 0.68	34.31 ± 0.75
1000°C	29.64 ± 0.59	31.52 ± 0.35	32.04 ± 0.93
1100°C	30.24 ± 0.18	30.79 ± 0.68	31.58 ± 1.89
1200°C	30.89 ± 0.68	30.96 ± 0.62	29.63 ± 0.57
1300°C	29.44 ± 0.68	29.98 ± 0.39	29.04 ± 0.55

At 5°C/s of cooling rate displayed better behaviour than the cooling rate of 0.5°C/s and 50°C/s (Table 25). The testing at 20°C and 0°C showed similar behaviour in terms of toughness. Furthermore, at -50°C displays a minor increment in energy absorption. Figure 131 illustrates the tendency of the impact testing at a 5°C/s of cooling rate.

Table 25 Charpy testing at a cooling rate of 5°C/s with three temperatures of the test 20°C, 0°C and -50°C.

Austenitising temperature	Impact fracture energy at a cooling rate of 5°C/s		
	The temperature of the test		
	20°C	0°C	-50°C
	Joules	Joules	Joules
900°C	31.64 ± 0.51	31.65 ± 0.28	33.32 ± 1.17
1000°C	30.70 ± 0.83	33.20 ± 1.39	33.63 ± 0.91
1100°C	31.35 ± 0.19	31.62 ± 0.06	33.91 ± 0.75
1200°C	32.89 ± 0.43	31.82 ± 0.57	34.03 ± 0.31
1300°C	31.78 ± 0.03	31.54 ± 0.38	33.27 ± 0.90

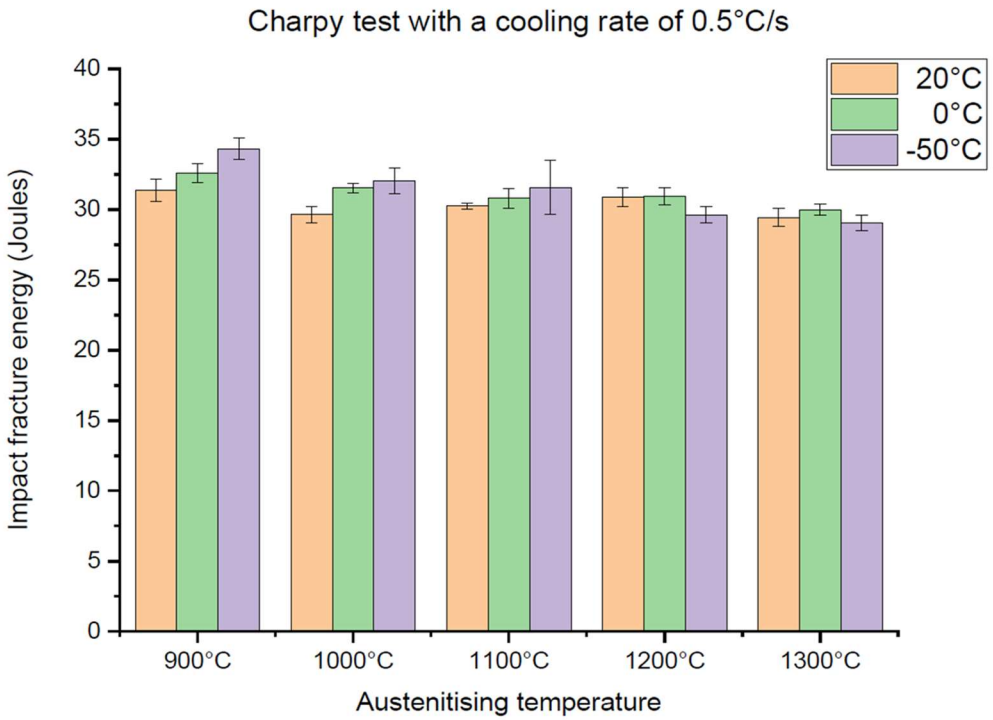

Figure 130 Impact fracture energy results with standard error at different temperatures of austenitisation and a cooling rate of 0.5°C/s.

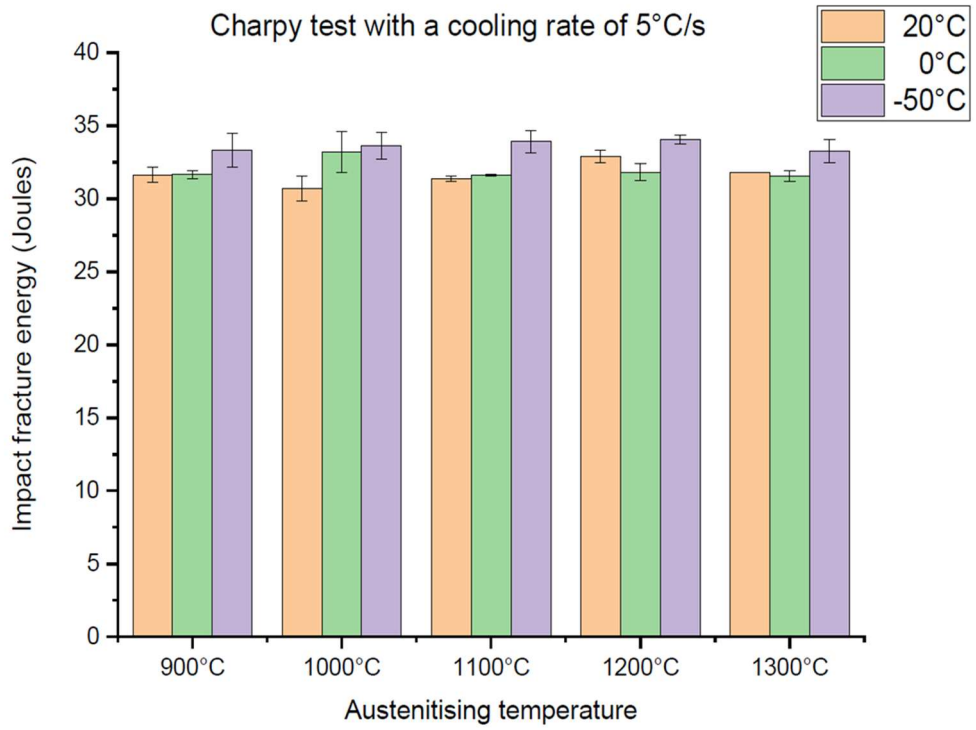

Figure 131 Impact fracture energy results with standard error at different temperatures of austenitisation and a cooling rate of 5°C/s.

Lastly, the results at 50°C/s of cooling rate are shown in Table 26. At lower austenitising temperatures showed the highest toughness compared to above 1100°C. At 1200°C and 1300°C displayed a declining behaviour of toughness compared with the cooling rates of 0.5°C and 5°C; also, with the lower austenitising temperatures at the same cooling rate. At these temperatures, a massive martensitic structure appears in the microstructure. Figure 132 illustrates the tendency of the impact testing at a 50°C/s of cooling rate.

Table 26 Charpy testing at a cooling rate of 50°C/s with three temperatures of the test 20°C, 0°C and -50°C.

Austenitising temperature	Impact fracture energy at a cooling rate of 50°C/s		
	The temperature of the testing		
	20°C	0°C	-50°C
900°C	33.98 ± 0.24	34.25 ± 1.37	33.81 ± 2.19
1000°C	31.38 ± 0.31	33.73 ± 1.15	34.37 ± 0.76
1100°C	30.21 ± 0.82	33.56 ± 0.47	31.55 ± 0.28
1200°C	29.97 ± 0.18	29.56 ± 0.83	30.97 ± 1.95
1300°C	29.79 ± 0.80	27.44 ± 0.96	29.05 ± 0.32

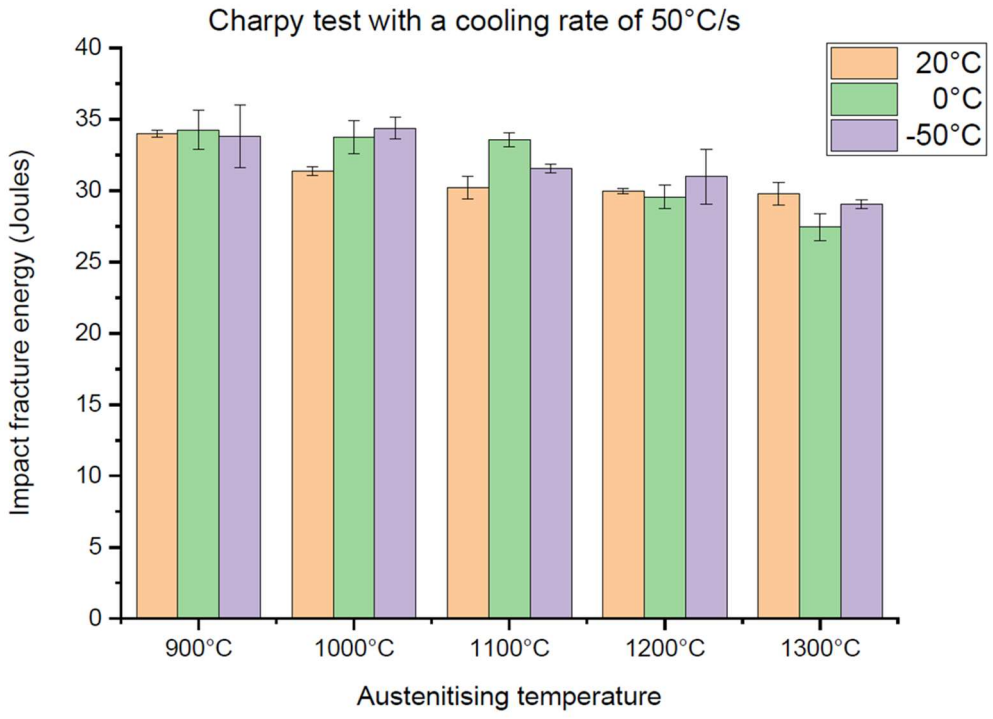

Figure 132 Impact fracture energy results with standard error at different temperatures of austenitisation and a cooling rate of 50°C/s.

After the impact testing was done, the fracture surfaces were analysed in the SEM. The conditions examined were the austenitising temperatures of 900°C and 1300°C with cooling rates of 0.5 and 50 °C/s. Figure 133 shows the images of the fracture in SEM at a cooling rate of 0.5°C/s. In all the conditions, a ductile fracture was observed. At 900°C, the dimples appeared more distributed in the image.

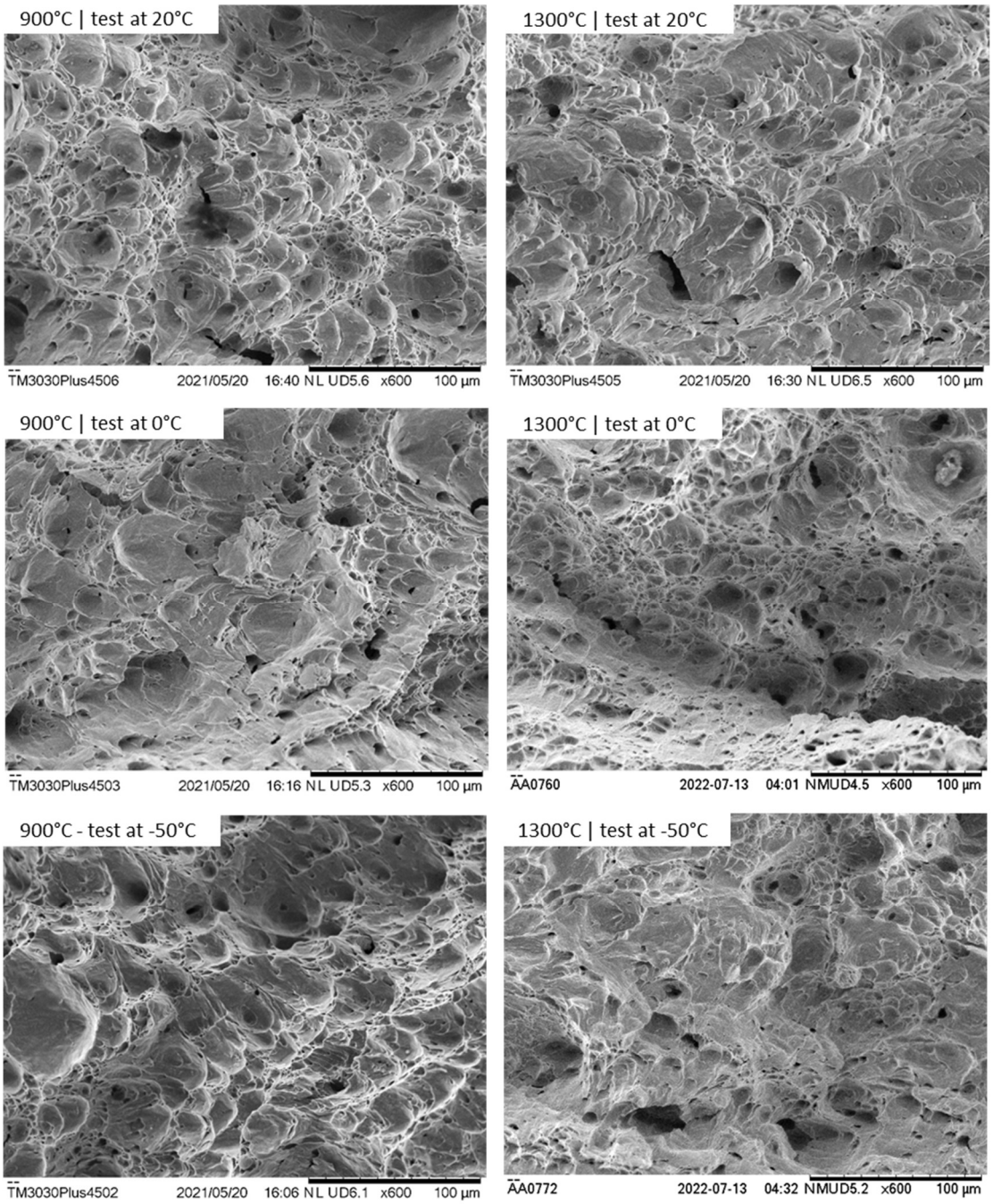

Figure 133 SEM images of a fracture zone in Charpy testing at 0.5°C/s of cooling rate.

Figure 134 illustrates the fracture SEM images at 50 °C/s. At 50°C/s of cooling rate was observed as a ductile fracture in all the conditions. There was no clear pattern of intergranular fracture in any of the conditions. The effect of slow and high cooling rates was associated with the transgranular fracture mechanism (ductile).

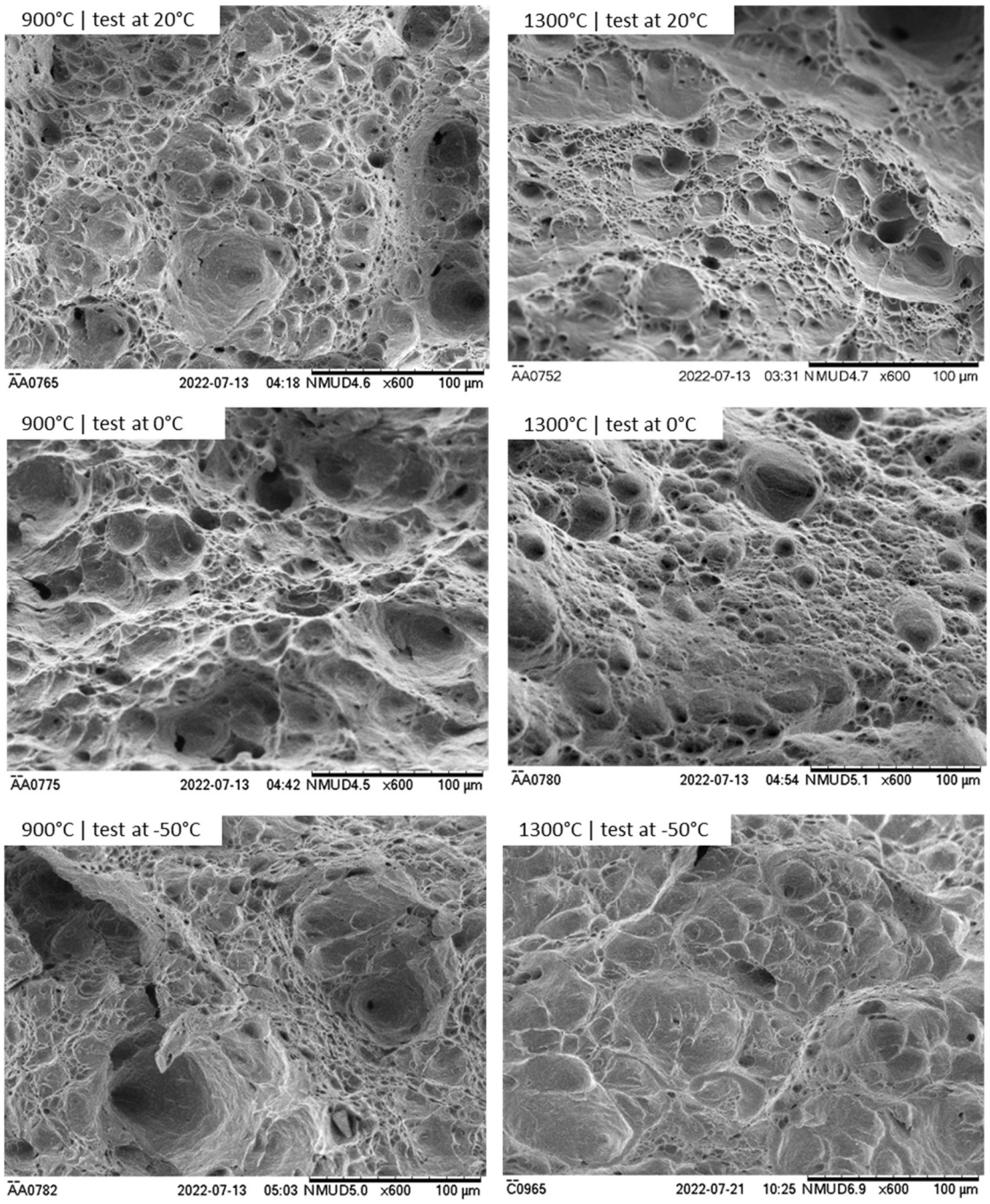

Figure 134 SEM images of a fracture zone in Charpy testing at 50°C/s of cooling rate.

Summary

Chapter 4 shows the results obtained in the present work. The chapter started with the characterisation of the raw material. Then, it continued with the hardness behaviour in the heat affected zone welding zone in the X80 steel. After that, it showed the transition temperatures obtained in the dilatometry and theoretical formulas to compare with the experimentation values. Then, the CCT diagrams were used to evaluate the microstructures present in each treatment.

Afterwards, the solubility of niobium was calculated, and the prior austenite grain size was performed between 900°C to 1300°C. After that, it was reviewed the resulting microstructures at 0.5°C/s, 5°C/s and 50°C/s using SEM and optical microscopy. Then, the precipitates were evaluated with the carbon extraction replica technique. As a final characterisation, EBSD was used to quantify the phases in each treatment.

Finally, the mechanical properties of hardness, tensile and impact were reported. The impact test was done at 20°C, 0°C and -50°C using sub scale Charpy specimens. The frozen temperature was selected to evaluate if existed a ductile-brittle transition temperature (DBTT). The sub scale Charpy specimens allowed to observe a tendency between the different heat treatments of the material.

Chapter 5

Discussion

5.1 Prior austenite grain size effect on the microstructure

The initial prior austenite grain size was critical to understand the microstructure evolution after the heat treatment. In this work, a holding time of 30 minutes for 10mm thick sections was selected to ensure complete austenitisation[139,140]. The X80 raw material had an austenite grain diameter of 3 ± 0.17µm at 850°C with an Ac_3 of 810°C. The PAGs increased with the austenitisation temperature from 3.15 ± 0.29µm at 900°C to 97.9 ± 18.12µm at 1300°C. Above 1200°C, the solubility precipitates of niobium rapidly increased, affecting the PAGs. At 1280°C, the niobium precipitates were completely dissolved, ultimately obtaining a rapid PAGs growth between this temperature and 1300°C.

A homogeneous structure was observed in the as-received steel during the initial characterisation. The microstructure showed an equiaxed and well-distributed form in the austenite grains. It is well known that the prior austenite grain size directly affects the mechanical properties and the microstructural evolution. Because of that, it is essential to measure and control the PAGs to understand the subsequent behaviour after heat treatment [141-145].

The heat affected zone displays a microstructural evolution with different phases only in a few millimetres. Because the welding fusion zone reaches temperatures up to 1500°C, near the fusion line formed coarse PAGs. It was observed that the PAG's growth at the same cooling rate elevates at the same time the mechanical properties. Also, the prior austenite grain size had a critical function in the evolution of microstructures. This is exemplified in the coarse prior austenite grain size; coarse PAGs evolved in bainite and martensite phases meanly [146]. The next section of this Chapter will compare the effect of various cooling rates on the microstructural evolution and the resulting mechanical properties.

The behaviour of austenite grain size with the temperature enabled us to observe the influence on the decomposition kinetics and the following microstructures. [145,147,148]. It was observed that with a fine austenite grain size and slow cooling rate, the resulting microstructure consisted of polygonal ferrite and small areas with pearlite. However, when the PAGs started to coarsen, the resulting microstructure was meanly bainite at a slow cooling rate. This occurs because the grain boundaries limit the bainite sheaf growth. But in coarse PAGS, the bainite sheaf has plenty of space to build up inside the coarse austenite grain[149,150]. In addition, at a 50°C/s of cooling rate, ferrite microstructure transformed from initially fine austenite grain size was observed. At coarse PAGs and 50°C of cooling rate, the resulting microstructure was predominantly martensite when the temperature increased to 1300°C. The martensite microstructure promptly increased the mechanical properties of the material.

5.2 Selecting the austenitisation temperatures

The austenitisation temperatures were selected with the Iron Carbon adapted HAZ diagram (Figure 135). From this diagram, it was possible to observe how the temperature influences the grain growth and recrystallised zone depending on the fine or coarse austenite [139]. During dilatometry testing, the A_{C3} temperature was ~810°C; because of this, the analysis of this research started at 900°C. At this temperature, it was obtained a minor change in the PAGs compared with the raw material. The highest temperature of this analysis was 1300°C; at this temperature, it was possible to observe the effect of coarse austenite grains in the microstructure evolution. The heat affected zone's area was no longer than 6 mm from the fusion zone. Also, the Fe-C diagram displayed other zones affected by the temperature: partially transformed (interphase) and tempered zone; however, those zones are not part of this research.

Then, temperatures were selected between the limit conditions range because it was necessary to obtain a tendency of resulting microstructures. The temperature range of 100°C was selected to have a trend. With those ranges of temperatures was straightforward to observe the microstructure evolution and the niobium solubility effect when austenitisation temperature increases. The temperature ranges allowed us to observe the effect of austenite at fine and coarse grain size. As was evaluated in the previous chapters, the austenite grain growth is one of the most critical parameters in the analysis of welding. During this research, 30 min of holding time was chosen to study the effect of prior austenite grain size when the austenite was fully transformed [115].

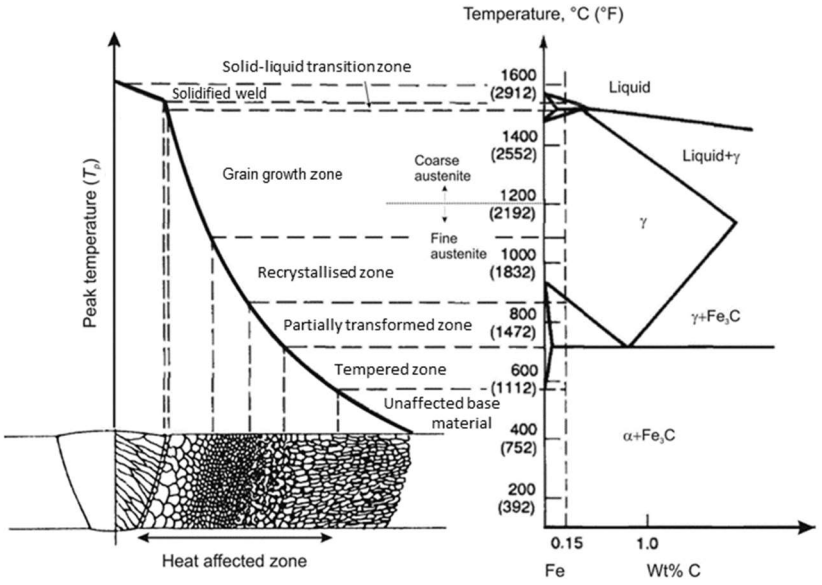

Figure 135 Iron Carbon diagram represents microstructural variation in the HAZ [74].

5.3 Prior austenite grain size effect on the mechanical properties

The effect of prior austenite grain size on the mechanical properties was observed during all the heat treatments. The microhardness and tensile strength increased simultaneously as the temperature was increased. The prior austenite grain size determines the resulting phases in the austenite decomposition. Coarse austenite grain size positively affects the formation of bainite and martensite because the bainite sheaf has more space to build up inside the grains [149,150].

Figure 136 shows the behaviour of microhardness in the different heat treatments and austenitisation temperatures. At 0.5°C/s of cooling rate was observed the bainite effect in the hardness above 1100°C. Also, at 50°C/s of cooling rate the appeared of martensite directly affected the microhardness meanly above 1200°C.

During testing, bainite and martensite had the highest values of tensile strength. On the other side, fine austenite grain size favoured the formation of polygonal ferrite and pearlite. Fine austenite grain size remains more grain boundaries; those boundaries allow the nucleation of reconstructive mechanisms such as pearlite and polygonal ferrite [36,42,149,151]. At a 50°C/s of cooling rate and above 1200°C of austenitisation temperature was shown a significant increase in tensile strength, in these conditions the PAGs grew from 44.8 ± 1.93 to 97.9 ± 18.2 (Figure 137). At those temperatures, the martensite volume fraction was above 89%.

In terms of the prior austenite grain size effect, the most significant change in tensile strength was at 0.5°C/s. At 1000°C, the strength was 498 MPa, and at 1100°C was 598 MPa; this increase was a 20% difference (Figure 137). At 0.5°C/s and 5°C/s with temperatures up to 1100°C, the tensile strength was similar with less than 4% differences. In the microhardness testing, the significant hardness increase appeared at 50°C/s of cooling rate; in the PAGS of 1100°C to 1200°C, the growth is 12%, while at 1200°C to 1300°C the increment is 18%.

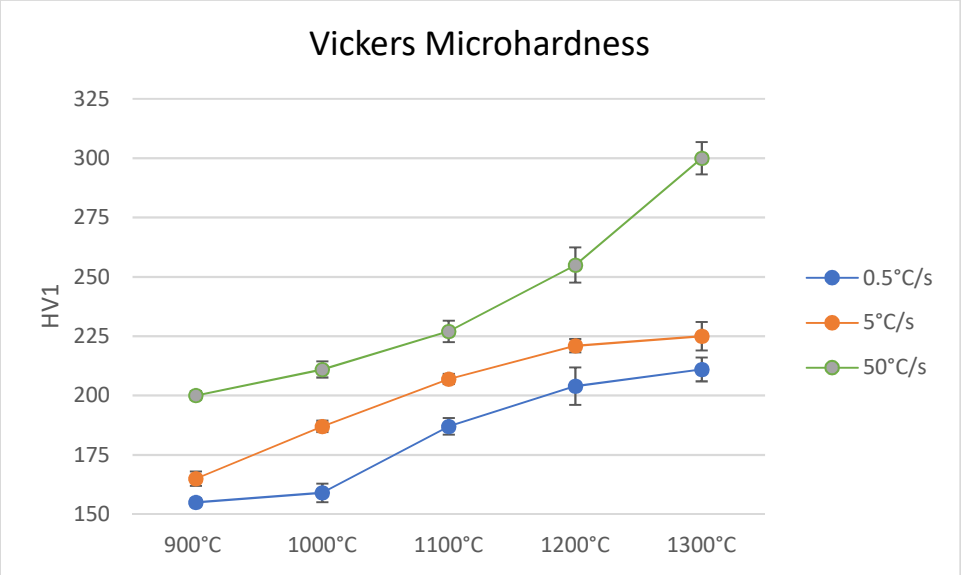

Figure 136 Microhardness values at cooling rates of 0.5°C/s, 5°C/s and 50°C/s with austenitisation temperatures between 900°C and 1300°C.

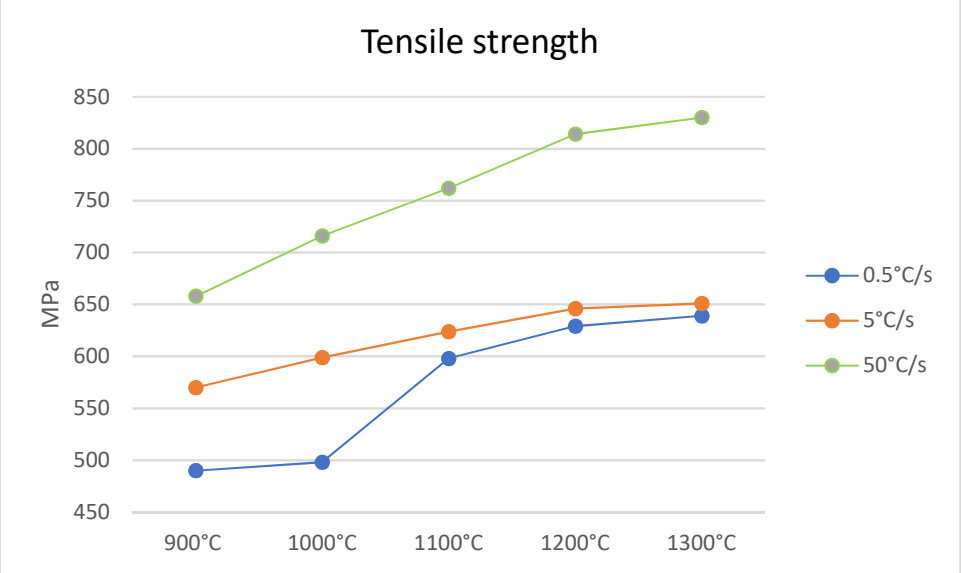

Figure 137 Tensile strength at cooling rates of 0.5°C/s, 5°C/s and 50°C/s with austenitisation temperatures between 900°C and 1300°C.

The elongation was another analysed mechanical property; and it tended to trend in the opposite direction to that of tensile strength and microhardness. The increase of austenitisation temperature reduced at the same time the elongation. The lowest elongation value appeared at a cooling rate of 50°C/s; above 1200°C, the elongation drastically falls to 18%; this fall is related to the increase of martensite volume fraction at high austenitisation temperatures. The highest elongation appeared at the smallest prior austenite grain size and slow cooling rate; in these conditions, the microstructure was a mixture of polygonal ferrite and pearlite (Figure 138).

The elongation remained diminished as the austenitisation temperature raised, except at 1000°C and 0.5°C/s of cooling rate. At this temperature, the elongation slightly increased compared with the lowest austenitisation temperature. At 900°C and 1000°C appeared, discontinuous yielding (Section 4.12), a typical behaviour in low carbon steels. This phenomenon occurred during the deformation above the yield point, resulting from the interaction between mobile dislocation and solute atom[152]. The increase in holding time and austenitisation temperatures inhibit the discontinuous yielding because it diminishes the solute carbon concentration in the microstructure [152].

The highest elongation diminish was between 1000°C and 1100°C, particularly in the cooling rates of 0.5°C/s and 50°C/s. In these conditions, the elongation reduced drastically. At 0.5°C/s, the transformation evolved from polygonal ferrite + pearlite to polygonal ferrite + quasi-polygonal ferrite with bainite. At 50°C/s, the microstructure evolved from a mixture of ferrite to mainly a combination of martensite with small zones of bainite and quasi-polygonal ferrite. The increase in martensite volume fraction reduced the elongation significantly at high cooling rates.

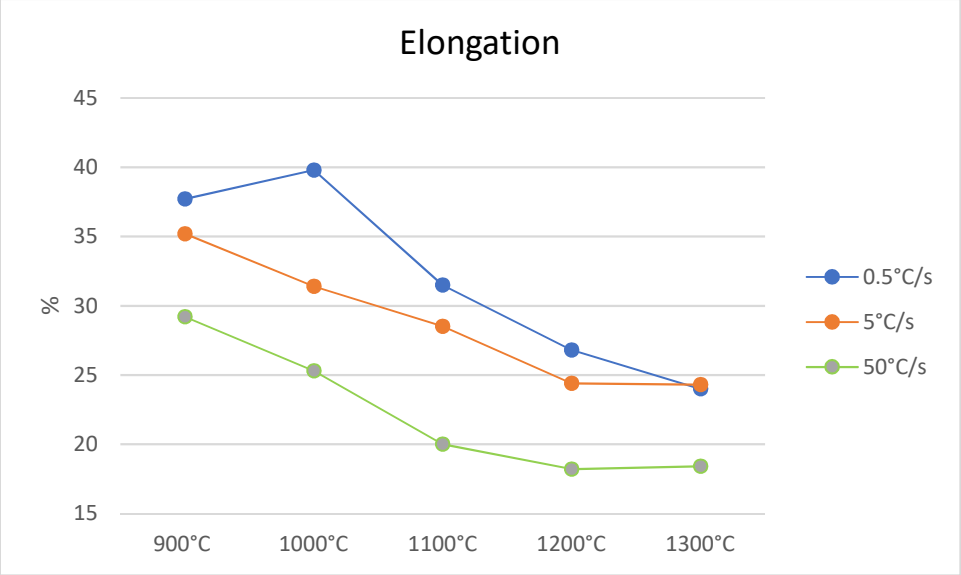

Figure 138 Elongation at cooling rates of 0.5°C/s, 5°C/s and 50°C/s with austenitisation temperatures between 900°C and 1300°C.

Also, the prior austenite grain size affected the toughness of the material. Figures 139-141 show the material's toughness at different testing temperatures. During the fracture analysis in the SEM, a ductile fracture was observed in all conditions [153-155] (Figures 133-134). It did not appear to have an intergranular fracture in any analysed samples. The lowest temperature testing was selected at -50°C. This temperature offered a reference to understand the material's behaviour at sub-ambient temperatures.

The first testing was performed at room temperature. At 0.5°C/s and 5 °C/s displayed similar behaviour; the energy absorption did not show a relevant change in toughness. At high austenitisation temperatures, the energy absorption did not significantly differ at room temperature and 0°C. In these conditions, the microstructure showed an increase in bainite volume fraction. At the cooling rate of 50°C/s, the highest austenitisation temperature showed the lowest impact energy; this was related to the evolution of mostly martensite microstructure (Figures 139-140).

The increase of austenitisation temperatures formed M/A constituents at a medium cooling rate. The presence of M/A constituents has been widely studied in previous works. Different authors have reported that the appearance of M/A constituents decreases the material's toughness [156-160]. However, the acquired results did not show a negative effect of toughness.

The behaviour was stable at the cooling rate of 5°C/s, with values between ~ 31 to 33 J. At this temperature, it appeared the M/A constituents at 1200°C and 1300°C. The formation of M/A constituents in the microstructure did not show a decrease in the material toughness. The mixture of bainite and M/A constituents in the microstructure showed a steady behaviour in toughness; this was also observed in the lowest temperature testing (Figures 139-141).

Figure 141 shows the impact testing at -50°C. At slow and high cooling rates had similar behaviour in toughness. The toughness decreased when the prior austenite grain size was coarse, while the fine PAGs showed the most increased toughness. At 5°C/s showed stable behaviour even in high austenitisation temperatures. These impact values could be related to the mixture of bainite and M/A constituents at high austenitisation temperatures. The martensite and bainite microstructures were more susceptible to toughness diminish.

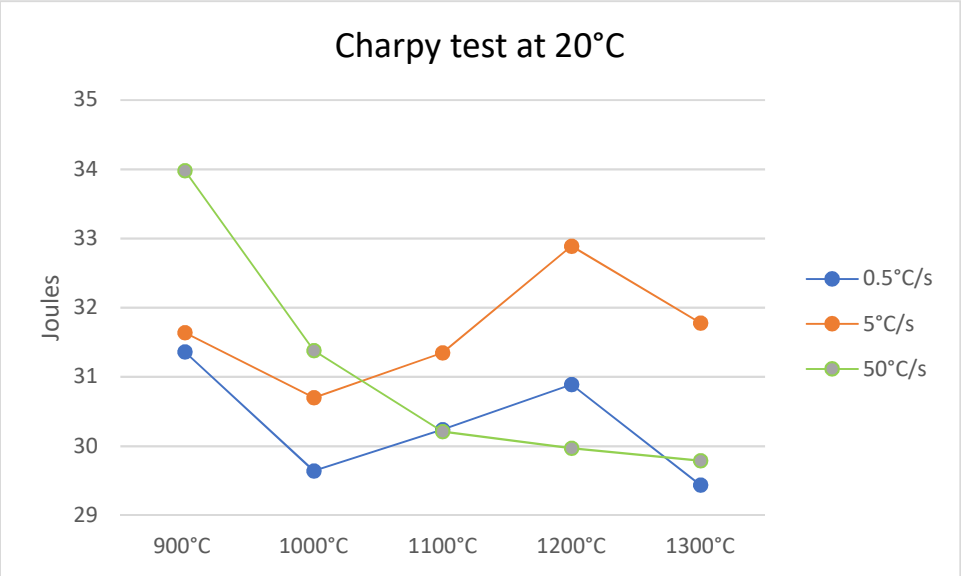

Figure 139 Impact testing at 20°C with cooling rates of 0.5°C/s, 5°C/s and 50°C/s with austenitisation temperatures between 900°C and 1300°C.

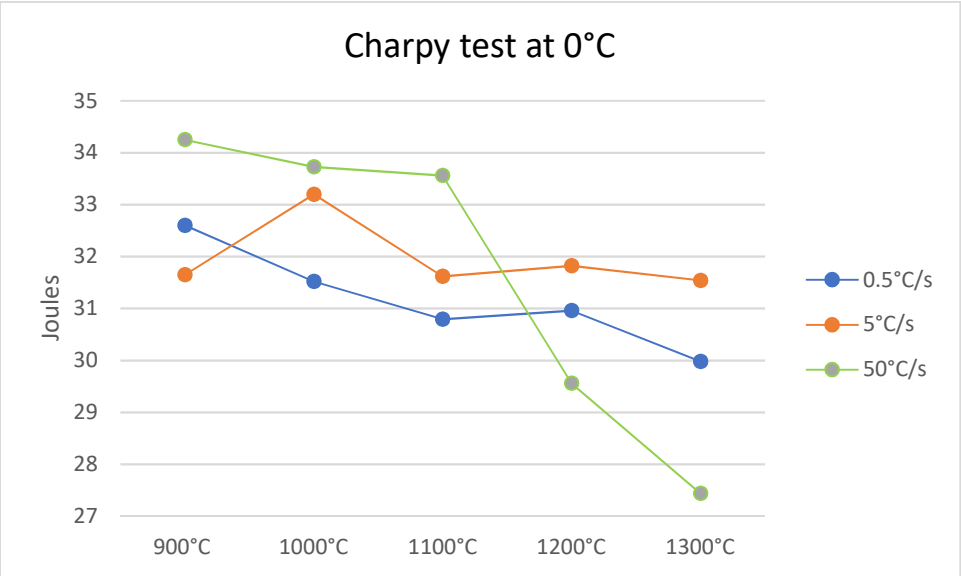

Figure 140 Impact testing at 0°C with cooling rates of 0.5°C/s, 5°C/s and 50°C/s with austenitisation temperatures between 900°C and 1300°C.

The highest toughness values at a slow cooling rate appeared in a mixture of polygonal ferrite and pearlite microstructure. The effect of pearlite on toughness has been documented in previous works. The size of pearlite colonies is essential to control the material's toughness; cementite bands in a pearlite colony are a relevant pattern in the toughness. Thick cementite plates and coarse grain size in the pearlite results in toughness diminish.

Furthermore, fine cementite plates in fine pearlite colonies provide a better toughness, obtaining a pattern of ductile fracture [161,162]. Appendix I.8 shows the fine cementite plates in the pearlite at 900°C and 1000°C of austenitisation temperature. Some studies have reported that ferrite/pearlite microstructures are more susceptible to low temperatures in impact testing [163]. However, even at low testing temperatures, the toughness did not decrease in the polygonal ferrite/ pearlite microstructure.

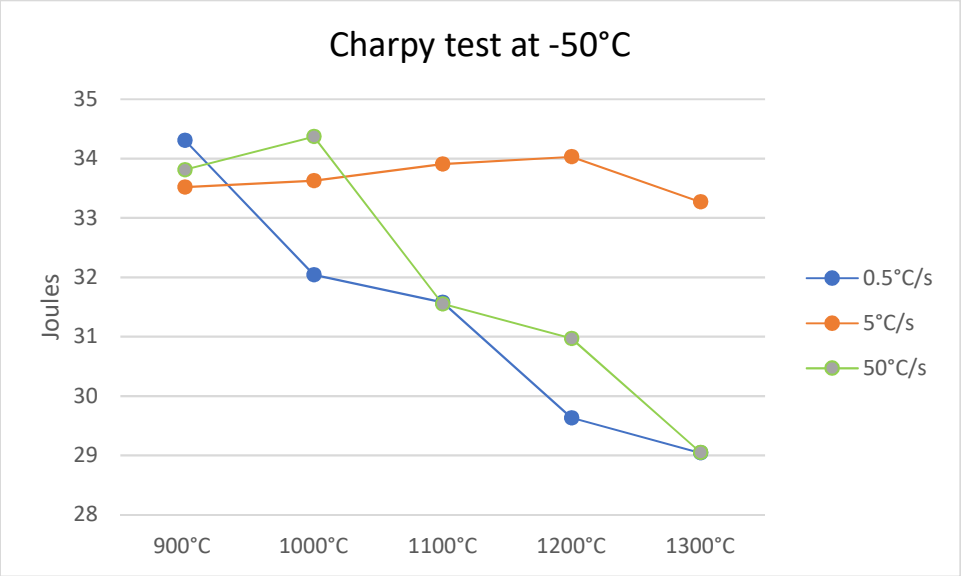

Figure 141 Impact testing at -50°C with cooling rates of 0.5°C/s, 5°C/s and 50°C/s with austenitisation temperatures between 900°C and 1300°C.

Finally, a clear transition zone was not observed during the impact testing because of the lower temperatures. Different researchers have reported a transition zone in X70 and X80 steel at -40°C with similar carbon content but less niobium in the material's composition[164-166]. At high austenitisation temperatures, a rapid decrease in the toughness appeared except at 5°C/s of cooling rate; this temperature was related to the formation of M/A constituents. The results indicate that the material could resist at least -50°C without the embrittlement phenomenon.

5.4 Precipitation

Grain growth and recrystallisation are restricted using elements such as vanadium, titanium, aluminium and niobium. Niobium has better behaviour in delaying the recrystallisation of austenite; this effect in recrystallisation was essential because the material had 0.094% Nb. The solubility control of the refining additions was crucial in the behaviour of prior austenite grain size (Figure 142). The minor reheating temperature was related to the small prior austenite grain size. This effect was linked with the solubility of carbides in the solution, such as NbC, NbCN, and TiN [167-169].

The precipitation affects the austenite grain boundaries as well. The boundaries of austenite grains are crucial in nucleation sites for different microstructures such as ferrite, martensite and bainite. At high temperatures, previous precipitates dissolve shaping new finer precipitates in the following process [168-170]. Figure 143 shows the calculated niobium and titanium in solution using the solubility products NbC[48], NbCN[47], and TiN[134]. NbC and NbCN calculus showed similar niobium in solution at the same austenitisation temperatures. While TiN required above 1100°C to dissolve the titanium in solution.

The temperature influences the precipitation kinetics. At high temperatures, the growth kinetics leads rapidly in the niobium carbides. However, titanium requires more temperature to dissolve. Above 1280°C, the niobium carbides all dissolved; while titanium nitrides will dissolve at 1,653°C. This solubility product of niobium and titanium was observed in the behaviour of prior austenite grain size. At 1200°C, the niobium solubility was 0.050%; at 1280°C elevated to 0.090%, and finally, at 1300°C increased to 0.1%. At 1300°C, the titanium in solution was 0.005%, and the material contained 0.014% Ti. At the highest temperature of the testing, all the niobium was in solution, but the titanium was dissolved only in 0.005 %wt. This titanium solubility effect explained why the austenite grain did not grow more than 100 μm on average because titanium nitrides suppressed grain growth after niobium was all in solution[171].

The niobium solubility has an essential effect on austenite decomposition. Niobium increases the boosts coarse carbide formation in bainite and lath-type martensite[172]. Also, the fine precipitates of niobium which are uniformly allocated in the grains, increase the strength. The effect is a consequence of the interaction between dislocations and dispersions [173]. This is because the NbC carbides act as a barrier in the dislocations increasing the strengthening effect.

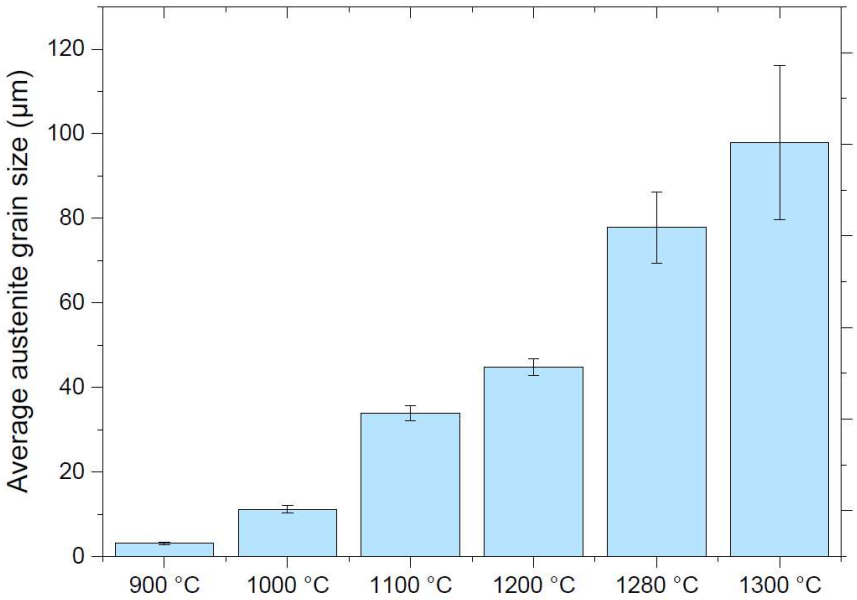

Figure 142 Average austenite grain size at different temperatures.

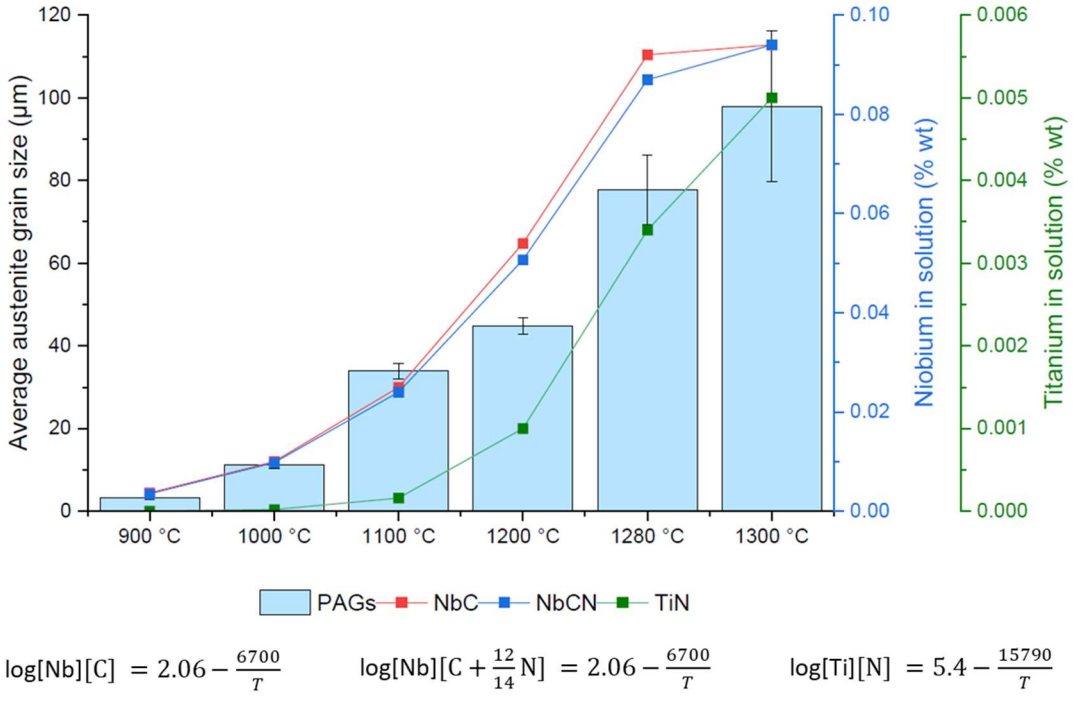

Figure 143 Comparative of austenite grain size with the calculated niobium and titanium in solution using the solubility products NbC[48], NbCN[47] and TiN[134] at different austenitisation temperatures.

5.5 Weld thermal cycle design for X80 steel

The heat affected zone is the most critical area in welding. In the welding process, fusion temperatures reach temperatures above 1500°C in the material base near the fusion line[74]. The temperature variance between the material base and weld metal produces a $\triangle$T. The area localised near the fusion zone achieves high temperatures and a significant increment in grain growth. As the base metal is far from the melting zone, ΔT decreases to the point where the temperature is below Ac_3. The Partially austenitised (Ac3 > T > Ac1) and tempered zone (Ac1 > T) are affected by the welding. However, there did not experience austenite grain growth and were not considered in this research.

As explained in the background, the heat affected zone produces a modification in the microstructure and the effect on the material´s mechanical properties. The velocity and power source in welding are used to control the cooling rate during application. High-velocity results in fast cooling rates because the heat transfer could not sufficiently elevate the base material's temperature; therefore, the plate cooling down faster. The same phenomenon appears with the heat source; thus, the cooling rate in the heat affected is affected by the heat source and velocity during welding application.

The heat affected zone is affected by the cooling rate, the austenitising temperature and holding time. These parameters directly affect the final microstructure of the material[1]. In the case of the material examined in this research, the microstructure is essential because of the high niobium content of 0.094%. Niobium content restricts the grain growth of austenite during the heating process. Also, the niobium in the solution contributes to the formation of different microstructures, such as bainite.

The API standard in X80 steel specifies a maximum of 0.22% of carbon[2]. The carbon content is essential to satisfy the maximum carbon equivalent. At high carbon content, the welding tends to form martensite producing a brittle material. The X80 steel of this research contained 0.06% C and a carbon equivalent of 0.39, according to the International Institute of Welding. This number indicates the weldability behaviour; according to the classification of weldability with a CE(IIW) of the material, it had very good weldability (Table 27)[174]. Also, the carbon equivalent was used to predict the hardenability in the heat-affected zone.

Table 27 Common value classifications of carbon equivalent [174]

Carbon equivalent (CE)	Weldability
Up to 0.35	Excellent
0.36-0.40	Very good
0.41-0.45	Good
0.46-0.50	Fair
Over 0.50	Poor

In the X80 mechanical properties, the API standard specifies a minimum YS of 80,000 psi (552 MPa) and a maximum of 100,000 psi (690 MPa), while a minimum TS of 90,000 psi (621 MPa) and a maximum of 120,000 psi (827 MPa) and a minimum elongation of 20.5% [175]. The raw material of this research had a yield strength of 610 MPa and ultimate strength of 630 MPa with 24% elongation. Therefore, the raw material accomplished the X80 API standard. The cooling rates at 0.5°C/s and 5°C/s showed a TS decrease compared with the API Standard at low and medium austenitisation temperatures (Between 900°C and 1100°C). In the case of a cooling rate at 50°C/s, all the austenitising temperatures show ultimate strength above the X80 standard.

After the carbon equivalent is reviewed, the next step in the weld thermal cycle design is evaluating the austenitising temperatures in the heat affected zone. The grain growth zone includes temperatures from 1100°C to 1500°C and recrystallised zone from 900°C to 1100°C. Then, the temperature ranges were selected, and dilatometry testing obtained transition temperatures. The Ac_1 temperature was 730°C while the Ac_3 temperature was 810°C. After the dilatometry, PAGs was measured at 850°C and 900°C using picric acid etching. At 850°C the PAGs was 3.0±0.17 while at 900°C was 3.15±0.29. The PAGs variation between 850°C and 900°C was minimal. The lower temperature selected was 900°C to evaluate the effect of the austenite grain size on the microstructure evolution. The upper temperature was chosen according to the TMC capability; the maximum temperature was 1300 °C. Finally, an evaluation of each 100°C provided an accurate trend of microstructure evolution and the effect on the mechanical properties.

Another critical welding parameter is the holding time. Usually, the holding time during the welding is short[75]. However, this research evaluated the effect of PAGs when the austenite transformation is complete. The holding time of 30 min was selected to complete the transformation of austenite and avoid the material could have partially transformed. In the end, the cooling rate was determined. Three velocities of cooling were chosen to analyse the behaviour of cooling at a slow temperature of 0.5°C/s with slow air cooling, at medium cooling of 5°C/s with forced air and finally at 50°C/s using mist cooling.

Those cooling rates allow obtaining the two mechanisms of transformation, the reconstructive with the diffusion of atoms and the displacive with the plane strain deformation.

Prior austenite grain size is a critical property in the analysis of microstructure evolution [176]. The precipitates solubility affects the PAGS. Depending on the austenitisation temperature, the precipitates started to dissolve in the solution, which increased the austenite grain size. This effect was observed in the variety of austenitisation temperatures. At 850°C the PAGs was 3.0±0.17 while, at 900°C was, 3.15±0.29; the low niobium solubility at low austenitisation temperatures resulted in a minimum change in the PAGs. At 900°, niobium dissolution was only 0.004%; the low niobium solubility restricted the grain growth. At higher temperatures, the niobium in the solution increases, affecting the PAGs. The niobium in solution maintained a similar trend to austenite grain growth. The niobium was totally in solution at 1282°C. Above 1200°C, the precipitates dissolved markedly, and at the same time, the austenite grain growth rapidly increased. At 1300°C, when the niobium was fully solved, the austenite grain growth increased by 25% compared with 1280°C of austenitisation temperature.

After evaluating the transition temperatures (Ac3 and Ac1) and the austenitisation temperature range, the temperature's effect on precipitate solubility was critical. Different authors have investigated the effect of niobium precipitates such as Palmiere[48] (NbC), Irvine[47] (NbCN) and Wang[134] (TiN). Those researchers have studied the niobium solubility in austenite at different temperatures. The niobium solubility is essential to understand the effect on the austenite decomposition.

The transition temperatures during cooling were another significant effect in studying austenite decomposition. Using dilatometry testing was possible to measure those temperatures (Ar)[177]. At lower cooling rates, the transition temperatures were higher. And, when the cooling rates increased, the Ar temperatures decreased. Also, the transition temperatures were affected by the prior austenite grain size. The coarse PAGs reduced the Ar temperature, and the fine PAGs increased the transition temperature. This effect was observed in Section 4.2 of the last chapter.

The last parameter in the design of the thermal weld cycle was the cooling rate[178]. During the welding, the application velocity and the heat power are the adjusted parameters to obtain the desired cooling rates. This research used between 0.5 and 50°C/s of cooling rate to evaluate the effect on the final microstructure. Faster cooling incremented the quantity of M/A constituents and martensite; however, martensite structures reduced the toughness. Slow cooling rates resulted in polygonal ferrite and pearlite microstructure.

These microstructures increased elongation but negatively affected the material's tensile strength. Then, the CCT diagrams were used to have an approximation of the cooling strategy. CCT diagrams were performed with the different prior austenite grain sizes. The increment of different microstructures appeared above 1100°C. Over that temperature, M/A constituents and bainite appeared in the microstructure at a medium cooling rate. Also, it was observed that martensite appeared in coarse prior austenite grain size and high cooling rates. Nevertheless, martensite is not a desirable phase because of its adverse effects on toughness.

Therefore, the thermal weld cycle's design was a combination of cooling rate and prior austenite grain size. It was impossible to consider only one parameter because those factors' combinations directly affected the mechanical properties. Some microstructures had better behaviour in terms of strength and toughness. The bainite and M/A constituents improved the mechanical properties compared with martensite (reduced toughness) or polygonal ferrite (low tensile strength)[179]. The following section shows the effect of the volume fraction of phases on the mechanical properties.

5.6 Effect of cooling rate on the mechanical properties

The microstructure evolution in the X80 steel is influenced by various conditions such as chemical composition, initial prior austenite grain size, austenitisation temperature, holding time and the cooling rate. The control of temperatures during austenitisation and cooling rate was critical in processing the material. Inadequate control during processing involves a modification in the austenite decomposition affecting the microstructure and consequently the mechanical properties [32].

The cooling rate was the last parameter to define the final microstructure of the material. The austenitisation temperature and holding time were the main parameters in the grain growth effect, but the cooling rate significantly affected austenite decomposition. The chemical composition also affects grain growth; however, the chemical composition was equal in all the analysed samples in this research. The CCT diagram simulation allowed the understanding of resulting microstructures during the cooling [55].

As explained in the previous chapters, the heat affected zone is a crucial area in welding. The heat affected zone is affected by the heat flow between the weld and the base metal. The grains near the fusion zone experiments a rapid increase in grain growth because of the high temperature. The grain growth zone includes temperatures above 1100°C until fusion temperatures, while recrystallised zone reaches temperatures above A_{C3} and below 1100°C.

Also, the grain growth and recrystallised zones are determined by the prior austenite grain size; above 1200°C is formed coarse austenite, while below 1200°C is considered fine austenite. Figure 135 shows the iron-carbon diagram representing the variations in the HAZ [74].

The influence of austenitising temperatures in the HAZ is critical because it greatly influences the austenite grain size and austenite decomposition at the temperature where the cooling starts and the transformation begins. A coarse austenite grain size allows the formation of bainite and martensite microstructures. Also, this phenomenon is influenced by the solubility of carbides at high temperatures. However, the fine austenite grain size in slow and medium cooling rates forms polygonal ferrite with pearlite microstructures, obtaining a decrease in strength and increment in ductility. At high cooling rates, fine austenite grain size formed phases of ferrite, bainite and martensite in the final microstructure. The presence of martensite in the microstructure significantly increased the strength of the material.

5.6.1 Effect of slow cooling rate on the mechanical properties

The slow cooling rate at 0.5°C/s showed the best properties in terms of the material's ductility. At 900°C and 1000°C, polygonal ferrite was formed with pearlite. While at 1100°C, the microstructures evolved to a mixture of PF, QF, and bainite. When the temperature increased above 1200°C, the microstructures transformed mainly bainite with ferrite areas. Figure 144 illustrates the effect between the mechanical properties and volume fractions of phases elaborated in the thermomechanical simulation.

At low austenitisation temperatures, the formation of polygonal ferrite with pearlite had the lowest strength and the highest ductility. The austenite grain boundaries are nucleation sites of polygonal ferrite and pearlite. Pearlite and ferrite have a reconstructive transformation mechanism led by atom diffusion[39]. These microstructures showed the lowest ultimate strength in the testing, ~500 MPa.

The strength values were compared with other research; for example, Bott and Vieira reported ultimate strength values ~ 450 MPa with a chemical composition of 0.04% C and 1.86% Mn, PAGs ~ 3.5μm and a cooling rate of 1.5°C/s. In this research, the volume fraction of ferrite was ~95%, and the other 5% was formed by bainite and MA constituents. Also, microhardness was reported with values close to 150HV [180].

The bainite appeared in the microstructure when the temperature increased above 1100°C. At 1100°C, the microstructure was a mixture of polygonal ferrite quasi polygonal ferrite with bainite. Above 1200°C, bainite transformed into the primary structure, and the ferrite started to vanish. Bainite plates have a highest density dislocation than the displacive microstructures [43]. This effect was observed in the ultimate tensile strength; when bainite was formed in the microstructure, the strength increased by ~ 20%. The increase in bainite volume fraction was associated with the solubility of niobium at high temperatures and, consequently, with the rapid rise of prior austenite grain size.

The prior austenite grain size was compared with the Tafteh material; in that work, the chemical composition was 0.06%C, 1.65%Mn and 0.034% Nb. In Tafteh's work, the prior austenite grain size was 37.7µm at 1300°C during 1 min [181]. The higher niobium content in the present research (0.094%Nb) allowed to remain the prior austenite grain size at 97.9µm at 1300°C for 30 min in a sample of 12 mm width.

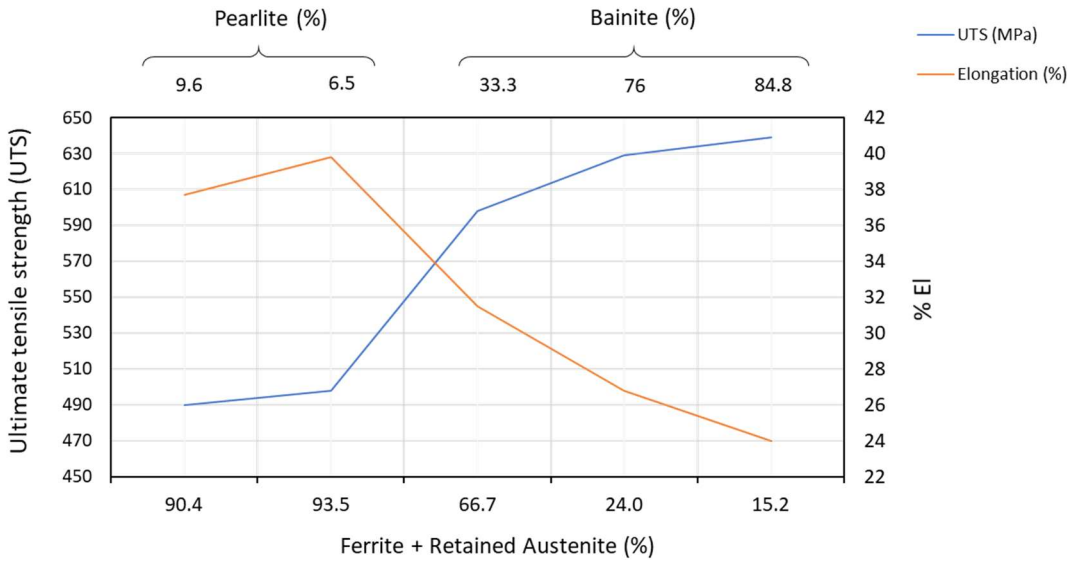

Figure 144 Relation between mechanical properties with volume fraction of phases elaborated in the thermomechanical simulation at 0.5°C/s of cooling rate.

Finally, the energy absorbed at 20, 0 and -50°C of temperature testing was analysed. Figure 145 shows the relation between energy absorption and hardness at different testing temperatures. The material increased its capability to absorb energy at a high percentage of ferrite volume fraction. Pearlite is characterised by convenient crack nucleation places, specifically at ferrite-cementite interfaces. But, the crack propagates in ferrite during a brief distance till collision with a lamellar of cementite. In this collision, the energy is absorbed in the propagation[40]. The pearlite microstructure did not affect the absorbed energy during the testing. However, the increase in bainite volume fraction reduced the energy absorbed in all the testing temperatures.

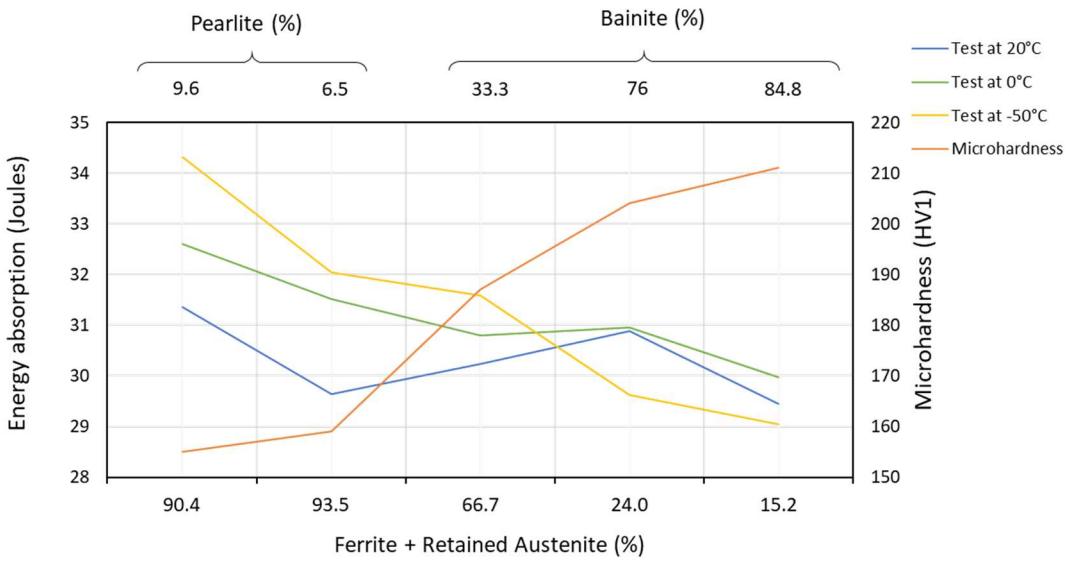

Figure 145 Relation between energy absorption and microhardness with volume fraction of phases at 0.5°C/s of cooling rate. The Impact testing was done at 20°C, 0°C and -50°C.

5.6.2 Effect of medium cooling rate on the mechanical properties

The medium cooling rate showed an increase in mechanical properties compared with the slow cooling rate. At 900°C of austenitisation temperature was the highest increase of tensile strength compared with a slow cooling rate. At 900°C, the polygonal ferrite had a volume fraction of 91.4%, with a tensile strength close to 570MPa; this increase was 16% higher than the TS at 0.5°C/s.

With an increase in the austenitisation temperature at 1000°C, the microstructure evolved into quasi-polygonal ferrite and bainite zones. Above 1100°C, the bainite transformed in the dominant microstructure and continued increasing its volume fraction at the highest temperatures. However, the tensile strength did not show a considerable increase. M/A constituents appeared at coarse PAGs; these constituents showed a tensile strength increase of 9.6% compared with the microstructure at 1100°C.

Grain growth zone temperatures (above 1100°C) showed a rapid increase in the volume fraction of bainite and at the same time an increase in mechanical properties. During the nucleation of bainite, carbon must divide within the austenite grains forming subunits that grow without diffusion[182]. Above 1200°C appeared M/A constituents in the microstructure. M/A constituents which appeared in bainite are characterised by carbon enriched. During austenite decomposition, carbon enriched partitioned in the remaining austenite forming the constituents [183].

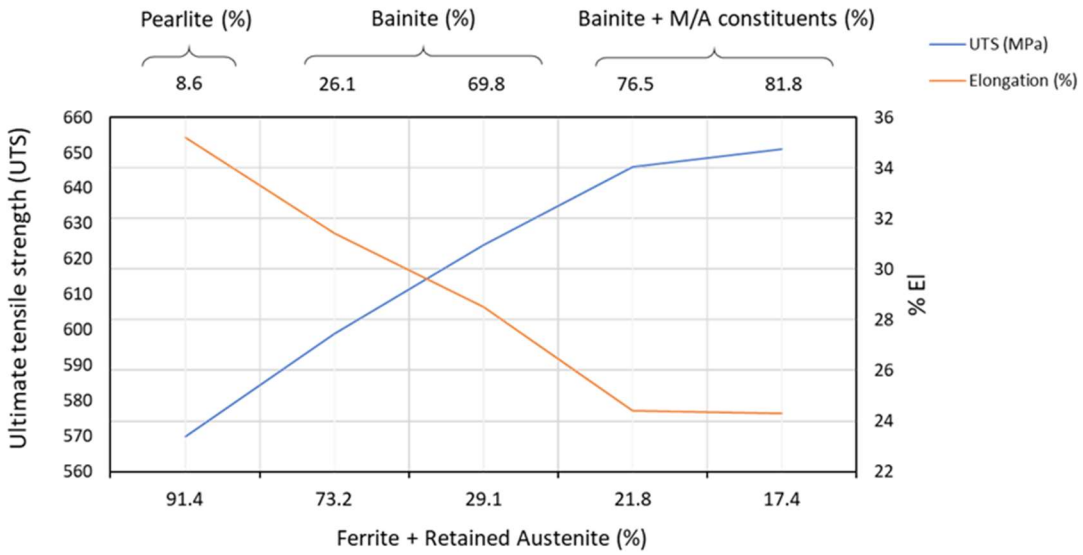

Figure 146 Relation between mechanical properties with volume fraction of phases elaborated in the thermomechanical simulation at 5°C/s of cooling rate.

The energy absorbed did not drastically change in all the testing conditions. Even In the testing at -50°C, the values had a stable behaviour. Ferrite with pearlite showed the lowest energy absorption in most of the conditions. Above 1000°C appeared bainite, and the strength continued increasing in the presence of this phase without significant change in the energy absorbed. The maximum absorbed energy variability between the different temperature tests was 9% at 1000°C; the average variation was less than 6% in the other conditions.

M/A constituents increased the strength in the microstructure, as observed between the austenitisation temperature at 1100°C and 1200°C. However, different authors reported a decrease in toughness because of these M/A constituents [184]. Also, the cooling rate´s effect on forming M/A constituents was not apparent. Some authors reported that a slow cooling rate increased the volume fraction of M/A constituents [185,186], while others reported the opposite effect[187]. However, those reports needed to be clarified because the prior austenite grain size was not identical in those studies. The present work showed the effect of the cooling rate with the same prior austenite grain size. It was observed that M/A constituents at 5°C/s were not visualised in the same manner at 0.5°C/s.

Some studies reported that M/A constituents could avoid the cracks' propagation, therefore increasing toughness. However, other studies reported that the initiation of cracks started in the coarse M/A constituents. Thus, the distribution and size homogenisation of M/A constituents is essential for good toughness behaviour [188]. This homogenisation of M/A constituents could explain the strength increase without diminishing the material's toughness.

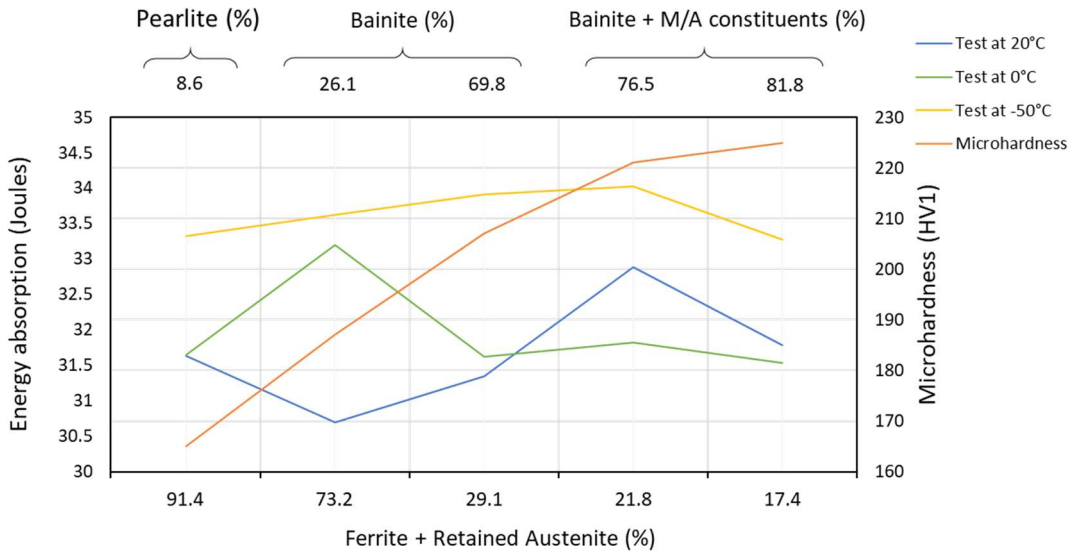

Figure 147 Relation between energy absorption and microhardness with volume fraction of phases at 5°C/s of cooling rate. The Impact testing was done at 20°C, 0°C and -50°C.

5.6.3 Effect of high cooling rate on the mechanical properties

The cooling rate at 50°C/s showed the highest ultimate tensile strength in all the austenitisation conditions. The martensite was presented in all austenitisation temperatures and increased until 95.4% of volume fraction at 1300°C. The increase in strength decreased the ductility at the same time. The highest tensile strength was 830 MPa with a ductility of 18.4% at 1300°C; at this austenitisation temperature, the martensite volume fraction was 95.4%. The lowest strength was 658 MPa with 29.2% of ductility at 900°C of austenitisation temperature; at this temperature, the martensite volume fraction was 26.4%.

The martensite was essential in increasing tensile strength compared with the other phases. The diffusionless transformation characterises the martensite, and the two morphologies associated with the martensite are lath and plate. The lath martensite in low carbon steels tends to endure brittle fracture [36]. Figure 148 illustrates the relation between phase volume fraction and mechanical properties. The increase in martensite fraction also increases the tensile strength due to the solubility of carbon and the effect of martensite plastic behaviour [189].

The martensite mechanical properties highly depend on morphology but also crystallography. The most important characteristics of martensite crystallography are laths, blocks, and packets. The laths have their name because of their shape; some authors define them with a ratio of 30:7:1 between length, width and thickness.

Different laths with similar crystallographic orientation shape a block (Figure 149). Depending on the material's chemical composition, the block could form sub-blocks. When multiple blocks have the same habit plane, it creates a packet. The interface between martensite and austenite on a macroscopic scale is defined as the habit plane. Usually, the size of blocks and packets is related to the prior austenite grain size and the cooling rate [190]. However, a slight change in the tensile strength was observed during experimentation at the highest austenitisation temperatures (above 1200°C). The prior austenite grain size increased from 44.8µm to 99.7µm at those temperatures, and the tensile strength increased.

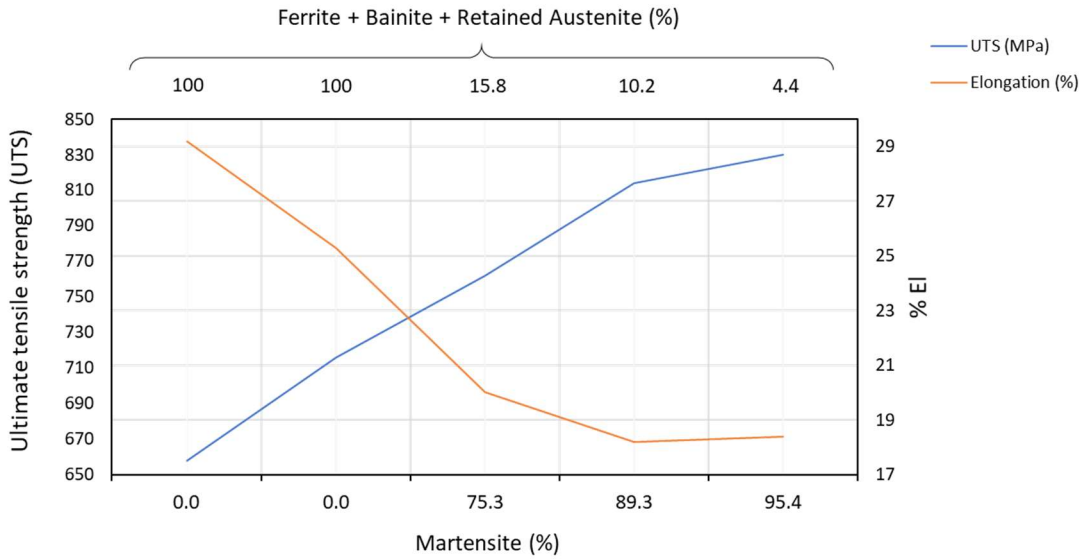

Figure 148 Relation between mechanical properties with volume fraction of phases elaborated in the thermomechanical simulation at 50°C/s of cooling rate.

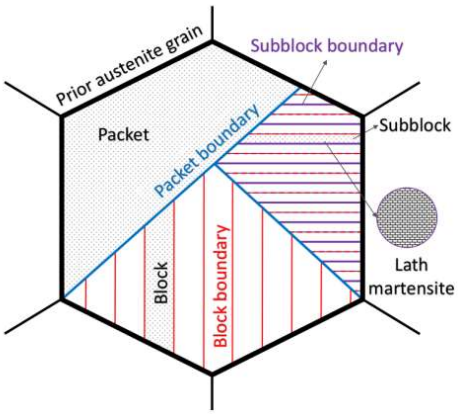

Figure 149 Hierarchical microstructure schematic of lath martensite [190]

The toughness of the material had the expected behaviour (Figure 150). When the martensite volume fraction increased, the material's toughness decreased. The highest effect was observed at 0°C and -50°C of temperature testing and above 1200°C. You, Shang et al. reported that the density of laths with high misorientation angle of boundaries had a better effect on the toughness of the material. Also, the authors reported the advantage of niobium additions to obtain the optimum packets in the crystals [191]. The highest toughness decreased between 900°C and 1300°C was ~23%. The high misorientation angle shown at high temperatures could avoid the highest diminished when the martensite volume fraction increases to 95.4%.

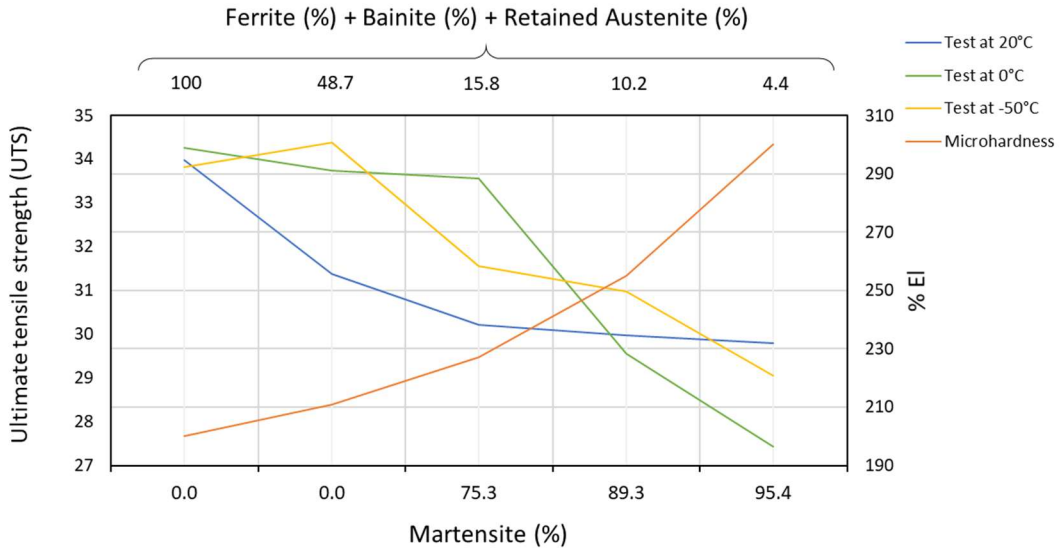

Figure 150 Relation between energy absorption and microhardness with volume fraction of phases at 50°C/s of cooling rate. The Impact testing was done at 20°C, 0°C and -50°C.

Summary

Chapter 5 explains the obtained results with the different parameters in this research. It described the effect on the mechanical properties in terms of prior austenite grain size, the solubility of niobium and the cooling rate. The results were compared with the literature of different authors. The mechanical properties analysed were tensile strength, ductility, microhardness and impact. The effect of the morphology was evaluated with the volume fraction of phases. At low cooling temperatures, a mixture of pearlite and ferrite was obtained in lower austenitisation temperatures and bainite and ferrite above 1100°C of austenitisation. At a medium cooling rate, a mixture of ferrite with bainite and M/A constituents was obtained at a high austenitisation temperature. Finally, at a 50°C/s of cooling rate, a mixture of martensite, ferrite and bainite was obtained in the resulting microstructures at high temperatures of austenitisation.

Chapter 6

Conclusion and future work

6.1 Conclusions

The thermomechanical processing allowed to study the properties of X80 steel and the effect in heat affected zone. This steel is API classification, and the hydrocarbon industry is the main application. This industry demands high strength, high ductility and excellent weldability. The heat affected zone is the most critical area in welding because most failures occur in that region.

The thermomechanical processing design used the heat treatment simulation to have a proximity of the effect on temperatures and cooling rate in the heat affected zone. The austenitisation temperatures impact the niobium solubility during the testing; high temperatures increase the niobium solubility and consequently grow the austenite grain size. The austenite decomposition was followed by different cooling rates affecting the phase volume fraction. The combination of prior austenite grain size and cooling rates results in various final microstructures and mechanical properties. For example, the tensile strength at a slow cooling rate had a tensile strength range from 490 MPa to 639MPa and a ductility range from 39.8% to 24%. At a medium cooling rate, the tensile strength range slightly increased from 570 MPa to 671 MPa and the ductility range from 35.2% to 24.3%. Finally, at a high cooling rate, the tensile strength range significantly increased from 658 MPa to 830 MPa and the ductility range from 29.2% to 18.4%.

The following points were the most critical issues during this work:

1.- The cooling rate is a critical parameter in studying austenite decomposition. The effect in the final microstructure is visualised with the change from 0.5°C/s to 50°C/s of cooling rate. The cooling rate has a direct impact on mechanical properties. Slow cooling rates diminish the tensile strength and increase the ductility. At the same time, high cooling rates increase the tensile strength but decrease the ductility. This effect is related to the final microstructures obtained at these cooling rates. Therefore, cooling rate control during welding is critical to get the desired microstructure and the expected mechanical properties.

2.- The austenitisation temperatures are crucial in studying grain growth. High austenitisation temperatures increase precipitation solubility, affecting the prior austenite grain size. At low austenitisation temperatures, the grain growth change is minimal. However, when the temperature elevates, the niobium solubility increase, producing rapid growth in the austenite grains. Also, the austenite grain size allowed to observe an array of microstructures. At fine PAG's (from 900°C to 1000°C) the microstructure evolves from different forms of ferrite and pearlite to predominant bainite and martensite microstructures at coarse PAG's (above 1100°C).

3.- The precipitates of niobium and titanium are decisive to retards the grain growth during the austenitisation, the highest effect was above 1100°C of reheating temperature. At 1282 °C all the niobium is completely solved in the microstructure; however, the TiN continue retarding the grain growth above that temperature. The precipitation effect was observed with the TEM carbon extraction replica technique.

4.- From the evaluated heat treatments, the highest tensile strength was at coarse prior austenite grain size and high cooling rate. The presence of martensite was crucial to elevate the strength. However, the ductility diminished simultaneously. The highest strength obtained an elevated martensite volume fraction, but these conditions had the lowest toughness values. The opposite effect was shown at the slow cooling rate. The strength decreased in fine prior austenite grain size, but the ductility had the best results. Also, toughness had an excellent performance. At 5°C/s of cooling rate and austenitisation temperatures above 1200°C appeared M/A constituents. These constituents are not desirable in terms of toughness strength.

5.- The most remarkable combination of mechanical properties was obtained at 50°C/s and 1000°C of austenitisation temperature. In these conditions, the microstructure was predominantly ferrite. At this temperature was obtained the best mixture of tensile strength, ductility and toughness.

6.2 Future work

This section mentions some suggestions and aspects of future work in the austenite decomposition studies and the effect of mechanical properties on pipeline steels. After analysing the results, I would like to reduce the holding time during the heat treatment if I could extend my research for more time. This would minimise austenite grain growth affecting the austenite decomposition. I would perform testing with 1 or 2 min of holding time instead of 30 min. This implies smaller PAGs affecting the final microstructure and the mechanical properties. The reduction of holding time would allow a close simulation of the welding process where the holding times are usually short.

After performing the simulation with a reduction in holding time, I would analyse the final microstructure and the effect on mechanical properties. The analysis of mechanical properties and microstructure allows scaling the strategy to perform testing with the industry. The industry capabilities of the cooling rate could be analysed. However, the range between 0.5 to 50°C/s cooling rate offers a good strategy for expecting the final microstructure. I would change the temperature testing of the Charpy test in the mechanical properties. I will reduce the temperature because it was not a transition zone at -50°C. I performed a couple of impact tests on the raw material at -80°C, and even at that temperature, it did not show a significant change (less than 3%). Because of that, I would perform a test at -100 or -120°C.

Another aspect not considered in this research is the quantification of precipitates. During the testing, the precipitates were observed at different temperatures using the carbon extraction replica technique. However, the experimentation part only covered qualitative observation. It is possible to understand the precipitation effect better at different austenitisation temperatures using quantification. In the EBSD, I will use the Channel 5 Software to obtain more information about the final microstructure; for example, it could give you more details about dislocations.

Finally, designing thicker samples is another aspect to consider for future research on thermomechanical processing simulation. In the future, it is necessary to have more material to obtain at least 10 mm width; this will enable us to compare the toughness with other materials' specifications quickly. Also, it is possible to realise a HAZ simulation in the Gleeble machine. Haz simulation will allow observing the effect of the temperature directly on the HAZ. An entire simulation of the HAZ can offer welding optimisation comparing parameters used in the TMC. The cooling could be changed in the maximum temperature because at 50°C/s, a high percentage of martensite appears above 1200°C. According to the literature, accepting cooling rates could be between 5 to 20°C/s to avoid martensitic microstructure. The cooling strategy must be evaluated using the CCT diagrams with the cooling rate and the PAGs. The PAGs will diminish if the holding time is reduced.

References

1. Hymel, M. L. *Globalisation, environmental justice, and sustainable development: the case of oil*. *Macquarie Law Journal* vol. 7 (2007).
2. Fantazzini, D., Höök, M. & Angelantoni, A. Global oil risks in the early 21st century. *Energy Policy* **39**, 7865–7873 (2011).
3. Bardi, U. Peak oil, 20 years later: Failed prediction or useful insight? *Energy Res. Soc. Sci.* **48**, 257–261 (2019).
4. Chapman, I. The end of Peak Oil? Why this topic is still relevant despite recent denials. *Energy Policy* **64**, 93–101 (2014).
5. Lutz, C., Lehr, U. & Wiebe, K. S. Economic effects of peak oil. *Energy Policy* **48**, 829–834 (2012).
6. Harsem, Ø., Eide, A. & Heen, K. Factors influencing future oil and gas prospects in the Arctic. *Energy Policy* **39**, 8037–8045 (2011).
7. Reed, J. C. Effects of oil development in Arctic America. *Biol. Conserv.* **2**, 273–277 (1970).
8. Gulas, S., Downton, M., D'Souza, K., Hayden, K. & Walker, T. R. Declining Arctic Ocean oil and gas developments: Opportunities to improve governance and environmental pollution control. *Mar. Policy* **75**, 53–61 (2017).
9. Johnston, P. F. Artic Energy Resources and Global Energy Security. *J. Mil. Strateg. Stud.* **12**, (2010).
10. Ermida, G. Strategic decisions of international oil companies: Arctic versus other regions. *Energy Strateg. Rev.* **2**, 265–272 (2014).
11. Beyer, J., Trannum, H. C., Bakke, T., Hodson, P. V. & Collier, T. K. Environmental effects of the Deepwater Horizon oil spill: A review. *Marine Pollution Bulletin* vol. 110 28–51 at https://doi.org/10.1016/j.marpolbul.2016.06.027 (2016).
12. Auping, W. L., Pruyt, E., Jong, S. De & Kwakkel, J. H. The geopolitical impact of the shale revolution : Exploring consequences on energy prices and rentier states. *Energy Policy* **98**, 390–399 (2016).
13. Annual Energy Outlook 2020 with projections to 2050. *US Energy Information Administration* https://www.eia.gov/outlooks/aeo/pdf/aeo2020.pdf (2020).
14. Committee on Climate Change. *Net Zero Technical report Committee on Climate Change*. www.theccc.org.uk/publications (2019).
15. Xiaoguang, T. *et al.* Distribution and potential of global oil and gas resources. *Pet. Explor. Dev.* **45**, 779–789 (2018).

16. Zhang, J. Oil and gas trade between China and countries and regions along the 'Belt and Road': A panoramic perspective. *Energy Policy* **129**, 1111–1120 (2019).

17. Pan, X. *et al.* Analysis of China ' s oil and gas consumption under different scenarios toward 2050 : An integrated modeling. *Energy* **195**, 116991 (2020).

18. Metz, Z. A., Reynolds, P. A., Chen, D. & Zhou, G. *Historical pipeline construction cost analysis*. *Int. J. Oil, Gas and Coal Technology* vol. 4 (2011).

19. Xu, Mayu; Aizhu, C. China starts building southern part of China-Russia East gas pipeline. *Reuters* https://www.reuters.com/article/us-china-naturalgas-pipeline/china-starts-building-southern-part-of-china-russia-east-gas-pipeline-idUSKCN24T0VU#:~:text=The full China-Russia East,region in Russia to China. (2020).

20. Kyriakides, S. & Corona, E. *Mechanics of Offshore Pipelines: Volume 1 Buckling and Collapse*. *Elsevier* (2007).

21. Natural gas explained. *U.S. Energy Administration Information* https://www.eia.gov/energyexplained/natural-gas/natural-gas-pipelines.php (2019).

22. Oil and Natural Gas Pipelines. *Canadian Oil and Natural Gas Producers* https://www.capp.ca/explore/oil-and-natural-gas-pipelines/ (2019).

23. Llano, M. Ductos, ¿por dónde circulan los hidrocarburos en México? *Heinrich Böll Stiftung* https://mx.boell.org/es/2017/07/26/ductos-por-donde-circulan-los-hidrocarburos-en-mexico (2017).

24. Dyl, K. New natural gas pipelines are adding capacity from the South Central, Northeast regions. *US Energy Information Administration* https://www.eia.gov/todayinenergy/detail.php?id=41933 (2019).

25. Biezma, M. V., Andrés, M. A., Agudo, D. & Briz, E. Most fatal oil & gas pipeline accidents through history: A lessons learned approach. *Eng. Fail. Anal.* **110**, 1–14 (2020).

26. Solving preferential weld corrosion inn C-Mn Steels. *TWI Ltd* https://www.twi-global.com/technical-knowledge/faqs/faq-what-are-the-causes-of-and-solutions-to-the-preferential-weld-corrosion-in-c-mn-steels.

27. Askari, M., Aliofkhazraei, M. & Afroukhteh, S. A comprehensive review on internal corrosion and cracking of oil and gas pipelines. *J. Nat. Gas Sci. Eng.* **71**, (2019).

28. Smith, A. J. & Murphy, M. M. Transportation of Shale Gas and Oil Resources. in *Environmental and Health Issues in Unconventional Oil and Gas Development* (eds. Kaden, D. & Rose, T.) 286 (Elsevier, 2016). doi:https://doi.org/10.1016/C2015-0-01468-X.

29. Graeber, D. J. PHMSA: California oil pipeline corroded. *United Press International* (2015).

30. Deardo, A. J. Microalloyed Steels : Fifty Years of Progress - An Interpretive Review. (2008).

31. Villalobos, J. C., Del-Pozo, A., Campillo, B., Mayen, J. & Serna, S. Microalloyed steels through history until 2018: Review of chemical composition, processing and hydrogen service. *Metals (Basel).* **8**, (2018).

32. Rosado, D. B., Waele, W. De & Vanderschueren, D. Latest developments in mechanical properties and metallurgycal of high strenght line pipes. *Sustain. Constr. Des.* **4**, 1–10 (2013).

33. Sharma, S. K. & Maheshwari, S. A review on welding of high strength oil and gas pipeline steels. *J. Nat. Gas Sci. Eng.* **38**, 203–217 (2017).

34. Cheyenne Plains Gas Pipeline (CPGP). *Kinder Morgan* https://pipeportal.kindermorgan.com/portalui/DefaultKM.aspx?TSP=CPD (2015).

35. Kirkwood, P. R. *The Birth and Evolution of HTP (High Temperature Processed) Linepipe Steels*. *CBMM* (2018).

36. Krauss, G. *Steel, Processing, Structure and Performance*. (ASM International, 2005).

37. Krauss, G. Microstructures, Processing, and Properties of Steels. *Prop. Sel. Irons, Steels, High-Performance Alloy.* **1**, 126–139 (2018).

38. Heat, S., Fundamentals, T., Dossett, J. & Totten, G. E. Introduction to Steel Heat Treatment. *Steel Heat Treat. Fundam. Process.* **4**, 3–25 (2018).

39. Bhadeshia, H. K. D. H. Some phase transformations in steels. *Mater. Sci. Technol.* **15**, 22–29 (1999).

40. R W K Honeycombe. *Steels Microstructure and Properties*. (Edward Arnold, 1981).

41. Bhadeshia, H. K. D. H. Interpretation of the Microstructure of Steels. *University of Cambridge* (2008).

42. *Phase Diagrams Understanding the basics*. (ASM International, 2012).

43. Perricone, M. J. Bainitic Structures. *Metallogr. Microstruct.* **9**, 179–185 (2018).

44. Deacon, R. M. Martensitic Structures. *Metallogr. Microstruct.* **9**, 165–178 (2018).

45. Speer, J. G. & Gaster, R. J. Austenitizing in Steels. *Steel Heat Treat. Fundam. Process.* **4**, 309–316 (2018).

46. T. Gladman. *The Physical Metallurgy of Microalloyed Steels*. (The Institute of Materials, 1997).

47. DeArdo, A. J. Niobium in modern steels. *Int. Mater. Rev.* **48**, 371–402 (2003).

48. Palmiere, E. J., Garcia, C. I. & De Ardo, A. J. Compositional and microstructural changes which attend reheating and grain coarsening in steels containing niobium. *Metall. Mater. Trans. A* **25A**, 277–286 (1994).

49. Thermomechanical Controlled Processing (TMCP) delivering the advantages of Niobium technology. 1–12 (2022).

50. Homsher, C. N. Determination of the non-recrystallization temperature (TNR) in multiple microalloyed steels. PhD Thesis. (The Colorado School of Mines, 2013).

51. Romano-Acosta, L. F., García-Rincon, O., Pedraza, J. P. & Palmiere, E. J. Influence of thermomechanical processing parameters on critical temperatures to develop an Advanced High-Strength Steel microstructure. *J. Mater. Sci.* **56**, 18710–18721 (2021).

52. Pineda-Martinez, E. Study of the Microstructural Refinement of a High Niobium Microalloyed Steel Under Controlled Hot Deformation. PhD Thesis. (The University of Sheffield, 2020).

53. Petrov, R. H., Jonas, J. J., Kestens, L. A. I. & Gray, J. M. Microstructure and texture development in pipeline steels. in *Oil and gas pipelines integrity and safety handbook* (ed. Revie, R. W.) 159–185 (John Wiley & Sons, 2015).

54. Jiang, Y. & Yin, S. Recent results on key performance indicator oriented fault detection using the DB-KIT toolbox. in *Proceedings IECON 2017 - 43rd Annual Conference of the IEEE Industrial Electronics Society* vols 2017-January 7103–7108 (Institute of Electrical and Electronics Engineers Inc., 2017).

55. Bäcke, L. *Modeling the Microstructural Evolution during Hot Deformation of Microalloyed Steels. PhD Thesis.* (KTH Royal Institute of Technology, 2009).

56. Cuddy, L. J. *Microstructures Developed During Thermomechanical Treatment of HSLA Steels*.

57. Zhang, H., Wei, B. & Liu, Y. Influence of Secondary Dendrite Arm Spacing on the Mechanical Properties and Fracture Behavior of Al-Si-Mg Alloy Castings. *Metals (Basel).* **9**, (2019).

58. Zhu, M. *et al.* Progresses in Dendrite Coarsening During Solidification of Alloys. *Jinshu Xuebao/Acta Metall. Sin.* **54**, 789–800 (2018).

59. Beckermann, C. Macrosegregation. in *ASM Handbook, Volume 15: Casting* 348–352 (ASM International, 2008).

60. Chastukhin, A. V., Ringinen, D. A., Khadeev, G. E. & Efron, L. I. Effect of reheat conditions on microstructure evolution and precipitation behavior in high strength linepipe steel. in *Materials Science Forum* vol. 762 165–170 (Trans Tech Publications Ltd, 2013).

61. Zajac, S. & Jansson, B. Thermodynamics of the Fe-Nb-C-N System and the Solubility of Niobium Carbonitrides in Austenite. *Metall. Mater. Trans. B* **29**, 163–176 (1998).

62. Roy, S., Chakrabarti, D. & Dey, G. K. Austenite grain structures in Ti- and Nb-containing high-strength low-alloy steel during slab reheating. *Metall. Mater. Trans. A Phys. Metall. Mater. Sci.* **44**, 717–728 (2013).

63. Buchmayr, B. Thermomechanical Treatment of Steels – A Real Disruptive Technology Since Decades. *Steel Res. Int.* **88**, 1–14 (2017).

64. Allgood, L. E. Submerged Arc Welding Variables. in *ASM Handbook, Volume 6A: Welding Fundamentals and Processes* vol. 6A 335–343 (2011).

65. Ogborn, J. S. Submerged Arc Welding. in *ASM Handbook, Volume 6: Welding, Brazing and Soldering* (eds. Olson, D. L., Siewert, T. A., Liu, S. & Edwards, G. R.) vol. 6 202–209 (1993).

66. Leroy Olson, D. C. E. D. C. B. Submerged Arc Welding. in *Metals Handbook Welding, Brazing and Soldering* vol. 6 114–152 (American Society of Metals, 1983).

67. Tsai, C. L. Heat Flow in Fusion Welding. in *ASM Handbook, Volume 6A: Welding Fundamentals and Processes* vol. 6A 55–66 (2011).

68. Myhr, O. R. & Grong, O. Factors Influencing Heat Flow in Fusion Welding. in *ASM Handbook, Volume 6A: Welding Fundamentals and Processes* vol. 6A 67–81 (2011).

69. DuPont, J. N. Fundamentals of Weld Solidification. in *ASM Handbook, Volume 6A: Welding Fundamentals and Processes* vol. 6A 96–114 (2011).

70. Lippold, J. C. *Welding Metallurgy and Weldability*. (John Wiley & Sons, 2015).

71. Kou, S. *Welding Metallurgy*. (Wiley-Interscience, 2003).

72. Chen, C.C. and Pollack, A. Influence of Welding on Steel Weldment Properties. in *ASM Handbook, Volume 6: Welding, Brazing and Soldering* vol. 6 416–428 (1993).

73. Connor, L. P. *Welding Handbook. Vol. I: Welding Technology*. *American Welding Society, 1987,* vol. 1 (1987).

74. Maalekian, M. Solid-State Transformations in Weldments. in *ASM Handbook, Volume 6A: Welding Fundamentals and Processes* vol. 6A 122–145 (2011).

75. Rothwell, B. *Understanding the weldability of niobium-bearing HSLA steels*. https://www.researchgate.net/publication/237811519.

76. Samuels, L. E. Mechanical Grinding and Polishing. in *ASM Handbook, Volume 9: Metallography and Microstructures* vol. 9 257–280 (2004).

77. Vander Voort, G. F. & Manilova, E. P. Hints for imaging phases in steels. *Adv. Mater. Process.* **163**, 32–37 (2005).

78. García de Andrés, C., Caballero, F. G., Capdevila, C. & San Martín, D. Revealing austenite grain boundaries by thermal etching: Advantages and disadvantages. *Mater. Charact.* **49**, 121–127 (2003).

79. Zhang, L. & Guo, D. C. A general etchant for revealing prior-austenite grain boundaries in steels. *Mater. Charact.* **30**, 299–302 (1993).

80. Vander Voort, G. F. Wetting Agents in Metallography.pdf. *Mater. Charact.* **35**, 135–137 (1995).

81. Brewer, A. W., Erven, K. A. & Krauss, G. Etching and image analysis of prior austenite grain boundaries in hardened steels. *Mater. Charact.* **27**, 53–56 (1991).

82. Vander Voort, G. F. Revealing Prior-Austenite Grain Boundaries. (2014).

83. García De Andrés, C. *et al.* Metallographic techniques for the determination of the austenite grain size in medium-carbon microalloyed steels. *Mater. Charact.* **46**, 389–398 (2001).

84. Cho, K. S. *et al.* A novel etchant for revealing the prior austenite grain boundaries and matrix information in high alloy steels. *Mater. Charact.* **59**, 786–793 (2008).

85. Vander Voort, G. F. *Metallography Principles and Practice*. *ASM International* (1999).

86. Romano-Acosta, L. F. Microstructure Development of Complex Phase Steels During Thermomechanical Processing. PhD Thesis. (The University of Sheffield, 2020).

87. Rakshe, B. D. Microstructural evaluation in structural steels containing dilute niobium concentrations. PhD Thesis. (The University of Sheffield, 2020).

88. Chemical book. *Picric acid properties*. https://www.chemicalbook.com/ChemicalProductProperty_EN_CB1195194.htm (2022).

89. University of Wisconsin-Madison. *Safe Handling of Picric Acid (CHM-GUI-006)*. (2017).

90. ASTM Standard. E112-12:Standard Test Methods for Determining Average Grain Size. *ASTM Int.* **E112-12**, 1–27 (2012).

91. Edax. Step Size Selection for EBSD Mapping. *Edax insight* 1 https://www.edax.com/-/media/ametekedax/files/resources/tips_tricks/stepsizeselectionforebsdmapping.pdf.

92. Kang, J. Y., Park, S. J. & Moon, M. B. Phase analysis on dual-phase steel using band slope of electron backscatter diffraction pattern. *Microsc. Microanal.* **19**, 13–16 (2013).

93. WU, J., Wray, P. J., Garcia, C. I., Mingjian, H. & Deardo, A. J. Image Quality Analysis: A New Method of Characterizing Microstructures. *ISIJ Int.* **45**, 254–262 (2005).

94. DeArdo, A. J., Garcia, C. I., Cho, K. & Hua, M. New method of characterizing and quantifying complex microstructures in steels. *Materials and Manufacturing Processes* vol. 25 33–40 at https://doi.org/10.1080/10426910903143415 (2010).

95. Zhao, H., Wynne, B. P. & Palmiere, E. J. A phase quantification method based on EBSD data for a continuously cooled microalloyed steel. *Mater. Charact.* **123**, 339–348 (2017).

96. Kang, Jun-Yun; KIM, DO Hyun; Baik, Sung II; AHN, TAe-Hong; KIM, Young-Woon; Han, Heung-NAm; OH, Kyu Hwan; Lee, Hu-Chul; Ho Han, S. Phase Analysis of Steels by Grain averaged EBSD functions. *ISIJ Int.* **51**, 130–136 (2011).

97. *Channel 5 User Guide*. (Oxford Instruments, 2014).

98. Sun, C., Yang, S. & Liu, G. Evolution of microstructures of a low carbon bainitic steel held at high service temperature. *Acta Metall. Sin. (English Lett.* **27**, 436–443 (2014).

99. Kang, S. *et al.* The analysis of bainitic ferrite microstructure in microalloyed plate steels through quantitative characterization of intervariant boundaries. *Mater. Sci. Eng. A* **669**, 459–468 (2016).

100. Tomaz, R. F. *et al.* Complex phase quantification methodology using electron backscatter diffraction (EBSD) on low manganese high temperature processed steel (HTP) microalloyed steel. *Journal of Materials Research and Technology* vol. 8 2423–2431 at https://doi.org/10.1016/j.jmrt.2019.01.021 (2019).

101. Li, X., Ramazani, A., Prahl, U. & Bleck, W. Quantification of complex-phase steel microstructure by using combined EBSD and EPMA measurements. *Mater. Charact.* **142**, 179–186 (2018).

102. Shrestha, S. L. *et al.* An automated method of quantifying ferrite microstructures using electron backscatter diffraction (EBSD) data. *Ultramicroscopy* **137**, 40–47 (2014).

103. JEOL Ltd. *Multi-purpose Electron Microscope JEM-F200*. https://www.jeol.co.jp/s3/en/catalog/EM/jemf200_e_05.pdf (2016).

104. Ahmed, I. I. *et al.* Analysis of intergranular carbide precipitate in HAZ of martensitic stainless steel. *J. Eng. Sci. Technol.* **12**, 1037–1047 (2017).

105. Dossett, J. L. & Boyer, H. E. Fundamentals of the Heat Treating of Steel. in *Practical Heat Treating* (ASM International., 2006).

106. Saunders, N., Guo, Z., Li, X., Miodownik, A. P. & Schillé, J. P. Using JMatPro to model materials properties and behavior. *The Journal of The Minerals, Metals & Materials Society* vol. 55 60–65 (2003).

107. Guo, Z., Saunders, N. & Schille, J. P. Modelling phase transformations and material properties critical to simulation of heat treatment distortion in steels. *Proc. 17th IFHTSE Congr.* **2**, 753–756 (2008).

108. Guo, Z., Saunders, N., Miodownik, P. & Schille, J. P. Modelling phase transformations and material properties critical to the prediction of distortion during the heat treatment of steels. *Int. J. Microstruct. Mater. Prop.* **4**, 187–195 (2009).

109. Saunders, N., Guo, Z., Li, X., Miodownik, P. & Schillé, J.-P. *The Calculation of TTT and CCT diagrams for General Steels*. *Termotech Ltd. Surrey Technology Centre* (2004) doi:10.1.1.565.9926.

110. Zhan, Y. Z. & Zhuang, Y. H. Dilatometry Determination of Phase Diagrams Using Equilibrated Alloys. in *Handbook of Metal Injection Molding* 21 (2012).

111. Hunkel, M., Surm, H. & Steinbacher, M. Dilatometry. in *Handbook of Thermal Analysis and Calorimetry* vol. 6 103–129 (2018).

112. Bhadeshia, H. K. D. H. Dilatometry. *Univ. Cambridge, Mater. Sci. Metall.* 6 (2002).

113. Yuan, X. Q., Liu, Z. Y., Jiao, S. H., Ma, L. Q. & Wang, G. D. The Onset Temperatures of g to a-Phase Transformation in Hot Deformed and Non-deformed Nb Micro-alloyed Steels. *ISIJ Int.* **46**, 579–585 (2006).

114. Mintz, B., Banerjee, J. R. & Banks, K. M. Regression equation for Ar3 temperature for coarse grained as cast steels. *Ironmak. Steelmak.* **38**, 197–203 (2011).

115. Heating and Holding Times. in *ASM Handbook, Volume 4B: Steel Heat Treating Technologies* (ed. Dossett, J; Totten, G. E.) vol. 4B 479–480 (2014).

116. Matjeke, V. J., van der Merwe, J. W. & Vithi, N. L. Determination of critical transformation temperatures for the optimisation of spring steel heat treatment processes. *Metals (Basel).* **11**, (2021).

117. Trzaska, J. Calculation of critical temperatures by empirical formulae. *Arch. Metall. Mater.* **61**, 981–986 (2016).

118. Barralis, J. & Maeder, G. *Métallurgie Tome I: Métallurgie Physique.* (Collection Scientifique ENSAM, 1982).

119. Choquet, P. & et. al. *Mathematical Model for Predictions of Austenite and Ferrite Microstructures in Hot Rolling Processes*. (1985).

120. Ouchi, C., Sampei, T. & Kozasu, I. *The Effect of Hot Rolling Condition and Chemical Composition on the Onset Temperature of r-a Transformation after Hot Rolling**.

121. Ouchi, C. & et al. The Effect of Hot Rolling Condition and Chemical Composition on the Onset Temperature of Gamma-Alpha Transformation After Hot Rolling. in *Transactions of the ISIJ* 214–222 (1982).

122. Shiga, C. & et al. *Development of Large Diameter High Strength Line Pipes for Low Temperature Use*. (1981).

123. Besson, V. *TMTS user manual*. (2017).

124. Loveday, M. S. *et al.* Measurement of flow stress in hot plane strain compression tests. *Mater. High Temp.* **23**, 85–118 (2006).

125. Edenhofer, B., Joritz, D., Rink, M. & Voges, K. *Carburizing of steels*. *Thermochemical Surface Engineering of Steels: Improving Materials Performance* (Woodhead Publishing Series in Metals and Surface Engineering, 2015).

126. ASTM E384 - 17. Standard Test Method for Microindentation Hardness of Materials. *ASTM Int.* **E384-17**, 40 (2017).

127. ASTM Standard. E8/E8M-16A: Standard Test Methods for Tension Testing of Metallic Materials. *ASTM Int.* **E8/E8M-16a**, 30 (2020).

128. American, A. & Standard, N. Designation: E23 − 18 Standard Test Methods for Notched Bar Impact Testing of Metallic Materials 1. doi:10.1520/E0023-18.

129. Libretexts. *General lab techniques*. file:///C:/Users/pctech/Downloads/Full (1).pdf (2021).

130. Huppi, G.S.; Damkroger, B.K.;Dallam, C. B. Metallography and Microstructures of Weldments. in *ASM Handbook, Volume 9: Metallography and Microstructures* vol. 9 1047–1056 (2004).

131. Matsuzaki, A. & Bhadeshia, H. K. D. H. Effect of austenite grain size and bainite morphology on overall kinetics of bainite transformation in steels. *Mater. Sci. Technol.* **15**, 518–522 (1999).

132. Zhao, S., Donglai, W., Li, R. & Zhang, L. Effect of cooling rate on phase transformation and microstructure of NbTi microalloyed steel. *Mater. Trans.* **55**, 1274–1279 (2014).

133. Kasatkin, B.A.;Vinokur, B. B. . Calculation models for determining the critical points of steel. *Metalloved. i Termicheskaya Obrab. Met. 1* 20–22 (1984).

134. Wang, L., Xue, Z. L., Chen, Y. L. & Bi, X. G. Understanding TiN precipitation behavior during solidification of SWRH 92A tire cord steel by selected thermodynamic models. *Processes* **8**, (2020).

135. ASTM E562-01. Standard Test Method for Determining Volume Fraction by Systematic Manual Point Count. *ASTM Int.* **ASTM E562**, 7 (2011).

136. Ryde, L. Application of EBSD to analysis of microstructures in commercial steels. *Mater. Sci. Technol.* **22**, 1297–1306 (2006).

137. Callister, W. D. *Materials Science and Engineering An Introduction*. (John Wiley & Sons, 2007).

138. Brayshaw, W. J., Roy, M. J., Sun, T., Akrivos, V. & Sherry, A. H. Iterative mesh-based hardness mapping. *Sci. Technol. Weld. Join.* **22**, 404–411 (2017).

139. Duan, L. na, Wang, J. man, Liu, Q. you, Sun, X. jun & Cao, J. chun. Austenite Grain Growth Behavior of X80 Pipeline Steel in Heating Process. *J. Iron Steel Res. Int.* **17**, 62–66 (2010).

140. Ostrovskii, G. A., Sarrak, V. I., Shepelyakovskii, K. Z. & ~ntin, R. I. Effect of refining austenite grains on the properties of carbon steels after low temperature tempering. *Met. Sci. Heat Treat.* **9**, 458–462 (1967).

141. Esmailian, M. The effect of cooling rate and austenite grain size on the austenite to ferrite transformation temperature and different ferrite morphologies in microalloyed steels. *Iran. J. Mater. Sci. Eng.* **7**, 7–14 (2010).

142. Yan, P. & Bhadeshia, H. K. D. H. Austenite-ferrite transformation in enhanced niobium, low carbon steel. *Mater. Sci. Technol. (United Kingdom)* **31**, 1066–1076 (2015).

143. Yuan, X., Chen, L., Zhao, Y., Di, H. & Zhu, F. Dependence of grain size on mechanical properties and microstructures of high manganese austenitic steel. in *Procedia Engineering* vol. 81 143–148 (Elsevier Ltd, 2014).

144. Bleck, W., Wolfgang, B. & Kriangyut, P.-O. Grain Refinement and Mechanical Properties in Advanced High Strength Sheet Steels.

145. Suarez, M. A. *et al. The effect of grain refinement on the mechanical properties of a micro alloyed steel*. *Revista Mexicana de Física* vol. 58 http://www.redalyc.org/articulo.oa?id=57025089006 (2012).

146. Mayer, G. G. *et al. Grain refinement and mechanical properties of€low-carbon steel by means of equal channel angular pressing and annealing*.

147. Jacques; J.P. Influence of Austenite Grain Size. *Phase Transform. steels Fiussionless Transform. high strength steels Model. Adv. Anal. Tech.* (2012).

148. Chandan, A. K., Bansal, G. K., Kundu, J., Chakraborty, J. & Chowdhury, S. G. Effect of prior austenite grain size on the evolution of microstructure and mechanical properties of an intercritically annealed medium manganese steel. *Mater. Sci. Eng. A* **768**, (2019).

149. Hasan, S. M., Kumar, S., Chakrabarti, D. & Singh, S. B. Effect of prior austenite grain size on the formation of carbide-free bainite in low-alloy steel. *Philos. Mag.* **100**, 2320–2334 (2020).

150. Bhadeshia, H. K. D. H. *Bainite in Steels*. (Maney Publishing, 2015).

151. Ding, Z., Xu, Z., Liang, B., Dong, L. & Li, H. Microstructure of Pearlite Independently Nucleating on Grain Boundary Proeutectoid Phase in 100Mn13 Steel. *ACS Appl. Mater. Interfaces* (2020) doi:10.1021/acs.cgd.0c00014.

152. Chen, J.-Z., Du, Q., -Ping, Z. G. & Zhang, B. Toward Eliminating Discontinuous Yielding Behavior of the EA4T Steel. *Mater. MDPI* **14**, 9 (2021).

153. Joo, M. S., Suh, D.-W., Bae, J.-H. & Bhadeshia, H. K. D. H. *Toughness Anisotropy in X70 and X80 Linepipe steels*. http://www.msm.cam.ac.uk/phase-trans/2012/X80.html.

154. Mohseni, P., Solberg, J. K., Karlsen, M., Akselsen, O. M. & Østby, E. Cleavage fracture initiation at M-A constituents in intercritically coarse-grained heat-affected zone of a HSLA steel. *Metall. Mater. Trans. A Phys. Metall. Mater. Sci.* **45**, 384–394 (2014).

155. Valtonen, K. *et al.* Impact wear and mechanical behavior of steels at subzero temperatures. *Tribol. Int.* **129**, 476–493 (2019).

156. Huda, N., Midawi, A. R. H., Gianetto, J., Lazor, R. & Gerlich, A. P. Influence of martensite-austenite (MA) on impact toughness of X80 line pipe steels. *Mater. Sci. Eng. A* **662**, 481–491 (2016).

157. Gianetto, J. A. Microstructure and Toughness of Simulated Grain Coarsened Heat Affected Zones in X80 Pipe Steels. *Proc. Int. Pipeline Conf.* **10th**, 8 (2014).

158. Far, S. M. Influence of thermal simulated and real tandem submerged arc welding process on the microstructure and mechanical properties of the coarse-grained heat-affected zone. *Mater. Manuf. Process.* **26**, 1423–1429 (2011).

159. Tian, Y., Li, Q., Wang, Z. dong & Wang, G. dong. Effects of Ultra Fast Cooling on Microstructure and Mechanical Properties of Pipeline Steels. *J. Mater. Eng. Perform.* **24**, 3307–3314 (2015).

160. Lan, L., Qiu, C., Zhao, D., Gao, X. & Du, L. Analysis of martensite-austenite constituent and its effect on toughness in submerged arc welded joint of low carbon bainitic steel. *J. Mater. Sci.* **47**, 4732–4742 (2012).

161. Qaban, A. & Naher, S. *Evaluation of Toughness of High Strength Low Alloy (HSLA) Steels as a Function of Carbon Content*. *International Journal of Mechanical and Production Engineering (IJMPE)* vol. 7 http://openaccess.city.ac.uk/http://iraj.in (2019).

162. Kavishe, F. P. L. & Baker, T. J. Effect of prior austenite grain size and pearlite interlamellar spacing on strength and fracture toughness of a eutectoid rail steel. *Mater. Sci. Technol. (United Kingdom)* **2**, 816–822 (1986).

163. Hanamura, T., Yin, F. & Nagai, K. Ductile–Brittle Transition Temperature of Ultrafine Ferrite/ Cementite Microstructure in a Low Carbon Steel Controlled by Effective Grain Size. *ISIJ Int.* **44**, 610–617 (2004).

164. Shin, S. Y., Hwang, B., Kim, S. & Lee, S. Fracture toughness analysis in transition temperature region of API X70 pipeline steels. *Mater. Sci. Eng. A* **429**, 196–204 (2006).

165. Shin, S. Y., Woo, K. J., Hwang, B., Kim, S. & Lee, S. Fracture-toughness analysis in transition-temperature region of three American petroleum institute X70 and X80 pipeline steels. *Metall. Mater. Trans. A Phys. Metall. Mater. Sci.* **40**, 867–876 (2009).

166. Liu, D. *et al.* Evaluation of Mechanical Properties and Microstructure of X70 Pipeline Steel with Strain-Based Design. *Metals (Basel).* **12**, 1616 (2022).

167. Gladman, T. T. & Dulieu, D. Grain-Size Control in Steels. *Met. Sci.* **8**, 167–176 (1974).

168. Lee, S. J. & Lee, Y. K. Prediction of austenite grain growth during austenitization of low alloy steels. *Mater. Des.* **29**, 1840–1844 (2008).

169. Hulka, K. K. A. S. U. Application of Niobium in Quenched and Tempered High. *Mater. Sci. Forum* **500–501**, 519–526 (2005).

170. Graux, A. *et al.* Precipitation and grain growth modelling in Ti-Nb microalloyed steels. *Materialia* **5**, (2019).

171. El-Kashif, E., Asakura, K., Koseki, T. & Shibata, K. Effects of boron, niobium and titanium on grain growth in ultra high purity 18% Cr ferritic stainless steel. *ISIJ Int.* **44**, 1568–1575 (2004).

172. Stout, R. D. Weldability of Microalloyed Steels. *Proc. an Int. Symp. High-strength* 488–497 (1975).

173. Gao, W. L., Leng, Y., Fu, D. F. & Teng, J. Effects of niobium and heat treatment on microstructure and mechanical properties of low carbon cast steels. *Mater. Des.* **105**, 114–123 (2016).

174. Wilson, B. Carbon Equivalency in Welded Steel Components with LIBS. *Thermo Fisher Scientific* (2019).

175. *API 5L: Specification for Line Pipe*. (American Petroleum Institute, 2004).

176. Białobrzeska, B., Konat, Ł. & Jasiński, R. The influence of austenite grain size on the mechanical properties of low-alloy steel with boron. *Metals (Basel).* **7**, (2017).

177. Isasti, N., Jorge-Badiola, D., Taheri, M. L. & Uranga, P. Phase transformation study in Nb-Mo microalloyed steels using dilatometry and EBSD quantification. *Metall. Mater. Trans. A Phys. Metall. Mater. Sci.* **44**, 3552–3563 (2013).

178. Arya, H. K., Singh, K. & Saxena, R. K. Effect of weld cooling rates on mechanical and metallurgical properties of submerged arc welded pressure vessel steel. *J. Press. Vessel Technol. Trans. ASME* **140**, (2018).

179. Kong, J.-H. *et al. THE DEVELOPMENT AND APPLICATION OF X80 LINE PIPE STEEL AND PIPES IN CHINA International Symposium on Microalloyed Steels for the Oil and Gas Industry*.

180. Bott, I. S., Vieira, A. A. H., De Souza, L. F. G. & Rios, P. R. Microstructural evaluation of API 5L X80 pipeline steels submitted to different cooling rates. *Mater. Sci. Forum* **638–642**, 3146–3151 (2010).

181. Tafteh, R. Austenite Decomposition in an X80 linepipe steel. Master's Thesis. (The University of British Columbia, 2011).

182. Bhadeshia, H. K. D. H. POSCO Lectures : The Bainite Reaction. 1–36 (2010).

183. De Araujo Silva, R., De Souza, L. F. G., Morales, E. V., Rios, P. R. & De Souza Bott, I. Formation of microphases and constituents from remaining austenite decomposition in API X80 steel under different processing conditions. *Mater. Res.* **18**, 908–917 (2015).

184. Huda, N., Midawi, A., Gianetto, J. A. & Gerlich, A. P. Continuous cooling transformation behaviour and toughness of heat-affected zones in an X80 line pipe steel. *J. Mater. Res. Technol.* **12**, 613–628 (2021).

185. Wang, C., Wu, X., Liu, J. & Xu, N. Transmission electron microscopy of martensite/austenite islands in pipeline steel X70. *Mater. Sci. Eng. A* **438–440**, 267–271 (2006).

186. Wang, S. C. & Yang, J. R. Effects of chemical composition, rolling and cooling conditions on the amount of martensite/austenite (M/A) constituent formation in low carbon bainitic steels. *Mater. Sci. Eng. A* **154**, 43–49 (1992).

187. Matsuda, F. *et al.* Review of mechanical and metallurgical investigations of martensite-austenite constituent in welded joints in Japan. *Weld. World, Le Soudage Dans Le Monde* **37**, 134–154 (1996).

188. Li, B. zhou, Li, C. sheng, Jin, X. & Zhang, J. Effect of M–A constituents formed in thermo-mechanical controlled process on toughness of 20CrNi2MoV steel. *J. Iron Steel Res. Int.* **26**, 1340–1349 (2019).

189. Pushkareva, I., Allain, S., Scott, C., Redjaïmia, A. & Moulin, A. Relationship between Microstructure, Mechanical Properties and Damage Mechanisms in High Martensite Fraction Dual Phase Steels. **55**, 2237–2246 (2015).

190. Gallardo-Basile, F. J., Naunheim, Y., Roters, F. & Diehl, M. Lath martensite microstructure modeling: A high-resolution crystal plasticity simulation study. *Materials (Basel).* **14**, 1–20 (2021).

191. You, Y., Shang, C., Wenjin, N. & Subramanian, S. Investigation on the microstructure and toughness of coarse grained heat affected zone in X-100 multi-phase pipeline steel with high Nb content. *Mater. Sci. Eng. A* **558**, 692–701 (2012).

Appendix I

Microstructures in the optical microscope and SEM at high magnifications.

Higher and lower magnifications in the optical microscope and scanning electron microscope were added to observe the effects of the heat affected zone microstructure and the simulation of heat treatment. Appendix I.1 shows the microhardness pattern through the heat affected zone and the evolution of microstructure.

Appendix I.2-I.7 shows the optical microstructures in the heat treatment simulation in TMC. The austenitisation temperatures were 900°C, 1000°C, 1100°C, 1200°C and 1300°C with cooling rates of 0.5°C/s, 5°C/s and 50°C/s. Appendix I.8-I.10 illustrates the same microstructures evaluated in a scanning electron microscope.

Appendix I.1-a

HAZ microhardness pattern in the X80 steel.

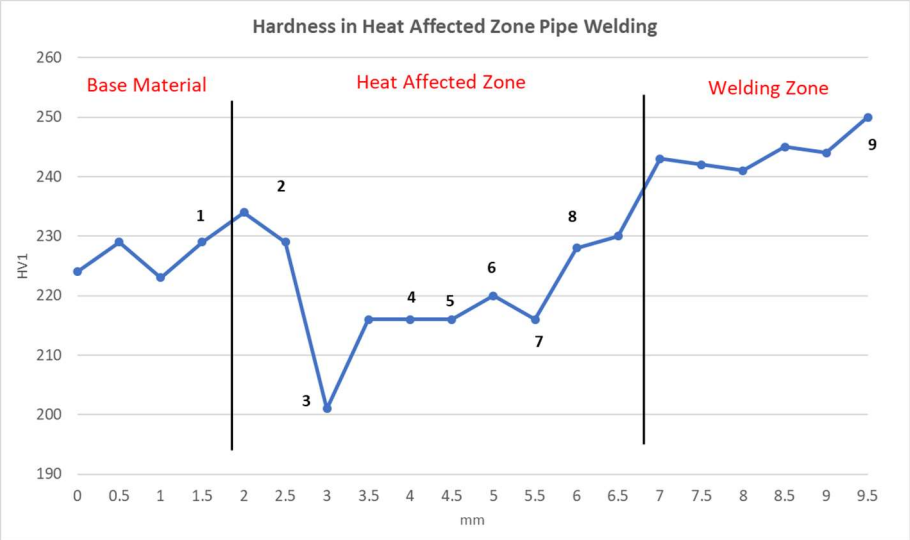

Appendix I.1-b

Evolution of the welding microstructure in the heat affected zone.

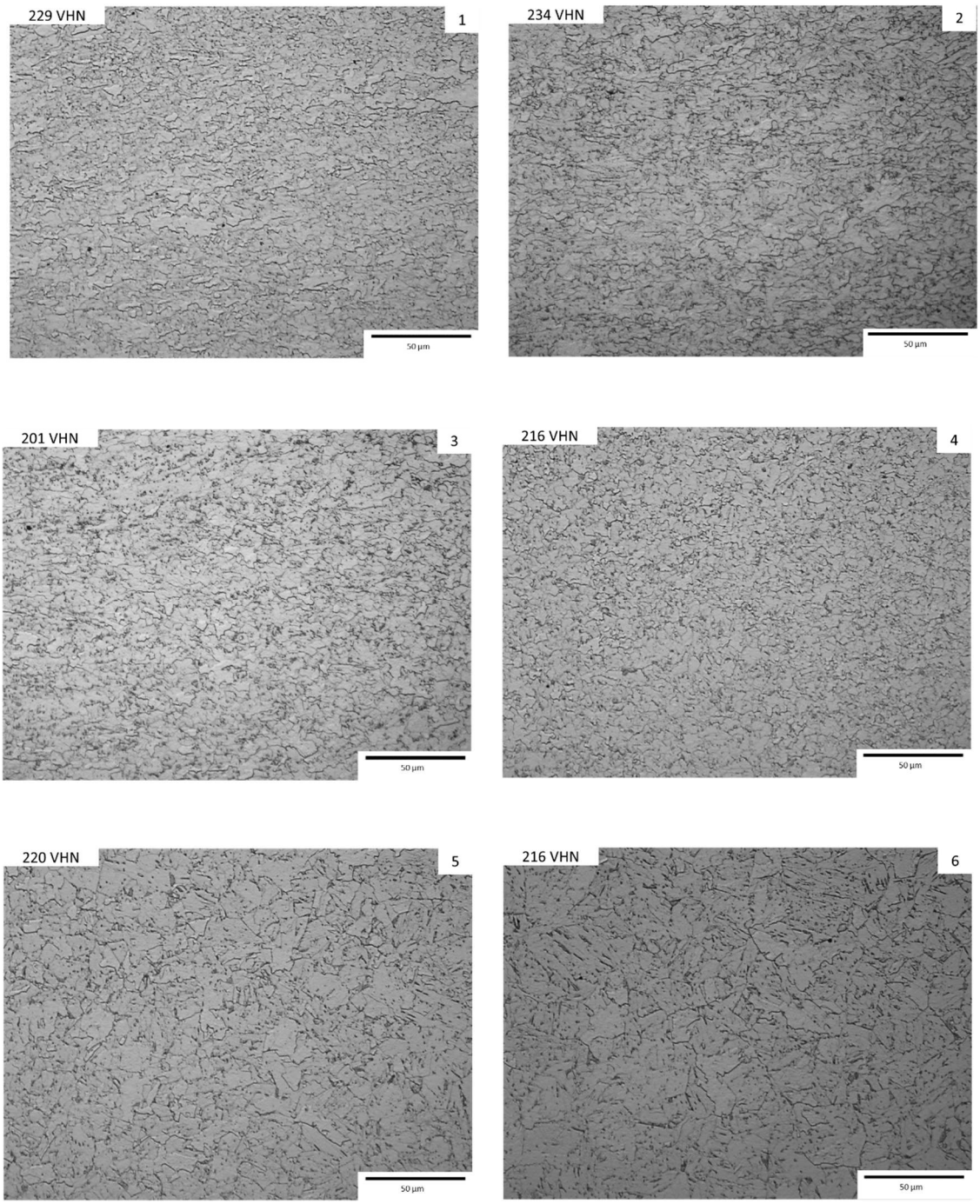

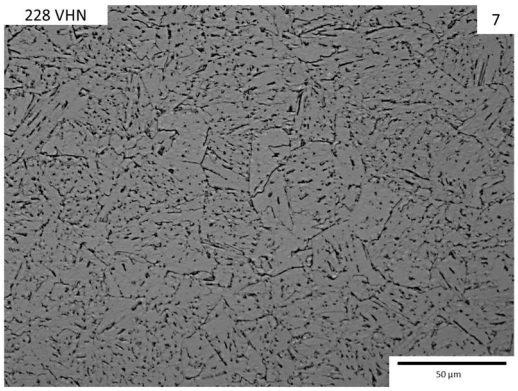
228 VHN
7
50 µm

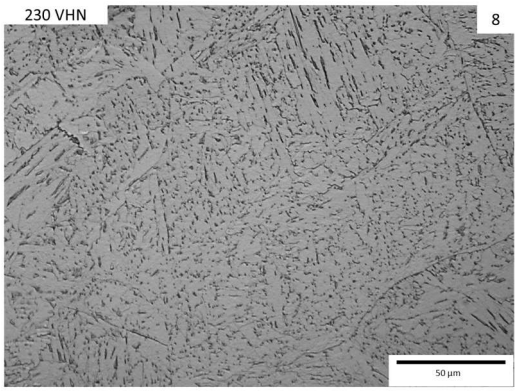
230 VHN
8
50 µm

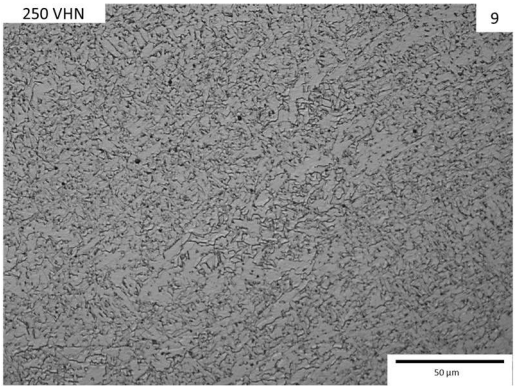
250 VHN
9
50 µm

Appendix I.2

Microstructure evolution at 900°C, 1000°C, 1100°C, 1200°C and 1300°C with a cooling rate of 0.5°C/s

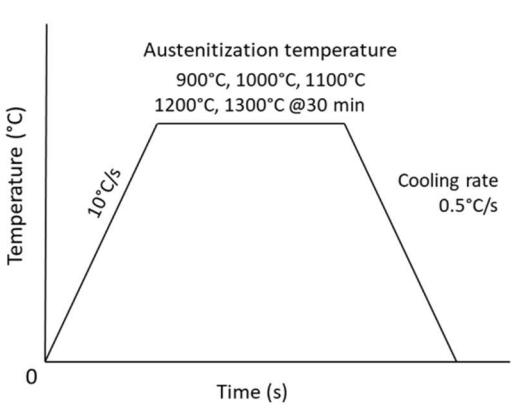

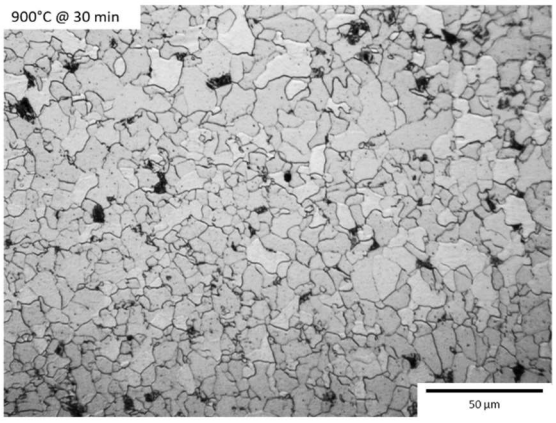

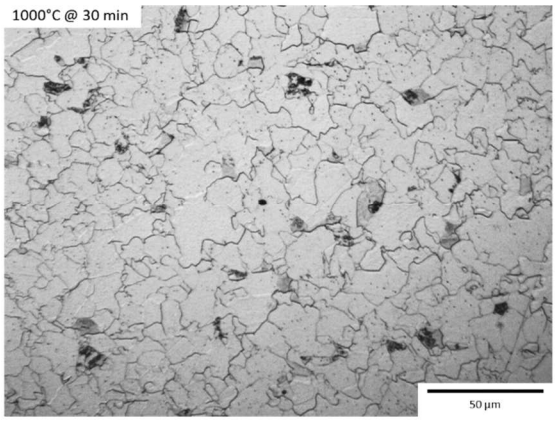

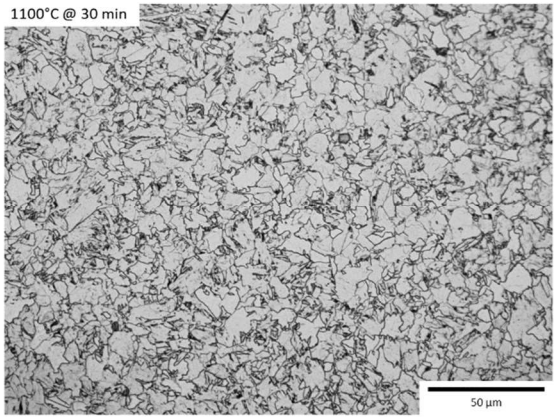

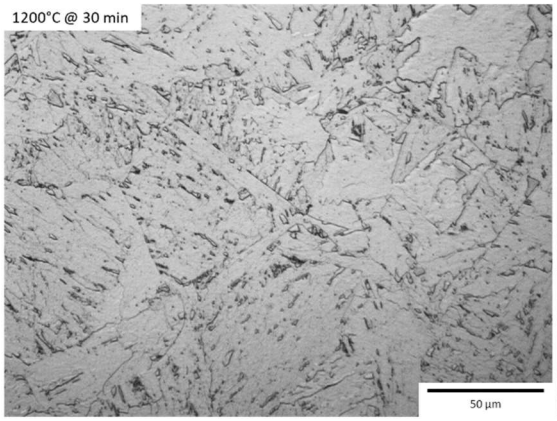

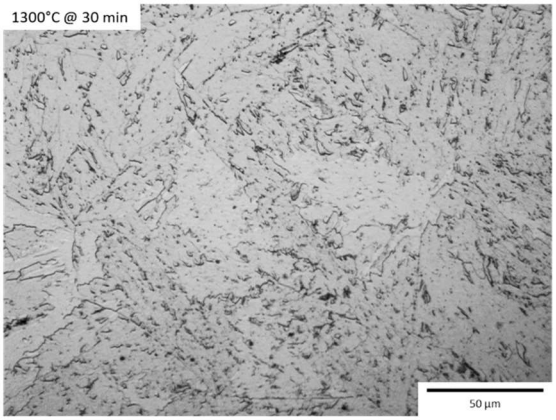

Appendix I.3

Microstructure evolution at 900°C, 1000°C, 1100°C, 1200°C and 1300°C with a cooling rate of 0.5°C/s.

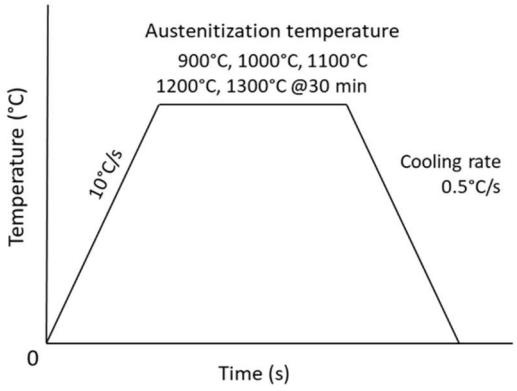

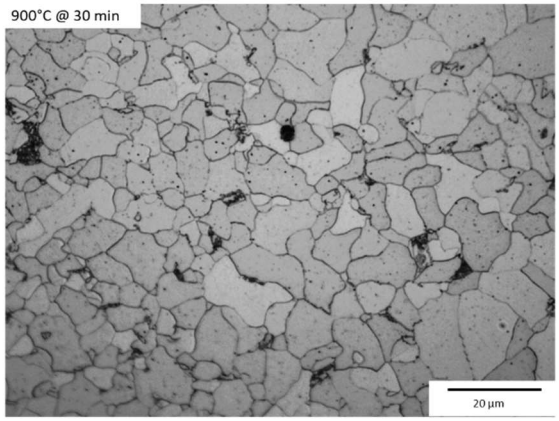

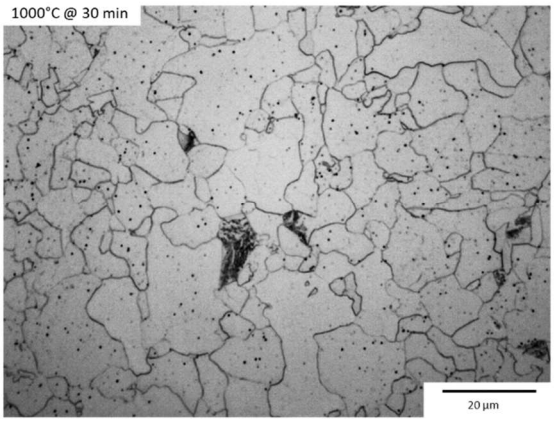

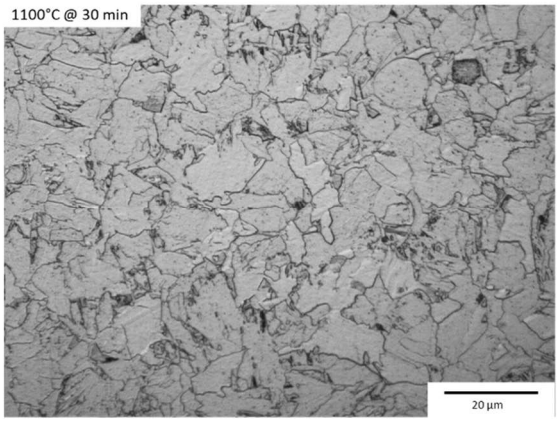

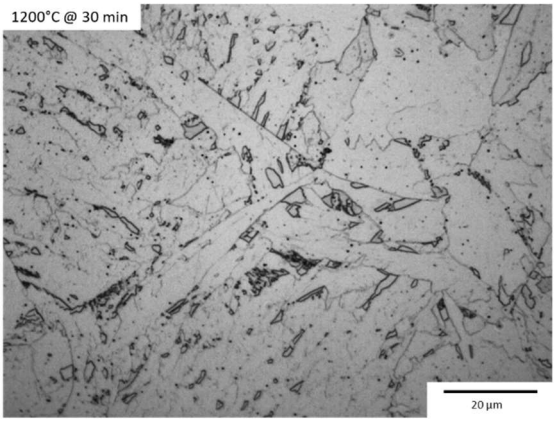

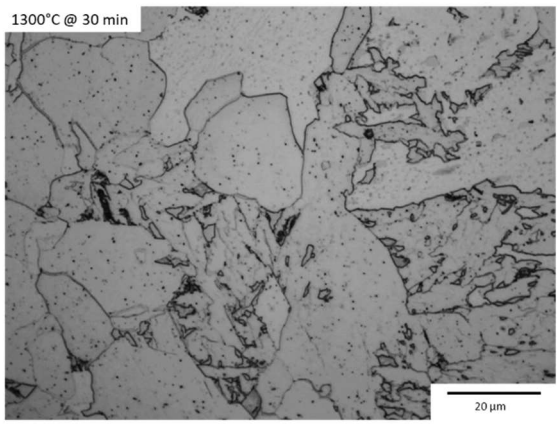

Appendix I.4

Microstructure evolution at 900°C, 1000°C, 1100°C, 1200°C and 1300°C with a cooling rate of 5°C/s.

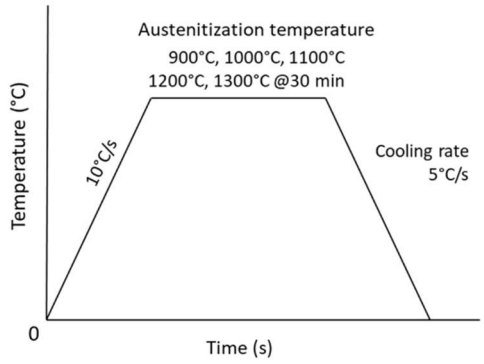

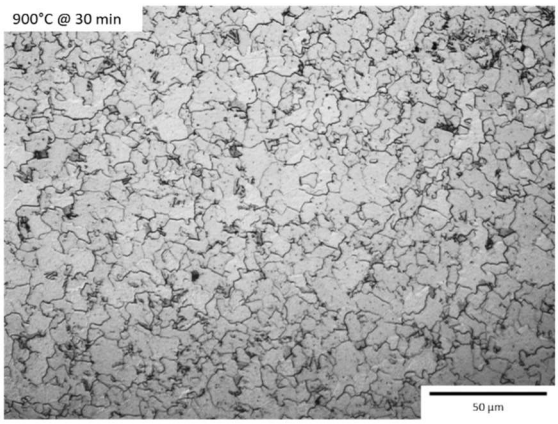

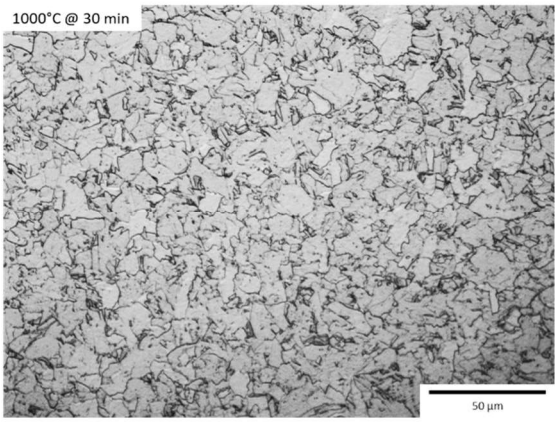

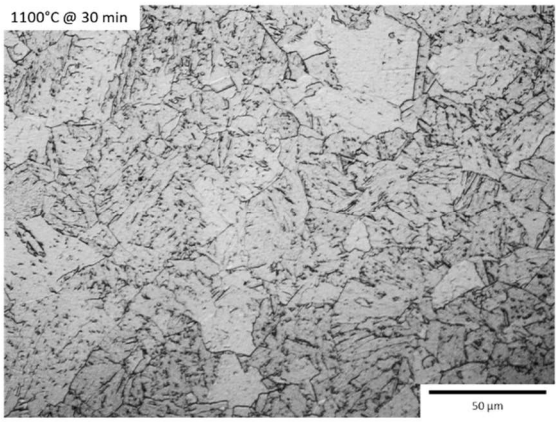

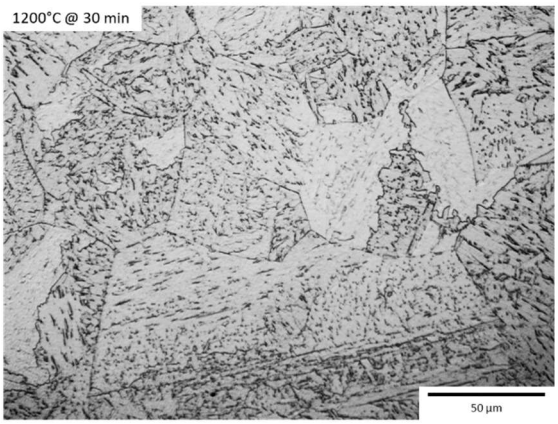

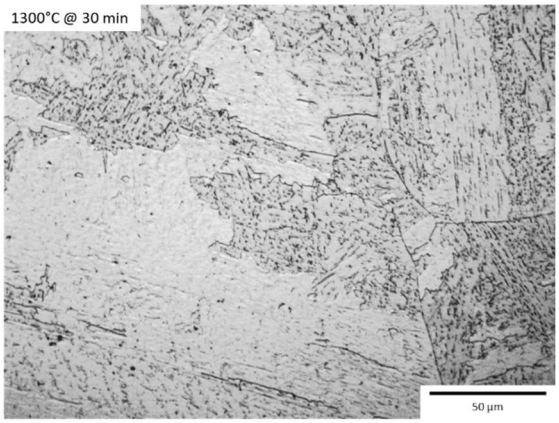

Appendix I.5

Microstructure evolution at 900°C, 1000°C, 1100°C, 1200°C and 1300°C with a cooling rate of 5°C/s.

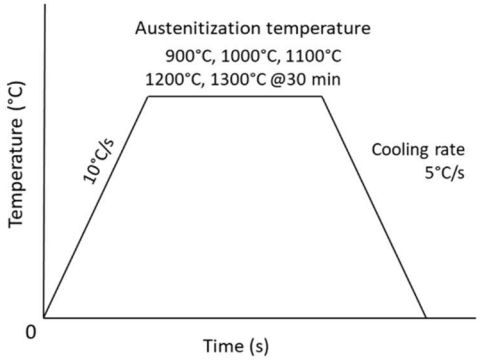

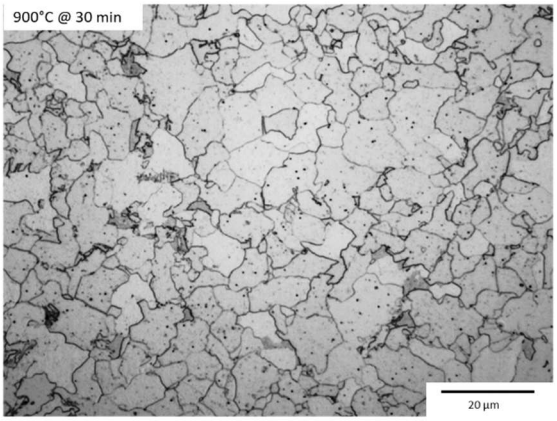

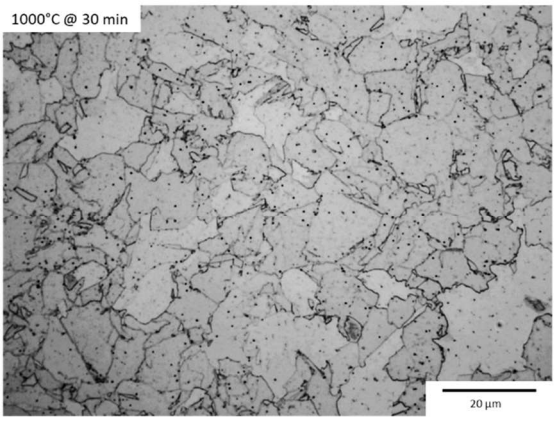

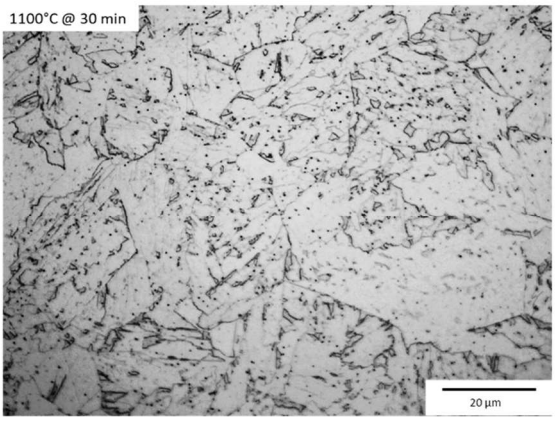

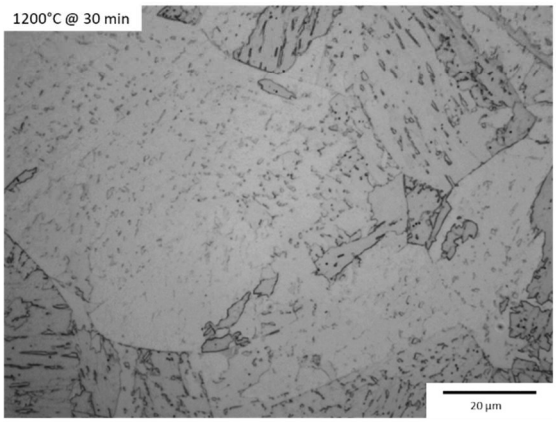

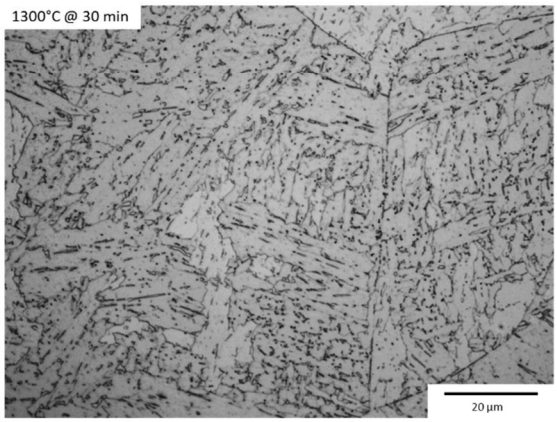

Appendix I.6

Microstructure evolution at 900°C, 1000°C, 1100°C, 1200°C and 1300°C with a cooling rate of 50°C/s.

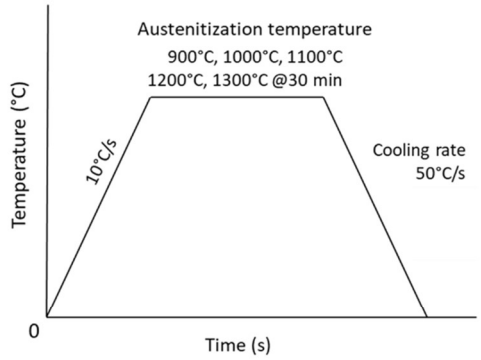

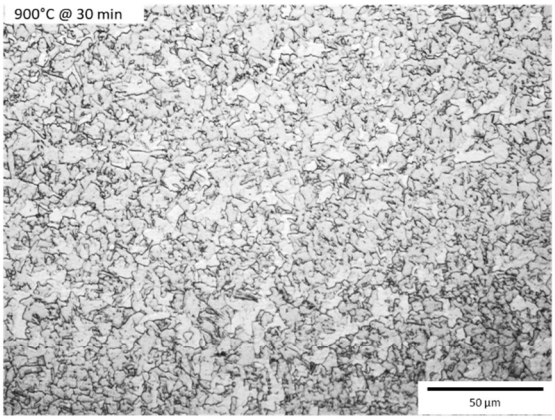

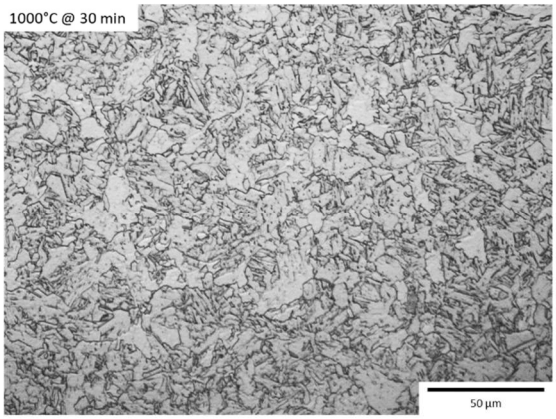

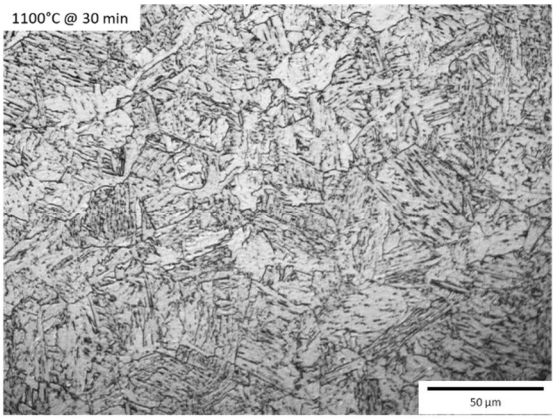

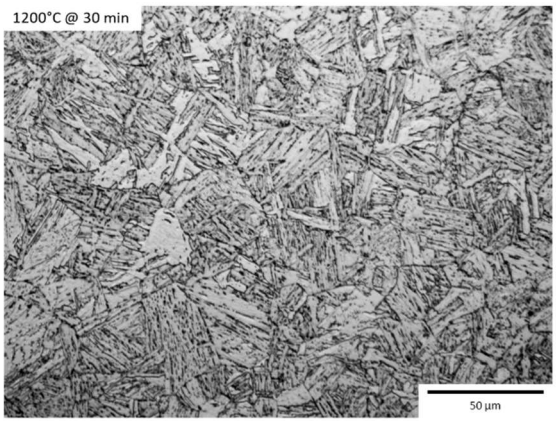

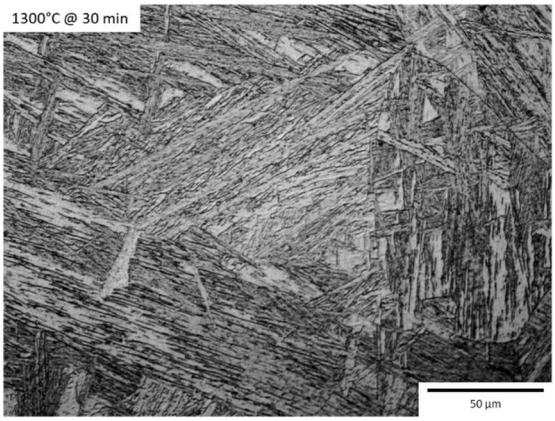

Appendix I.7

Microstructure evolution at 900°C, 1000°C, 1100°C, 1200°C and 1300°C with a cooling rate of 50°C/s.

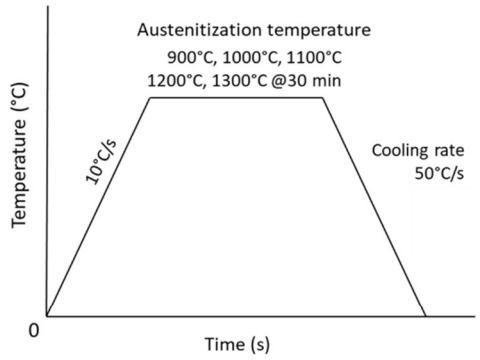

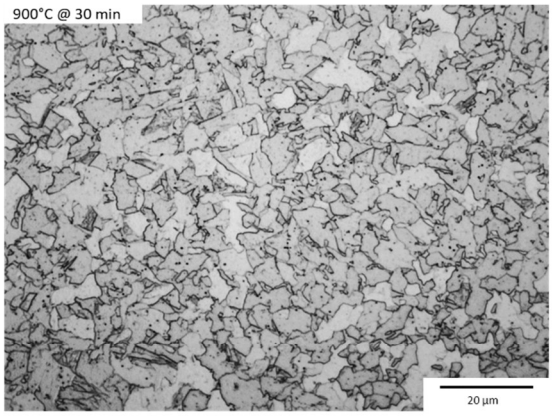

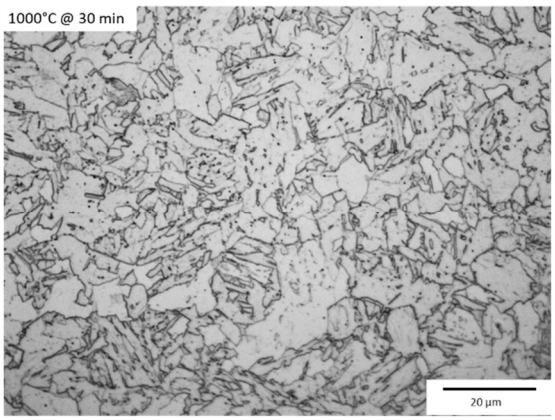

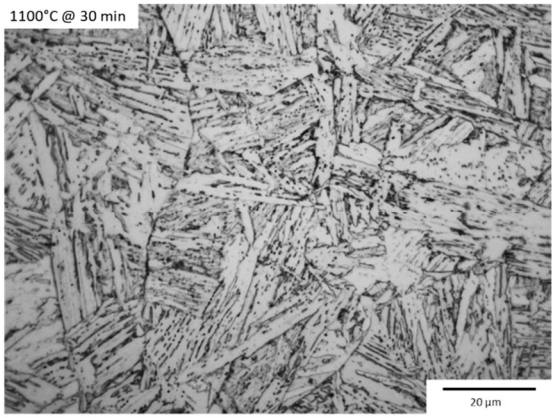

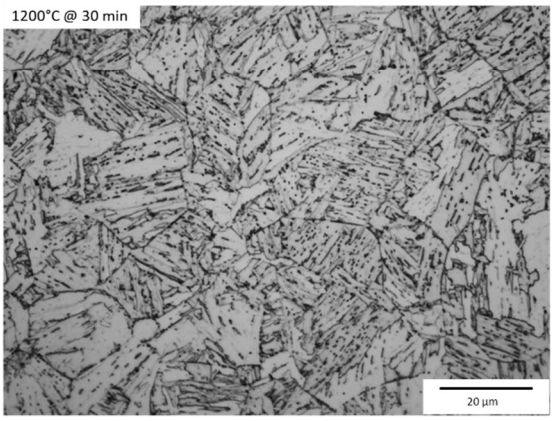

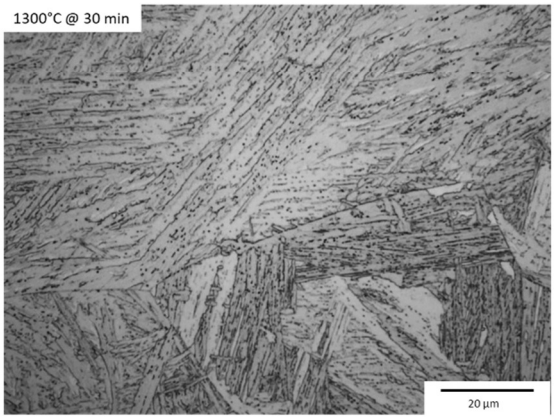

Appendix I.8

Microstructure evolution at 900°C, 1000°C, 1100°C, 1200°C and 1300°C with a cooling rate of 0.5°C/s in SEM.

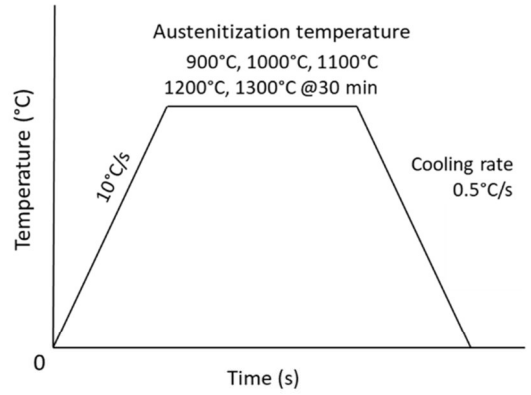

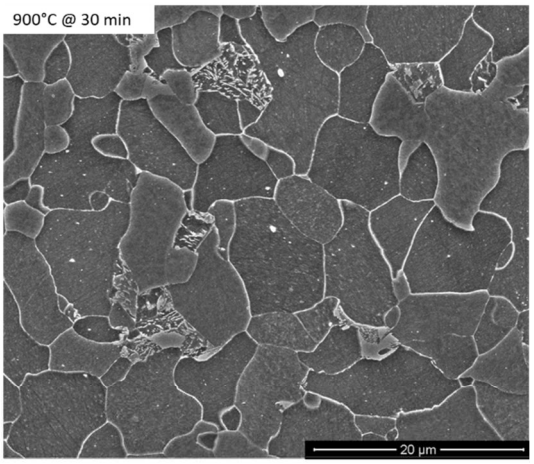

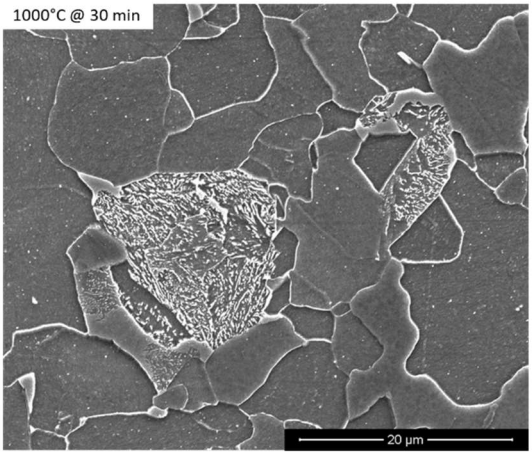

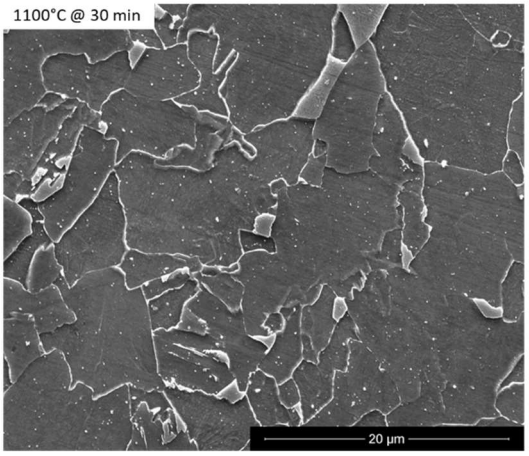

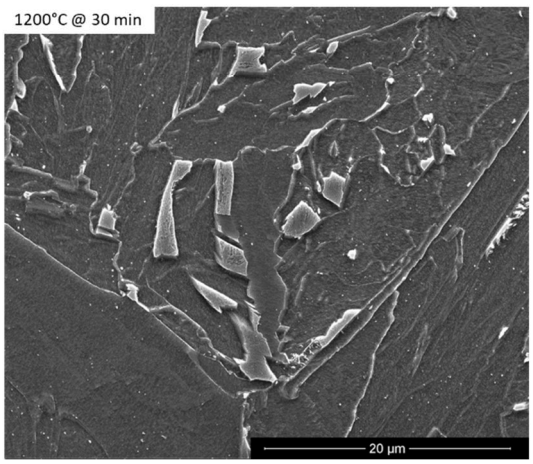

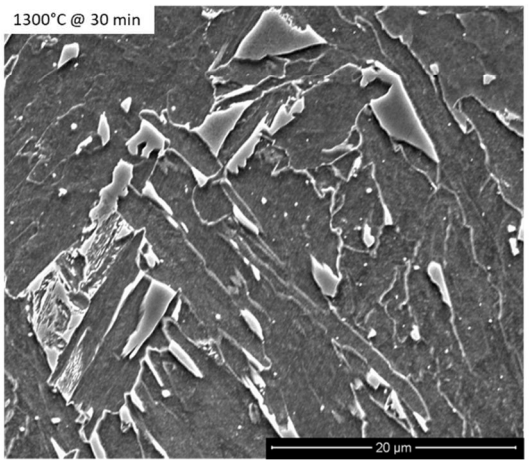

Appendix I.9

Microstructure evolution at 900°C, 1000°C, 1100°C, 1200°C and 1300°C with a cooling rate of 5°C/s in SEM.

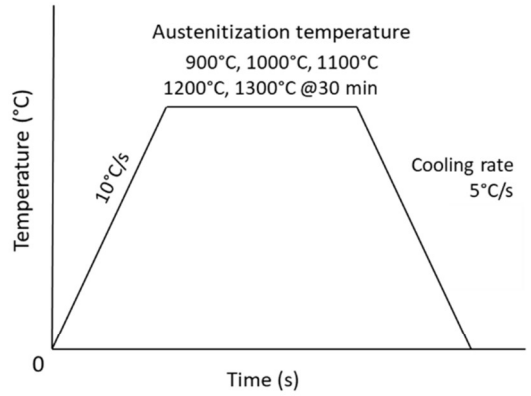

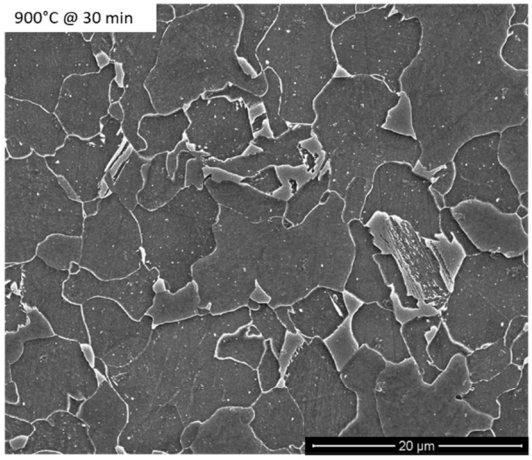

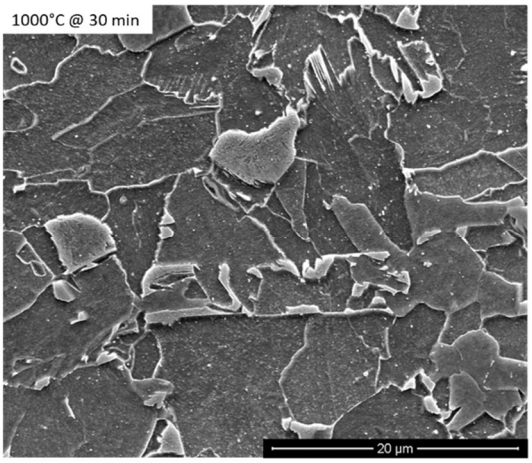

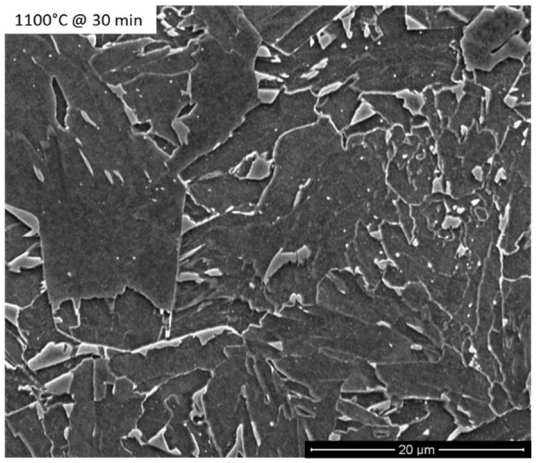

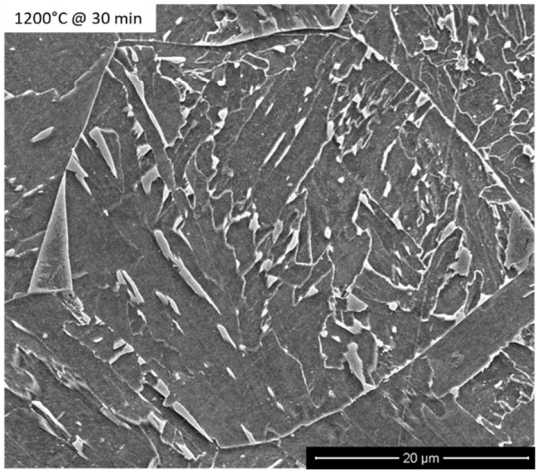

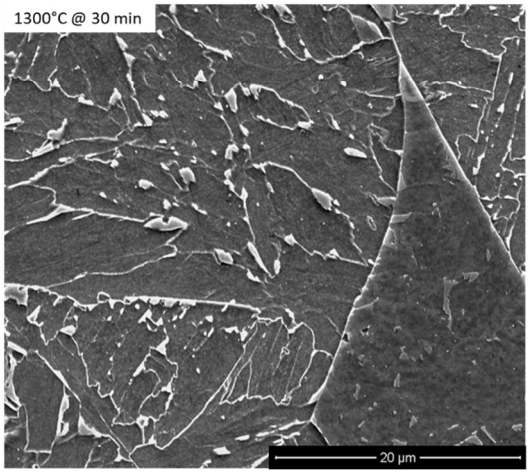

Appendix I.10

Microstructure evolution at 900°C, 1000°C, 1100°C, 1200°C and 1300°C with a cooling rate of 50°C/s in SEM.

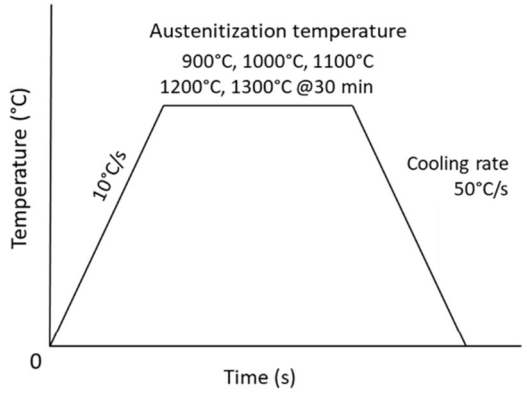

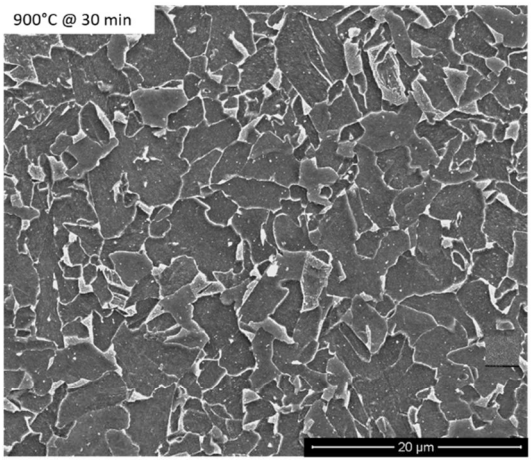

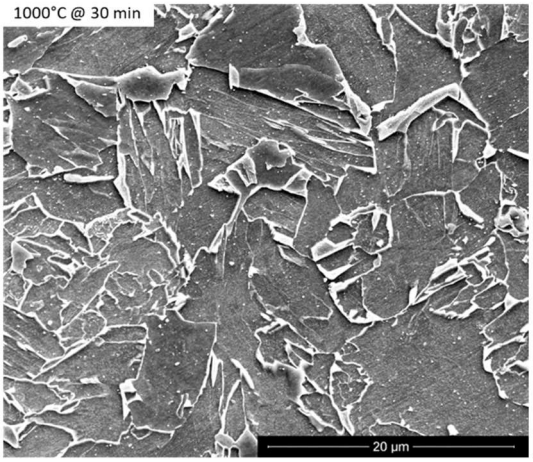

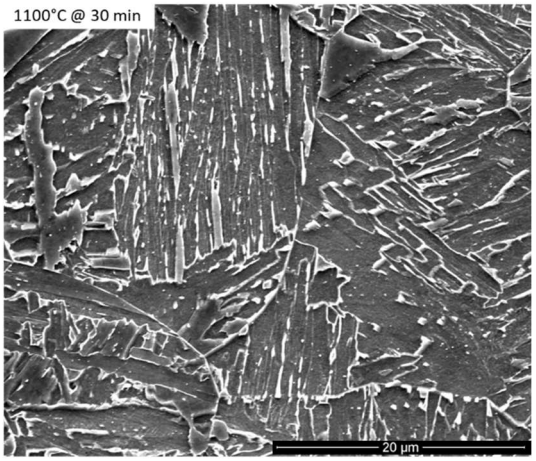

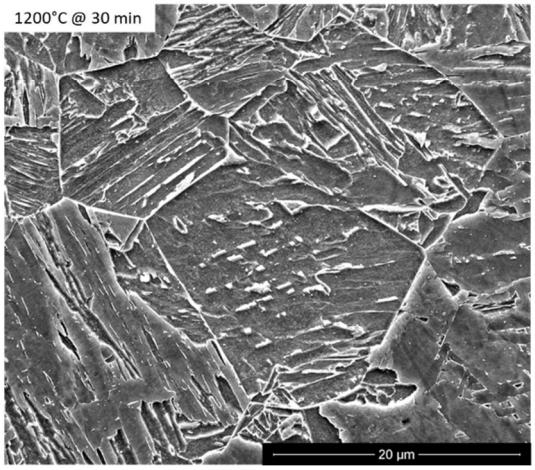

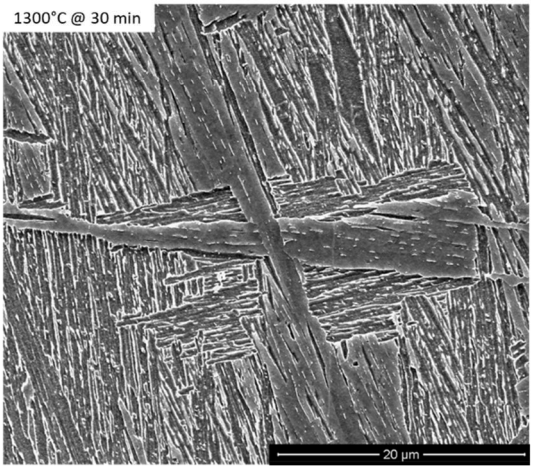

Appendix II

Electron backscattered diffraction mapping

The resulting microstructure is crucial in the evaluation of mechanical properties. The distribution and quantity of phases is critical to determine the influence of each phase on the mechanical properties. EBSD is an important technique in the analysis and quantification of phases. X80 steel meanly consists of a mixture of different microstructures such as ferrite, bainite, martensite, and at slow cooling rates appear pearlite. Also, small quantities of retained austenite in the microstructure could appear depending on the cooling rate.

The next EBSD maps were constructed to identify and detect the quantity of the phases in each condition, except the phases with ferrite and pearlite. Section 4.8 explains the procedure to separate the phases, the procedure is based on the crystal structure of the material using the EBSD. In the quantification of phases were used grain orientation spread, band contrast map, and the aspect ratio which appears in grains. The first criterion in the grain identification was the misorientation angle higher or equal to 5°, after that the minimum grain area must be greater than 0.4μm^2 or 10 pixels.

Appendix II-1

EBSD maps at 1100°C of austenitisation temperature and 0.5°C/s of cooling rate

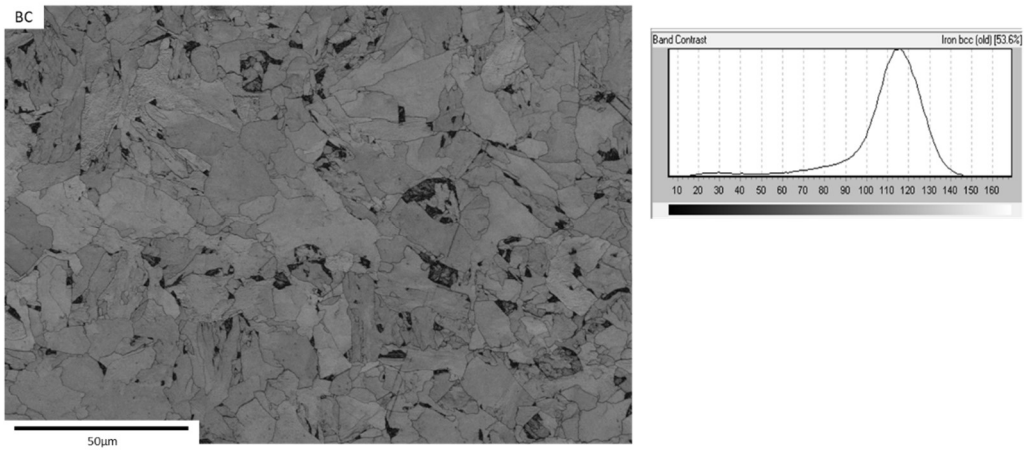

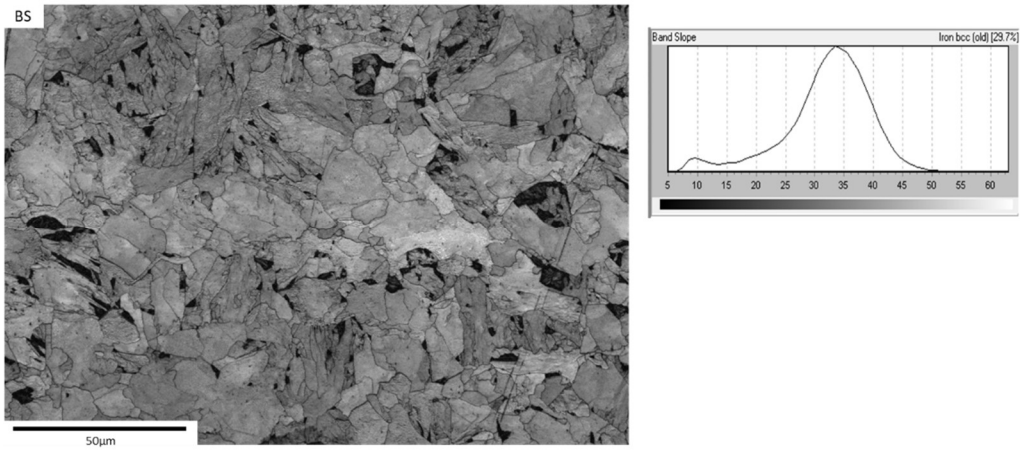

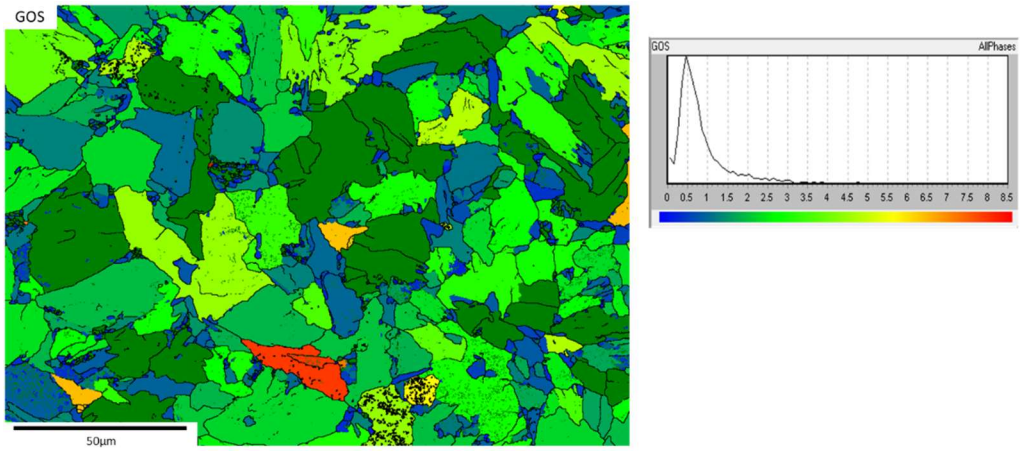

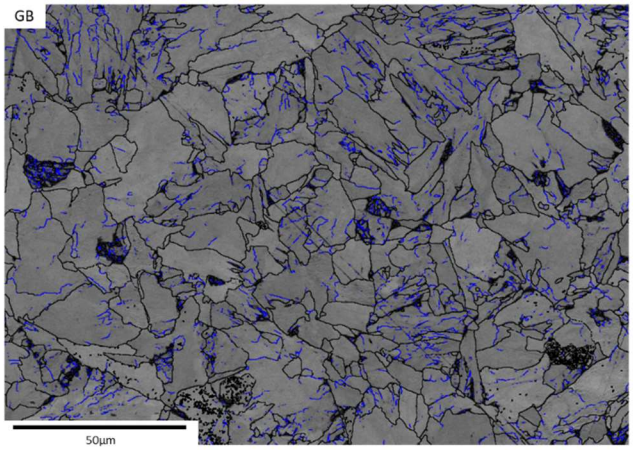
GB
50µm

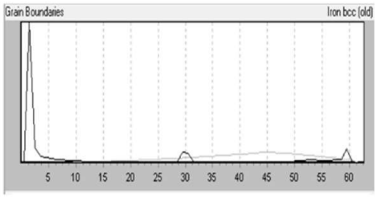
Grain Boundaries
Iron bcc (old)
5
10
15
20
25
30
35
40
45
50
55
60

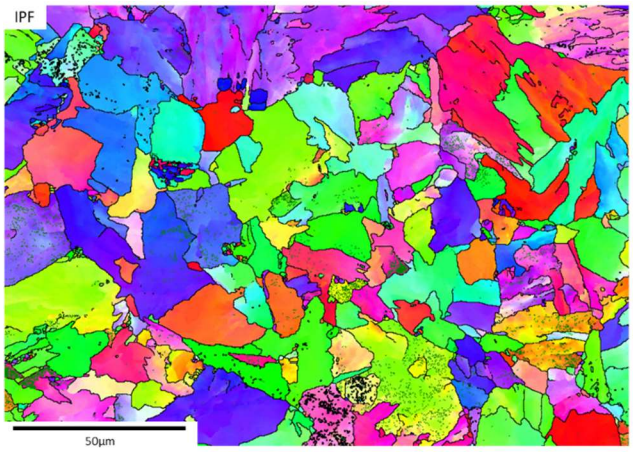
IPF
50µm

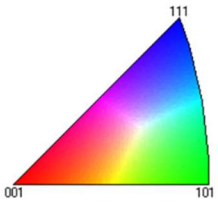
111
001
101

Appendix II-2

EBSD maps at 1200°C of austenitisation temperature and 0.5°C/s of cooling rate

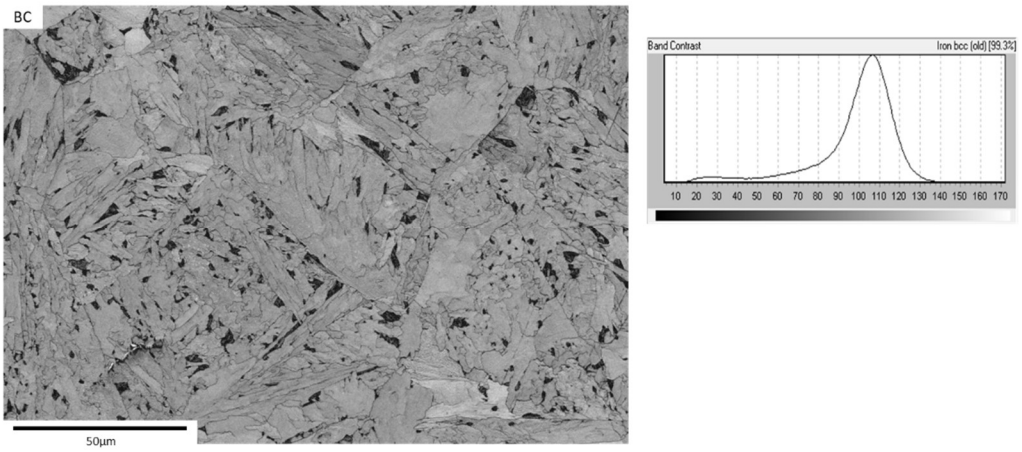

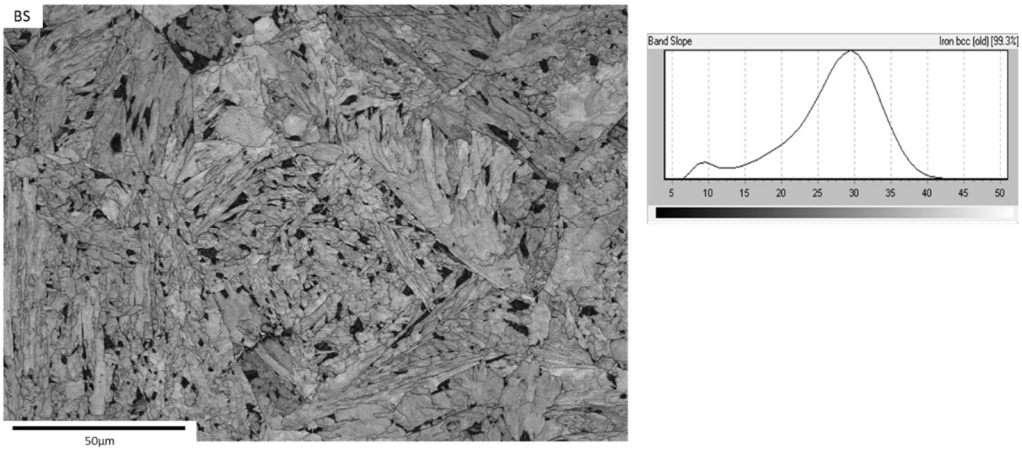

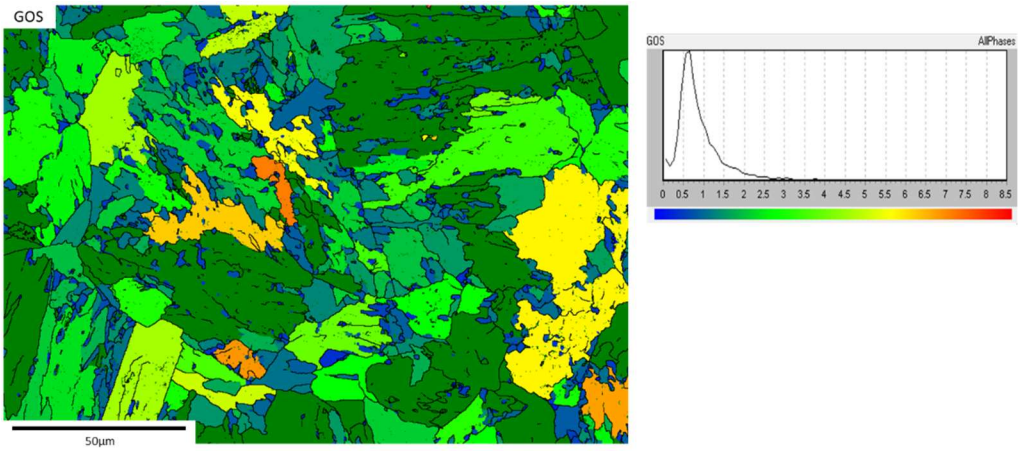

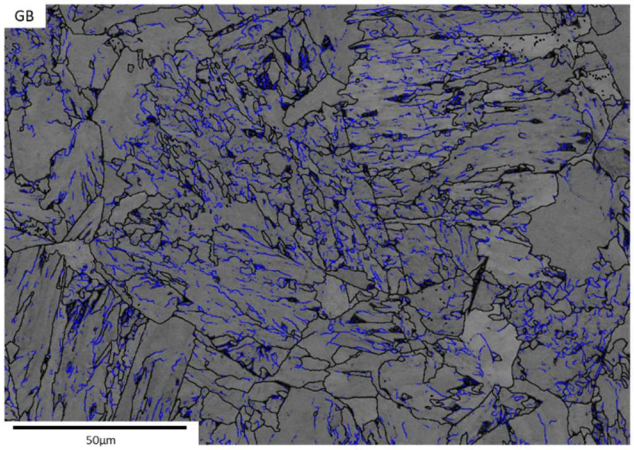
GB
50µm

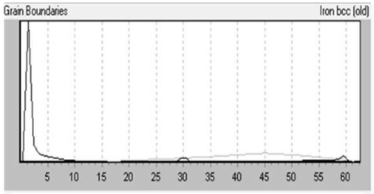
Grain Boundaries
Iron bcc (old)
5 10 15 20 25 30 35 40 45 50 55 60

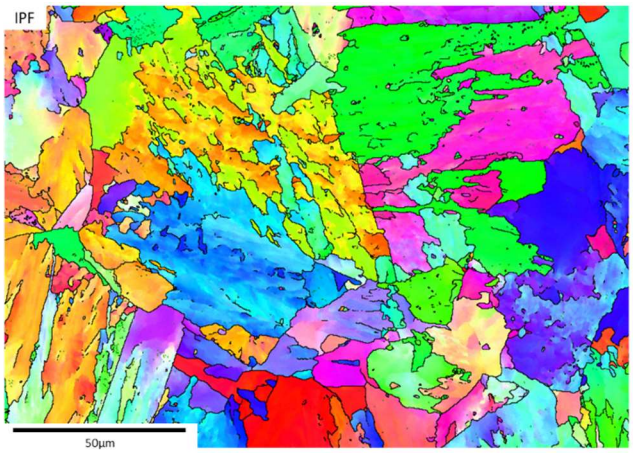
IPF
50µm

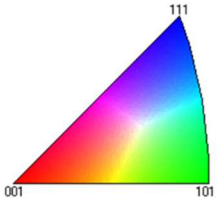
111
001
101

Appendix II-3

EBSD maps at 1300°C of austenitisation temperature and 0.5°C/s of cooling rate

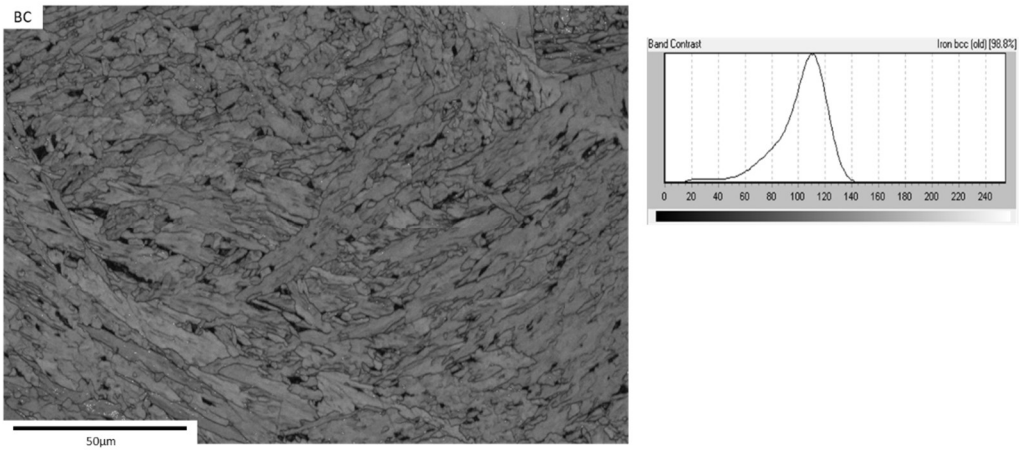

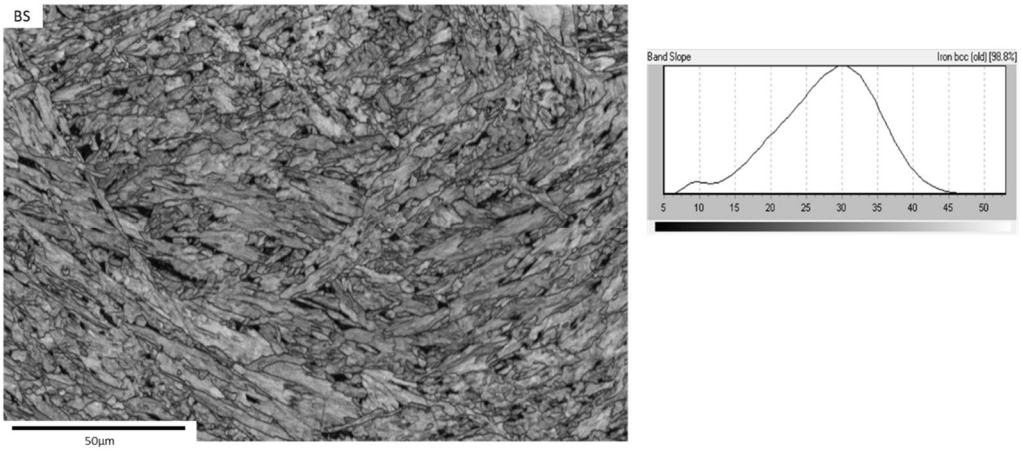

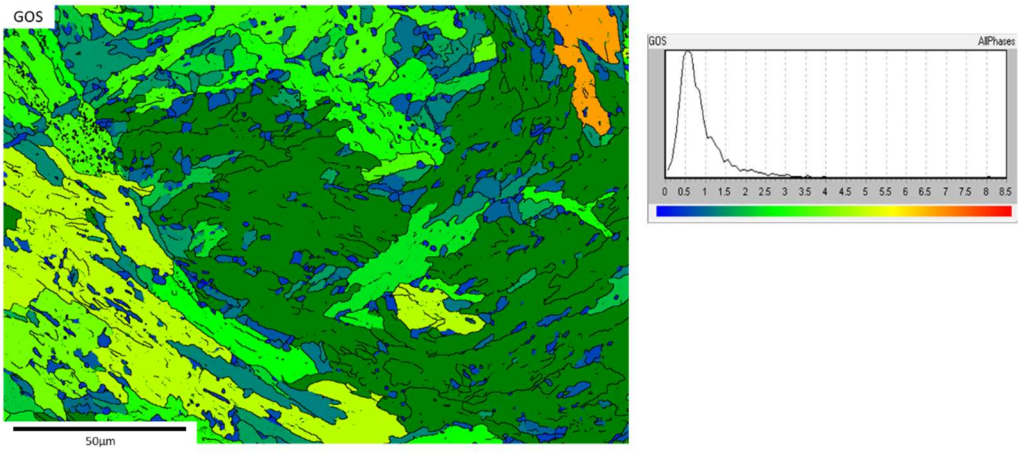

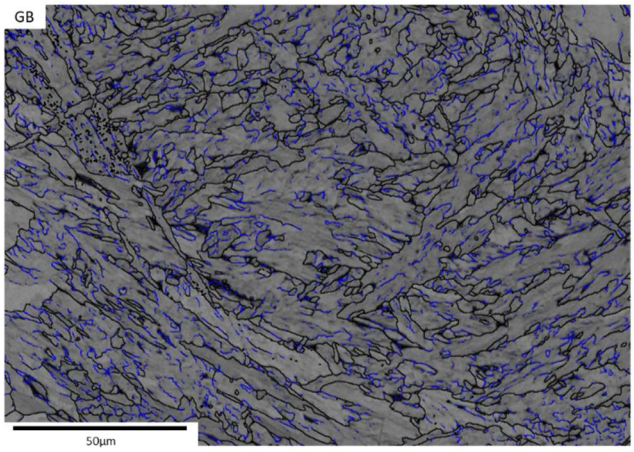
GB
50µm

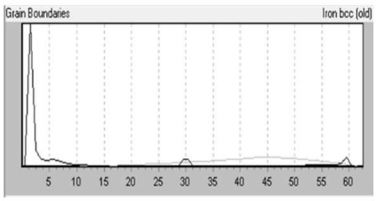
Grain Boundaries
Iron bcc (old)
5
10
15
20
25
30
35
40
45
50
55
60

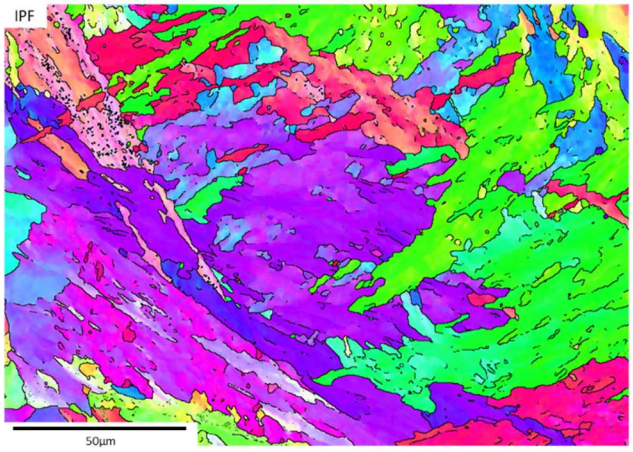
IPF
50µm

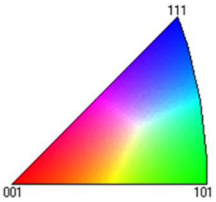
111
001
101

Appendix II-4

EBSD maps at 1000°C of austenitisation temperature and 5°C/s of cooling rate

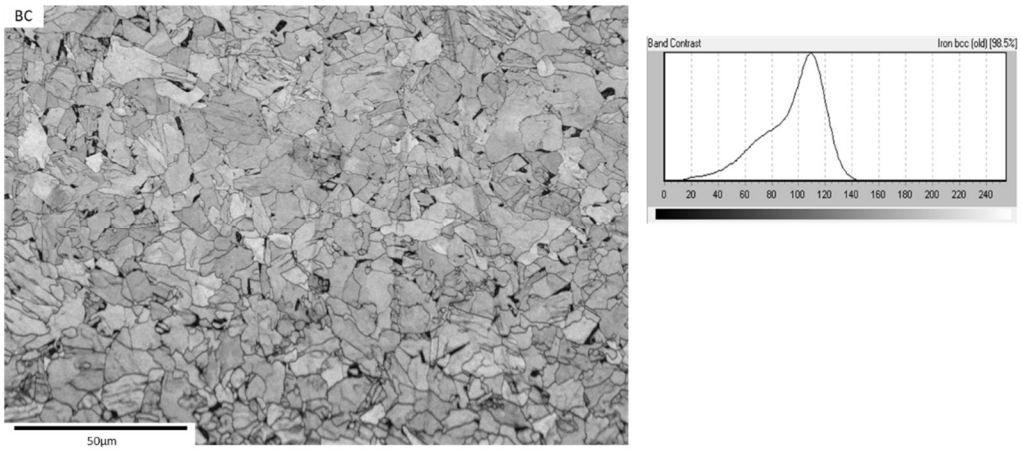

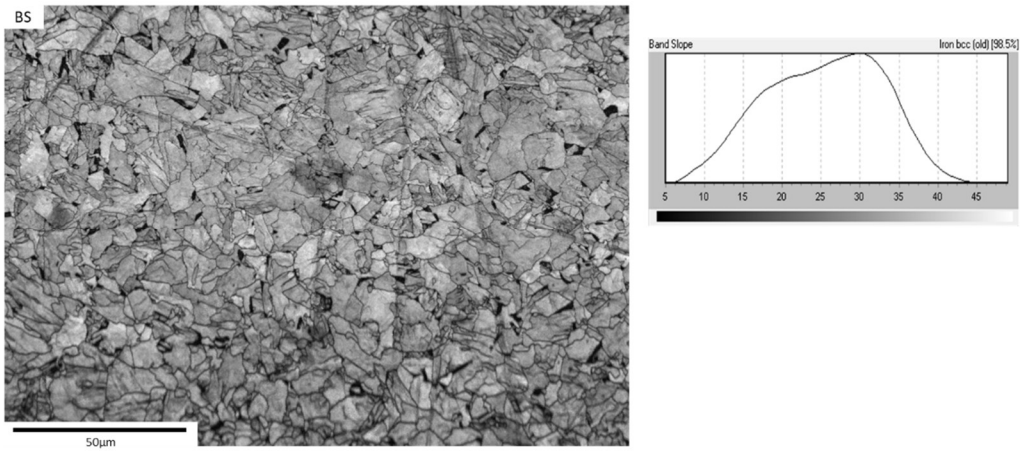

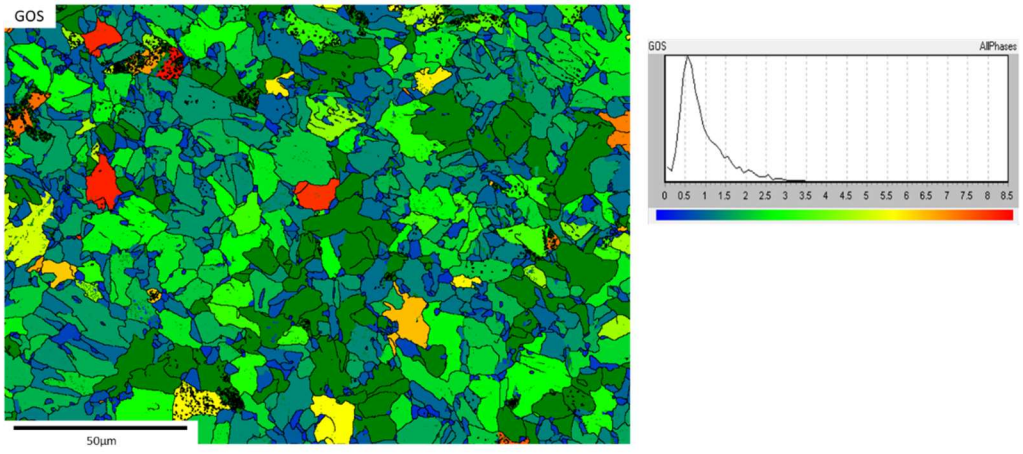

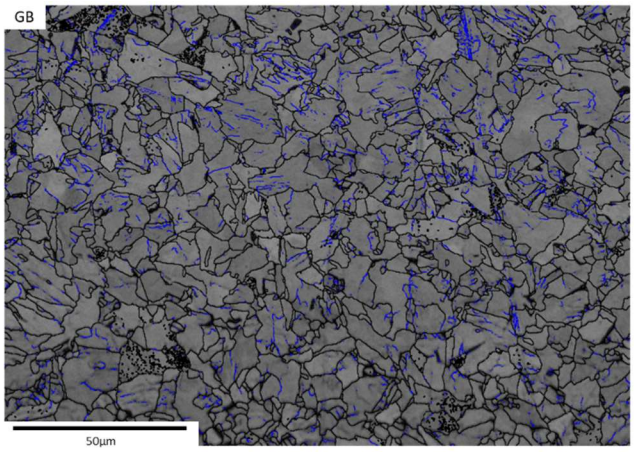
GB
50µm

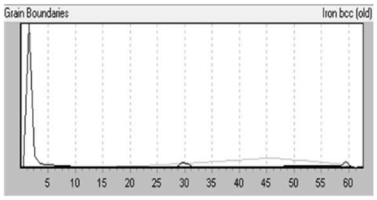
Grain Boundaries
Iron bcc (old)
5 10 15 20 25 30 35 40 45 50 55 60

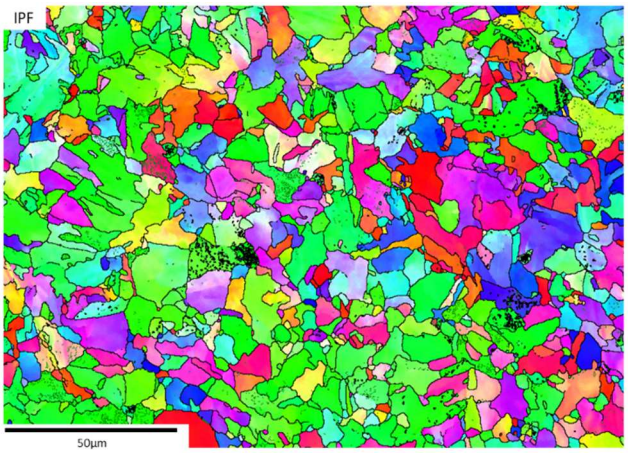
IPF
50µm

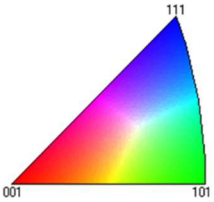
111
001
101

Appendix II-5

EBSD maps at 1100°C of austenitisation temperature and 5°C/s of cooling rate

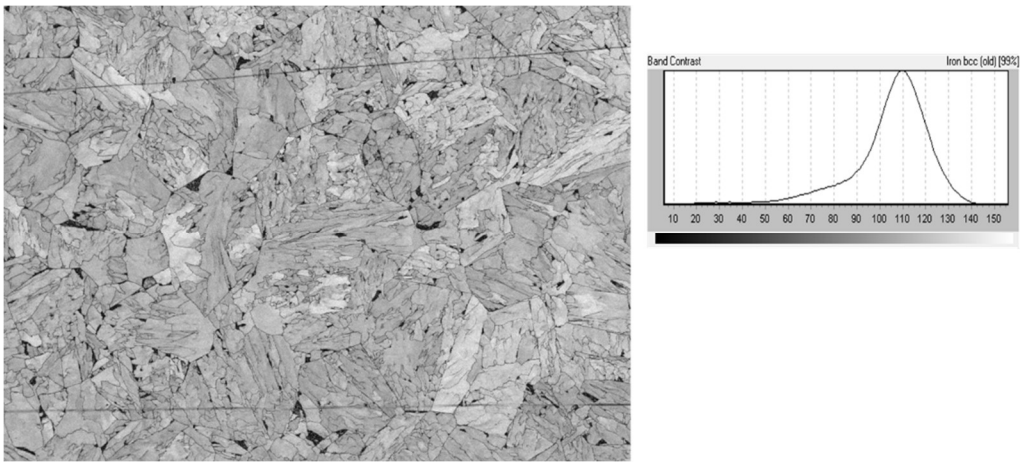

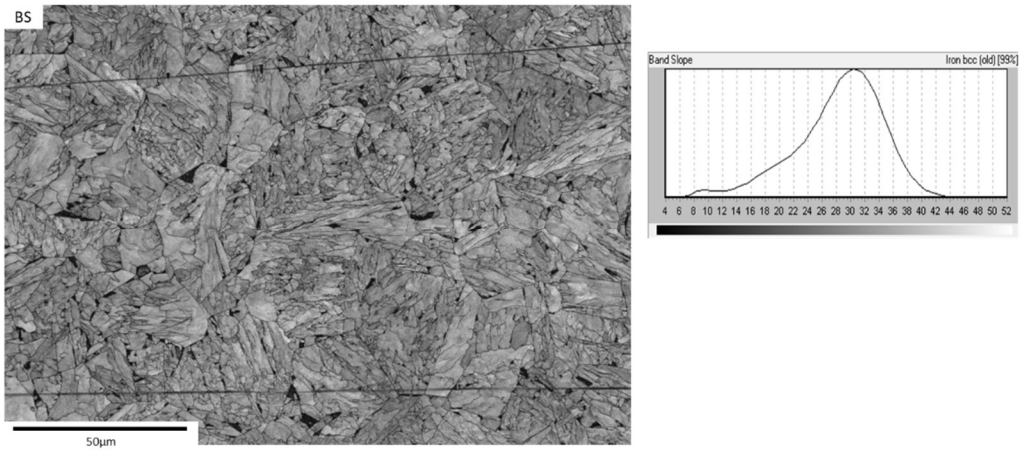

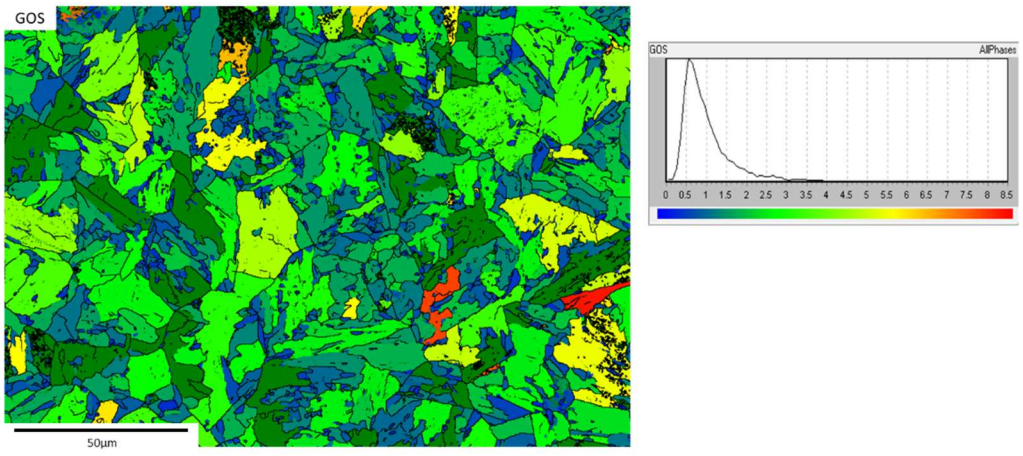

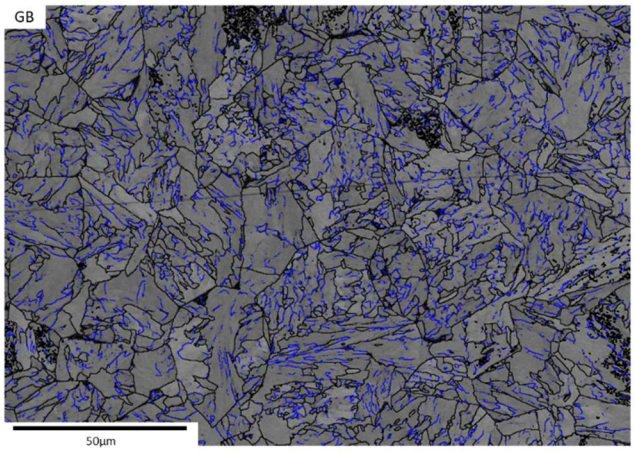
GB
50µm

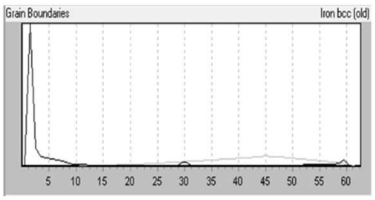
Grain Boundaries
Iron bcc (old)
5 10 15 20 25 30 35 40 45 50 55 60

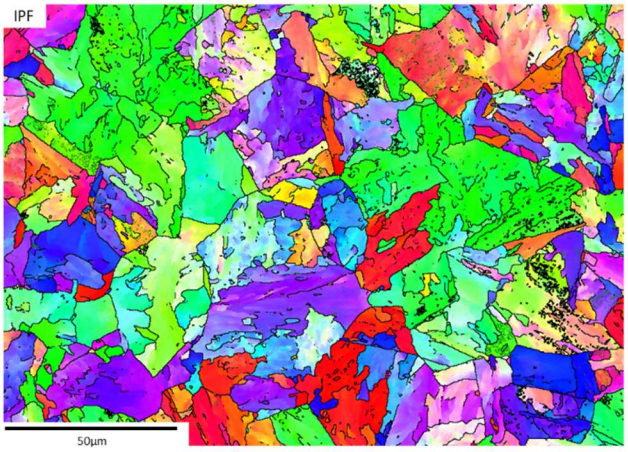
IPF
50µm

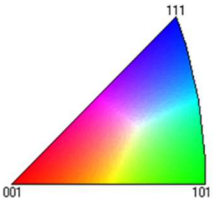
111
001
101

Appendix II-6

EBSD maps at 1200°C of austenitisation temperature and 5°C/s of cooling rate

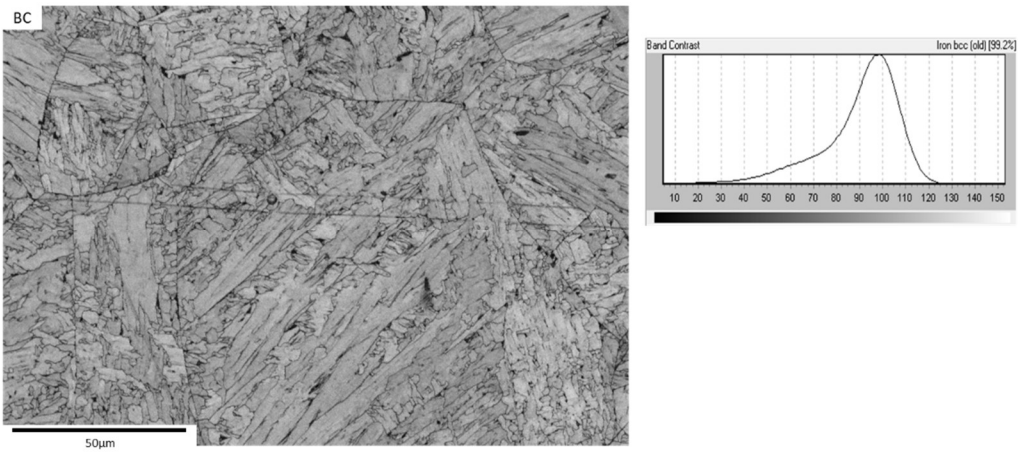

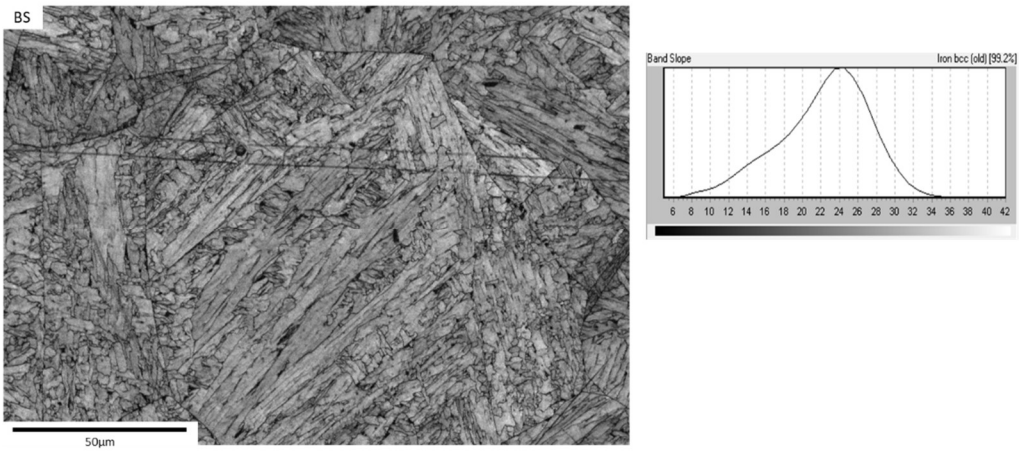

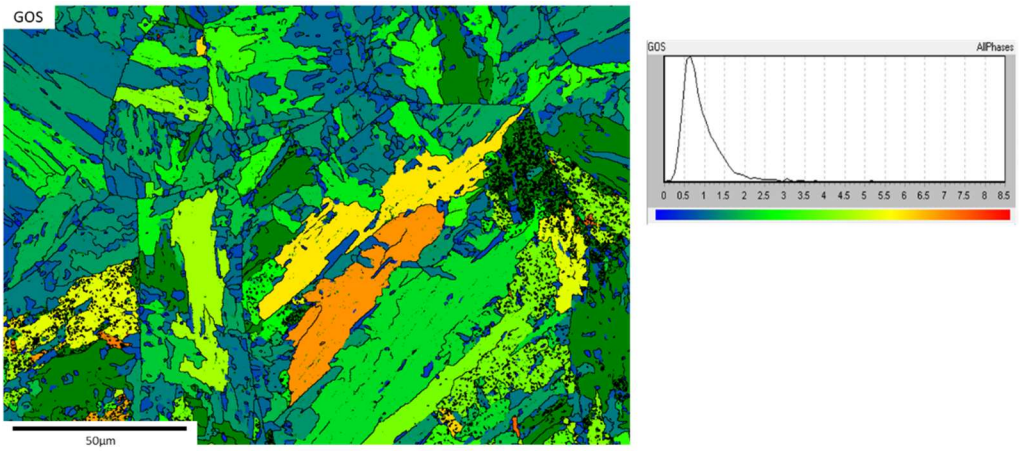

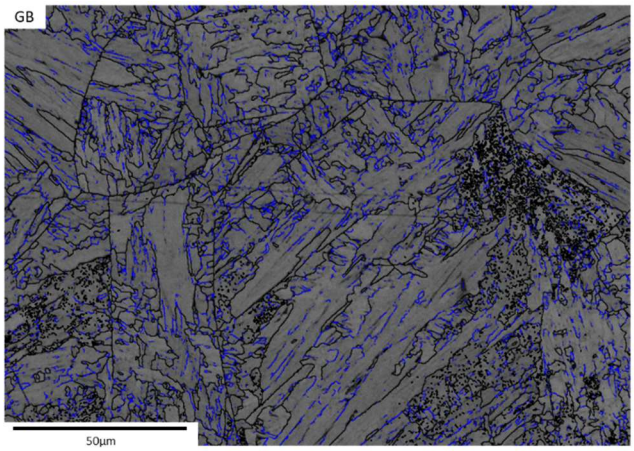
GB
50µm

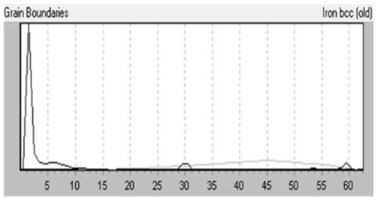
Grain Boundaries
Iron bcc (old)
5 10 15 20 25 30 35 40 45 50 55 60

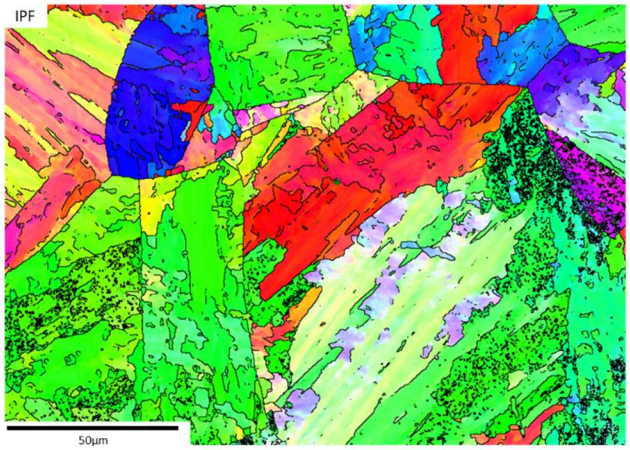
IPF
50µm

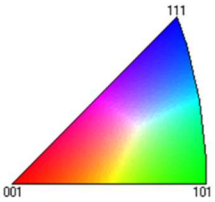
111
001
101

Appendix II-7

EBSD maps at 1300°C of austenitisation temperature and 5°C/s of cooling rate

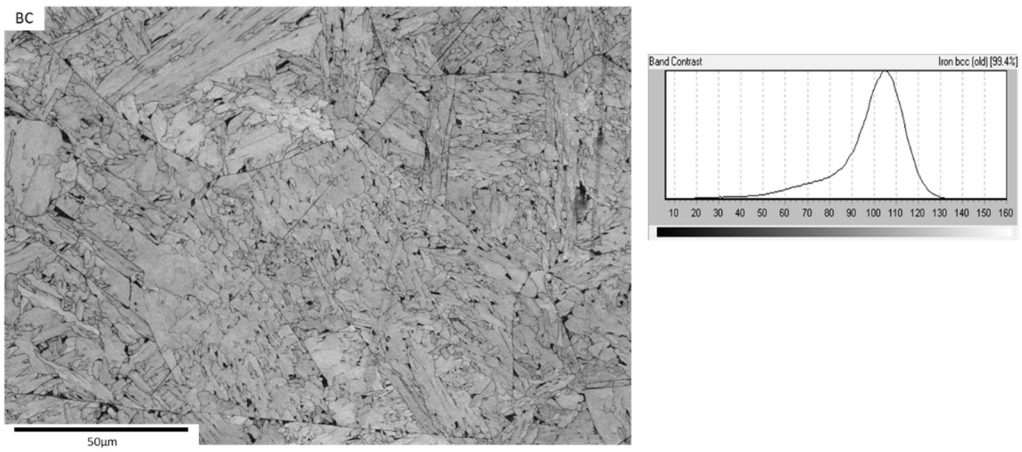

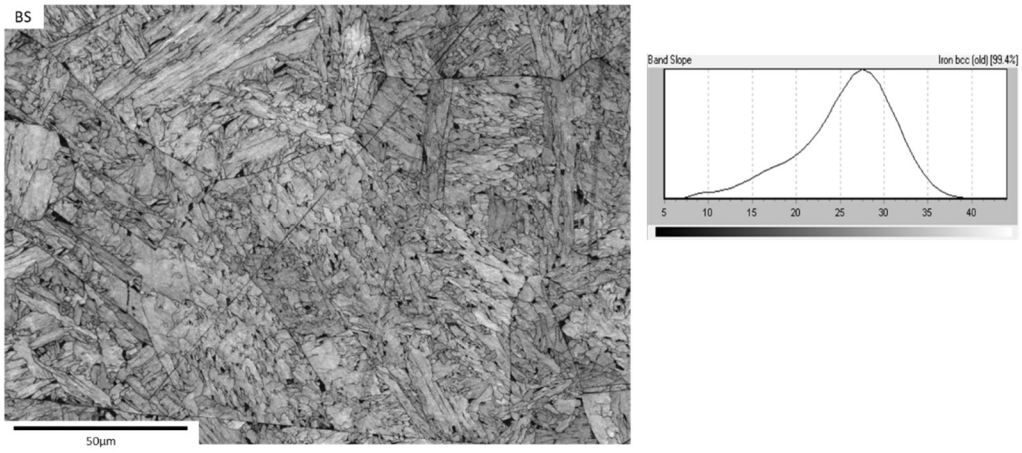

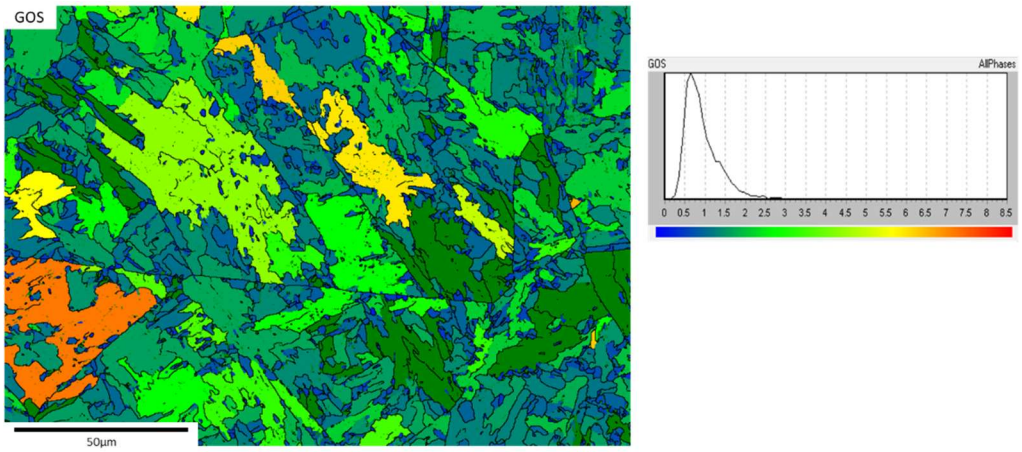

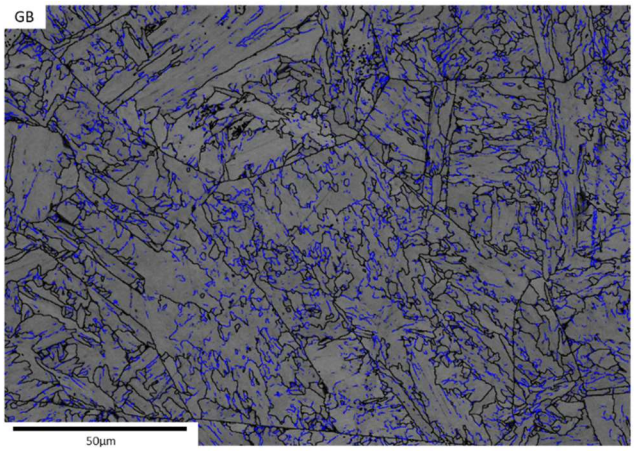
GB
50µm

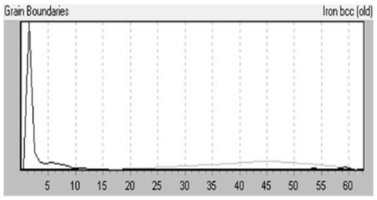
Grain Boundaries
Iron bcc (old)
5 10 15 20 25 30 35 40 45 50 55 60

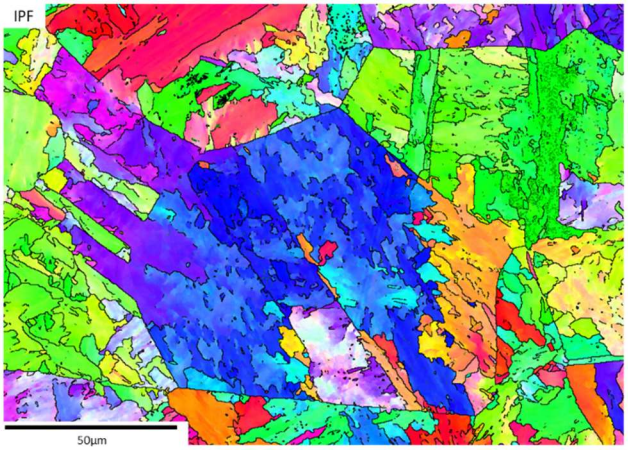
IPF
50µm

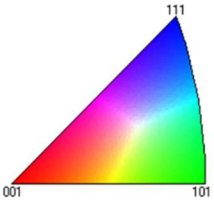
111
001
101

Appendix II-8

EBSD maps at 1100°C of austenitisation temperature and 50°C/s of cooling rate

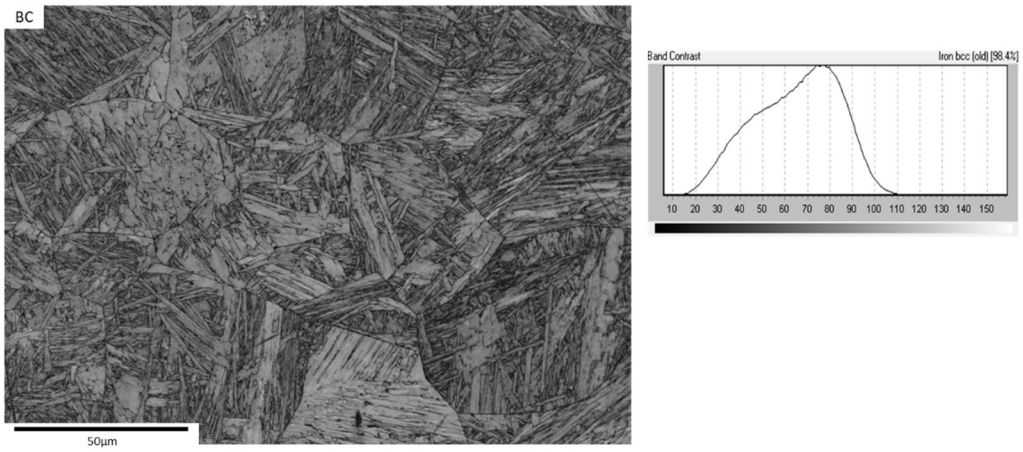

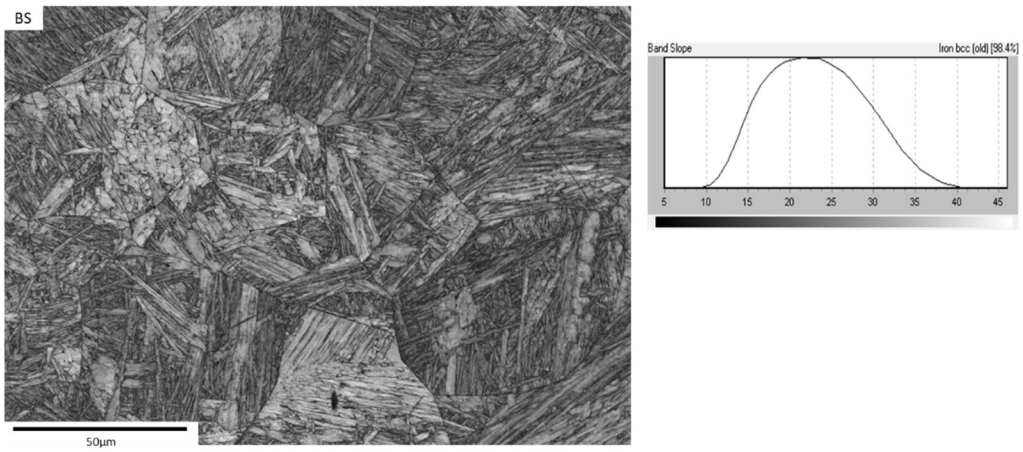

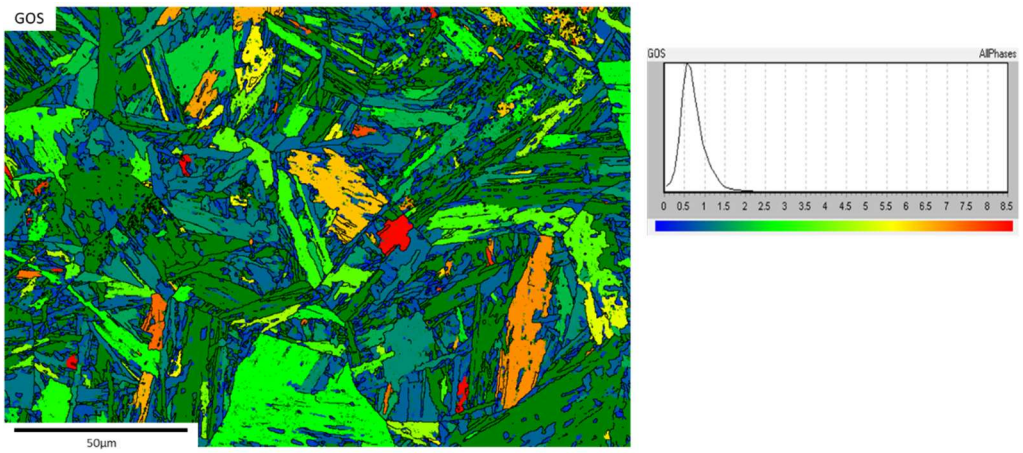

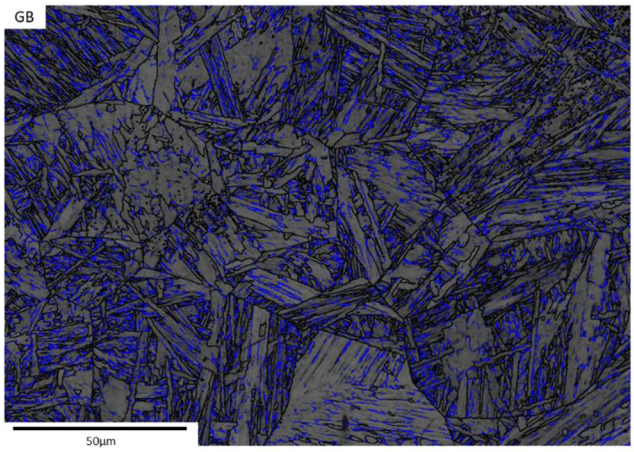
GB
50µm

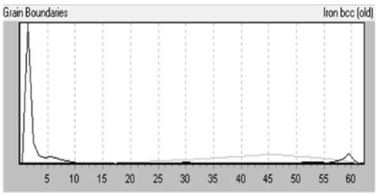
Grain Boundaries
Iron bcc (old)
5 10 15 20 25 30 35 40 45 50 55 60

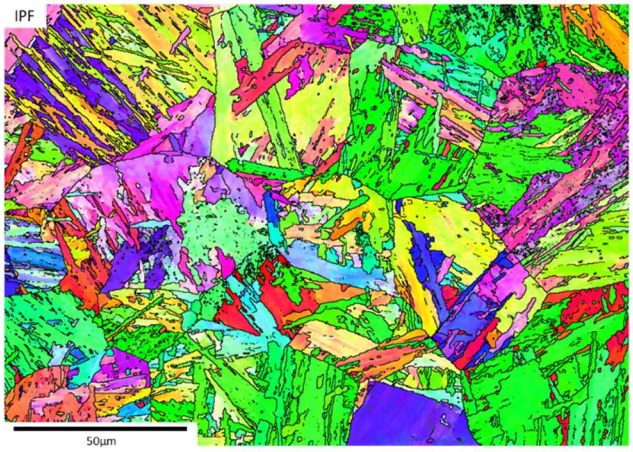
IPF
50µm

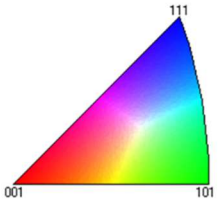
111
001
101

Appendix II-9

EBSD maps at 1200°C of austenitisation temperature and 50°C/s of cooling rate

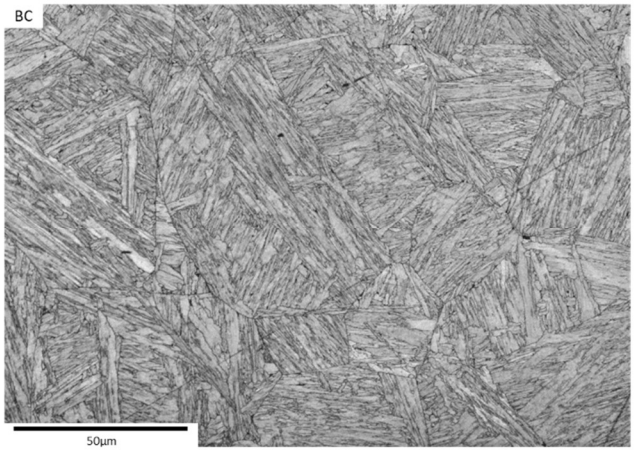

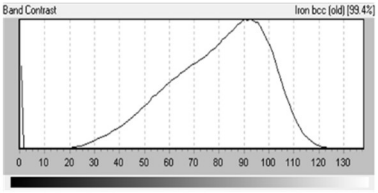

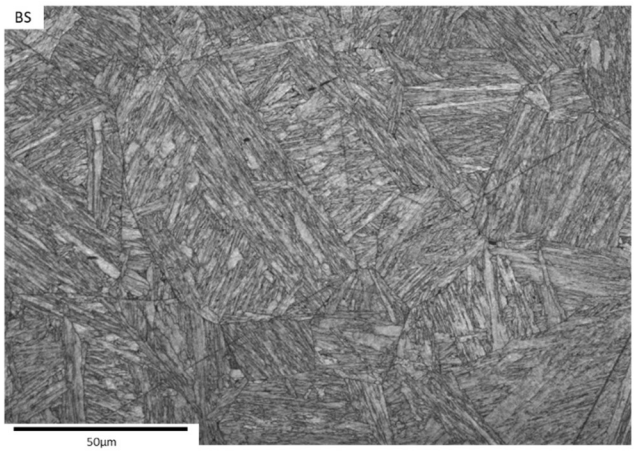

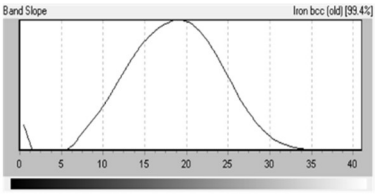

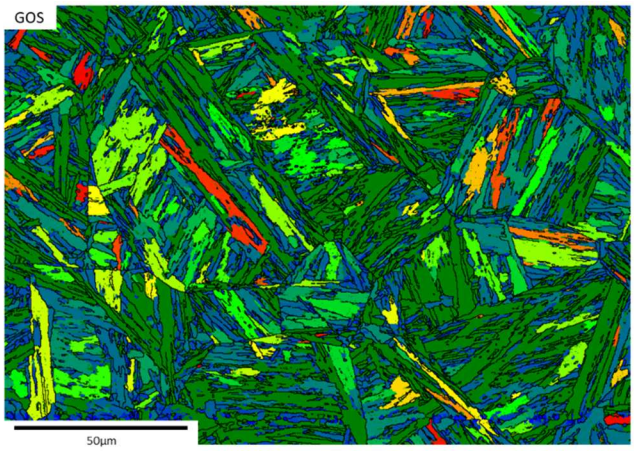

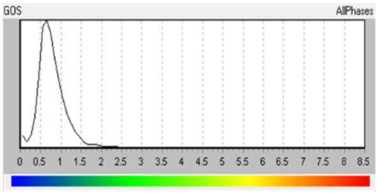

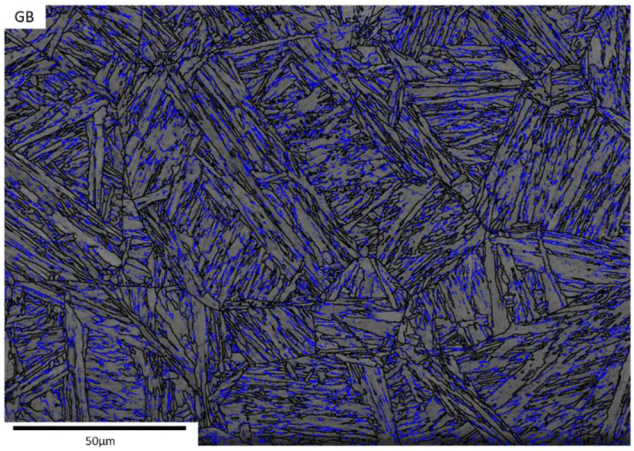
GB
50µm

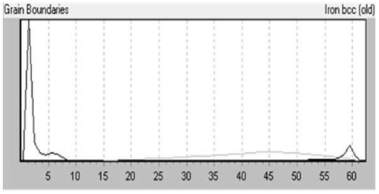
Grain Boundaries
Iron bcc (old)
5 10 15 20 25 30 35 40 45 50 55 60

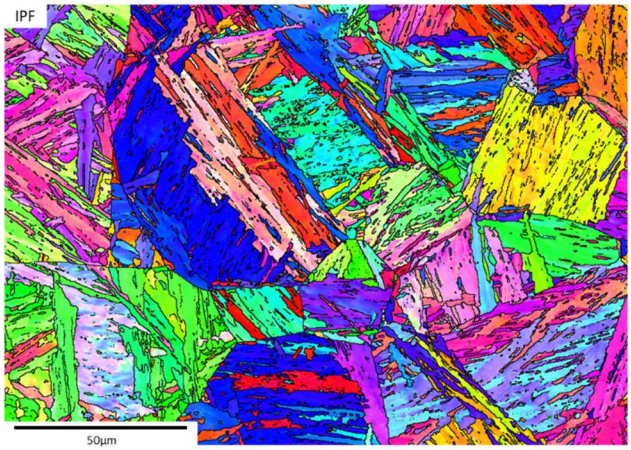
IPF
50µm

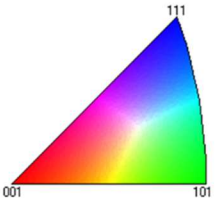
111
001
101

Appendix II-10

EBSD maps at 1300°C of austenitisation temperature and 50°C/s of cooling rate

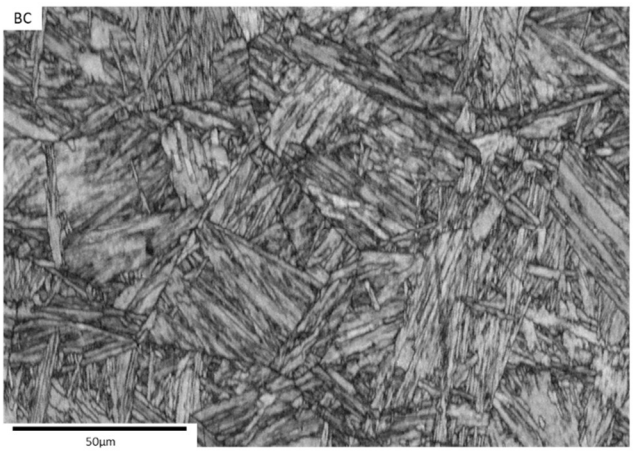

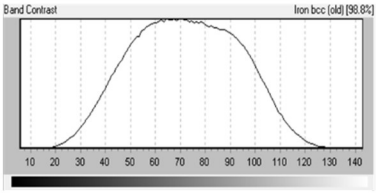

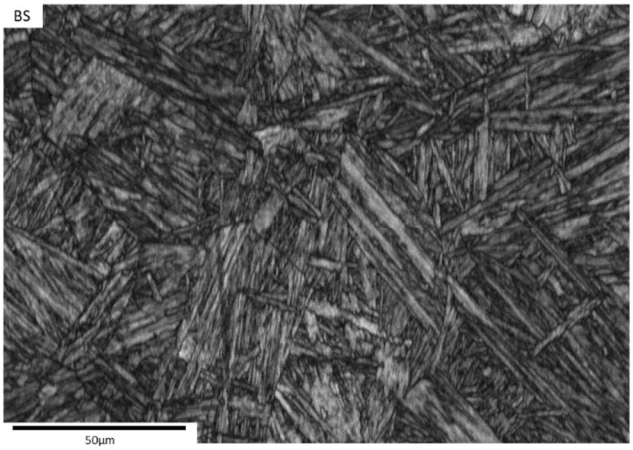

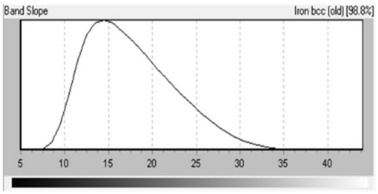

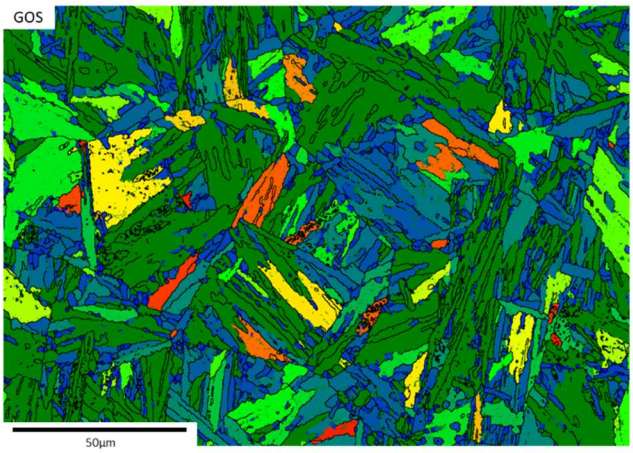

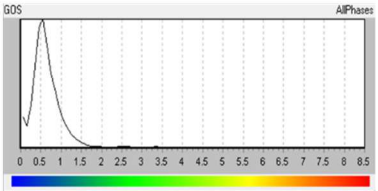

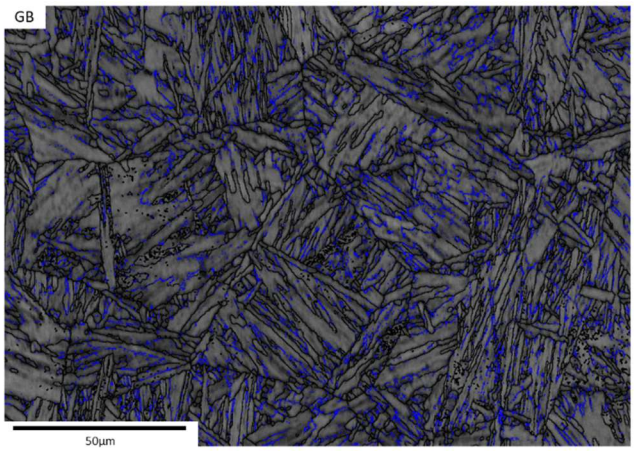
GB
50µm

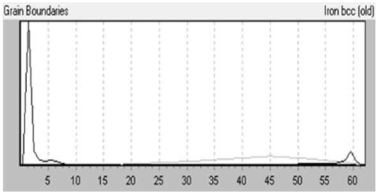
Grain Boundaries
Iron bcc (old)
5
10
15
20
25
30
35
40
45
50
55
60

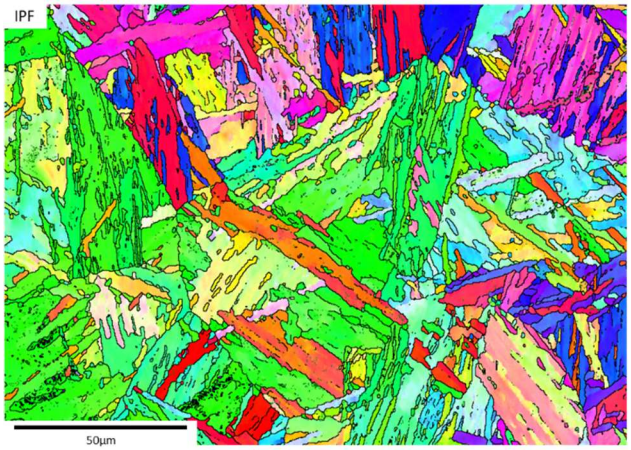
IPF
50µm

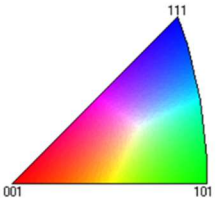
111
001
101